WHOI-93-50

(1)

Woods Hole Oceanographic Institution
Massachusetts Institute of Technology

Joint Program in Oceanography/ Applied Ocean Science and Engineering

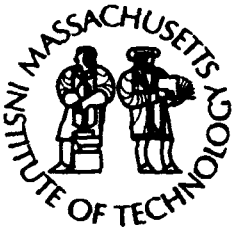

DOCTORAL DISSERTATION

Surface Exposure Geochronology Using Cosmogenic Nuclides: Applications in Antarctic Glacial Geology

by

Edward J. Brook

February 1994

WHOI-93-50

Surface Exposure Geochronology Using Cosmogenic Nuclides: Applications in Antarctic Glacial Geology

by

Edward J. Brook

Woods Hole Oceanographic Institution
Woods Hole, Massachusetts 02543

and

The Massachusetts Institute of Technology
Cambridge, Massachusetts 02139

February 1994

DOCTORAL DISSERTATION

Funding was provided by the National Science Foundation under Grants DPP88-17406, DPP91-17458, EAR91-06810, the Ocean Ventures Fund of the Woods Hole Oceanographic Institution and by a National Defense Science and Engineering Graduate Fellowship from the Office of Naval Research.

Approved for publication; distribution unlimited.

Approved for Distribution:

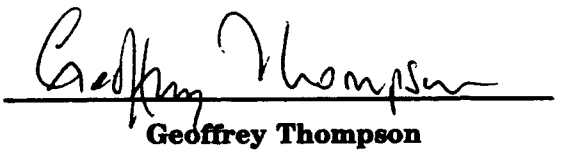

Geoffrey Thompson
Department of Marine Chemistry and Geochemistry

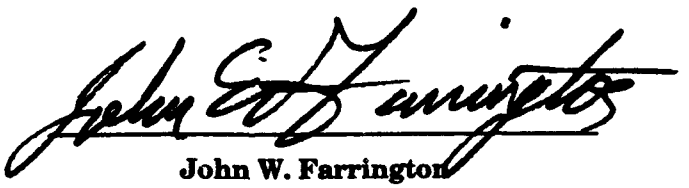

John W. Farrington
Dean of Graduate Studies

SURFACE EXPOSURE GEOCHRONOLOGY USING COSMOGENIC NUCLIDES: APPLICATIONS IN ANTARCTIC GLACIAL GEOLOGY

by

EDWARD JEREMY BROOK

B. S., Duke University, 1985
M. S., University of Montana, 1988

submitted in partial fulfillment of the requirements for the degree of

DOCTOR OF PHILOSOPHY

at the

MASSACHUSETTS INSTITUTE OF TECHNOLOGY

and the

WOODS HOLE OCEANOGRAPHIC INSTITUTION

September 1993

Signature of Author 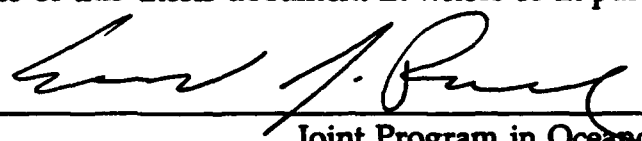

Joint Program in Oceanography
Massachusetts Institution of Technology
Woods Hole Oceanographic Institution

Certified by 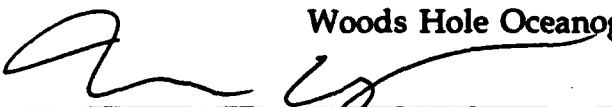

Dr. Mark D. Kurz
Thesis Supervisor

Accepted by 

Dr. Edward A. Boyle, Acting Chairman
Joint Committee for Chemical Oceanography
Massachusetts Institution of Technology
Woods Hole Oceanographic Institution

Surface Exposure Geochronology Using Cosmogenic Nuclides: Applications in Antarctic Glacial Geology

by

Edward Jeremy Brook

Abstract

Cosmogenic ^{3}He, ^{26}Al, and ^{10}Be have been measured in a variety of Antarctic glacial deposits in the McMurdo Sound-Dry Valleys region. The goals of this project were to provide age constraints for Antarctic glacial events, to investigate production mechanisms of ^{3}He, ^{10}Be, and ^{26}Al in terrestrial rocks, to constrain the importance of loss of ^{3}He from quartz due to diffusion, and to refine methods of exposure-age dating.

Moraines deposited in Arena Valley by the Taylor Glacier, an outlet glacier of the East Antarctic Ice Sheet, have exposure ages from ~120 kyr to 2 myr. ^{10}Be and ^{3}He ages of 122 ± 29 and 134 ± 54 kyr, respectively, for the Taylor II moraine are consistent with deposition during isotope stage 5e (~ 120 kyr) and with aerial expansions of the East Antarctic Ice Sheet during interglacial periods. Mean ^{10}Be exposure ages for older moraines in the valley are 362 ± 26 kyr (Taylor III), 1.1 ± 0.1 myr (Taylor IVa) and 1.9 ± 0.1 myr (Taylor IVb). Because these older moraines were deposited at most ~200 m above the Taylor II limit their ages suggest that major ice sheet advances during the last 2 myr have been broadly similar in magnitude to changes during the last glacial-interglacial cycle. ^{10}Be ages for stratigraphically older drift deposited by the Taylor Glacier allow extension of this conclusion to ~ 3 myr.

^{10}Be measurements in high altitude, pre-Pleistocene glacial deposits in the Dry Valleys preclude rapid uplift of the Transantarctic Mountains (400-1000 m/myr) suggested by controversial biostratigraphic studies of Sirius Group tills. Comparison of measured ^{10}Be concentrations in Sirius Group deposits with those predicted with a model of the effects of uplift on ^{10}Be production suggests minimal uplift of the Transantarctic Mountains over the last 3 myr.

^{3}He, ^{10}Be and ^{26}Al ages for the "late Wisconsin" Ross Sea Drift, a glacial drift deposited on the coast of McMurdo Sound by the Ross Sea Ice Sheet, range from 8-106 kyr. The age range suggests that this deposit does not, as previous studies suggested, represent a single ice advance in response to lowered sea level at the last glacial maximum. The age range may reflect several ice sheet advances during the last glacial period.

Paired measurements of ^{3}He and ^{10}Be in a number of quartz sandstones from the Dry Valleys region show that cosmogenic ^{3}He is not completely retained on time scales of greater than 200 kyr. The ^{3}He and ^{10}Be data, combined with measurements of ^{3}He concentrations in quartz as a function of grain size, suggest effective ^{3}He diffusion coefficients in quartz from ~10^{-19} to 10^{-17} cm^2 s^{-1}. These values are one to three orders of magnitude greater than previous experimental determinations extrapolated

to low temperature. The data also suggest that ^{3}He diffusion rates in quartz do not follow simple volume diffusion trends and are probably sample dependent.

Crushing quartz grains *in vacuo* releases variable concentrations of ^{3}He and ^{4}He and releases helium with surprisingly high isotopic compositions, up to 148 x R_a (R_a = atmospheric $^{3}He/^{4}He$ ratio : 1.384×10^{-6}). The high ratios suggest that crushing releases cosmogenic ^{3}He. As a result, *in vacuo* crushing cannot be used to correct ^{3}He concentrations in quartz for a magmatic or "non-cosmogenic" component, as is possible in olivine and clinopyroxene phenocrysts in volcanic rocks.

Replicate analyses of quartz samples show widely varying ^{4}He concentrations and constant ^{3}He concentrations. These data allow constraint of the nucleogenic $^{3}He/^{4}He$ production ratio to less than 0.05 ± 0.2 R_a. Corrections to exposure ages for nucleogenic ^{3}He are in most cases < 1 % of total ^{3}He.

Depth profiles of ^{10}Be and ^{26}Al in two quartz sandstone bedrock cores have exponential attenuation lengths of 145 ± 5 and 145 ± 6 g cm^{-2} (^{10}Be) and 153 ± 13 and 152 ± 5 g cm^{-2} (^{26}Al). The close agreement between the apparent attenuation lengths for the two nuclides supports previous suggestions that the $^{26}Al/^{10}Be$ ratio does not change with depth and therefore can be used as an independent chronometer. ^{3}He profiles in 0.5-0.7 mm and 1.0-1.3 mm grains in one of the cores have scale lengths of 135 ± 6 and 152 ± 7 g cm^{-2}, respectively. In the second core the exponential scale length for ^{3}He (0.5-0.7 mm grains) is significantly higher, 227 ± 14 g cm^{-2}. Models incorporating ^{3}He production by muons and neutrons, erosion, and diffusion suggest that, to explain the core data, muon-induced production rates of ^{3}He must be greater than previously believed. Previously overlooked (n,T) or (n,^{3}He) reactions on Si and O by relatively low energy (e.g., 10's of MeV) neutrons produced in muon capture reactions are a possible explanation for the discrepancy.

Thesis Supervisor: Mark D. Kurz, Associate Scientist

Acknowledgments

Properly thanking all the people who contributed to this dissertation is a perhaps impossible task. I can only hope that all the help, advice, and encouragement that I received can someday be repaid in kind.

Great thanks goes to Mark Kurz, who, as thesis advisor, was responsible for some of the original insights that led to this work, developed collaboration with geologists working in Antarctica, untiringly and expertly raised funds to support the research, and worked hard to make field expeditions successful. Mark's research philosophy allowed great freedom in pursuing many of the problems discussed in the dissertation, and his generosity with time in the lab, advice and scientific insight, and above all encouragement, were greatly appreciated.

The other members of my thesis committee provided a great deal of assistance in many ways. Grant Raisbeck, with Francoise Yiou, graciously allowed me to make ^{10}Be and ^{26}Al analyses at the Tandetron in Gif-sur-Yvette, provided laboratory space and equipment for preparing targets, and devoted much time and energy to insuring the quality of the results. Grant also contributed very significantly to the quality of the dissertation by carefully reading manuscripts and offering keen insights into many of the conclusions of the work. Scott Lehman kept my geological reasoning on track, encouraged my future interest in this field, and waded through and improved my sometimes only partly literate prose. Bill Jenkins was always available to offer his considerable expertise in almost every field imaginable, helped out in the lab with sticky technical questions, and very generously provided computer facilities. Bill also introduced me to finite difference modeling and provided advice about how to go about getting the models to work. John Edmond encouraged my interest in cosmogenic isotopes from the very beginning, was always willing to share his enthusiasm, and offered many excellent suggestions about problems that were encountered along the way.

Many, many other people at WHOI, MIT, and in France, provided important and crucial assistance during the course of this work. Erik Brown graciously collaborated in the continuation of some of his work and taught me most of what I know about preparing samples for ^{10}Be and ^{26}Al analysis. Erik also read, and made important comments on, many manuscripts and thesis drafts, and made floor space for me in his apartment in Paris. Tom Trull was always willing to discuss ^{3}He diffusion and other cosmogenic ^{3}He issues, and provided an important last-minute explanation of a finite-difference model. Most importantly, Tom let me use his sailboat mooring in Quissett Harbor. J. Lestringuez and D. Deboffle expertly kept the Tandetron running and cheerfully put up with my inability to speak french.

Robert Ackert, as an Antarctic field companion and now fellow Joint Program student, contributed significantly to this dissertation in a number of ways. Robert's guidance in the field was crucial in selecting the appropriate places to sample, and to keeping us warm, fed, and alive. His knowledge of

Antarctic geology and insights into glacial geology and glacialogy have been a great help in formulating my ideas.

David Kammer and Tim Kenna provided a great deal of laboratory assistance. Dave was always willing to drop what he was doing to cheerfully lend a hand with whatever other thing that needed to be done, always managed to order spare parts and gas tanks before I needed them, and was a willing and definitely able (and now missed) tennis partner. Tim, a relative newcomer to the lab, was equally willing to help and offer good suggestions about how to get things done, and to take me for boat rides. Both Dave and Tim put up graciously with my mad bouts of accelerator target preparation

As always, tremendous thanks is due to Dempsey Lott for providing his considerable expertise in facing all manner of equipment problems. Dempsey, Bill Jenkins, and other members of the helium isotope laboratory continually provided an atmosphere of friendly anarchy that made the lab a great place to work.

George Denton, Dave Marchant, Shawn Higgins, and Tom Wilch, all at the University of Maine, generously took much of their time to explain Antarctic glacial geology. George in particular was always willing to explain his ideas and help me interpret my data. Much of the work presented here would not have been possible without the assistance of these excellent geologists.

Members of the chemistry department administrative staff, including Susan Kadar, Susan Casso, Joye Wirsen, and Molly Lumping, always were willing to help out in their various areas of expertise, and helped make finishing this document a (relatively) painless task. The Education Department at WHOI provided financial support and cheerfully endured all of my questions about finishing my thesis. This work was also partially supported by a National Defense Science and Engineering Graduate Fellowship from the Office of Naval Research. Despite rumours to the contrary, this had very little to do with the Central Intelligence Agency.

Finally, and most importantly, I must thank my family. My parents, Susan and Richard Brook, provided moral and financial support throughout my travels through the world of higher education. My wife, Sally Hacker, helped focus many of my thoughts, provided lots of encouragement near the end of this dissertation, cheerfully endured a difficult commute between Woods Hole and Providence, and made home a great place to come home to after the hard days of trying to put all of this together.

Table of Contents

List of Figures

List of Tables

Chapter 1

Introduction

Introduction

Lack of adequate chronology is a primary problem of terrestrial Quaternary geology, particularly for events beyond the range of radiocarbon dating (e.g., > 40 kyr). Exposed geological surfaces, such as striated bedrock, moraine boulders, fault scarps, and meteor craters, have obvious significance, but traditional absolute dating methods are not directly applicable to studying such features. New methods, based on the accumulation of cosmic-ray produced nuclides in rocks, are particularly promising for directly dating geological surfaces.

In 1934, Grosse et al. first suggested that cosmic rays produce rare isotopes in terrestrial rocks. In 1955, Davis and Schaeffer suggested that cosmogenic ^{36}Cl could be used to date terrestrial surfaces. Early studies were hampered by the limited sensitivity of available analytical techniques. However, recent developments in accelerator mass spectrometry and improvements in noble gas mass spectrometry now allow accurate measurement of a number of cosmogenic nuclides in terrestrial rocks. The most commonly measured are ^{3}He, ^{21}Ne, ^{10}Be ($t_{1/2}$=1.5 x 10^{6} yr), ^{26}Al ($t_{1/2}$=7.2 x10^{5} yr), and ^{36}Cl ($t_{1/2}$=3x 10^{5} yr). In the last decade a number of groups have developed the capability to make these measurements and application to geological problems is beginning (e.g., Kurz et al., 1990; Phillips et al., 1990; Brown et al., 1991; Nishiizumi et al., 1991; Phillips et al., 1991; Anthony and Poths, 1992; Brook et al., 1993). Several groups are also developing the capability to measure *in situ* ^{41}Ca ($t_{1/2}$=1.02 x 10^{3} yr) and ^{14}C ($t_{1/2}$=5.7 x 10^{3} yr) (Fink et al., 1991; Jull et al., 1992).

This dissertation describes thxe application of cosmogenic nuclides to several problems of Antarctic glacial geology, where the fundamental goal is to provide new age constraints for glacial deposits related to Quaternary and

earlier Antarctic glaciation. It also describes a number of efforts toward further understanding of cosmogenic nuclide production mechanisms, production rates, and assumptions inherent in exposure age dating.

Production of Cosmogenic Nuclides in Terrestrial Rocks

Background

The primary flux of galactic cosmic rays (GCR) is composed mostly of protons (~85%), alpha particles (~15%), and a small percentage of heavier nuclei (Lal and Peters, 1967; Pomerantz, 1971). These high energy particles interact with molecules in the earth's atmosphere, producing secondary protons, neutrons, electrons, muons, and a variety of other particles. Cosmogenic nuclides are produced in terrestrial rocks by a number of different mechanisms, including spallation of major elements by secondary cosmic-ray neutrons, capture of thermal neutrons and muons produced by cosmic ray interactions in the atmosphere and in rocks, and spallation by neutrons produced in muon capture reactions (Kurz, 1986b; Lal and Peters, 1967; Lal, 1987).

Table 1 lists the most commonly measured cosmogenic nuclides in terrestrial rocks that show promise for surface exposure studies. Of these, ^{3}He and ^{21}Ne are stable noble gases that can be measured with conventional magnetic sector noble gas mass spectrometers (e.g., Kurz, 1986b; Graf et al., 1991; Staudacher and Allegre, 1991; Brook and Kurz, 1993; Kurz and Brook, 1993; Poreda and Cerling, 1993). The stable isotopes are useful for surface exposure studies because they can act as integrators of cosmic ray exposure on long time scales, potentially up to several million years. Stability can also be a disadvantage because of the possibility of an "inherited" component not

related to the exposure age of the sample, either from previous exposure to cosmic rays, nuclear reactions within the earth, or primordial noble gases.

The other nuclides in Table 1 are all long-lived radionuclides, and are most efficiently measured with accelerator mass spectrometers (principles of AMS are briefly reviewed in Chapter 2). The half-lives of these isotopes limit their utility for dating to specific age ranges dictated by the half-life and measurement precision. The availability of a number of nuclides with different half-lives, however, offers the possibility of examining "disequilibrium" effects that can be used to study erosion, past ice or soil cover, tectonic uplift or other tectonic activity, and a variety of other processes (see further discussion in Lal, 1991; Brown et al., 1991; and Chapter 5).

Of the nuclides listed in Table 1, ^{3}He, ^{10}Be, and ^{26}Al are the most widely measured and have been employed in the studies of Antarctic glacial chronology described in the following chapters. The production of ^{3}He, ^{10}Be, and ^{26}Al in terrestrial rocks, the methods of surface exposure dating, and the major geological and geochemical conclusions of this dissertation are discussed in the following sections of this chapter.

Table 1. Commonly measured cosmogenic nuclides in rocks, target elements, half-lives, and approximate sea level production rates.

Isotope	Half-life (yr)	Targets	Production Rate (at g^{-1} yr^{-1})
^{3}He	stable	O,Si, Mg, Fe, Al	100-150
^{21}Ne	stable	Mg, Al, Si, Fe	80-160
^{10}Be	1.5×10^{6}	O, Si, Mg, Fe,Al	6 (quartz)
^{26}Al	7.2×10^{5}	Si, Al, Fe, Mg	37
^{36}Cl	3.0×10^{5}	Fe, K, Cl, Ca	8 (basalt)
^{14}C	5.7×10^{3}	O, Si, Mg, Fe	20

^{3}He Production Mechanisms

^{3}He is produced in terrestrial rocks primarily by spallation reactions with cosmic ray neutrons (Kurz, 1986a,b; Lal, 1987). Spallation refers to a variety of nuclear reactions involving disintegration of the nucleus due to a collision with a particle. More specifically, it refers to inelastic collisions where the incident particle energy is well above the binding energy of the target nucleus and at least one of the interacting particles is a complex nucleus (Shen, 1976). Energies involved in spallation reactions therefore must be 10's of MeV or greater, i.e., well above the binding energy of the nucleus. While neutrons are the dominant particle involved in spallation reactions in terrestrial rocks, a small percentage (< 10 %) of the total production is due to spallation by secondary cosmic-ray protons and alpha particles (Lal, 1991). The total cosmic-ray proton and neutron fluxes are actually approximately equal at high energies (> 1000 MeV), but the differential energy spectra of neutrons and protons are very different below this value. The former shows a strong increase with decreasing energy and the latter falls off sharply due to proton ionization losses (Lal and Peters, 1967). Measured excitation functions ("excitation function" refers to the relationship between nuclear reaction cross section and particle energy) for production of cosmogenic nuclides by protons and neutrons normally have a threshold energy at a few tens of MeV and reach roughly constant values near that energy (e.g., Walton et al., 1976; Qaim et al., 1982). Because these thresholds are at energies where the neutron component of cosmic rays dominates, most of the production is by neutrons (Lal and Peters, 1967). Furthermore, because the differential energy spectrum is exponential, with increasing numbers of particles with decreasing energy, most of the spallation-produced isotopes are produced at energies near the threshold energy.

Production of cosmogenic nuclides by spallation in rocks should be grossly dependent on rock composition, since it is not possible to produce an isotope heavier than the target element. Composition dependence also results from differing production cross sections in different elements. Helium production by spallation has been considered independent of rock composition within broad limits of about 20% (Kurz, 1986b; Lal, 1987; Brook and Kurz, 1993). This conclusion is supported by several observations. First, ^{3}He measurements in olivine and clinopyroxene phenocrysts from the same samples from Hawaiian lava flows have indistinguishable cosmogenic ^{3}He concentrations (Kurz, 1986a,b). Second, ^{3}He production rates in chondrites show only a weak, if any, compositional dependence (Eugster, 1988). Third, ^{3}He ages in quartz sandstones for an Antarctic moraine in the Dry Valleys region calculated with production rates based on olivine phenocrysts in Hawaiian basalts (Brook et al., 1993 [Chapter 4]; Chapter 5) agree well with ^{10}Be ages calculated with production rates calibrated in quartz in glacial deposits in northern California (Nishiizumi et al., 1989).

Lal (1991) calculated ^{3}He production rates in a variety of common rock-forming elements (Si, Mg, Fe, O, and Al) that show some slight compositional dependences (Table 2). His calculations are based primarily on cross-sections for ^{3}He production by protons and assumed values of the cosmic ray neutron flux. Cross sections for protons are used because the relevant information for neutron interactions is not generally available. As a result, the calculations have large uncertainties, reported to be 25-30 % or greater (Lal, 1991), but they are useful for examining relative production rates in different materials. Table 2 verifies the general conclusion that production rates do not vary greatly with rock composition in olivines, clinopyroxenes, and quartz. The most significant composition dependence in Table 2 is a result of the

relatively low production rate in iron. The use of production rates determined from magnesium-rich olivines (e.g. Kurz, 1986a,b; Cerling, 1990) to calculate ^{3}He exposure ages in quartz (Brook and Kurz [Chapter 3]; Chapter 5, Chapter 6) is justified by Table 2, since predicted differences between ^{3}He production in Mg_2SiO_4 and SiO_2 are less than 10% (Table 2).

Table 2. Calculated ^{3}He production rates (at g^{-1} yr^{-1}) at sea level and > 60° geomagnetic latitude in a number of common rock forming elements and minerals from the elemental production rate dependence reported by Lal (1991).

Target	Production Rate	Mineral	Production Rate
O	83	SiO_2	74
Mg	50	Mg_2SiO_4	68
Al	47	Fe_2SiO_4	50
Si	66	$MgSiO_3$	70
Fe	28	$FeSiO_3$	56

Thermal neutron capture may in some cases also produce appreciable ^3He. ^3He is produced by thermal neutrons from ^6Li *via* the reaction $^6Li(n,\alpha)T\text{-}^3He$ (Morrison and Pine, 1955). Cosmogenic thermal neutrons are produced in the atmosphere and in rocks by the thermalization of fast neutrons and by muon capture reactions (Yamashita et al., 1966; Lal, 1987). The importance of this production mechanism depends on the lithium concentration in the rock and the concentrations of all other elements that absorb thermal neutrons. The rate of ^3He production by this mechanism is given by eq. 1:

$$P = F\frac{\sigma_{Li}[Li]}{\sum\sigma_i[X]_i} \qquad (1)$$

where σ is thermal neutron cross section, [X] is concentration, and F is the thermal neutron production rate. Helium production by this mechanism is of course dependent on rock composition, but does not appear to be significant relative to spallation in most rocks at depths of less than one meter (Kurz, 1986b; Lal, 1987; Brook and Kurz, 1993 [Chapter 3]).

Nuclear interactions with muons (negative μ-mesons) produce a number of cosmogenic nuclides. Muons are charged particles with mass of approximately 0.1 times the proton mass. They are unstable and rapidly decay to an electron, neutrino, and anti-neutrino. In interacting with matter they are captured by the nuclear coulomb field and cascade rapidly to the 1s level, where they decay or are captured by the nucleus (Charalambus, 1971). This process is represented by the reaction: $\mu^- + (Z,A) \rightarrow (Z\text{-}1, A)^* + \nu_\mu$, where a proton changes into a neutron. The nucleus remains in an excited state and typically de-excites by emitting a number of particles, usually neutrons, producing a (Z-1,A-X) nucleus, where X is the number of neutrons emitted

(Charalumbus, 1971). Muogenic ^{3}He can be produced in a number of ways. Direct muon capture reactions on Li produce very small amounts (less than ~ 10^{-3} at g^{-1} yr^{-1} at sea level) of ^{3}He and ^{4}He through reactions like: $^{6}Li(\mu^{-},3n)^{3}He$ or $^{7}Li(\mu^{-},4n)^{3}He$ (Kurz, 1986b; Lal, 1987). These production rates are not significant in surface rocks (Kurz, 1986b; Lal, 1987). Thermal neutrons produced in muon capture reactions can also produce ^{3}He *via* the thermal neutron reaction with Li described above (Lal, 1987; Chapter 7). In addition, neutrons emitted in muon capture reactions can have energies above 10 MeV (Charalumbus, 1971) and calculations of Lal (1987) suggest that they can also produce small quantities ^{3}He by spallation (see Chapter 7 for further discussion). In general, the muon-induced reactions do not appear to be important at rock depths of less than one meter, producing less than 10 % of the total ^{3}He in most common rocks. However, muons are weakly interacting particles. As described in Chapter 7, muon stopping in rocks has an exponential scale length of ~ 1700 g cm^{-2}, while neutron interactions have a scale length of ~ 150 g cm^{-2}. As a result, with increasing depth the muon-produced component should become more important. This effect was observed by Kurz (1986b), who attributed anomalously high ^{3}He concentrations below one meter in a Hawaiian drill core to production by muons. Because of differences in attenuation for neutrons and muons, erosion of rock surfaces can increase the importance of the muon-produced component (Kurz, 1986b) and anomalous ^{3}He depth profiles in Antarctic sandstone bedrock are attributed to this effect in Chapter 7.

Small quantities of ^{3}He are also produced by natural radioactivity in the earth's crust as a result of uranium and throrium decay. In the crust the primary production mechanism is the thermal neutron reaction with ^{6}Li described above (Morrison and Pine, 1955). In this case the thermal neutrons

are indirect products of U and Th decay due to (α,n) reactions on common rock-forming elements. The importance of this mechanism of ^{3}He production depends on U, Th, and Li concentrations and the thermal neutron absorption properties of the material in question (e.g., equation 1). Cosmogenic ^{3}He concentrations can be corrected for this "nucleogenic" component in quartz using the measured ^{4}He concentration and an assumed nucleogenic $^{3}He/^{4}He$ production ratio. This correction is effective because cosmic rays do not produce appreciable amounts of ^{4}He relative to the natural quantities in most rocks. In the following chapters the radiogenic production ratio of $0.011 \pm 0.04 \times R_a$ (where R_a is the atmospheric $^{3}He/^{4}He$ ratio) determined by Trull et al. (1991) is employed as a correction factor. As discussed in Chapter 7 and in Brook and Kurz (1993) [Chapter 3] there is some uncertainty concerning this correction because the Li, U, and Th content of each sample, as well as the total thermal neutron capture cross section, are not known. The correction is in most cases quite small (< 1%), however, and contributes little uncertainty to exposure ages. As suggested in Chapter 3, in uranium rich rocks with young exposure ages this ^{3}He component could be important.

^{10}Be and ^{26}Al Production Mechanisms

In terrestrial surface rocks ^{10}Be and ^{26}Al are produced primarily by spallation of major elements. In quartz, the mineral in which most *in situ* ^{10}Be and ^{26}Al measurements have been made, ^{10}Be is produced primarily by spallation of oxygen, and ^{26}Al primarily by spallation of ^{28}Si (Nishiizumi et al., 1989; Sharma and Middleton, 1989). Both nuclides can also be produced by muon capture reactions (for example, $^{16}O(\mu-,4p3n)^{10}Be$ and $^{28}Si(\mu-,p2n)^{26}Al$). Nishiizumi et al. (1989) have calculated the relative contributions

of both mechanisms. The importance of the muon-produced component relative to the spallation component changes with latitude and altitude because the muon flux is attenuated differently than the neutron flux. The altitude effect is most significant. Nishiizumi et al. (1989) estimated that at 3.34 km altitude, 44 degrees N magnetic latitude, muons produce 7% of the total ^{26}Al and 6 % of total ^{10}Be. At sea level the proportions are 17.5 and 15.6 %, respectively. These estimates are theoretical calculations, their uncertainties are not adequately evaluated, and direct measurent of the production rates by this mechanism will be necessary to further constrain them.

Natural radioactivity in the crust can also produce small quantities of ^{10}Be and ^{26}Al. This subject was reviewed comprehensively by Sharma and Middleton (1989). The most important reactions are $^{7}Li(\alpha,p)^{10}Be$, $^{23}Na(\alpha,n)^{26}Al$, $^{9}Be(n,\gamma)^{10}Be$, $^{10}B(n,p)^{10}Be$, and $^{13}C(n,\alpha)^{10}Be$ (Sharma and Middleton, 1989). Alpha particles are produced in uranium and thorium decay, and as discussed above, the neutrons involved in these reactions are derived primarily from (α,n) reactions. In crustal rocks such as granites and sandstones, ^{10}Be production by these mechanisms is insignificant, producing equilibrium concentrations of $\sim 10^{3}$ at g^{-1} at most. Calculated equilibrium concentrations of ^{26}Al in many common rock types are significantly higher, up to 5×10^{6} at g^{-1} in granites. This concentration corresponds to ~ 100 kyr of exposure at sea level, and is therefore potentially significant in exposure dating. Chapters 5 and 6 discuss this issue further, and suggest the presence of significant nucleogenic ^{26}Al in some Antarctic quartz samples with young exposure ages.

Principles of Surface Exposure Chronology Using Cosmogenic Nuclides

Introduction

In theory, surface exposure ages are simply calculated from the measured concentration of a cosmogenic nuclide and its production rate. For a stable isotope the age (t) is simply:

$$t=N/P \qquad (2),$$

where N is concentration and P is production rate. For a radioactive isotope the age equation is:

$$t=\frac{\ln(1-N\lambda/P)}{-\lambda} \qquad (3),$$

where λ is the decay constant. The common assumptions of isotope geochronology are implicit in these simple calculations, which assume no non-cosmogenic component of the nuclide of interest, closed system behavior (no gain or loss except due to production and radiodecay), and known and constant production rates.

In addition, because the exposure age of the surface, rather than the age of the rock, is being measured, a number of other important issues must be considered. These include the possibility of snow or soil cover of the surface of interest in the past, erosion, and the effects of shielding by surrounding topography. Production rates, the general effects of erosion, and topographic shielding, are discussed further below. All of these assumptions are also

discussed in the chapters that follow in the context of applied exposure dating problems.

Because many of these assumptions are sample dependent, care in sample collection is crucial. In addition to the assumptions listed above, the stability and geometry of each sample must be carefully considered. Adequate understanding of each geological situation and the potential pitfalls of exposure dating are necessary, as illustrated by the discussions concerning dating moraine boulders in Chapters 4, 5, and 6.

Production Rate Calibration

Calibration of absolute production rates is a fundamental problem in cosmogenic nuclide research. Calculations of production rates using known nuclear cross sections, cosmic ray fluxes, and rock compositions are possible, but difficult, because adequate information, including accurate cross-sections for neutron interactions and detailed knowledge of the time-history of the cosmic ray flux and energy spectrum, are not available (Lal and Peters, 1967; Lal, 1991). Calibration using surfaces of known age is the preferred method. The major difficulty with this approach is finding appropriate surfaces with well-established ages.

^{3}He production rates have been calibrated by two groups working independently (Kurz, 1986a,b; Cerling, 1990; Kurz et al., 1990). Kurz et al. (1990) reported production rates in olivine based on ^{3}He measurements in radiocarbon dated lava flows from Hawaii. Cerling (1990) reported production rates in olivine from a variety of basalt bedrock surfaces, the majority of the data coming from a well-dated wave-cut bench in the Provo shoreline of glacial lake Bonneville in Utah, USA (Cerling, 1990). Production rate calibration and comparison of production rates is complicated by the

altitude and latitude effects described below (see further discussion in Brook and Kurz (1993) [Chapter 3]). The measured rates do show approximate agreement, however. The production rate of Cerling (1990), recalculated to account for the (Bard et al., 1990) ^{14}C calibration, is 398 ± 8 at g^{-1} yr^{-1} at 1445 m altitude. Scaled to sea level and high latitude (to normalize for the effects of the earth's magnetic field) using scaling from Lal (1991) this rate is 117 ± 4 at g^{-1} yr^{-1}. The Kurz et al (1990) production rate is based on ^{14}C-dated Hawaiian lava flows < 2000 years old at different altitudes; scaling it to sea level and high latitude using Lal (1991) gives a mean of 178 ± 41 at g^{-1} yr^{-1}. The large uncertainty is primarily due to the low age of the samples and resulting low cosmogenic ^{3}He concentrations. Kurz et al. (1990), however, also reported several production rates for samples between 600 and 15,000 yr that varied by a factor of two. They suggested variability in the earth's dipole moment as one possible explanation for this effect. In theory, variations in the magnetic field strength would cause production rate variations because of the "filtering" efffect of the field on incoming charged cosmic ray primaries (see Brook and Kurz (1993) [Chapter 3]). Because of the analytical uncertainties for the measurements in the youngest samples this potentially important suggestion is subject to verification. Therefore, the production rate based on the youngest samples only is used here. Note that at high latitudes (> 50 degrees N or S) the magnetic field does not affect cosmic rays (Lal and Peters, 1967). Dipole moment variations should therefore not cause production rate changes in Antarctica.

To arrive at Antarctic production rates used in Chapter 5, 6, and 7 the altitude and latitude scaling factors of Lal (1991) were used to scale the two sets of data to sea level and high latitude (> 60^{o} N or S) and the simple

uncertainty-weighted mean of the two was calculated, giving 118 ± 9 at g^{-1} yr^{-1}

^{10}Be and ^{26}Al production rates used in Chapters 5, 6, and 7 come from Nishiizumi et al. (1989) and are based on measurements in glacially polished surfaces in the Sierra Nevada Mountains. At sea level and high latitude those rates are 6 and 37 at g^{-1} yr^{-1}, respectively, with a 10% uncertainty based primarily on uncertainty in the age of the glacial event forming the surface (Nishiizumi et al., 1989; Lal, 1991).

Production rate calibration used during the course of this work has evolved over the past several years and the rates adopted here have changed slightly from initial production rate calculations used in Brook and Kurz (1993) [Chapter 3] and Brook et al. (1993) [Chapter 4]. Those studies employed ^{3}He production rates of Kurz et al. (1990) only and scaling from Lingenfelter (1963). Scaling the Kurz et al. (1990) production rates to sea level in Hawaii using Lingenfelter (1963) gives 147 at g^{-1} yr^{-1}, and scaling that rate to high latitude suggests a production rate of 191 at g^{-1} yr^{-1}. The altitude scaling based on Lingenfelter (1963) predicts a smaller increase in production rate with altitude than Lal (1991), and this effect offsets the decrease in production rate caused by including the lower rates from Cerling (1991). For example, Lingenfelter (1963) predicts a factor of 1.3 increase in the production rate between Hawaii and Antarctica and factor of 2.3 increase in production rate between sea level and 1200 m (the approximate altitude of most of the Arena Valley samples). Lal (1991), however, predicts a factor of 1.5 between Hawaii and Antarctica and 3.0 between sea level and 1200 m. The differences between the two approaches roughly cancel for samples at the latitude and altitude of Arena Valley and therefore updating the production rates does not change any of the conclusions of the earlier work (see further discussion of scaling

below). The new calculation does predict significantly lower ^{3}He production rates at sea level in Antarctica than previously suggested. Agreement between ^{3}He and ^{10}Be ages for low altitude (< 500 m) Ross Sea Drift samples calculated using the production rates described above (Chapter 6) suggests that the new approach is more accurate.

Scaling Production Rates for Altitude and Latitude

Because of the modulating affects of the earth's magnetic field and atmosphere on the cosmic ray flux, production rates must be scaled for altitude and latitude to calculate exposure ages (see Chapter 3 for further details). Most workers in this field have adopted the scaling factors published by Lal and Peters (1967) which are based on Lal (1958), but summarized in polynomial form in Lal (1991). These polynomials describe variations in "nuclear disintegration rate" as a function of altitude and latitude and were constructed by combining data from mobile neutron monitors or cloud chambers (either flown at one altitude and a variety of latitudes or one latitude at a variety of altitudes) and measurements of nuclear disintegration rates or "star" production in ionization chambers and nuclear emulsions. (Cosmic ray "stars" are the results of spallation reactions in photographic emulsions). The construction of the curves is described in Lal (1991) and Lal and Peters (1967), but the original information is published in most detail in Lal (1958).

The logic of the construction of the curves is as follows, derived primarily from Lal (1958). Because observations show that the nuclear disintegration rates measured in nuclear emulsions and cloud chambers are proportional to slow (< 30 MeV) neutron fluxes, the much more complete network of mobile neutron monitor data can be used as an index of relative

production rate variations. Neutron monitor data for one altitude at a number of latitudes, and altitude surveys at any one latitude, overdetermine the relative variations and are consistent (also see Lingenfelter, 1963). Lal (1958) used star production data to establish a proportionality between neutron flux and low energy star production rate for calculating production rates of cosmogenic nuclides in the atmosphere. He defined low energy stars as those formed by particles with energies of < ~ 400 MeV, forming stars with six prongs or less. Several corrections were made to the star production data that are included in the final published curves. The number of stars with less than 3 prongs is not well measured in emulsions and was calculated by Lal (1958) assuming an exponential relationship between number of stars and prong number for 1 and 2 pronged stars. The slope of the relationship varies with altitude and latitude, is only known with a precision of ~ 50 %, and is *only determined in two locations.* The total correction is ~ 20 % of the total star production and therefore this uncertainty is small but non-trivial. Although most of the cosmogenic nuclide production occurs below 400 MeV, Lal (1958) made an additional correction for stars with 7 prongs or greater using the same exponential relationship. According to Lal (1958) the high energy stars make up 8-30% of the total.

The uncertainties in the Lal (1991) polynomials are hard to evaluate, and some of the raw data are not published in a readily available form. However, given the discussion above, they must be on the order of 10 % based on the uncertainty in corrections for < 3 pronged stars. This uncertainty, combined with analytical uncertainties and uncertainties in independent ages used for calibration of 8-10 % (e.g, Lal, 1991), suggests a rough estimate of present production rate uncertainties (1-sigma) of ~ 15 %. Additional uncertainty, not explicity included in the 15 % estimate, may be

introduced by variations in scaling factors due to the solar cycle (Lal,1991; Brook and Kurz, 1993 [Chapter 3]), the correction for high energy neutrons described above, and possible variations in the earth's magnetic field strength (Kurz et al., 1990).

In summary, although the curves of Lal (1991) have been adopted by a number of workers in the field as a standard, and are readily available in polynomial form, they are based on older cosmic ray data and future work should attempt to verify and update them. Large amounts of cosmic ray neutron data collected after 1958 are available (see, for example, Coxell et al., 1965, and Potgeiter et al., 1980), which are consistent with the parameters used by Lal (1958). Attempts at verifying production rate variations with altitude by measuring production rates in lava flows as a function of altitude also suggest that the Lal (1991) scaling factors are accurate (Zreda et al., 1992), but more work of this kind is necessary. Experiments with artificial targets (e.g., Mabuchi et al., 1971; Kurz et al., 1991) placed at different locations should also be useful in this regard.

Effects of Topographic Shielding

Because the cosmic ray flux in the atmosphere has an angular dependence (e.g., Conversi and Rothwell, 1954), the production rate of cosmogenic nuclides depends on shielding by surrounding topography. The angular dependence, based on measurements in the atmosphere with angle-sensitive neutron detectors, has the form $\sin^x(\theta)$, where x is ~2.1-2.6 and θ is the vertical angle between horizontal and the horizon (Conversi and

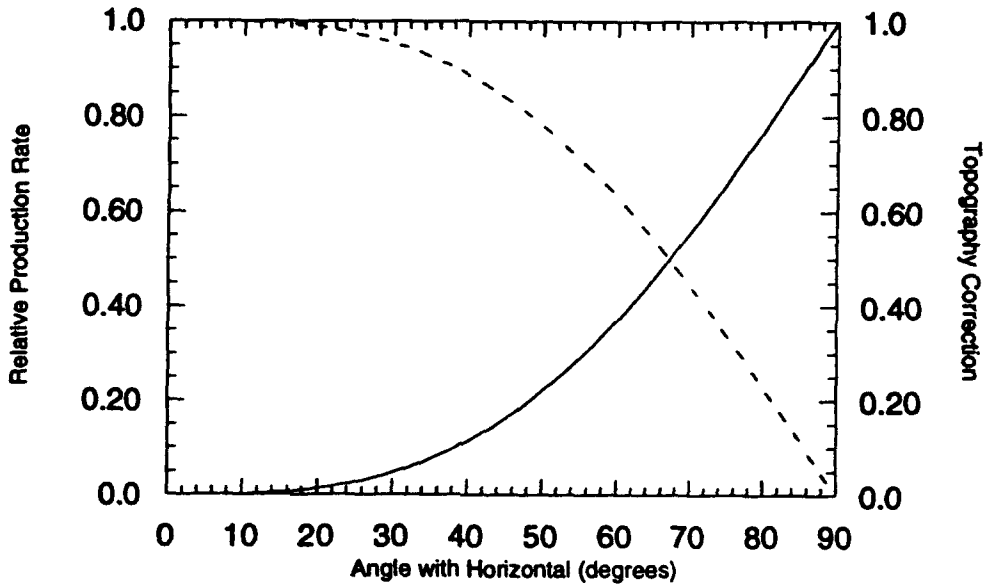

Figure 1. Effects of topographic shielding on cosmogenic nuclide production rates. Solid line shows the relationship between shielding angle (angle between horizontal and horizon) and normalized integrated production rate. The dashed line shows the corresponding correction factor for the production rate. The curves are numerical integrations of the $\sin^{2.3}$ (theta) dependence of production rate reported by Nishiizumi et al. (1989), weighted for the variation in solid angle with theta.

Rothwell, 1954; Lal and Peters, 1967). Numerically integrating this function over θ=0 to 90 degrees, accounting for the change in solid angle over that range, gives a correction factor that can be used to adjust the production rate to account for topographic shielding (Fig. 1). In practice, this curve would be used by measuring shielding angles for all topography surrounding the sample and making the appropriate weighted or integrated correction to the production rate. For angles < 20-30 degrees the correction is minor to insignificant (Fig. 1). For all samples discussed in this dissertation the correction is negligible and was not applied.

Depth Dependence of Cosmogenic Nuclides in Rocks and Erosion Effects

Cosmic rays are attenuated exponentially in rocks in the same fashion as they are in air. The depth dependence of ^{3}He, ^{10}Be, and ^{26}Al concentrations has been measured in several bedrock drill cores of 1-2 m by Kurz (1986b); Brown et al. (1992), and during the course of this work (Chapter 7). These studies show exponential depth-dependence with a scale length ranging from 150-165 g cm^{-2}, with the exception of a anomolously long scale length of 227 ± 14 g cm^{-2} observed for ^{3}He in a core described further in Chapter 7. This exponential factor is used to normalize cosmogenic nuclide data for the effects of sampling over discrete intervals and to correct for shielding by overlying soil or rock cover. The exponential attenuation length is also fundamental information needed to calculate erosion rates (see below). Depth-profiles can also provide useful information about production mechanisms of cosmogenic nuclides and ^{3}He loss due to diffusion (Kurz, 1986b; Brown et al., 1992; Chapter 7).

Because of the attenuation of cosmic rays by rocks, erosion affects the build-up of cosmogenic nuclides and is an important consideration in

exposure dating. Assuming a constant erosion rate the concentration of a cosmogenic nuclide can be described by:

$$N = \frac{P}{\lambda + E/L}(1 - e^{-t(\lambda + E/L)}) \qquad (4),$$

where E is erosion rate in g cm^{-2} yr^{-1} and L is the exponential attenuation coefficient. Exposure ages can therefore be corrected for erosion if erosion rates can be independently constrained. The effect of erosion on apparent exposure ages depends on the erosion rate, the half-life of the nuclide, and the exposure time (Fig. 2). The top panel in Figure 2 shows that exposure ages can be significantly underestimated if erosion rates are not well-constrained. The figure also illustrates that the effect of erosion on the apparent age varies as a function of the half-life of the nuclide. Underestimation of the exposure age due to erosion is most significant for ^{26}Al, and least significant for ^{3}He.

Cosmogenic nuclides can also be used to determine erosion rates in a model-dependent way. At steady-state with respect to production and radio-decay equation 4 reduces to:

$$N = \frac{P}{\lambda + E/L} \qquad (5).$$

This behavior can also be seen in Fig. 2. The bottom panel in Figure 2 illustrates the effect of erosion on the concentrations of ^{3}He, ^{26}Al, and ^{10}Be as a function of time. Because concentrations reach steady states that depend on the erosion rate, erosion rates can be calculated if steady state has been reached. Without independent age constraint the erosion rate calculated this way is a

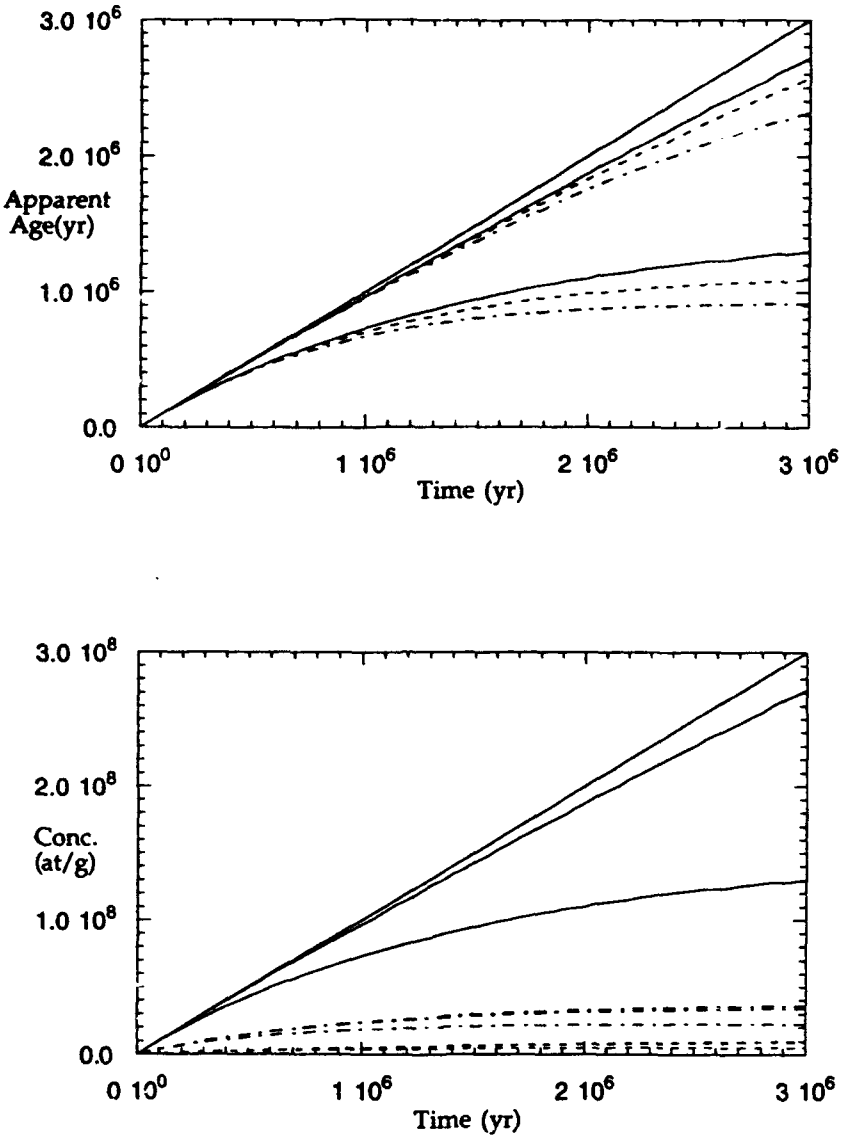

Figure 2. True age plotted against apparent age (top) and concentration (bottom) for ^{3}He (solid lines), ^{10}Be (dashed lines), and ^{26}Al (dot-dashed lines) for no erosion (top curve in each series), erosion rate= 1×10^{-5} g cm^{-2} yr^{-1} (middle curve in each series), and erosion rate=1×10^{-4} g cm^{-2} yr^{-1} (bottom curve in each series). The top figure shows how erosion can affect the apparent exposure age. The bottom figure illustrates the approach to steady state that allows calculation of erosion rates. See text for further discussion.

maximum. With two or more isotopes of different half-lives the erosion rate can be further constrained if both give the same erosion rate (Lal, 1991). Such calculations have not yet been employed in a systematic way in application to geologic problems. Preliminary studies, confirming low erosion rates in Antarctica (Nishiizumi et al., 1991), and investigating denudation in Venezuela (Brown et al., 1992b), are encouraging. In most of the Antarctic samples discussed here the effects of erosion are not significant (see Chapters 4, 5, and 6), but in other systems this may not necessarily be the case.

Summary of Existing Uncertainties in Exposure Age Dating

Cosmogenic nuclides have proven useful in providing new constraints for surface exposure geochronology. Future advances in this field will require further understanding of isotope systematics. The most important issue concerns obtaining better constraints on production rates and altitude-latitude variations in production rates for all significant production mechanisms. This absolute calibration requires measuring cosmogenic nuclides in independently well-dated surfaces. Lava flows and late Pleistocene age glacially eroded surfaces are the most promising candidates. A related calibration issue concerns the affects of the earth's magnetic field and potential field variations on production rates (e.g. Kurz et al., 1990). It will be crucial to understand the history and magnitude of these effects to fully utilize cosmogenic nuclides.

The uncertainties in altitude-latitude scaling factors have not been given much attention by most workers in this field but they are very important in improving precision of surface exposure geochronology. Existing uncertainties in the Lal (1991) scaling, which is used by most workers in this field, are at least 15 %. This can be improved by a reevaluation of

existing cosmic ray data and by gathering new cosmic ray data. An additional way of improving scaling factors is to place artificial targets at various altitude and latitude (e.g., Mabuchi et al., 1971; Yokoyama et al., 1977; Kurz et al., 1991).

Finally, further understanding of production mechanisms will be necessary to fully utilize the potential of cosmogenic nuclides. Current important problems related to the work discussed in this dissertation include further understanding the importance of ^{3}He loss from a variety of mineral phases (Chapter 3), nucleogenic production of ^{26}Al and ^{3}He (Chapters 5 and 6), and the importance of production of all isotopes by muons (Chapter 7).

Summary of Major Geological and Geochemical Conclusions

This dissertation concentrates on applications of cosmogenic nuclides in Antarctic glacial chronology, where these techniques are ideal due to low erosion and weathering rates. In addition, because Antarctic glacial chronology is in many cases not well constrained, uncertainties in production rates and other issues of isotope systematics are not crucial to many major questions.

Chapters 4, 5, and 6 describe several advances in understanding the history of Antarctic glaciation based on ^{3}He, ^{10}Be, and ^{26}Al measurements in Antarctic glacial deposits. Chapters 3 and 7 discuss issues of ^{3}He, ^{10}Be, and ^{26}Al systematics relevant to exposure age dating. The major conclusions of the work are the following:

1) Moraines in Arena Valley, Antarctica, deposited by the Taylor Glacier, an outlet glacier of the east Antarctic Ice Sheet, have exposure ages ranging from 120 kyr to ~ 2 myr. ^{3}He and ^{10}Be exposure ages for the youngest of these, the Taylor II moraine, confirm suggestions that it was deposited during

interglacial isotope stage 5 (~120 kyr). The dating supports the suggestion that East Antarctic outlet glaciers advance during global interglacial periods, when precipitation rates increase in the interior of East Antarctica. Other moraines in Arena Valley cannot be placed in the context of the deep sea isotope record with as much certainty, but Chapter 5 discusses the possible stage 9 (~300-350 kyr) or 11 (~ 370-440 kyr) origin of the next oldest moraine, Taylor III. The older moraines have climatic significance, however, because relatively small altitude differences (< 200-300 m) between the youngest and oldest deposits in Arena Valley suggest relatively small changes in outlet glacier profiles throughout the Quaternary and late Pliocene, and by inference, relatively small changes in the East Antarctic Ice Sheet. In addition, the sedimentological character of all of these deposits suggests deposition by cold-based ice, indicating climate conditions similar to the present in this part of Antarctica throughout most of the last ~ 2myr (Chapter 5).

2) Moraines and drift on the coast of McMurdo Sound, mapped as late Wisconsin by Stuiver et al. (1981), are Wisconsin in age, but ^{3}He and ^{10}Be exposure ages range from 8-106 kyr (Chapter 6). Chapter 6 suggests that the apparent drift limit, which has been used in reconstructions of a grounded ice sheet in McMurdo Sound at the late Wisconsin glacial maximum, may not strictly represent deposition at one time. The drift limit may represent several episodes of grounding line advance throughout the Wisconsin period. Analogous older drift, found above the presumed late Wisconsin drift limit, has exposure ages ranging from ~100-500 kyr. The clear separation between the two groups of ages indicates that exposure age dating can be used to distinguish the two deposits.

3) Constraints on uplift rates are possible using cosmogenic nuclides, because production rates are an exponential function of altitude. Chapter 5 uses this effect to constrain uplift rates of the Transantarctic Mountains. This analysis precludes controversial uplift rates of up to 1 km/myr over the last 3 myr, suggested based on biostratigraphic evidence from high altitude glacial deposits in the Beardmore Glacier region (McKelvey et al., 1991). Comparison of models of the effects of uplift over that time period on ^{10}Be concentrations with measurements in high altitude glacial deposits from the McMurdo Sound region suggests little or no uplift during the last 3 myr.

4) Crushing quartz *in vacuo* releases helium with a wide range of isotopic compositions and $^{3}He/^{4}He$ ratios up to 148 R_a (Chapter 3). $^{3}He/^{4}He$ ratios released by crushing roughly correlate with total ^{3}He concentrations, suggesting release of cosmogenic helium during crushing. This indicates that corrections for non-cosmogenic helium cannot be made by combination of crushing and melting as is possible in olivine and clinopyroxene in volcanic rocks. In addition, ^{4}He concentrations in replicate analyses of the same samples vary significantly, in some cases by up to a factor of 3. This variability is attributed to extreme heterogeneity in U and Th concentrations (Chapter 3).

5) Comparison of ^{10}Be and ^{3}He ages and detailed study of the dependence of ^{3}He concentrations on grain size in quartz suggest that ^{3}He loss due to diffusion significantly affects Antarctic samples older than ~200 kyr (Chapters 3, 4, and 5). As described in Chapter 3, this loss is significantly greater than predicted by laboratory experiments (Trull et al., 1991). The reason for this discrepancy remains unclear. The most likely explanation, however, is a

change in the diffusion mechanism at low temperatures that was not resolved by the experimental measurements.

6) Depth profiles of ^{3}He, ^{10}Be, and ^{26}Al in two cores collected from Antarctic sandstone bedrock (Chapter 7) confirm previous estimates of exponential production attenuation lengths of ~150-160 g cm^{-2}, with the exception of an anamolously long ^{3}He profile in one core (attenuation length of 227 ± 14 g cm^{-2}), attributed in Chapter 7 to the combined effects of ^{3}He production by muons, ^{3}He production by neutrons, and erosion, over a long (> 10 myr) time period. Including loss due to diffusion in the models of the combined effects of these processes suggests, however, that current estimates of ^{3}He production rates due to muon interactions are not sufficeint to explain the profile. Chapter 7 suggests that direct production of ^{3}He by spallation of major elements in rocks by neutrons produced in muon capture reactions may produce more ^{3}He than previous calculations (Lal, 1987) indicate.

References

Anthony, E. Y., and Poths, J. (1992). ^{3}He surface exposure dating and its implications for magma evolution in the Potrillo volcanic field. *Geochimica et Cosmochimica Acta* **56**(11), 4105-4108.

Bard, E., Hamelin, B., Fairbanks, R. G., and Zindler, A. (1990). Calibration of the ^{14}C timescale over the past 30,000 years using mass-spectrometric U-Th ages from Barbados corals. *Nature* **345**, 405-410.

Brook, E. J., and Kurz, M. D. (1993). Surface exposure chronology using in situ cosmogenic ^{3}He in Antarctic quartz sandstone boulders. *Quaternary Research* **39**, 1-10.

Brook, E. J., Kurz, M. D., Ackert, R. P., Denton, G. ., Brown, E. T., Raisbeck, M., and Yiou, F. (1993). Chronology of Taylor Glacier Advances in Arena Valley, Antarctica, using in situ cosmogenic ^{3}He and ^{10}Be. *Quaternary Research* **39**, 11-23.

Brown, E., Edmond, J. M., Raisbeck, G. M., Yiou, F., Kurz, M., and Brook, E. J. (1991). Examination of surface exposure ages of Antarctic moraines using in-situ produced ^{10}Be and ^{26}Al. *Geochimica et Cosmochimica Acta* **55**, 2269-2283.

Brown, E. T., Brook, E. J., Raisbeck, G. M., Yiou, F., and Kurz, M. D. (1992a). Effective attenuation lengths of cosmic rays producing ^{10}Be and ^{26}Al in quartz: Implications for exposure dating. *Geophysical Research Letters* **19**(4), 367-372.

Brown, E. T., Stallard, R. F., Raisbeck, G. M., and Yiou, F. (1992b). Determination of the denudation rate of Mount Roraima, Venezuela, using cosmogenic ^{10}Be and ^{26}Al. *EOS* **73**(43), 170.

Cerling, T. E. (1990). Dating geomorphological surfaces using cosmogenic ^{3}He. *Quaternary Research* **33**, 148-156.

Charalumbus, S. (1971). Nuclear transmutation by negative stopped muons and the activity induced by the cosmic ray muons.. *Nuclear Physics* **A166**, 145-161.

Conversi, M., and Rothwell, P. (1954). Angular distributions in cosmic ray stars at 3500 meters. *Il Nuovo Cimento* **XII**(2), 191-210.

Coxell, H., Pomerantz, M. A., and Agarwal, S. P. (1965). Survey of cosmic-ray intensity in the lower atmosphere. *Journal of Geophysical Research* **71**(1), 143-45.

Davis, R., and Schaeffer, O. A. (1956). Chlorine-36 in nature. *Annals of the New York Academy of Sciences* **62**, 107-121.

Eugster, O. (1988). Cosmic-ray production rates for ^{3}He, ^{21}Ne, ^{38}Ar, ^{83}Kr, and ^{126}Xe in chondrites based on ^{81}Kr-Kr exposure ages. *Geochimica et Cosmochimica Acta* **52**(6), 1649-1662.

Fink, D., Middleton, R., Klein, J., and Sharma, P. (1991). ^{41}Ca: Measurement by accelerator mass spectrometry and applications. *Nuclear Instruments and Methods in Physics Research* **B47**, 79-96.

Graf, T., Kohl, C. P., Marti, K., and Nishiizumi, K. (1991). Cosmic-ray produced neon in Antarctic rocks. *Geophysical Research Letters* **18**(2), 203-206.

Grosse, A. V. (1934). An unknown radioactivity. *American Chemical Society Journal* **56**, 1922-1924.

Jull, T., Wilson, A. E., Burr, G. S., Toolin, L. J., Donahue, D. J., and Lal, D. (1993). Measurements of cosmogenic ^{14}C produced by spallation in high altitude rocks. *Radiocarbon* **34**(3) 737-744.

Kurz, M.D. (1986a). Cosmogenic helium in a terrestrial igneous rock. *Nature* **320** (6061), 435-439.

Kurz, M. D. (1986b). In situ production of terrestrial cosmogenic helium and some applications to geochronology. *Geochimica et Cosmochimica Acta* **50**, 2855-2862.

Kurz, M. D., Colodner, D., Trull, T. W., Moore, R. B., and O'Brien, K. (1990). Cosmic ray exposure dating with in situ produced cosmogenic ^{3}He: Results from young lava flows. *Earth and Planetary Science Letters* **97**, 177-189.

Kurz, M. D., Brook, E. J., and Ackert, R. P. (1991). Suface exposure dating of Antarctic glacial deposits. *Antarctic Journal of the United States* **26(5)**, 85-86.

Kurz, M. D., and Brook, E. J. (1993). Surface exposure dating with cosmogenic nuclides (1993). In *Dating in a Surface Context* (Beck, C., Ed.), University of New Mexico Press, in press.

Lal, D. (1958). Investigations of nuclear interactions produced by cosmic rays. Ph.D. dissertation, Tata Institute of Fundamental Research, Bombay, India.

Lal, D. (1987). Production of ^{3}He in terrestrial rocks. *Chemical Geology (Isotope Geoscience Section)* **66**, 89-98.

Lal, D. (1991). Cosmic ray labeling of erosion surfaces: In situ nuclide production rates and erosion models. *Earth and Planetary Science Letters* **104**, 424-439.

Lal, D., and Peters, B. (1967). Cosmic ray produced radioactivity on the earth. In *Handbuch der Physic* (S. Flugge, Ed.), pp. 551-612, Springer-Verlag, New York.

Lingenfelter, R. E. (1963). Production of carbon-14 by cosmic ray neutrons. *Reviews of Geophysics* **1**(1), 35-55.

Mabuchi, H. Y., Gensho, Y., Wada, Y., and Hamaguchi, H. (1971). Phosphorous-32 induced by cosmic rays in laboratory chemicals. *Geochemical Journal* **4**, 105-110.

McKelvey, B. C., Webb, P. N., Harwood, D. M., and Mabin, M. C. G. (1990). The Dominion Range Sirius Group: a record of the late Pliocene-early Pleistocene Beardmore Glacier. In *Geological Evolution of Antarctica* (Thomson, M. R. A., Crame, J. A., and Thomson, J. W., Eds.), pp. 675-682, Cambridge University Press, New York.

Morrison, P., and Pine, J. (1955). Radiogenic origin of the helium isotopes in rock. *Annals of the New York Academy of Sciences* **62**, 71-92.

Nishiizumi, K., Winterer, E. L., Kohl, C. P., Klein, J., Middleton, R., Lal, D., and Arnold, J. R. (1989). Cosmic ray production rates of ^{10}Be and ^{26}Al in quartz from glacially polished rocks. *Journal of Geophysical Research* **94**(B12), 17,907-17,915.

Nishiizumi, K., Kohl, C. P., Arnold, J. R., Klein, J., Fink, D., and Middleton, R. (1991). Cosmic ray produced ^{10}Be and ^{26}Al in Antarctic rocks: exposure and erosion rates. *Earth and Planetary Science Letters* **104**, 440-454.

Phillips, F. M., Zreda, M. G., Smith, S. S., Elmore, D., Kubik, P. W., Dorn, R. I., and Roddy, D. J. (1991). Age and geomorphic history of Meteor Crater, Arizona, from Cosmogenic ^{36}Cl and ^{14}C in rock varnish. *Geochimica et Cosmochimica Acta* **55**, 2695-2698.

Phillips, F. M., Zreda, M. G., Smith, S. S., Elmore, D., Kubik, P. W., and Sharma, P. (1990). Cosmogenic chlorine-36 chronology from glacial deposits at Bloody Canyon, eastern Sierra Nevada. *Science* **248**, 1529-1532.

Pomerantz, M. (1971). *Cosmic Rays*, Van Nostrand Reinhold, New York.

Poreda, R. J., and Cerling, T. E. (1992). Cosmogenic neon in recent lavas from the western United States. *Geophysical Research Letters* **19**(18), 1863-1866.

Potgeiter, M. S., Moraal, H., Raubenheimer, B. C., and Stoker, P. H. (1980). Modulation of cosmic rays during solar minimum. Part 3. Comparison of the latitude distributions for the periods of solar minimum during 1954, 1956, and 1976. *South African Journal of Physics* **3**(3/4), 90-94.

Qaim, S.M., Wolfe, R., and Liskien, H. (1982). Exitation functions of (n,t) reactions on ^{27}Al, ^{59}Co, and ^{93}Nb. *Physical Review C* **25**(1), 203-207.

Sharma, P., and Middleton, R. (1989). Radiogenic production of ^{10}Be and ^{26}Al in uranium and thorium ores: implications for studying terrestrial samples containing low levels of ^{10}Be and ^{26}Al. *Geochimica et Cosmochimica Acta* **53**, 709-716.

Shen, B. S. P. (1976). Introduction: Spallation reactions and their occurences. In *Spallation Nuclear Reactions and Their Applications* (Shen, B. S. P. and Merker, M., Eds.), D. Reidel Publishing, Boston.

Staudacher, T., and Allegre, C. J. (1991). Cosmogenic neon in ultramafic nodules from Asia and in quartzite from Antarctica. *Earth and Planetary Science Letters* **106**, 87-102.

Stuiver, M., Denton, G. H., Hughes, T. J., and Fastook, J. L. (1981). History of the marine ice sheet in West Antarctica during the last glaciation: A working hypothesis. In: *The Last Great Ice Sheets* (Denton, G. H., and Hughes, T. J., Eds.), pp. 319-436, Wiley-Interscience, New York.

Trull, T. W., Kurz, M. D., and Jenkins, W. J. (1991). Diffusion of cosmogenic ^{3}He in olivine and quartz: Implications for surface exposure dating. *Earth and Planetary Science Letters* **103**, 241-256.

Walton, J. R., Heymann, D., Yaniv, A., Edgerley, D., and Rowe, M. W. (1976). Cross-sections for He and Ne isotopes in natural Mg, Al and Si, He isotopes in CAF_2, Ar isotopes in natural Ca, and radionuclides in natural Al, Si, Ti, Cr, and stainless steel induced by 12 to 45 MeV protons. *Journal of Geophysical Research* **81**(32), 5689-5699.

Yamashita, M., Stephans, L. D., and Patterson, H. W. (1966). Cosmic-ray produced neutrons at ground level: neutron flux rate and flux distribution. *Journal of Geophysical Research* **71,** 3817-3834.

Yokoyama, Y., Reyss, J., and Guichard, F. (1977). Production of radionuclides by cosmic rays at mountain altitudes. *Earth and Planetary Science Letters* **36,** 44-56.

Zreda, M. K., Phillips, F. M., Elmore, D., Kubik, P. W., Sharma, P., and Dorn, R. I. (1991). Cosmogenic chlorine-36 production rates in terrestrial rocks. *Earth and Planetary Science Letters* **105,** 94-109.

Chapter 2

Analytical Methods

Helium Isotope Measurements

Sample Processing

Samples for helium isotope measurements were in most cases hand-picked grains of olivine or quartz of various size fractions. Rock samples were crushed in a manganese steel jaw crusher, and sieved in polyester or stainless steel sieves. In most cases the 0.5-1 or 1-2 mm size fraction was analyzed, although a wider range of size fractions (0.45-2 mm) were analyzed during experiments described in Brook and Kurz (1993) [Chapter 3] that examined the grain-size dependence of ^3He concentrations.

Grains were picked from the sieved fractions under a binocular microscope. For quartz samples, whole quartz grains, rather than cemented multi-grain aggregates, which are very common in sieved fractions, were picked unless noted. For ^3He analysis in olivine, intact grains free of surface contamination and adhering groundmass were picked. All grains were rinsed with distilled water and cleaned ultrasonically in acetone, methanol, and ethanol. Where surface contamination (primarily iron and manganese oxides) was significant grains were first cleaned ultrasonically in 0.1 N HCl or HNO_3.

Helium Isotope Mass Spectrometry

Helium isotope concentrations and $^3He/^4He$ ratios were measured at WHOI using the extraction line and mass spectrometer locally referred to as "MS2." This system has been described before (Kurz 1982; Kurz et al. 1987; Trull, 1989), but pertinent information is summarized here. The mass spectrometer is an all-steel, 25.4 cm radius, 90 degree sector electromagnet, branch-tube design, with a faraday cup and electron multiplier for detecting

^4He and ^3He, respectively. MS2 has an external source electromagnet and modified Nier-type ion source. The extraction line is an all-steel, two-stage cryogenic system constructed in the WHOI laboratory (Lott and Jenkins, 1984). The line and mass spectrometer are automated and controlled by a DEC PDP11/73 computer.

Gas Release

Gases are liberated from the samples in two ways. Mineral grains can be crushed *in vacuo* in stainless steel tubes ("crushers") attached directly to the extraction line. The samples are placed in the bottom of the tube, on top of a removable, reusable, stainless steel disk that protects the tube bottom. A magnetic steel cylinder is placed above the sample, and crushes the samples when moved up and down by three computer controlled electromagnetic coils placed around the outside of the crusher vessel. Crushing 40 times normally reduces quartz and olivine grains of up to 2 mm diameter to particles less than 0.1 mm diameter.

Samples can also be heated and melted in an ultra high vacuum resistively heated furnace with a tantalum crucible, also connected directly to the extraction line. The furnace is a double-vacuum design, heated by a tungsten-mesh heating element outside the crucible, within a secondary vacuum system pumped by an oil diffusion pump. The secondary vacuum and extraction line are isolated from each other and from outside air by a double gold O-ring flange at the top of the crucible. Water cooled electrical feed-throughs provide power through the bottom flange of the furnace. Samples are introduced into the crucible *via* a rotating "6-shooter" or "10-shooter" device which consists of a flat stainless steel cylinder with drilled holes that hold the samples. The cylinder rotates around a bushing in a

stainless steel Conflat™ flange, and is operated by a rotary motion feed-through. The mechanism is rotated until the desired sample is over a hole in the flange, directly above the crucible, and dropped in the hot zone. The flange containing the rotation mechanism, and another flange below it, are cooled by water flowing through aluminum flange jackets that thermally isolate the samples from the furnace hot zone. Granular samples can be loaded directly into the sample holes in the "6-shooter" or "10-shooter" mechanism, and powdered samples are normally weighed into aluminum foil sample holders ("boats") that fit in the holes. No detectable excess blank is contributed by the aluminum boats. Power to the heating element is supplied from a variable transformer feeding a step-down transformer. Furnace temperatures are calibrated by measuring the power (voltage x current) through the heating element while measuring temperature in the bottom of the crucible with an optical pyrometer, through a pyrex window. During the work described here the normal practice was to completely melt olivine or quartz samples at an applied power of ~ 2700 watts, which corresponds to ~ 1600° C. Numerous furnace blanks at this and higher temperatures, before and after analyzing samples, indicated that this temperature was sufficient to completely release all helium from the samples.

Gas Processing

The gas extraction line consists of a gettering system and two stage cryogenic gas separation system (Fig. 1) described by Lott and Jenkins (1984). The line is constructed of 3/4 inch stainless steel tubing and all valves are pneumatically activated and controlled by the computer. Released gases are first exposed to two titanium sponge getters, one held at a 800° C and the other at room temperature to sorb H_2. Remaining gases are then exposed to a

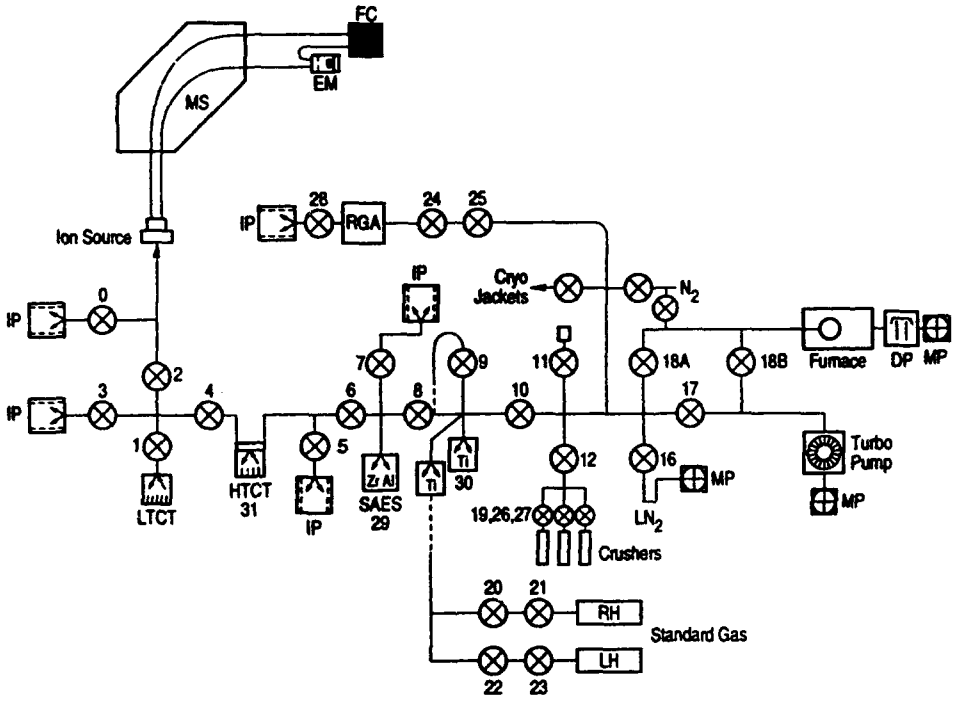

Figure 1. Diagram of noble gas extraction line used for helium isotope mass spectrometry of rock samples. IP=ion pump, RGA=rare gas analyzer, MP=mechanical pump, DP=diffusion pump, EM=electron multiplier, FC=faraday cup, LTCT=low temperature cryogenic trap, HTCT=high temperature cryogenic trap, Ti=titanium sponge getter, SAES=zirconium-aluminum gette.

Zr-Al SAES™ getter for further purification and removal of H_2. The helium content of a small aliquot of the sample gas is analyzed by a VG Ratiomatic quadropole mass spectrometer and this measurement is used to determine how much of the sample is inlet to the cryogenic system and mass spectrometer. The purpose of this step is to limit the amount of helium actually in the mass spectrometer because previous work has shown that measured $^3He/^4He$ ratios can be affected by sample size (Kurz, 1982; Trull, 1989). This step also avoids "memory" effects from large samples. The samples are split automatically by the computer program controlling the extraction line, and the fraction of the sample inlet is calibrated by splitting air standards of known helium concentration. At this point the remaining gases are exposed to a stainless steel frit at 26° K and then a charcoal trap at less than 16° K. Both traps are cooled by a single helium compressor. The charcoal trap is warmed to a nominal temperature of 36° K to release helium to the mass spectrometer, while retaining neon. The temperatures of the traps are measured with a silicon diode (charcoal trap) and thermocouple (stainless steel frit). In practice, because temperature calibration of the sensors is not absolute, the optimum release temperature for helium is determined experimentally by measuring helium and neon while warming the trap. After sample inlet both traps are heated to approximately 65° K and remaining trapped gases are pumped away by ion pumps.

Helium concentration and isotope ratio measurements are standardized by comparison with air standards. Air standards are collected in a calibrated, stainless-steel standard volume at known temperature, pressure, and relative humidity, and expanded into one of two large stainless steel tanks. During the expansion reactive gases are trapped on charcoal at liquid nitrogen temperatures. Standards are always collected at the same location

(Vineyard Sound beach at the WHOI Quisset Campus). Small aliquots of the large air standard are used as daily running standards and inlet to the extraction line *via* two aliquoting valves. The primary standard during this work was approximately 1.6-1.7 x 10^8 cm^3 STP He. The exact value is determined to approximately 0.05 % and is dependent on the temperature, pressure, and humidity during collection of the standard. The isotopic ratio of air is assumed to be constant at $^3He/^4He = 1.384 \times 10^{-6}$ (Clarke et al., 1976). A total of 48 samples, standards, and blanks can be processed in a typical daily run.

Mass Spectrometry

Samples are inlet to the mass spectrometer for 30s and the instrument is operated in static mode. The ^4He beam is measured with a faraday cup (resolution of 1:230) and the ^3He beam is measured with a Johnston Laboratories focused mesh electron multiplier (slit set for a resolution of 1:650). The latter resolution is sufficient to completely resolve the HD peak from ^3He. During analysis, the acceleration voltage is adjusted to switch the peaks, while the magnetic field remains constant. At the beginning of each analysis the mass spectrometer centers the HD^+ peak on the electron multiplier, then steps the voltage to measure ^3He and ^4He. The ^3He peak and baseline are measured 15 times and at the same time the ^4He peak height is measured on the faraday cup. The ^4He baseline is measured at the beginning of the cycle, before inlet, because the ^4He beam creates secondary electrons that interfere with baseline measurements. The electron multiplier is operated in analog mode and the ^3He and ^4He peaks are integrated for 56s, while the baseline measurement is integrated for 14 s. The ^4He baseline is integrated for 25s.

^{4}He peak heights and ^{3}He/^{4}He ratios are calculated for each measurement by fitting a straight line to the 15 integrations of the ^{4}He peak and extrapolating to the time of inlet. ^{3}He/^{4}He ratios are calculated by extrapolating the ^{3}He/^{4}He ratio of each integration to inlet time in the same fashion. This extrapolation is necessary due to depletion of the sample during analysis and grow-in of background.

Helium blanks during the course of this work ranged from 2-3 x 10^{-11} cm^3 STP ^{4}He. The isotopic ratio of any individual blank is not well determined, but long term averages are of approximately atmospheric composition. This suggests that the blank is most likely due to small atmospheric leaks in the extraction line and mass spectrometer through copper gasket mini-Conflat™ and VCR™ seals. In practice, the blank levels, which are quite low compared to other laboratories, are the ultimate analytical limit.

In a typical day, 15 to 20 primary air standards, 10 to 15 blanks, and several samples are run. Sample helium concentrations and isotope ratios are calculated based on daily means of helium concentrations and isotope ratios of standards and blanks. Uncertainty in any individual analysis is a combination of uncertainties in extrapolating to time of inlet and the variability of the air standards over the course of the day. Reproducibility of daily air standard ^{4}He concentration and ^{3}He/^{4}He ratio were generally 0.2-0.6 % and 1-1.5 %, respectively (1-sigma), prior to December 1992. The precision improved to generally 0.1 % for the air size and < 1% for the ratio after December 1992, apparently due to more efficient ion source cleaning. Blank corrections are made using the average ^{4}He concentration of the blank and an assumed atmospheric ^{3}He/^{4}He ratio. For almost all of the samples described in this thesis blank corrections were minor (< 1-2 %).

Reproducibility of Helium Isotopic Composition of Standard Rocks

Over the course of this work several rock samples were measured in replicate as a check on the long term reproducibility of helium isotope measurements. A mid-ocean ridge basalt glass, ALV892-1a, chosen for it's very low vesicularity, is used as a primary furnace standard in the laboratory. 21 measurements (Table 1) yielded a mean concentration of $8.78 \pm 0.19 \times 10^{-6}$ cm^3 STP g^{-1} ^4He with a $^3He/^4He$ ratio of $8.27 \pm 0.14 \times R_a$ (both uncertainties are one standard deviation; R_a is the atmospheric $^3He/^4He$ ratio). No discernible trend in either the helium concentration or isotope ratio with time is evident.

Two quartz samples were also measured in replicate over several years (Table 1). Sample SCW8-4-1 is a 500-710 micron sieved fraction of an Antarctic quartzite collected in 1987 from the Taylor II moraine in Arena Valley, in the Transantarctic Mountains. This sample has a ^{10}Be exposure age of approximately 350 kyr (Chapter 5). BW84-105 is a 500-1000 micron sieved fraction of sample from the Taylor IVb moraine in the same valley and has ^{10}Be exposure ages of approximately 2 myr. This sample was used for diffusion studies by (Trull et al. 1991). As discussed by (Brook and Kurz, 1993 [Chapter 3]), and in Chapter 2, ^4He concentrations in replicate quartz analyses vary significantly, in some cases by up to a factor of 3 (see Table 1). This variability is not an analytical artifact but reflects a real variability in the quartz grains, presumably due to heterogeneous uranium and thorium concentrations. In quartz samples with significant concentrations of cosmogenic ^3He, however, ^3He concentrations are reproducible (one standard deviation) within 9.1 % (BW84-105) and 7.5 % (SCW87-4-1). The better reproducibility for SCW87-4-1 is likely to be due to the restricted size fraction,

since previous work has shown that helium concentrations can be size dependent in quartz due to diffusive loss (Brook and Kurz, 1993).

^{10}Be and ^{26}Al Measurements

^{10}Be and ^{26}Al were measured in collaboration with Grant Raisbeck, Francoise Yiou, and Erik Brown at the 2 MV Tandetron Accelerator Mass Spectrometry (AMS) Facility at Gif-sur-Yvette, France. AMS ^{10}Be and ^{26}Al measurements with this instrument have been described previously (Raisbeck et al. 1984; Raisbeck et al. 1987; Bourles 1988; Brown et al., 1990), and an additional overview of chemical processing and measurement procedures is provided below. The principles and advantages of accelerator mass spectrometry have also been described in detail before (see particularly a review by Elmore and Phillips (1987) and references therein) but a review of pertinent information is provided here.

Sample Processing

Samples were either quartz sandstones or quartz-bearing metamorphic or granitic rocks. Samples sizes varied, but were chosen to give a final quantity of approximately 10^7 atoms of ^{10}Be in the final target material. This normally also yields between 3 and 6 x 10^7 atoms of ^{26}Al in terrestrial surface exposure samples. Contamination by ^{10}Be produced in the atmosphere is a potential probiem in surface exposure studies (Brown et al., 1991; Nishiizumi et al. 1989) and leaching procedures used were designed to prevent this contamination. Quartz sandstone samples were sieved and in most cases the 0.5-1.0 mm size fraction was used for analyses to eliminate smaller grains that could have higher concentrations of surface contaminant ^{10}Be. In some cases, where this material was not available, smaller (down to 0.1 mm) or

larger (up to 1 mm) size fractions were also used. Samples of well-lithified massive quartz (cobbles or boulders containing extremely lithified quartzites or vein quartz) were processed differently since they do not naturally split across pre-existing grain boundaries when crushed in a rock crusher. These samples were crushed in a jaw crusher or steel mortar and pestle to less than 0.5 mm (in some cases < 1 mm). This smaller size fraction was chosen to make chemical dissolution faster and to insure that any contaminating mineral phases (feldspar primarily) would be eliminated in acid leaching steps. Granitic samples were also crushed in this fashion.

All samples were leached in 25% reagent grade HNO_3, normally two times, either in ultrasound for four hours, or by shaking on a shaker table for four hours, to remove surface contamination and iron and manganese oxides. HCl would also be an appropriate acid for this step. Quartz samples were leached in 50% HF (Johnson Matthey-Ultrapure) in at least three, and up to five, separate steps of shaking for 24 hrs on a shaker table in screw-top teflon beakers, until a total of between 30 and 50% of the sample mass was gone. This type of procedure has been found to eliminate completely meteoric ^{10}Be (Brown 1991; Nishiizumi et al. 1989) and no signs of this contamination (unusually low $^{26}Al/^{10}Be$ ratios, poor reproducibility of replicates) were observed in this study. Leached samples were dried, weighed, spiked with 500 µg of stable Be (Merk Titrisol™ 1000 ppm Be standard) that has been shown to have a $^{10}Be/^{9}Be$ ratio of $< 1\text{-}2 \times 10^{-15}$ (G. Raisbeck, personal communication, 1991), and dissolved completely in 25 or 50% HF. When completely dissolved, samples were evaporated three times in teflon beakers in concentrated trace metal grade or sub-boiling distilled HNO_3 to remove traces of HF, which interferes with solvent extraction separation of Be and Al and can interfere in atomic absorption analyses of Al. After

evaporation the samples were brought to approximately 10 ml (exact amount determined by weight) in 2% trace metal grade distilled HNO_3, and a small aliquot was removed for stable aluminum analysis. After analysis the sample was spiked with enough stable aluminum (Johnson Matthey Atomic absorption standard - 1000 ppm) to make the total quantity in the sample approximately *1000 μg*.

Several samples of granite and metamorphic rocks containing large percentages of quartz and feldspar (see Chapters 5 and 6) were processed slightly differently. These were also crushed to <0.5 or 1 mm, and then sequentially dissolved in HF in five steps to separate quartz from feldspar and other minerals, relying on the relatively lower reactivity of quartz (Kohl and Nishiiizumi 1992). After each step the samples were examined under a binocular microscope to qualitatively evaluate the amount of quartz in the samples. After five HF leachings no mineral phases other than quartz were visible. Stable aluminum concentrations in these samples ranged from 70 to 130 ppm, well within the range measured for "pure" quartz from Dry Valley quartz sandstones (generally ~ 100 ppm or less).

Stable Al and Be measurements by GFAAS and ICAPES

Initially, stable aluminum concentrations were measured by graphite furnace atomic absorption spectroscopy (GFAAS) at the Centre de Spectrometrie Nucleare et de Spectrometrie de Masse, in Orsay, France. After these initial measurements aluminum was measured by induction coupled plasma emission spectroscpy (ICPES) at WHOI, using an Instruments SA Jobin-Yvon JY38 VHR-C rapid sequential scanning ICPES with an automated grating drive (Bankston, 1988). An intercalibration experiment gave agreement of better than 3% for samples originally intended for GFAAS

analysis (lower dilution than used for ICPES). For ICPES analyses, 1 ml aliquots of the sample in 2% HNO_3 were weighed and diluted to approximately 10 ml by weight. These samples were analyzed at the ICPES facility using normal aspiration with a peristolic pump, and argon as the carrier gas. Al was measured at the 237.312 nanometer wavelength. Because the samples were spiked with Be several Be standards were analyzed for Al to check for interferences on the aluminum wavelength, but none were found. Aluminum concentrations were calculated from standard curves using matrix matched, gravimetrically prepared, standards. The machine was run in autosampler mode and the four standards were run at the beginning and end of the runs. Quality control standards run every five samples indicated a precision of better than 2% (1-sigma). Concentrations were calculated by correcting the measured values of the quality control standards to the true values and interpolating the correction throughout the run.

Be was also measured by ICPES during calibration and testing of cation exchange columns. The 313.107 nanometer wavelength was used and analyses were made in the same fashion as described above, except that in this case both Be and Al were measured sequentially in the same samples.

Separation and Purification of ^{10}Be and ^{26}Al

AMS analysis requires that fairly pure BeO and Al_2O_3 be prepared from the spiked samples. It is particularly important to remove boron and magnesium, which may cause isobaric interferences (^{10}B on ^{10}Be and ^{26}Mg on ^{26}Al). In addition, experiments at the Tandetron have demonstrated that in ^{26}Al analysis $^{9}Be^{17}O$, $^{9}Be^{17}OH$, and $^{10}B^{16}O$ injected into the accelerator can also interfere with ^{26}Al, indicating that careful attention to completely

separating B and Be from Al is necessary (G. Raisbeck, personal communication, 1992).

In the beginning of this work, Al and Be were separated from spiked samples using solvent extraction techniques (Brown, 1990). Be was separated by extracting the Be-acetylacetonate (Be-AcAc) complex into carbon tetrachloride in the presence of EDTA. Samples in 2% HNO_3 were adjusted to pH 8 by the addition of 25% 4Na-EDTA solution in 125 or 250 ml borosilicate beakers. 2ml of acetylacetone was added and the solution was occasionally gently swirled to mix the reagents over 20 min. The sample was then added to a borosilicate glass separatory funnel with 10 ml carbon tetrachloride and shaken vigorously for 1-2 min. Because Be does not form strong complexes with EDTA, Be-AcAc is extracted into carbon tetrachloride, while Al-EDTA stays in aqueous solution. The organic phase of the extraction was separated into the original beaker containing the sample. An additional 10 ml of carbon tetrachloride and 1 ml of acetylacetone were added to the aqueous phase in the funnel and shaken again for 1-2 min. The resulting organic phase was added to the material in the beaker. The aqueous phase (containing aluminum) was saved in a low density polyethelene bottle for later processing. 5ml of concentrated HCl (two-bottle distilled or trace metal grade acid) was added to the organic phase in the beaker, and the beaker was set on low-medium heat on a hotplate to evaporate the solution The addition of acid is necessary to break the Be-AcAc bond. Be-AcAc is extremely volatile and omission of this step results in loss of Be upon heating. The solution normally evaporates to a brown precipitate containing Be and organic material. 5 ml of concentrated HNO_3 (two-bottle distilled or trace metal grade) was added and the solution evaporated slowly to dryness. Then 5 ml of nitric acid and 0.5 ml of perchloric acid were added and the solution

again evaporated to dryness. Finally, an additional 5 ml of HNO_3 was added and the solution evaporated to dryness again. At this point the sample is normally a white-yellow-brown precipitate. The precipitate was dissolved by adding 100 µl HNO_3 and 5 ml of deionized water. The entire extraction procedure was then repeated one time, and the aqueous phase from the second extraction combined with the aqueous phase from the first. The material in the beaker after the second extraction and evaporation steps was transferred to a 15 ml centrifuge tube by adding 50 µl of HCl and ~ 1 ml of water to dissolve the precipitate (repeating this three times to insure efficient transfer). The solution was brought to pH 8 by adding ammonia, where $Be(OH)_2$ precipitates. After 10 minutes of centrifugation the supernatant was poured off into the sample beaker and the precipitate was washed with pH 8 water by mixing the precipitate with ~ 5 ml of pH 8 water on a vortex mixer. This procedure was repeated three times for a total of four precipitations and three washings. The purpose of this step is to remove boron, which does not precipitate as a hydroxide. The precipitate from the final centrifugation was transferred to a 10 ml quartz crucible by adding 100 µl HNO_3 and ~ 1 ml deionized water, mixing on the vortex mixer, and pouring the solution into the crucible. This was repeated a total of three times. The solution in the crucible was evaporated to dryness at low setting on a hotplate, then heated on the hotplate at high temperature for 30 minutes. At this point the material is usually white and powdery in appearance and is a non-stochiometric mixture of $Be(OH)_2$ and BeO. The material is then heated in a bunsen burner flame or electrical ashing furnace for thirty minutes to convert all of it to BeO.

The aluminum remaining in the aqueous phase of the above extraction was also initially extracted by a solvent extraction procedure.

Because EDTA forms strong complexes with Al, the EDTA must first be oxidized. This was done by repeated evaporation in concentrated HNO_3. This step was experimented with and the best strategy was to to add ~ 20 ml HNO_3 to the samples and heat them, covered with a watch glass, at medium temperature overnight on a hotplate, followed by two additional open beaker evaparations in 20 ml HNO_3. Poor yields in aluminum target preparation (see below) are attributed to inefficiency in this step, and oxidation with concentrated H_2O_2 and HNO_3 appears to be a better alternative (E. Brown, personal communication, 1992). The reaction with H_2O_2 can be somewhat violent, however, and small additions of ~ 1 ml at a time are necessary to keep the sample in the beaker. After oxidation, the Al-EDTA solution typically evaporated to a yellow crystalline mass (Na-nitrate crystals). This material was re-dissolved in 20-30 ml of deionized water. 5 ml of a reagent made from 95 ml deionized water, 5 ml ammonia, and 0.1 g 2-methyl 8-quinolinol (2-methyl 8-hydroxyquinoline) was added to the solution and pH was adjusted to approximately 10 with ammonia. The quinolinol reagent forms very weak complexes with aluminum, but much stronger complexes with other elements (Brown et al. 1992). The solution was added to a separatory funnel and extracted twice with 15 ml chloroform. The organic phase was reserved until the procedure was completed in case of procedural errors. Al was extracted from the combined aqueous phase from the two repetitions by adjusting the pH to 7-8 and adding 3 ml acetylacetone. After a five minute wait the solution was extracted in a separatory funnel (2 times) with carbon tetrachloride and aluminum targets were prepared as described for beryllium targets.

Several minor problems were encountered with the above techniques and some new methods were investigated. The largest problem is the

necessity to oxidize large amounts of EDTA to extract Al. This is time consuming, is not always reliable, and uses large amounts of acid. In addition, the extractions employing the quinolinol reagent and chloroform produce brown-gray precipitates and form emulsions, both of which are difficult to deal with in separatory funnels. One way to avoid this is to separate Be and Al first by ion exchange chromatography. A procedure was developed based on separation methods described by Ehmann and Kohman (1958) and Fairhall (1960). This work indicated that Be, an alkaline earth element, and Al, a group IIIa element, could effectively be separated by cation exchange. Two cation exchange columns were built from 0.7 cm ID, 1 cm OD borosilicate glass. The columns were loaded with 10 ml of DOWEX AG50-X 100-200 mesh cation exchange resin, and the resin was cleaned with 10 bed volumes of 6N HCl. The separation efficiency of the columns was tested using an artificial Be and Al standard and a replicate sample (KBA89-108) that had both been spiked with Al and Be (~0.5 mg Be and 1 mg Al). The latter was used to insure that there were no unusual matrix effects associated with dissolved quartz. Columns were preconditioned with 5 bed volumes of 1 N HCl. The test sample and standard were evaporated to dryness and taken up in ~ 10 ml of 1 N HCl. Each was loaded on a column and the elutant was collected in a 30 ml borosilicate beaker until the liquid level above the resin bed reached the bed surface. 10 aliquots of 1 N HCl were then added to the column, and the elutant from each addition was collected in a separate 10 ml beaker. Following the 1N HCl step, 5, 10 ml aliquots of 6 N HCl were added and the elutant from each was collected in the same fashion. All elutants were evaporated to dryness and then diluted in 2 % HNO_3 and analyzed for Be and Al simultaneously using the Instruments SA JY38 VHR-C ICPES. Good separation of Be and Al is obtained by this method (Fig. 2). The

efficiency of this separation procedure was further tested by measuring the Be and Al contents of the Be and Al fractions of four samples and a blank processed by the routine column method. This experiment showed that while no detectable Be was found in the Al fraction, the quantity of Al recovered in the Al fraction ranged from 75 to 100 %. This is most likely due to over-loading of the cation exhange resin with other cations in the rock matrix and increasing the resin volume would probably solve that problem. Alternatively, it may be necessary to extract Al and Be using an acetylacetone extraction prior to the column chemistry. Fine-tuning of the column procedure will require further work but as it stands it yields adequate results in most cases.

For routine sample processing by the column method, the samples were taken up in 1N HCl after the last HNO_3 evaporation step, and the aliquot for Al analysis was removed at that point. After spiking with stable Al the samples were loaded on the preconditioned columns. Be was eluted with 100 ml of 1 N HCL using four successive 25 ml aliquots of 1 N HCl, and all the elutant was collected in a 125 or 250 ml beaker. Al was eluted with 50 ml of 6N HCl (two 25 ml aliquots), and all the elutant was collected in a 125 or 250 ml beaker. The Al fraction was evaporated to dryness in the presence of a few ml of HNO_3 to oxidize any organic material left over from the columns, then transferred to centrifuge tubes and precipitated and rinsed as above. The Be fraction was evaporated to near dryness and dissolved in 2% HNO_3. The solvent extraction procedure for Be as described above was then performed. Initially the Al target was prepared by evaporating the HCl solution containing Al that came off the column to dryness, adding 1-2 ml of HNO_3 to oxidize organic material from the resin, evaporating that to dryness, then simply precipitating $Al(OH)_3$ as described above for $Be(OH)_2$.

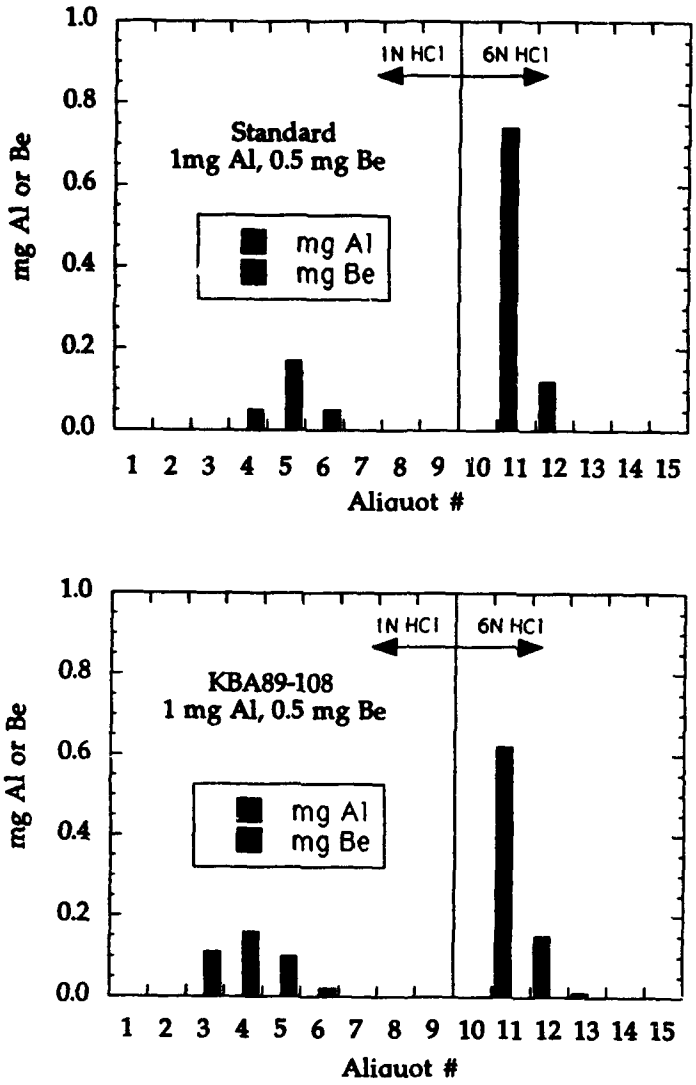

Figure 2. Chromatagram showing separation of Be and Al by cation exchange chomatography.

This did not markedly improve the performance of the aluminum targets in the accelerator; $^{27}Al^{3+}$ ion currents remained below 100 nA and peaks in the E vs. dE spectrum that have been attributed to the injection of $^{9}Be^{17}O$ and $^{10}B^{16}O$ remained in the spectra (see below). In an attempt to improve target performance the Al fraction from the cation exchange procedure was further processed by the 2-methyl 8-quinolinol method, or by a second cation exhange procedure. In either case the sample was first evaporated to dryness at low temperature and 1-2 ml of HNO_3 was added and evaporated to dryness to oxidize any residual organic matter. The latter procudure used a 15 ml disposable polyethelene column and 10 ml of DOWEX AG50X 100-200 mesh cation exchange resin, with cleaning and elution as described above for the first cation exhange step. The Al fraction from the second cation exchange step was again evaporated to dryness, and 1-2 ml of HNO_3 was added and evaporated to dryness to oxidize any residual organic matter. Precipitation of $Al(OH)_3$ and preparation of Al_2O_3 proceeded as described above for Be and Al. This procedure was tested on three samples near the end of this work and it resulted in targets that had ion currents in excess of 200 nA, which is excellent performance for the Tandetron, and reduced the magnitude of the neighboring peaks (see Fig. 5, below) significantly.

Accelerator Mass Spectrometry of ^{10}Be and ^{26}Al

Principles

Accelerator mass spectrometry (AMS) has revolutionized the measurement of rare long-lived radionuclides in terrestrial materials in the last two decades. Prior to the development of AMS, these measurements were severely limited by the lack of sensitivity of conventional decay counting techniques. The general principles of AMS have been described in a

large number of publications, including Elmore and Phillips (1987), Litherland (1987), Middleton and Klein (1987), Raisbeck et al. (1984), and Raisbeck et al. (1987). Raisbeck et al. (1984) and Raisbeck et al. (1987) also provided specific information about the operation of the Tandetron for ^{10}Be and ^{26}Al analysis. AMS combines the mass discrimination of sensitive mass spectrometers with the advantages of a multi-MV energy beam. The advantages of the high energy beam include the ability to use an electron stripping step to eliminate molecular interferences, the use of energy filtering devices like carbon foils to reduce isobaric interference, and the ability to use energy sensitive detectors, like the E_R vs. ΔE detectors described below, for the ultimate measurements and for discriminating among isobars.

The Tandetron AMS facility at Gif-sur-Yvette is illustrated schematically in Fig. 3. The general operating principles are described here, and the details of ^{10}Be and ^{26}Al analysis are described below. The cesium sputter ion source produces a beam of negative ions accelerated at a potential of 20 KV. An electrostatic analyzer focuses the beam, which is bent by a 90^o injection magnet. The beam tube within the injection magnet is electrically insulated from the rest of the system and voltage across this section of the tube is switched during analysis to alternatingly inject a beam of the radioactive or stable isotope. The beam is accelerated to a nominal potential of 2 MV (differs slightly depending on the element analyzed). Because the beam consists of negative ions, elements that do not form negative ions are effectively removed. The negative beam passes through a stripper canal filled with argon. Collisions in the canal strip electrons from the elements in the beam, and also break apart molecular ions. The resulting beam consists normally of positive ions of the element of interest, in a variety of charge states, and is accelerated to ground.

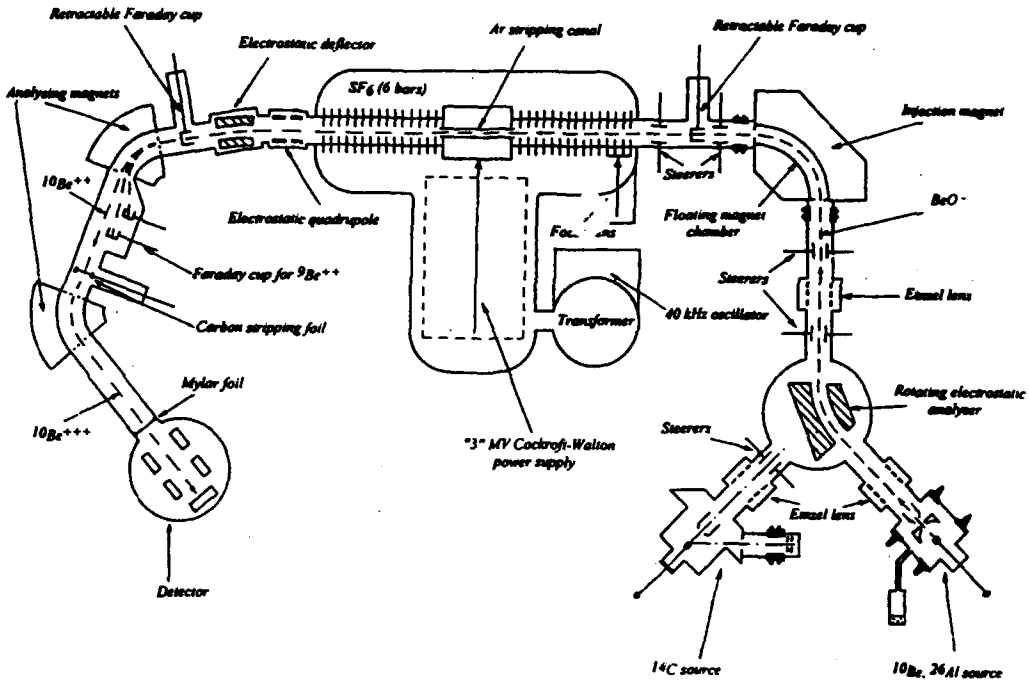

Figure 3. Schematic diagram of the Tandetron AMS at Gif-sur Yvette. See text for explanation.

The beam is further steered by an electrostatic deflector and a first analyzing magnet, after which the stable isotope beam is normally detected in a faraday cup. The rare isotope beam is further bent by a second analyzing magnet. The detector system at the Tandetron facility at Gif-sur-Yvette is a gas ionization detector normally referred to as a ΔE *vs.* E_r detector. The detector is filled with a partial pressure of argon gas and methane, and separated from the beam line by a mylar foil. Ions passing through the detector ionize the detector gas, and the degree of ionization is measured across a series of plates kept at a potential difference of a few hundred volts. The series of plates allows measurement of both the rate of energy loss (ΔE) of the particle, and the total or residual (E_r) energy. Most light ions have a unique ΔE *vs.* E_r signature, allowing separation of isobars, for example, ^{10}B from ^{10}Be (Figures 4 and 5).

^{10}Be Analysis

AMS Be targets are prepared in the laboratory at Orsay by mixing the BeO in the quartz crucible with graphite. The resulting material is pressed in a molybdenum target holder (ion source cathode) and sintered under argon at 1800° C in a resistively heated furnace. The ion source is operated at a cathode voltage of 3-4 KV (e.g., 3-4 KV is the energy of the Cs sputter beam). BeO^- ions are produced in the source, and after focusing the injection magnet voltage alternates between injecting $^9BeO^-$ for 5 s and $^{10}BeO^-$ for 100 s. The BeO^- ions are accelerated at a potential of 2.2 MV and electron stripping in the stripper canal produces positive Be ions, with Be^{2+} being the most abundant. The beam is accelerated in the second part of the tandem accelerator, then passes through the electrostatic analyzer, which selects for the Be^{2+} charge state. The two analyzing magnets further discriminate against ions of other

mass/energy states. The first magnet is set to direct the $^{9}Be^{2+}$ beam to a Faraday cup, and the $^{10}Be^{2+}$ beam is sent past, through a 200 $\mu g/cm^2$ carbon foil, designed to reduce the ^{10}B signal. The ^{10}B isobar is a significant problem for ^{10}Be analysis and the carbon foil causes $^{10}B^{2+}$ ions to lose energy faster than $^{10}Be^{2+}$ ions, allowing B and Be to be more effectively separated at the second analyzer magnet. At the carbon foil exit, the second analyzer magnet current is set to select for Be^{3+} ions instead of Be^{2+} ions. This further reduces the ^{10}B background in the detector because the at this energy the 3^+ charge state of Be is favored relative to B (Raisbeck et al. 1984). The beam then enters the detector region, where ΔE and E_R are measured and recorded on a Canberra model 88 bidimensional multichannel analyzer. ^{10}Be is measured by counting the number of arrivals in a predetermined window in the ΔE *vs.* E_R spectrum (Figs. 4 and 5). Normally the ^{10}B and ^{10}Be peaks are well resolved because the ions have different energy loss and residual energy characteristics. In fact, the ^{10}B count rate is routinely measured during ^{10}Be analysis. At high boron ion currents (> 40,000 cps), however, "pileup" occurs in the detector. In practice, therefore, it is sometimes necessary to limit the ion current, thus limiting the precision of the ^{10}Be measurement. Typical $^{9}Be^{2+}$ ion currents for the targets made for this work were between 500 and 1500 μamps, fairly normal for samples of this type. Boron contamination was observed in some targets and its source is not completely clear. It is possible, however, that atmospheric dust and perhaps sea-salt aerosols play a role. However, preparing targets in a Class 100 clean room did not appear to alleviate this problem.

A normal measurement consists of a nu of 100s ^{10}Be measurement periods, each grouped with two ^{9}Be measurement periods.

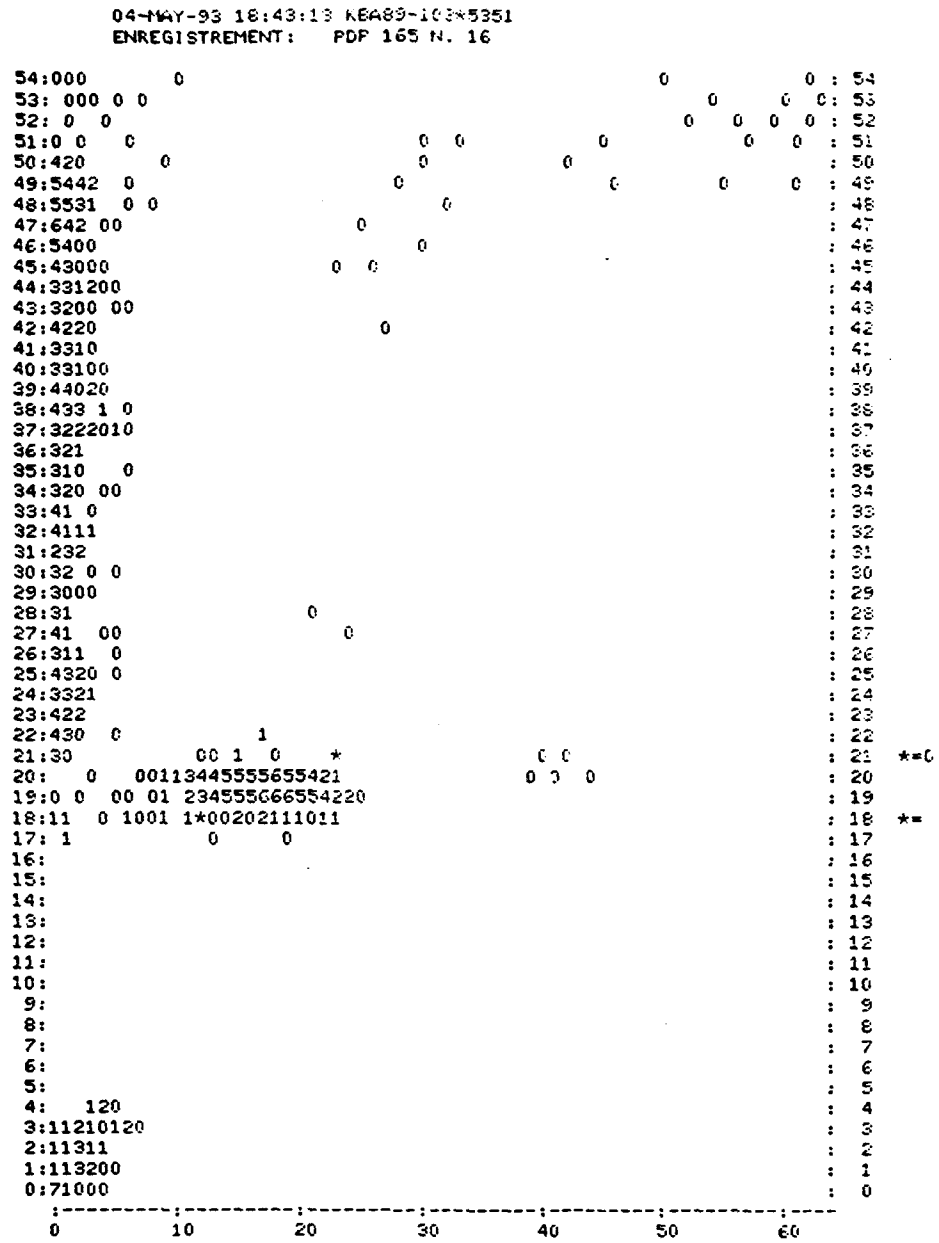

Figure 4. ^{10}Be ΔE *vs.* Er spectra for quartz sample KBA89-104. The plot shows the energy and energy loss data collected on a multi-channel analyzer, each number on the plot is the log (base 2) of the number of events in each ΔE vs. E region. The rectangular region between the two stars is the window of interest for ^{10}Be and counts that fall within this window are counted as ^{10}Be events.

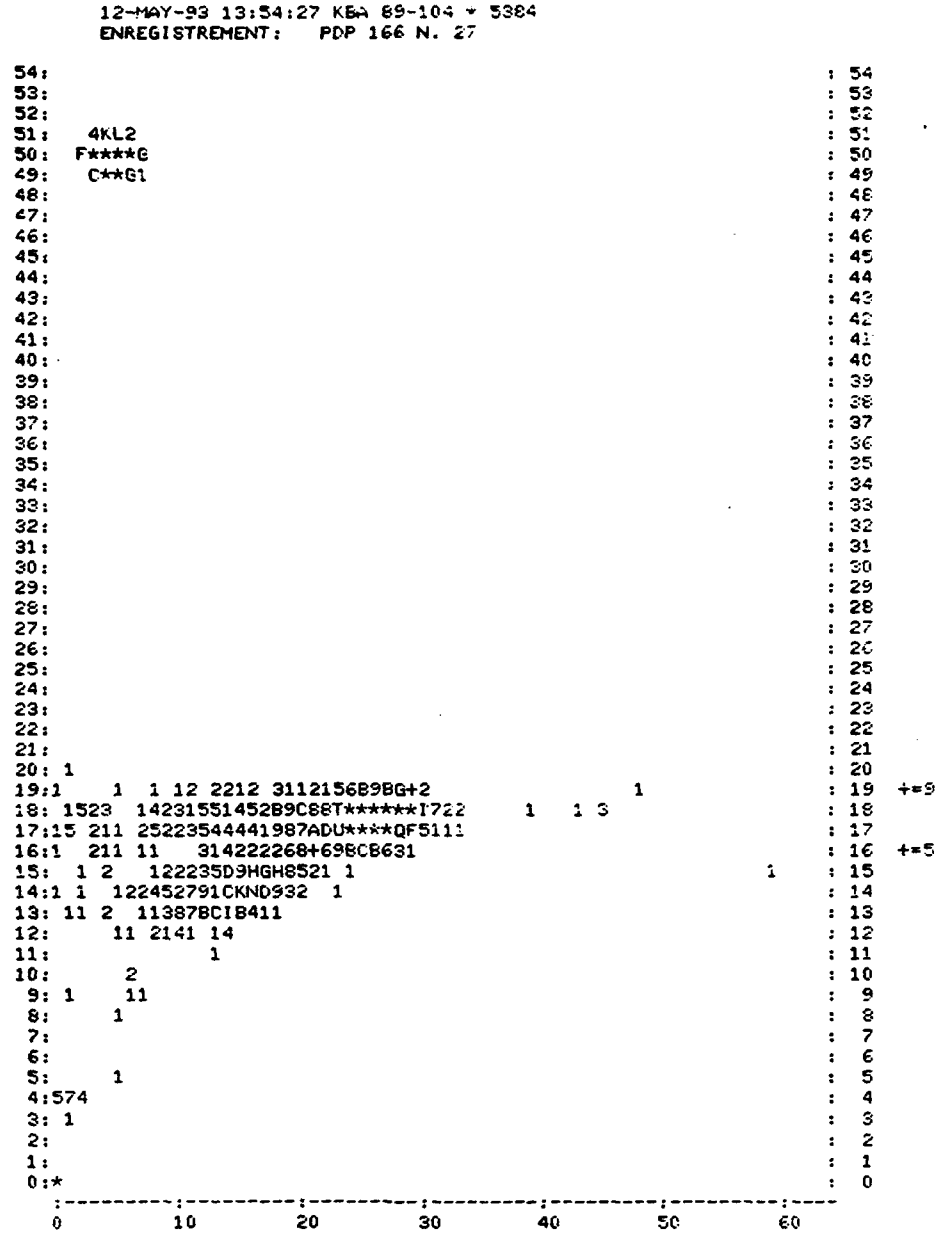

Figure 5. ^{26}Al ΔE *vs.* Er spectra for quartz sample KBA89-104. As in Fig. 4 the upper right and lower left corners of the ^{26}Al window are denoted by the plus signs. The peak to the lower left side of the window is attributed to the injection of $^{9}Be^{16}OH$ and $^{10}B^{16}O$ ions into the accelerator (see text).

Measurements are continued until a sufficient number of ^{10}Be events are recorded in the detector. The $^{10}Be/^{9}Be$ ratio is calculated by comparing the measured ratio of ^{10}Be counts to average ^{9}Be ion current for the two surrounding ^{9}Be measurement periods to the count/current ratio for a standard of known $^{10}Be/^{9}Be$ ratio (NIST Standard Reference Material #4325, $^{10}Be/^{9}Be = 2.68 \times 10^{-11}$). The standard is run three times during the day and the count/current ratio usually varies by less than 3 %. All samples contain a known amount of ^{9}Be, and ^{10}Be concentrations are calculated from the measured $^{10}Be/^{9}Be$ ratio. Uncertainties are calculated based on counting statistics for individual samples and an additional 5 % uncertainty that accounts for instrumental drift. Blank targets prepared during the course of this study had $^{10}Be/^{9}Be$ ratios of $\sim 2 \times 10^{-15}$ (near the optimum for this instrument).

^{26}Al Analysis

^{26}Al analysis is very similar to ^{10}Be analysis, with a few important exceptions. Al^-, rather than AlO^-, is injected into the accelerator because of a very strong interfering $^{26}MgO^-$ beam. Production of Al^- ions is not as efficient as AlO^- production, limiting Al^{3+} ion currents to ~200 nA or less, however, using Al^- is advantageous because Mg^- ions are not formed, minimizing potential interferences from ^{26}Mg. After the stripper region in the accelerator the dominant charge state is Al^{3+}, requiring that the terminal voltage be set at 1.93 MV to allow the analyzer magnets to bend the Al beam enough to reach the detectors. The carbon foil is not used, and ^{27}Al is detected with a faraday cup between the first and second magnets, on the opposite side of the beam from the ^{9}Be detector (Fig. 3). Detector gas pressure is slightly lower than in ^{10}Be analysis due to the lower range of ^{26}Al ions.

The aluminum standard was prepared from a commercially available ^{26}Al standard by mixing it with stable ^{27}Al and is described by Raisbeck et al. (1983). It has a $^{26}Al/^{27}Al$ ratio of 4.52×10^{-11}. Data aquisition and calculations are similar to those described for ^{10}Be above.

As mentioned above there are some important isobaric interferences in ^{26}Al spectra. The first, not mentioned previously, is due to occasional voltage break-downs (sparks) in the ion source that cause $^{26}MgH^-$ ions to be injected into the accelerator. Charge exchange in the accelerator region of the Tandetron can then produce ^{26}Mg ions with very similar ΔE v. Er characteristics to $^{26}Al^{3+}$. A circuit that stops data collection during a spark removes this potential interference. There are also a number of peaks in ^{26}Al spectra which are very close to, but resolved from, the region of interest for ^{26}Al data collection. As mentioned above, experiments at the Tandetron have identified that these probably represent interference associated with $^{9}Be^{17}O$ or $^{10}B^{16}O$ (G. Raisbeck, personal communication, 1992), which, due to charge exchange, can produce ions with similar rigidity to ^{26}Al. There is some concern that they will "tail" into the ^{26}Al window if large enough (Fig. 5). As described above, clean chemical separation appears to minimize these interference problems.

Lithium Measurements

Lithium concentrations were measured in selected quartz samples by flame atomic absorption spectrophotometry using a Perkin-Elmer Model 403 with an air/acetylene flame, hollow cathode Li lamp, red filter in, at the 670.8 nm wavelength. Samples were cleaned in 25 % HNO_3, completely dissolved in a 3:1 HF:HNO_3 mixture, then evaporated to dryness three times in concentrated HNO_3 and brought up to a known volume in 0.3 N HNO_3. To

avoid losses due to ionization of lithium in the flame small quantities of a 100,000 ppm CsCl solution were added to all samples and standards to make the final Cs concentration 1000 ppm. Standard curves were generated with a sequence of four standards in 0.3 N HNO_3 from 0 to 2 ppm. Internal precision of the measurements was 0.5 %, accuracy, based on a consistency standard, was better than 0.5 %. Five replicate measurements of sample BW84-105 yielded 16.9 ± 0.5 μg/g Li (2.5 % precision); four replicates of BW84-87 gave 5.6 ± 0.5 μg/g (8.9% precision). Analysis of BW85-105 by standard additions yielded a concentration of 17.1 μg/g, indicating that there are no significant matrix effects in the samples that affect the calibration using standard curves.

More detailed Li measurements were made for two additional samples as part of the investigation of the depth dependence of ^3He production (Chapter 7). These samples were first leached overnight in 1N HCl and then completely dissolved in HF and processed as above. Lithium concentrations were measured in the leachates and the total dissolutions. All of the lithium concentration data are shown in Table 2.

Table 1. Replicate helium isotope analyses for ALV892-1a basalt glass and quartz grains from two Antarctic sandstones. $^3He/^4He$ ratio reported relative to the atmospheric ratio (R_a) ($R_a=1.384x10^{-6}$).

ALV892-1A Basalt Glass			SCW87-4-1 0.5-0.71 mm quartz grains			
Date	^4He (cc STP/g) x 10^6	$^3He/^4He$ (R/Ra)	Date	^4He (cc STP/g) x 10^6	$^3He/^4He$ (R/Ra)	^3He (cc STP/g) x 10^{12}
4/19/90	8.96	8.41	8/1/90	0.98	1.45	1.96
5/5/90	8.84	8.41	10/2/90	1.13	1.38	2.15
12/7/90	8.97	8.44	10/9/90	1.51	1.02	2.13
5/7/91	8.78	8.10	11/6/90	0.87	1.92	2.30
8/14/91	8.59	8.29	3/6/91	0.96	1.48	1.95
10/17/91	8.73	8.14	5/7/91	3.81	0.45	2.38
10/22/91	8.97	8.10	11/10/91	0.45	3.15	1.97
10/28/91	8.98	8.29	11/16/91	0.95	1.50	1.97
2/18/92	8.84	8.10	11/21/91	0.96	1.60	2.12
2/20/92	8.72	8.31	12/3/92	1.93	0.00	1.95
3/20/92	8.59	8.06	**Mean**	**1.35**	**1.40**	**2.09**
3/22/92	8.63	8.38	**SD**	**0.95**	**0.84**	**0.16**
3/31/92	8.73	8.45	**% SD**	**70.18%**	**60.33%**	**7.51%**
4/8/92	8.99	8.48				
5/4/92	8.89	8.11				
5/7/92	8.70	8.33	**BW84-105 0.5-1mm quartz grains**			
5/14/92	8.93	8.10	8/18/86	1.44	9.88	19.72
5/20/92	8.82	8.32	4/26/90	0.64	19.51	17.19
7/30/92	8.33	8.16	4/26/90	2.51	5.15	17.94
12/18/92	8.39	8.29	5/11/92	0.12	125.65	20.54
3/24/93	8.94	8.40	1/27/93	0.22	67.72	20.79
Mean	**8.78**	**8.27**	**Mean**	**1.07**	**39.73**	**19.67**
SD	**0.19**	**0.14**	**SD**	**0.92**	**47.99**	**1.78**
% SD	**2.16%**	**1.70%**	**% SD**	**85.70**	**120.78**	**9.07**

Table 2. Lithium concentrations in selected Antarctic quartz samples.

Sample	Li (μg/g)
BW84-105	17.0
BW84-105	16.5
BW84-105	16.6
BW84-105	16.8
BW84-105	17.8
mean±1 sd	**16.9±0.5**
BW84-87	5.9
BW84-87	5.1
BW84-87	5.3
BW84-87	6.1
mean±1 sd	**5.6±0.5**
BW84-71	6.6
BW84-71	6.4
BW84-134	3.6
AA86-14	5.0
AA86-14	5.1
AA86-15	5.0
AA86-15	5.2
BW84-33	9.3
AA86-5	7.7
AA86-16	5.8
BAK90-81 leach*	4.6
BAK90-81 bulk	3.28
KBA89-77-12 leach*	below detection
KBA89-77-12 bulk	5.0

* overnight leach in 1 N HCl at 70 degrees C.

References

Bankston, D. C. (1988). General guidelines for operating a rapid sequential inductively coupled plasma-atomic emission spectrometer. WHOI Technical Memorandum WHOI-4-88, 23 p.

Bourles, D. (1988). Etude de la geochimie de l'isotope cosmogenique ^{10}Be et de son isotope stable ^{9}Be en millieu oceanique. Application a la datation des sediments marins. Ph.D. dissertation, University of Paris, Paris, France.

Brook, E. J., and M. D. Kurz (1993). Surface exposure chronology using in situ cosmogenic ^{3}He in Antarctic quartz sandstone boulders. *Quaternary Research* **39**, 1-10.

Brook, E. J., Kurz, M. D., Ackert, R. P., Denton, G. ., Brown, E. T., Raisbeck, M., and Yiou, F. (1993). Chronology of Taylor Glacier Advances in Arena Valley, Antarctica, using in situ cosmogenic ^{3}He and ^{10}Be. *Quaternary Research* **39**, 11-23.

Brown, E. T. (1990). *The Geochemistry of Beryllium Isotopes: Applications in Geochronometry*. Ph.D. Thesis MIT/WHOI, WHOI-90-47.

Brown, E., Edmond, J. M., Raisbeck, G. M., Yiou, F., Kurz, M., and Brook, E. J. (1991). Examination of surface exposure ages of Antarctic moraines using in-situ produced ^{10}Be and ^{26}Al. *Geochimica et Cosmochimica Acta* **55**, 2269-2283.

Brown, E. T., Brook, E. J., Raisbeck, G. M., Yiou, F, and Kurz, M. D. (1992). Effective attenuation lengths of cosmic rays producing ^{10}Be and ^{26}Al in quartz: Implications for exposure dating. *Geophysical Research Letters* **19**(4), 367-372.

Clarke, W. B., Jenkins, W. J., and Top, Z. (1976). Determination of tritium by mass spectrometric measurement of ^{3}He. *International Journal of Applied Radiation and Isotopes* **27**, 515-522.

Ehmann, W., and Kohman, T. P. (1958). Cosmic-ray induced radioactivities in meteorites-I: Chemical and radiometric procedures for aluminium, beryllium, and cobalt. *Geochimica et Cosmochimica Acta* **14**, 340-368.

Elmore, D. and Phillips, F. M. (1987). Accelerator mass spectrometry for measurement of long-lived radionuclides. *Science* **236**, 543-550.

Fairhall, A. W. (1960). *The Radiochemistry of Beryllium*. National Academy of Sciences, National Research Council, Nuclear Science Series NAS-NS 3013.

Kohl, C. P. and Nishiiizumi, K. (1992). Chemical isolation of quartz for measurement of in-situ produced cosmogenic nuclides. *Geochimica et Cosmochimica Acta* **56**(9), 3583-3588.

Kurz, M. D. (1982). Helium Isotope Geochemistry of Oceanic Volcanic Rocks: Implications for Mantle Heterogeneity and Degassing. Ph.D. Thesis MIT/WHOI, WHOI-82-32.

Kurz, M. D., Gurney, J. J., Jenkins, W. J., and Lott, D. E. (1987). Helium isotope variability within single diamonds from the Orapa kimberlite pipe. *Earth and Planetary Science Letters* **86**, 57-68.

Litherland, A. E. (1987). Fundamentals of accelerator mass spectrometry. *Philosophical Transactions of the Royal Society of London* **A323**, 5-21.

Lott, D. E. and Jenkins, W. J. (1984). An automated cryogenic charcoal trap system for helium isotope mass spectrometry. *Reviews of Scientific Instruments* **55**, 1982-1988.

Middleton, R. and Klein, J. (1987). ^{26}Al: measurement and application. *Philosophical Transactions of the Royal Society of London* **A323**, 121-143.

Nishiizumi, K., Winterer, E. L., Kohl, C. P., Klein, J., Middleton, R., Lal, D., and Arnold, J. R. (1989). Cosmic ray production rates of ^{10}Be and ^{26}Al in quartz from glacially polished rocks. *Journal of Geophysical Research* **94**(B12), 17,907-17,915.

Raisbeck, G. M., Yiou, F., Klein, J., and Middleton, R. (1983). Accelerator mass spectrometry measurement of cosmogenic ^{26}Al in terrestrial and extraterrestrial matter. *Nature* **301**, 690-692.

Raisbeck, G. M., Yiou, F., Bourles, D., Lestringuez, J., and Deboffle, D. (1984). Measurement of ^{10}Be with a tandetron accelerator operating at 2MV. *Nuclear Instruments and Methods in Physics Research* **B5**, 175-178.

Raisbeck, G. M., Yiou, F., Bourles, D., Lestringuez, J. and Deboffle, D. (1987). Measurements of ^{10}Be and ^{26}Al with a tandetron AMS facility. *Nuclear Instruments and Methods in Physics Research* **B29**, 22-26.

Trull, T. (1989) Diffusion of helium isotopes in silicate glasses and minerals: implications for petrogenesis and geochronology. Ph.D. Thesis MIT/WHOI, WHOI-89-15.

Trull, T. W., Kurz, M. D., and Jenkins, W. J. (1991). Diffusion of cosmogenic ^{3}He in olivine and quartz: implications for surface exposure dating. *Earth and Planetary Science Letters* **103**, 241-256.

Chapter 3

Surface Exposure Chronology Using *in situ* cosmogenic ^{3}He in Antarctic Quartz Sandstone Boulders*

* published in *Quaternary Research* v. 39, p. 1-10. Reprinted with permission from University of Washington Press.

Surface-Exposure Chronology Using *in Situ* Cosmogenic ^{3}He in Antarctic Quartz Sandstone Boulders

EDWARD J. BROOK AND MARK D. KURZ

Department of Marine Chemistry and Geochemistry, Woods Hole Oceanographic Institution, Woods Hole, Massachusetts 02543

Received December 4, 1990

In situ-produced cosmogenic helium (^3He_c) provides a new tool for constraining histories of Quaternary geomorphic surfaces. Before general application of the technique, however, the systematics and production rates of ^3He_c must be well understood. In a companion study, ^{3}He and ^{10}Be data from sandstone and granite boulders in the Dry Valleys region of Antarctica have been used to constrain the ages of an important moraine sequence formed by the Taylor Glacier. Data from these deposits also provide information about the systematics of ^{3}He in quartz that has important implications for geochronology based on ^3He_c. In contrast to previous results from olivine and clinopyroxene, crushing quartz *in vacuo* releases helium with high ^{3}He/^{4}He ratios (up to 148 × R_a, where R_a is the atmospheric ^{3}He/^{4}He ratio), indicating that crushing cannot be used to determine the isotopic composition of trapped (i.e., noncosmogenic) helium in quartz. Analysis of ^{3}He in different size fractions of the same samples indicates significant ^{3}He loss not predicted by existing ^{3}He diffusion data for quartz. The origin of the discrepancy is not clear, but loss from these samples is not as significant as suggested by the limited data of previous studies.

INTRODUCTION

Measurement of nuclides produced *in situ* in rocks by cosmic rays provides a new tool for studying exposure histories of geomorphic surfaces. Cosmogenic ^{3}He (^3He_c) is unique among the *in situ*-produced cosmogenic nuclides in that it is stable and has a high production rate (about 150–200 at g^{-1} yr^{-1} at sea level >60° geomagnetic latitude) and a low detection limit (~10^4 atoms in the WHOI laboratory). Several recent studies have demonstrated the utility of ^3He_c in determining exposure ages and erosion rates of olivine- and clinopyroxene-bearing volcanic rocks (Kurz, 1986a,b; Craig and Poreda, 1986; Kurz *et al.*, 1990; Cerling, 1990). This success is due to the well-understood systematics of ^{3}He in olivine and clinopyroxene, and low diffusion rates of ^{3}He in these minerals (Kurz, 1986b; Trull *et al.*, 1991). ^3He_c has also been measured in quartz, in which a number of studies suggest, based on a limited amount of data, that loss of ^3He_c due to diffusion may be significant (Cerling, 1990; Graf *et al.*, 1991; Trull *et al.*, 1991). It is important to understand further the behavior of ^3He_c in quartz, however, because quartz is common in continental rocks, is resistant to chemical and physical weathering, and is an ideal phase for determining *in situ* ^{10}Be and ^{26}Al (e.g., Nishiizumi *et al.*, 1989; Brown *et al.*, 1991).

In a companion study, Brook *et al.* (1993) use cosmogenic ^{3}He and ^{10}Be in quartz to constrain the ages of an important sequence of Quaternary moraines in Arena Valley, in the Dry Valleys region of Antarctica. In this paper, several important aspects of the data that are generally relevant to using ^3He_c as a geochronometer are summarized, including a discussion of constraints on ^{3}He production rates, noncosmogenic sources of ^{3}He, and problems of ^{3}He retention in quartz.

PRODUCTION OF COSMOGENIC HELIUM IN SURFACE ROCKS

Production Rates and Altitude–Latitude Dependence

^3He_c is produced primarily by spallation of major elements in rocks by cosmic ray neutrons (Lal and Peters, 1967; Kurz, 1986b). Within the top meter of the earth's surface other production mechanisms, e.g., muon-induced reactions and thermal neutron reactions with ^{6}Li, are in most cases insignificant relative to spallation (Kurz, 1986b; Lal, 1987). ^{3}He production by spallation is considered independent of rock composition (within ~20%) based on theoretical evidence (Lal, 1987, 1991) and measurements of ^3He_c in meteorites (Bogard and Cressy, 1973; Eugster, 1988).

Accurate production rates are of primary importance for geochronology based on cosmogenic nuclides. Calibration of ^{3}He production rates has concentrated so far on ^3He_c in olivine and clinopyroxene from dated basalt flows in Hawaii (Kurz, 1986b; Kurz *et al.*, 1990) and Utah (Cerling, 1990). Because the cosmic ray flux at the earth's surface is a function of altitude, latitude, and the solar cycle (e.g., Lal and Peters, 1967; Merker *et al.*, 1973), calibrated production rates at other locations must be scaled for these effects. The altitude dependence is normally considered an approximately exponential function

0033-5894/93 $5.00

of atmospheric pressure (e.g., Mabuchi *et al.*, 1971) that can be described by Eq. 1,

$$P = P_0 e^{(1033 - d)/L}. \quad (1)$$

where P_0 is sea-level production rate, P is production rate at altitude, d is depth in the atmosphere in g cm^{-2}, and L is an apparent vertical attenuation length (1033 g cm^{-2} is atmospheric depth, or pressure, at sea level).

Production rates vary with latitude due to the effect of the earth's magnetic field on incoming cosmic rays. At the top of the atmosphere, the flux of lower energy particles is higher at the poles than near the equator, while the flux of higher-energy particles (>~10 GeV) is independent of latitude (Lal and Peters, 1967). As a result, production rates in surface rocks at any single altitude are always higher at the poles than at lower latitudes, but the pole–equator difference decreases during periods of high solar activity because the magnitude of the lower energy flux is decreased by interaction with solar magnetic fields.

To compare calibrated production rates, it is convenient to scale them to a reference location (normally sea level at high latitudes). Neutron-monitor data and/or cosmic-ray star production data ("stars" are the results of nuclear reactions in photographic emulsions) collected at various altitudes and latitudes, and at different times during the solar cycle, allow construction of curves that can be used to scale production rates. A number of different sets of data have been used in this fashion, including the curves published by Lal (1991) (a summary of the work of Lal and Peters, 1967), Lingenfelter (1963), and the calculations of Yokoyama *et al.* (1977). In addition, data from the latitudinal neutron monitor surveys of Rose *et al.* (1956) and Pomerantz and Agarwal (1962) have been applied directly to scaling ^{3}He production rates (Kurz, 1986b).

Calibrated Production Rates

Three calibrations of the ^{3}He production rate have been attempted. Kurz *et al.* (1990) reported a sea-level production rate in Hawaii (20°N) of 125 ± 30 at g^{-1} yr^{-1}. To make this calculation, production rates determined for several ^{14}C-dated (calibrated ^{14}C ages) lava flows less than 1000 yr old were scaled to sea level using eq. 1, assuming L = 160 g/cm^2. The uncertainty in the resulting production rate is large because of the young ages of the flows; however, only the young flows are used here because they have the best preserved surfaces. Kurz *et al.* (1990) suggested, based on results from older flows, that the production rate may have varied significantly with time due to fluctuations in the earth's magnetic field intensity. At present this conclusion is tentative and the production rate is assumed to be constant with time for the purposes of this paper. Earlier, Kurz (1987) calculated a production rate at sea level in Hawaii of 97 ± 3 at g^{-1} yr^{-1}, but because of possible past soil cover at the site this is a minimum constraint, and because of the old age of the flow (28,180 ^{14}C yr B.P.) the accuracy of the radiocarbon date is open to question. Cerling (1990) reported a production rate from the Tabernacle Hill lava flow in Utah (39°N) at 432 at g^{-1} yr^{-1} at 1445 m, based on radiocarbon dates that indicate an age of 14,400 ^{14}C yr B.P. The Utah production rates have been revised and corrected for differences between U–Th and ^{14}C time scales (Bard *et al.*, 1990), giving 368 ± 8 g^{-1} yr^{-1} (T. Cerling, personal communication, 1992).

The three measured production rates, scaled to sea level and >60° geomagnetic latitude using the four methods described above, are compared in Table 1. Also included are theoretical calculations of the ^{3}He production rate, which in some cases agree fairly well with measured rates. Note that variations of production rates with latitude are usually referred to in terms of geomagnetic coordinates (either geomagnetic latitude or cut-off rigidity). However, because the dipole field is very close to geocentric on time scales greater than ~2000 yr (Tarling, 1983), geographic coordinates can be used to scale production rates.

Production rates scaled according to Yokoyama *et al.* (1977) (method 4 in Table 1) are significantly higher than previous predictions (e.g., Lal and Peters, 1967); this dis-

TABLE 1

Estimates of ^{3}He Production Rates Scaled to Sea Level and >50° Geomagnetic Latitude Using Four Scaling Methods Discussed in Text

	Altitude and latitude scaling method[a]			
	1	2	3	4
Measured production rates				
Kurz (1987)	156 ± 5	126 ± 4	143 ± 6	352 ± 11
Kurz *et al.* (1990)	201 ± 47	191 ± 59	178 ± 41	453 ± 105
Cerling (1990)	155 ± 5	161 ± 6	117 ± 4	225 ± 7
Theoretical production rates				
Lal (1991)			75[b]	
Yokoyama *et al.* (1977)				219[c]
Lal and Peters (1967)			150[d]	

[a] 1, Scaling based on latitude invariant vertical atmospheric attenuation length (160 g cm^{-2}) and neutron data of Pomerantz and Agarwal (1962) and Rose *et al.* (1956) averaged over solar maximum and minimum. 2, Scaling based on neutron production rates from Lingenfelter (1963), averaged over solar maximum and minimum. 3, Scaling based on Lal and Peters (1967) using polynomial fit of Lal (1991) that gives nuclear disintegration rates in the atmosphere. 4, Scaling based on Yokoyama *et al.* (1977).

[b] Based on cosmic ray neutron energy spectra and cross-sections for proton interactions.

[c] Based on ^{3}H production rate calculated using cross-sections for proton interactions and ^{3}H/^{3}He production ratio of Lal and Peters (1967).

[d] Based on atmospheric production rates of Lal and Peters (1967); estimated from published curves.

crepancy was also noted by Cerling (1990). This may be at least partially because the latitude scaling is based on data for high altitude (~10 km: Light *et al.*, 1973; Merker *et al.*, 1973). Given that the pole–equator difference in cosmic ray intensity increases with altitude (Lingenfelter, 1963; Lal and Peters, 1967), these data cannot be used as general scaling factors for production rates at all altitudes. Similarly, because the Rose *et al.* (1956) data were collected at sea level, and the Pomerantz and Agarwal data are from high altitude (3.4 km), they should not be directly applied (method 1 in Table 1) to scaling production rates independent of altitude, although the original intent of using these data (Kurz, 1986b) was to account for changes due to solar cycle variations.

The remaining approaches described in Table 1 are similar in method, although not identical. Using Lingenfelter (1963) gives agreement, within the substantial uncertainties, between the production rates of Kurz *et al.* (1990) and Cerling (1990) (Table 1), and the ^{3}He production rate of 191 ± 59 at g^{-1} yr^{-1} is adopted for exposure age calculations by Brook *et al.* (1993). This value also agrees well with a preliminary experimental determination of the production rate in water, which gives ~190 at g^{-1} yr^{-1} (Kurz *et al.*, in press). It should be emphasized, however, that at present there are significant uncertainties in absolute production rates and scaling factors. Production rates at geomagnetic latitudes >~60° are not affected by changes in magnetic field strength, as suggested for Hawaiian production rates by Kurz *et al.* (1990), although this phenomenon would affect production rates scaled from lower latitudes.

SAMPLE COLLECTION AND ANALYTICAL METHODS

Samples

Most of the samples discussed here are quartz sandstones collected from a well-exposed sequence of moraines in Arena Valley, the "Taylor II–IVb" moraines and drifts in the informal nomenclature of Denton *et al.* (1989). The sandstones are derived from rocks of the Beacon Supergroup, which make up much of the cliffs surrounding the valley (McElroy and Rose, 1987). Stratigraphy and relative weathering characteristics indicate that the moraines increase in age in the order II–III–IVa–IVb (Bockheim, 1982; Marchant, 1990). Sample locations are shown in Figure 1 of Brook *et al.* (1993), where the sampling and chronology of these deposits are described in more detail. Additional samples came from the surface of Taylor Glacier and from a Taylor Glacier moraine on the north wall of Taylor Valley near Rhone Glacier (Fig. 1b of Brook *et al.*, 1993). In general, the samples are quartz sandstones, 90–95% quartz, composed of moderately to well-rounded, moderately sorted quartz grains, with sizes ranging from 100 to 2000 μm. The larger (>1000 μm) grain sizes are relatively rare. Interstitial hematite and quartz cement, feldspar, and minor percentages of clay minerals are also present. An appendix to Brook *et al.* (1993) describes the samples in more detail. Further details of the geology of the region and the petrology of the Beacon Supergroup can be found in McElroy and Rose (1987), Matz *et al.* (1972), and Marchant (1990).

Analytical Methods

Samples from the upper several centimeters of the rock were cut with a rock saw, disaggregated, and sieved. Mineral separates were hand picked from size fractions ranging from 0.5 to 2 mm and cleaned ultrasonically in acetone, methanol, and ethanol. For the samples discussed here, whole quartz grains identified under a binocular microscope were analyzed (with two exceptions: see Table 2). Sample sizes generally ranged from 0.05 to 0.1 g. Samples were analyzed by crushing *in vacuo* and melting the resulting powder in a vacuum furnace or by melting whole grains with no crushing step. (Additional samples analyzed only by melting whole grains are discussed by Brook *et al.*, 1993.) Crushing releases mostly helium from inclusions, whereas heating releases both helium held in inclusions and helium in the mineral matrix. In olivine and clinopyroxene phenocrysts from basalt, this separation has been used to distinguish helium present in the rock prior to exposure from cosmic-ray-produced helium (Kurz, 1986a,b).

The helium released was measured using mass spectrometric techniques described elsewhere (Kurz *et al.*, 1987). Blanks were ~3–6 × 10^{-11} cm^3 STP (8–16 × 10^8 atoms) for ^{4}He and ~3–8 × 10^{-17} cm^3 STP (800–2000 atoms) for ^{3}He and are small (generally <1%) relative to measured concentrations. One sigma analytical errors are reported with the data in this paper, and long-term replicate measurements of quartz and basalt glass standards indicate a 1σ reproducibility of ^{3}He concentrations of <5–7%.

RESULTS AND DISCUSSION

Noncosmogenic Helium

To calculate exposure ages for quartz samples, the amount of ^{3}He present in the rocks due to processes other than cosmogenic production must be constrained. Possible sources include radiogenic production via the thermal neutron reaction $^6Li(n,\alpha)T \rightarrow {}^3He$ (Morrison and Pine, 1955) and a magmatic or mantle component (i.e., ^{3}He trapped in the mineral during formation).

As described above, previous studies of cosmogenic helium employed *in vacuo* crushing to separate magmatic from cosmogenic ^{3}He in olivine and clinopyroxene phenocrysts. Cerling (1990) also applied this technique to

TABLE 2

Helium Data for Arena and Taylor Valley Samples Analyzed by Crushing and Melting

Sample	$^4He_{cr}$ (10^{12} at g^{-1})	1σ	$^3He/^4He_{cr}$ (R/R_a)	1σ	$^3He_{cr}$ (10^6 at g^{-1})	1σ	^4He_m (10^{12} at g^{-1})	1σ	$^3He/^4He_m$ (R/R_a)	1σ	^3He_m (10^6 at g^{-1})	1σ	^3He_c (10^6 at g^{-1})	1σ
Taylor II														
SCW87-4-1	1.84	0.01	9.25	0.12	23.56	0.31	31.04	0.4	0.63	0.07	27.11	2.81	50.17	2.83
BW84-87	2.05	0.01	7.56	0.04	21.41	0.13	108.81	5.79	0.11	0.04	17.02	5.94	36.74	5.97
Base of Taylor Glacier														
BW84-71	4.7	0.01	1.97	0.02	12.83	0.16	46.32	0.16	0.85	0.01	54.36	0.92	66.41	0.98
Taylor III														
KBA89-50	1.18	0.01	9.26	0.10	15.16	0.17	33.86	0.26	0.64	0.02	29.99	0.74	44.62	0.78
BW84-134	1.93	0.01	7.56	0.04	20.23	0.12	43.98	0.92	0.82	0.02	49.85	1.39	69.38	1.42
BW84-33[a]	0.82	0.01	27.21	0.21	31.01	0.27	62.99	1.33	0.57	0.02	49.61	2.26	79.65	2.30
BW84-33[a]	0.19	0.01	24.74	0.27	6.44	0.07	34.66	1.22	1.67	0.03	80.05	3.11	85.96	3.12
Rhone Platform														
AA86-6c#1[b]	41.5	0.36	0.28	0.01	15.97	0.48	53.27	0.16	0.46	0.01	33.84	0.24	48.37	0.75
AA86-6c#2[b]	22.29	0.09	0.27	0.01	8.42	0.13	76.84	1.63	0.47	0.02	49.98	2.0	56.89	2.08
AA86-5	4.83	0.02	3.03	0.03	20.25	0.21	21.66	0.08	2.46	0.02	73.86	0.55	93.71	0.61
Taylor IVa														
KBA89-45-1#1	1.96	0.01	30.39	0.21	82.26	0.73	95.3	1.05	0.69	0.03	91.53	4.08	172.31	4.18
KBA89-45-1#2	1.29	0.01	50.66	0.38	90.38	0.79	44.93	0.54	1.09	0.06	67.6	3.64	157.28	3.73
KBA89-41-2	2.36	0.01	8.78	0.1	28.62	0.34	74.78	0.84	0.51	0.03	52.99	3.06	80.44	3.11
KBA89-40-1	4.1	0.01	1.24	0.03	7.03	0.14	25.26	0.38	0.48	0.05	16.92	1.73	23.50	1.74
Taylor IVb														
SCW87-3-1[c]	2.91	0.01	64.97	0.4	261.89	1.91								
SCW87-3-1[c]	18.05	0.07	9.78	0.1	244.47	2.56	26.42	0.12	13.64	0.12	498.79	6.03	742.58	6.56
AA86-14	0.87	0.01	50.41	0.24	60.54	0.31	23.22	0.09	13.12	0.06	421.43	2.57	481.60	2.59
AA86-15	5.25	0.02	14.41	0.07	104.72	0.71	27.34	0.15	17.74	0.05	671.32	4.2	775.54	4.26
BW84-105	2.35	0.05	55.72	0.1	180.96	3.63	38.07	0.02	7.71	0.07	406.04	3.62	586.38	5.13
Torr above IVb limit														
AA86-16	0.46	0.01	147.69	0.85	93.73	0.62	44.6	0.95	9.88	0.08	609.62	13.92	702.66	13.94

Note. He_{cr}, He_m, and ^3He_c designate helium released by crushing (cr), melting the residual powder (m), and cosmogenic ^3He(c). All samples are quartz sandstones unless noted. $^3He/^4He$ ratios are reported relative to the atmospheric ratio ($R_a = 1.38 \times 10^{-6}$). Grain size is 0.5–1 mm unless noted. Sample locations are given in Brook *et al.* (1993). $^3He_c = {}^3He_{total} - {}^3He_r$, where ^3He_r is radiogenic helium, calculated assuming a radiogenic $^3He/^4He$ production ratio of 0.011 ± 0.004 from Trull *et al.* (1991), and using the total concentration of ^4He in the sample.

[a] Aggregates of 0.1–0.5-mm grains.

[b] Granite boulder.

[c] Aggregates of 0.2–0.5-mm grains.

^3He in some quartz samples. The concentration of trapped (i.e., magmatic) ^3He in olivine and clinopyroxene can be calculated from Eq. 2 (below); ^3He_c is the difference (Eq. 3) between total and trapped ^3He (Kurz, 1986b),

$$^3He_{tr} = (^3He/^4He)_{cr}[^4He]_t \quad (2)$$

$$^3He_c = [^3He]_t - [3He]_{tr}, \quad (3)$$

where c, tr, cr, and t refer respectively to cosmogenic helium, trapped helium, helium released by crushing, and total helium. This calculation relies on the observation that the ^3He released by crushing olivine or clinopyroxene is not contaminated with ^3He_c (Kurz, 1986b; Trull *et al.*, 1991) and represents magmatic helium trapped in the rock.

The Dry Valleys data suggest that this correction is inappropriate for quartz. Extremely high and variable $^3He/^4He$ ratios and helium concentrations are released by crushing quartz *in vacuo* (Table 2 and Fig. 1). Even replicate crushing of the same sample in some cases results in highly variable $^3He/^4He$ ratios (samples KBA89-45 and SCW87-3-1). Some of these variations might be caused by differences in the efficiency of the crushing process that depend on sample size and geometry. The variability in $^3He/^4He$ ratios, however, more likely reflects the mobility of ^3He in the quartz crystal and/or heterogeneity of ^4He concentrations, since similar variability is not observed in olivine (Kurz, 1986a,b; Kurz *et al.*, 1990). This interpretation is supported by the fact that accessory minerals with high U and Th concentrations are known to be heterogeneously distributed in quartz and other minerals (e.g., Caruso and Simmons, 1985). The ratios and the ^3He concentrations roughly correlate with the total concentration of ^3He in the samples (Fig. 1), and the highest $^3He/^4He$ ratios (up to 148 × R_a) are well outside values for normal continental crustal rocks (Mamyrin

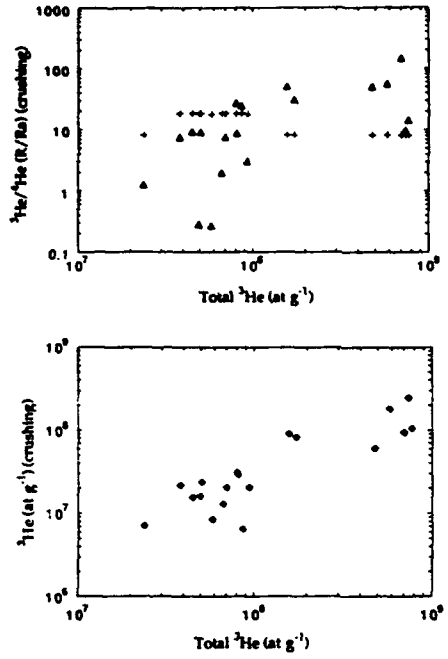

FIG. 1. Total ^{3}He (crushing + melting) plotted against ^{3}He/^{4}He ratio (R/R_a, where R_a is the atmospheric ^{3}He/^{4}He ratio: 1.384×10^{-6}) of helium released by *in vacuo* crushing (top) and concentration of ^{3}He released by *in vacuo* crushing (bottom) of Arena Valley quartz samples. Also plotted in top figure (crosses) are data from *in vacuo* crushing of olivine and clinopyroxene from Hawaiian lava flows (Kurz, 1986b). The data show a rough correlation between total ^{3}He and both the ^{3}He/^{4}He ratio and ^{3}He concentration released by crushing quartz, while the olivine and clinopyroxene data do not show such a relationship, indicating that cosmogenic helium is present in the gas released by crushing quartz and that *in vacuo* crushing therefore cannot be used to correct for trapped ^{3}He in quartz. The shift in the Hawaiian data at high total ^{3}He related to differences in lava geochemistry that are not related to cosmogenic processes. One sigma error bars are smaller than the plot symbols.

and Tolstikhin, 1984). These observations suggest that much of the ^{3}He released by crushing is cosmogenic. Regardless of the origin of the variability in the crushing data, correcting the quartz data for an inherited or noncosmogenic component of ^{3}He using Eqs. 2 and 3 is clearly inappropriate; in many of the older samples this would lead to a correction larger than the total ^{3}He concentration.

Instead, for these samples the assumption is made that radiogenic ^{3}He is the only important noncosmogenic component, since a significant mantle or magmatic component seems unlikely in quartz from continental environments. The magnitude of the radiogenic component can be constrained by using the measured ^{4}He concentration and a ^{3}He/^{4}He production ratio for radiogenic helium in quartz. Trull *et al.* (1991) estimated this ratio to be $0.011 \pm 0.004 \times R_a$, based on the ^{3}He/^{4}He ratio of helium released at the end of a step heating experiment using Taylor IVb sample BW84-105. This is consistent with, although somewhat higher than, calculated ratios for sandstones (Andrews, 1985), and a correction based on this ratio is generally less than 5% of total ^{3}He (Brook *et al.*, 1993). Because the correction is small, the fairly large uncertainty in the radiogenic production ratio contributes little to uncertainties in ^{3}He$_c$. However, there are some difficulties with this type of correction. The ratio measured by Trull *et al.* (1991) presumably represents only helium in the quartz matrix. ^{4}He is probably produced in accessory minerals and at grain boundaries, while radiogenic ^{3}He (via ^{6}Li $(n,\alpha)T$) is probably produced within the mineral matrix (the stopping distance for radiogenic thermal neutrons should be significantly shorter than for α particles). If radiogenic ^{3}He and ^{4}He are lost over the lifetime of the rock at different rates, the correction based on a radiogenic production rate will be incorrect. Because of this problem, we collected a sample from the surface of Taylor Glacier near the mouth of Arena Valley. Boulders on the glacier surface are derived from local cliffs above Arena Valley, are analogous to material input into the valley in the past (Taylor Glacier is cold-based at Arena Valley), and should have low exposure ages since Arena Valley is ~30–40 km from the farthest upglacier outcrops that would be the source for boulders on the glacier surface (Brook *et al.*, 1993). The total concentration of ^{3}He in sample KBA89-91-2 (Table 3) is 3.9×10^6 at g^{-1}, roughly an order of magnitude greater than predicted if all the ^{3}He in the sample were radiogenic, but equivalent to an exposure age of ~9000 yr (Brook *et al.*, 1993). The additional ^{3}He may be a result of a short exposure to cosmic rays, it may be radiogenic if the ^{3}He/^{4}He production ratio varies between samples, or it may represent an additional trapped ^{3}He component. In any case, as mentioned above, the value of the radiogenic correction (typically ~10^5 to 10^6 at g^{-1}) is generally small relative to the total ^{3}He concentrations (which range from ~10^7 to 10^9 at g^{-1}) in the Arena Valley samples (Table 2 and Brook *et al.*, 1993), suggesting that any noncosmogenic component is small in these samples. Radiogenic production of ^{3}He could be a more significant problem in samples with younger exposure ages, depending on ^{4}He concentrations.

Diffusion of Cosmogenic Helium in Quartz

Grain size effects. Diffusion experiments performed by Trull *et al.* (1991) indicated a diffusivity of cosmogenic ^{3}He in quartz of 2×10^{-20} cm^2 sec^{-1} (extrapolating experimental data to 0°C); based on these data they estimated that 0.5-mm grains will lose less than 10% of cosmogenic ^{3}He produced in 1 myr. This low diffusion co-

TABLE 3

Helium Data for Size Fractions of Taylor II Sample SCW87-4-1 and Taylor IVb Sample KBA89-25 and Total Concentrations for Taylor Glacier Sample KBA89-91-2

Size (mm)	^{4}He (10^{12} at g^{-1})		^{3}He/^{4}He (R/R_a)	1σ	^{3}He (10^6 at g^{-1})	1σ
Size fraction data						
SCW87-4-1						
0.4–0.5	40.18	0.31	0.79	0.01	43.88	0.85
0.5–0.71	26.25	0.15	1.45	0.02	52.79	0.89
0.71–0.85	21.93	0.10	2.22	0.03	67.27	0.81
0.85–1.0	40.53	0.46	1.65	0.05	92.72	3.21
1.0–1.3	32.89	0.38	1.83	0.08	83.21	3.90
1.3–1.6	46.37	0.52	1.37	0.05	88.05	3.42
1.6–2.0	50.43	0.56	1.87	0.06	130.66	4.17
KBA89-25						
0.4–0.5	23.92	0.10	7.41	0.05	245.26	8.85
0.5–0.71	55.72	0.66	4.40	0.08	339.49	1.87
0.71–0.85	45.68	0.51	8.62	0.13	544.72	7.29
0.85–1.0	190.79	2.16	2.14	0.04	565.86	10.02
1.0–1.3	71.99	0.81	6.29	0.08	627.09	12.58
1.3–1.6	172.58	1.94	3.10	0.08	740.68	10.77
1.6–2.0	33.37	0.10	16.77	0.15	774.19	19.76
Taylor Glacier surface						
KBA89-91-2						
0.5–1	20.61	0.16	0.14	0.01	3.88	0.26

Note. All samples analyzed by melting whole grains.

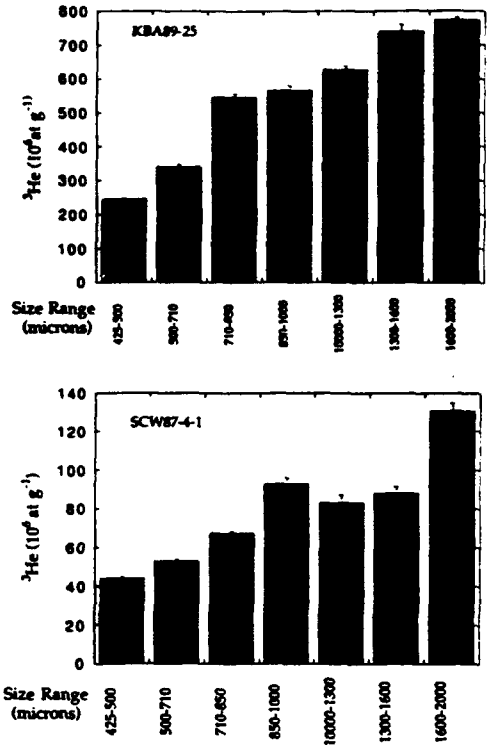

FIG. 2. Total ^{3}He in different size fractions of Taylor II sample SCW87-4-1 (bottom) and Taylor IVb sample KBA89-25 (top). Fractions were obtained by hand picking unbroken, rounded grains within each sieved fraction. Data show a size dependence of the ^{3}He concentration that is not predicted by measurements of ^{3}He diffusion in quartz (Trull *et al.*, 1991). See text for detailed discussion. These data are not corrected for radiogenic ^{3}He, but these corrections would be insignificant (<1%). Error bars are 1σ analytical errors.

efficient suggested excellent retention of ^{3}He in quartz, even over million-year time scales, and would predict that ^{3}He concentrations should not vary significantly with grain size in the Arena Valley samples. Preliminary size fraction experiments (Trull *et al.*, 1991) indicated significant grain-size effects that suggested larger amounts of loss, however. To test further the experimental results, seven size fractions (from 425 to 1000 μm) of sandstone samples SCW87-4-1 and KBA89-25 were analyzed. SCW87-4-1 is a sample from the Taylor II moraine, which is ~100,000 yr old based on correlations with other deposits in Taylor Valley (Denton *et al.*, 1989; Marchant, 1990), and has ^{3}He and ^{10}Be exposure ages ranging from ~100 to ~200,000 yr (Brown *et al.*, 1991; Brook *et al.*, 1993). KBA89-25 is from the Taylor IVb moraine, which is significantly older, with ^{3}He and ^{10}Be exposure ages ranging from 1 to 2 myr. The results (Fig. 2 and Table 3) for the Taylor IVb sample show an increase in concentration with increasing grain size, suggesting size-dependent loss of ^{3}He. The results for the Taylor II sample also show a size-dependent increase of ^{3}He concentration, but with a more complex pattern (Fig. 2).

Size fraction results and mechanisms of ^{3}He loss. The size fraction results can be compared to predictions based on diffusion modeling to give more insight into the problems of ^{3}He loss. Figure 3 shows the ratio of the measured concentration in each size fraction (C) to the concentration in the largest size fraction (Co) plotted against the log of the mean grain radius (a) for five different loss rates, described in terms of the fraction of ^{3}He remaining in the largest grains. These values are compared to predictions based on a simple model of the production and diffusion of ^{3}He (Trull *et al.*, 1991) that describes the fraction of ^{3}He remaining in a grain after any time interval for any given diffusion coefficient, assuming spherical grains. For grains experiencing loss by simple volume diffusion the points should fall along a line of constant Dt (product of diffusion coefficient and time). The calculations for KBA89-25, assuming 40% loss in the largest grains (open squares in Fig. 3), do fall between $Dt = 10^{-11}$ and $10^{-11.5}$, but assuming a true exposure age of approximately 2 myr, these high values of Dt would suggest a diffusion coefficient (D) of ~1.5–5 × 10^{-18} cm^2 sec^{-1}, approximately two orders of magnitude higher than the measured value of 2 × 10^{-20} cm^2 sec^{-1}.

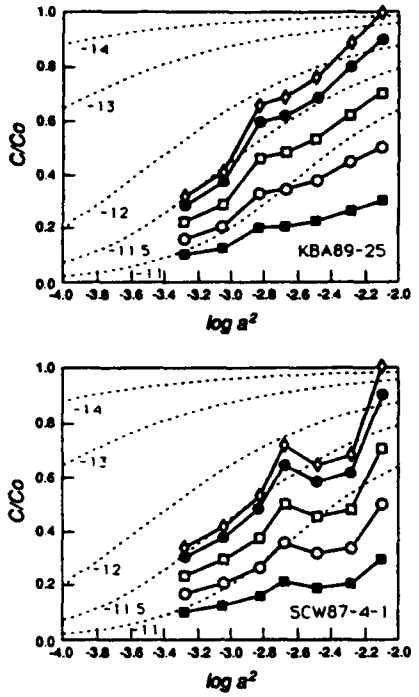

FIG. 3. Line segments show ratio of C (^{3}He concentration in each size fraction) to Co (^{3}He concentration in largest size fraction) calculated from the data in Figure 2 for different rates of ^{3}He loss, all plotted against the log of the mean grain radius (a). The symbols designated different assumed values of the fraction of ^{3}He remaining in the largest grains (open diamonds, 1.0; closed circles, 0.9; open squares, 0.7; open circles, 0.5; closed squares, 0.3); the data for the other grain sizes are normalized to that value. Labeled dashed lines show the relationship between C/Co and log (a^2) predicted by a simple model (Trull *et al.*, 1991) of the production and diffusion of ^{3}He in homogeneous spherical grains undergoing volume diffusion at constant values of log (D_t) (where D_t = diffusion coefficient × time in units of cm^2 sec^{-1} yr^{-1}). For KBA89-25 the data roughly fit model values of $D_t = 1 \times 10^{-11}$ to 3×10^{-12} but if the sample has been exposed for 2 myr, as suggested by ^{10}Be data for similar samples (Brook *et al.*, 1992), the data suggest a diffusion coefficient of ~ 1.5–5×10^{-16} cm^2 sec^{-1} for ^{3}He in quartz, approximately two orders of magnitude higher than measured values (Trull *et al.*, 1991). For SCW87-4-1 the data do not fall on a constant D_t path, suggesting an even more complicated behavior of cosmogenic ^{3}He in this sample.

Sample SCW87-4-1 reveals an even more complicated picture of ^{3}He loss. The results are not consistent with any single value of Dt, and although a plateau in the size vs concentration data exists (Figs. 2 and 3), the concentration in the largest size fraction is considerably higher than in the three fractions that make up the plateau. Even if the three size fractions making up the plateau had experienced no ^{3}He loss, the data for the smaller fractions would not be consistent with a single value of Dt.

^{10}Be results for sample SCW87-4-1 (Brown *et al.*, 1991) provide further information about ^{3}He loss from this sample. The ^{10}Be concentration measured in 0.5- to 1-mm grains of this sample is $4.9 \pm 0.4 \times 10^6$ at g^{-1}, and (assuming ^{10}Be concentrations are not size-dependent) this gives a ^{3}He/^{10}Be ratio of 26.7 ± 2.3 for the largest size fraction analyzed for ^{3}He (1600–2000 μm). This ratio is within uncertainty of the ^{3}He/^{10}Be production ratio in quartz of $\sim 24 \pm 7$ that can be calculated from the data of Nishiizumi *et al.* (1990). This is important for two reasons. First, it suggests complete retention of ^{3}He in the largest size fraction. Second, it suggests concordant ^{10}Be and ^{3}He ages of ~370,000 yr (Brook *et al.*, 1993), significantly older than the expected age of ~100,000 yr based on ^{10}Be and ^{3}He measurements for other samples on the same moraine (Brook *et al.*, 1993) and correlations with U–Th-dated lake deposits (Denton *et al.*, 1989), indicating that this may be an older boulder incorporated into a younger deposit.

Although the reasons for the discrepancy between the step-heating diffusion experiments and the size fraction data are not clear, there are several possibilities. A significant extrapolation of the experimental data is required to estimate the diffusivity at 0°C (Trull *et al.*, 1991). A change in slope in the D vs T relationship at low temperature might explain the apparently anomalous ^{3}He loss suggested by the size fraction data. In addition, for at least part of the year, rock surfaces can experience temperatures of up to ~15°C on sunny days (McKay and Friedman, 1985). ^{3}He diffusion is temperature-dependent, and surface heating may contribute to the observed loss. These factors cannot explain why the data do not follow a constant Dt path, however. It may be that the bulk grain size does not entirely control the diffusion path length of cosmogenic ^{3}He. Diffusion domain size may be governed by factors like silica cementation, cracking, internal grain boundaries inherited from previous histories of the grains (e.g., ghosts of grain boundaries in grains that were originally part of older quartzites), or by more subtle mineralogical or textural features. Many such features are visible in thin section in these samples, including strained quartz grains, several generations of silica cementation, internal fracturing, grains with domains of varying optical extinction angles in crossed polarized light, and deformed or "metamorphic quartz."

The general trend of increasing ^{3}He concentration with increasing grain size is still not easily explained, however, unless the domain-size distribution is somehow dependent on the size of the grains. Postdepositional alteration (e.g., recrystallization or internal fracturing of grains) might affect smaller grains more than larger grains, and in this respect the growth of quartz rinds on Antarctic quartzites (Friedman and Weed, 1987) may be important. Crystal damage caused by the spallation process might also enhance ^{3}He diffusion (Trull *et al.*, 1991).

Ejection of ^3He during spallation reactions is also a possible mechanism that would give rise to a size-dependent concentration trend but, given a probable path length of 50 μm or less for the spallation products (Trull *et al.*, 1991), this mechanism also will not explain the observed loss, predicting maximum concentration differences of approximately 10% within the 400- to 2000-μm size fraction (Trull *et al.*, 1991, and Gilletti and Kulp, 1955, discuss the ejection process in more detail).

Implications for geochronology. Several recent studies have suggested significant, and in some cases nearly complete, loss of ^3He_c from quartz (Cerling, 1990; Graf *et al.*, 1991). Although the grain-size dependence of ^3He concentrations discussed above suggests that loss does occur, the data reported here and in Brook *et al.* (1993) suggest that very large amounts of loss on short time scales (i.e., <10,000 yr) do not occur in the Arena and Taylor Valley samples. In particular, paired ^3He and ^{10}Be data (Brown *et al.*, 1991; Brook *et al.*, 1993) suggest that ^3He loss is ~30–50% for samples with exposure ages of ~2 myr. Whether loss from similar quartz samples is less significant for lower exposure ages (i.e., <100,000 yr), an age range in which analysis of ^{10}Be and ^{26}Al (but not ^3He) become limited by sample mass and other analytical considerations, still remains a somewhat open question. In light of the additional data presented here and in Brook *et al.* (1993), it is worth examining the evidence for loss cited by Graf *et al.* (1991) and Cerling (1990). For example, Cerling (1990) suggested large degrees of ^3He loss in samples with young (<20,000 yr) exposure ages, based on inconsistencies between ^3He results and independent chronological information for three samples. One of the samples was a microcrystalline quartz infilling in an Antarctic basalt ventifact (sample 8137); the significant grain size dependence of ^3He concentrations observed here is the likely explanation for the poor retention. A second sample was a quartz mineral separate from a rhyolite (sample 8078) believed to be 17,780 yr old. The helium data for this sample were corrected for an inherited component using crushing data, but if all the ^3He is assumed to be cosmogenic (total concentration is 7.8×10^6 at g^{-1}) an exposure age of 22,480 yr is obtained, and the difference between this age and the given age of the flow could represent a radiogenic ^3He component. The third sample with lower-than-expected ^3He concentration (sample 8078) was from a moraine boulder in a deposit with rock varnish ^{14}C ages of approximately 13,000 yr B.P. (Dorn *et al.*, 1987) and had a ^3He concentration lower than detection limits. Diffusion may be the explanation for this discrepancy, although it is also possible that the sample may have also recently lost a significant portion of its surface due to episodic erosion processes, perhaps due to range fires (e.g., Emery, 1944; Bierman and Gillespie, 1991).

Graf *et al.* (1991) reported a $(^3He/^{21}Ne)_c$ ratio of <0.1 for one sample of an Antarctic quartzite. They suggested less than 10% retention of ^3He_c based on reported $(^3He/^{21}Ne)_c$ ratios of >1 in feldspars in meteorites. An anomalously high $^{21}Ne_c/^{26}Al$ ratio (~1.4) in this sample was interpreted as evidence for a long period of deep burial (cosmogenic ^{26}Al will decay with a half-life of 720,000 yr while ^{21}Ne is stable), but $^{21}Ne_c$ is also sensitive to radiogenic production by reactions such as $^{18}O(\alpha,n)^{21}Ne$ (e.g., Wetherill, 1954). Corrections for radiogenic production of ^{21}Ne were not made by Graf *et al.* (1991) but could significantly affect the $(^3He/^{21}Ne)_c$ ratio.

In contrast, Staudacher and Allegre (1991) measured ^{21}Ne and ^3He in our sample BW84-105 (Taylor IVb moraine), finding a $(^3He/^{21}Ne)_c$ ratio of 2.76. Exposure ages calculated by Staudacher and Allegre with the ^3He and ^{21}Ne data suggest ~30–40% ^3He loss from this sample, more consistent with both the size fraction experiments described above and ^{10}Be results for this moraine (Brown *et al.*, 1991; Brook *et al.*, 1993).

The data reported here document the effect of grain size on cosmogenic ^3He concentrations and the lack of concordance with measured diffusivities. They indicate that adequate documentation of grain size and grain characteristics are crucial for understanding the distribution of cosmogenic ^3He in minerals. Although on million-year time scales helium is not quantitatively retained in quartz, it is not clear that this problem is significant on shorter (i.e., <100,000 yr) time scales. The available information, particularly the concordant paired ^{10}Be and ^3He results from the Taylor II moraine (Brook *et al.*, 1993), suggests that selection of large grain sizes in younger samples can minimize loss problems, at least in Antarctic samples. At higher ambient temperatures in other regions loss from quartz may be a more significant problem.

CONCLUSIONS

Extensive investigation of cosmogenic ^3He in quartz reveals several issues important for exposure age determination. Evidence for ^3He loss in older samples is found in detailed analysis of different quartz size fractions. Unusually high and variable $^3He/^4He$ ratios released by crushing quartz grains indicate that this component contains cosmogenic ^3He and a combination of crushing and melting analyses cannot discriminate cosmogenic from trapped or radiogenic helium in quartz. In the Antarctic samples discussed here, however, it appears that almost all (>~95%) of the total ^3He is cosmogenic.

The ^3He diffusion problem in quartz is important and requires further investigation. Because ^3He detection limits are low, it is important to establish the significance of ^3He loss due to diffusion in young samples (<100,000 years) in which sample mass and detection limits can

become limiting factors in AMS measurements of other cosmogenic nuclides. Available evidence suggests that in young samples the ^{3}He loss problems may be tractable, when appropriate samples and grain sizes are analyzed. In climates warmer than that of Antarctica, ^{3}He loss due to diffusion may be a more significant difficulty. In such environments, minerals with lower ^{3}He diffusion coefficients, such as olivine, may be preferable to quartz for surface exposure studies.

ACKNOWLEDGMENTS

We thank Tom Trull and Debra Colodner for making some of the early measurements reported here. We also thank Erik Brown, Grant Raisbeck, Tom Trull, John Stone, Thure Cerling, and Sally Hacker for useful comments and discussion, Marcia Davis for useful editorial comments, and Thure Cerling for unpublished production rates. Constructive reviews by Paul Bierman and Alan Gillespie added a number of improvements to the manuscript. Dave Kammer and Armine Gulesserian provided able laboratory assistance. E.J.B. acknowledges the support of a Department of Defense NDSEG Fellowship and the WHOI Education Office. This work was supported by NSF DPP 88-17406 and EAR 91-06820 (to M. Kurz). This is Woods Hole Oceanographic Institution Contribution 7897.

REFERENCES

Andrews, J. N. (1985). The isotopic composition of radiogenic helium and its use to study groundwater movement in confined aquifers. *Chemical Geology* 49, 339–351.

Bard, E., Hamelin, B., Fairbanks, R. G., and Zindler, A. (1990). Calibration of the 14-C timescale over the past 30,000 years using mass-spectrometric U-Th ages from Barbados corals. *Nature* 345, 405–410.

Bierman, P., and Gillespie, A. (1991). Range fires: A significant factor in exposure-age determination and geomorphic surface evaluation. *Geology* 19, 641–644.

Bockheim, J. G. (1982). Properties of a chronosequence of ultraxerous soils in the Trans-Antarctic Mountains. *Geoderma* 28, 239–255.

Bogard, D. D., and Cressy, P. J. (1973). Spallation production of 3-He, 21-Ne, 38-Ar from target elements in the Bruderheim chondrite. *Geochimica et Cosmochimica Acta* 37, 527–546.

Brook, E. J., Kurz, M. D., Denton, G. H., and Ackert, R. P. Jr. (1993). Chronology of Taylor Glacier advances in Arena Valley, Antarctica, using in situ cosmogenic ^{3}He and ^{10}Be. *Quaternary Research* 39, 11–23.

Brown, E., Edmond, J. M., Raisbeck, G. M., Yiou, F., Kurz, M., and Brook, E. J. (1991). Examination of surface exposure ages of Antarctic moraines using in situ produced 10-Be and 26-Al. *Geochimica et Cosmochimica Acta* 55(8), 2269–2284.

Caruso, L., and Simmons, G. (1985). Uranium and microcracks in a 1,000-meter core, Redstone, New Hampshire. *Contributions to Mineralogy and Petrology* 90, 1–17.

Cerling, T. E. (1990). Dating geomorphological surfaces using cosmogenic ^{3}He. *Quaternary Research* 33, 148–156.

Craig, H., and Poreda, R. J. (1986). Cosmogenic ^{3}He in terrestrial rocks: The summit lavas of Maui. *Proceedings of the National Academy of Science* 83, 1970–1974.

Denton, G. H., Bockheim, J. G., Wilson, S. C., and Stuiver, M. (1989). Late Wisconsin and early Holocene glacial history, inner Ross Embayment, Antarctica. *Quaternary Research* 31, 151–182.

Dorn, R., Turrin, B. D., Jull, A. J. T., Linick, T. W., and Donahue, D. J. (1987). Radiocarbon and cation ratio ages from rock varnish on Tioga and Tahoe moraine boulders of Pine Creek, Eastern Sierra Nevada, California, and the paleoclimatic implications. *Quaternary Research* 28, 38–49.

Emery, K. O. (1944). Brush fires and exfoliation. *American Journal of Science* 242, 506–508.

Eugster, O. (1988). Cosmic-ray production rates for ^{3}He, ^{21}Ne, ^{38}Ar, ^{83}Kr, and ^{126}Xe in chondrites based on ^{81}Kr–Kr exposure ages. *Geochimica et Cosmochimica Acta* 52(6), 1649–1662.

Friedman, I. E., and Weed, R. (1987). Microbial trace fossil formation, biogenous, and abiotic weathering in the Antarctic cold desert. *Science* 236, 703–705.

Giletti, B. J., and Kulp, J. L. (1955). Radon leakage from radioactive minerals. *American Mineralogist* 40, 481–496.

Graf, T., Kohl, C. P., Marti, K., and Nishiizumi, K. (1991). Cosmic-ray produced neon in Antarctic rocks. *Geophysical Research Letters* 18(2), 203–206.

Kurz, M. D. (1986a). Cosmogenic helium in a terrestrial igneous rock. *Nature* 320(6061), 435–439.

Kurz, M. D. (1986b). *In situ* production of terrestrial cosmogenic helium and some applications to geochronology. *Geochimica et Cosmochimica Acta* 50, 2855–2862.

Kurz, M. D. (1987). Erratum: Correction to Kurz (1986b). *Geochimica et Cosmochimica Acta* 51, 1019.

Kurz, M. D., Colodner, D., Trull, T. W., Moore, R. B., and O'Brien, K. (1990). Cosmic ray exposure dating with in situ produced cosmogenic ^{3}He: Results from young lava flows. *Earth and Planetary Science Letters* 97, 177–189.

Kurz, M. D., Gurney, J. J., Jenkins, W. J., and Lott, D. E. (1987). Helium isotope variability within single diamonds from the Orapa kimberlite pipe. *Earth and Planetary Science Letters* 6, 57–68.

Kurz, M. D., Brook, E. J., and Ackert, R. P. Surface exposure dating of Antarctic glacial deposits. *Antarctic Journal of the United States*, in press.

Lal, D. (1987). Production of ^{3}He in terrestrial rocks. *Chemical Geology (Isotope Geoscience Section)* 66, 89–98.

Lal, D. (1991). Cosmic ray labeling of erosion surfaces: *In situ* nuclide production rates and erosion models. *Earth and Planetary Science Letters* 104, 424–439.

Lal, D., and Peters, B. (1967). Cosmic ray produced radioactivity on the earth. *In* "Handbuch der Physic," pp. 551–612. Springer-Verlag, New York.

Light, E. S., Merker, M., Verschell, H. J., Mendell, R. B., and Korff, S. A. (1973). Time dependent worldwide distribution of atmospheric neutrons and of their products. *Journal of Geophysical Research* 78(16), 2741–2762.

Lingenfelter, R. E. (1963). Production of carbon-14 by cosmic ray neutrons. *Reviews of Geophysics* 1(1), 35–55.

Mabuchi, H. Y., Gensho, Y., Wada, Y., and Hamaguchi, H. (1971). Phosphorous-32 induced by cosmic rays in laboratory chemicals. *Geochemical Journal* 4, 105–110.

Mamyrin, B. A., and Tolstikhin, I. N. (1984). "Helium Isotopes in Nature." Elsevier, New York.

Marchant, D. (1990). "Surficial Geology and Stratigraphy in Arena Valley, Antarctica: Implications for Antarctic Tertiary Glacial History." Unpublished MS dissertation, University of Maine at Orono.

Matz, D. M., Pinet, P. R., and Hayes, M. O. (1972). Stratigraphy and petrology of the Beacon Supergroup, Southern Victoria Land. *In* "Antarctica Geology and Geophysics" (R. J. Adie, Ed.), pp. 353–358. Universitetsforlaget, Oslo.

McElroy and Rose (1987). "Geology of the Beacon Heights Area: Southern Victoria Land, Antarctica." New Zealand Geological Survey Miscellaneous Series Map 15. DSIR, Wellington, New Zealand.

McKay, C. P., and Friedman, E. I. (1985). The cryptoendolithic microbial environment in the Antarctic cold desert: Temperature variations in nature. *Polar Biology* 4, 19–25.

Merker, M., Light, E. S., Verschell, H. J., Mendell, R. B., and Korff, S. A. (1973). Time dependent worldwide distribution of atmospheric neutrons and their products. 1. Fast neutron observations. *Journal of Geophysical Research* 78(16), 2727–2740.

Morrison, P., and Pine, J. (1955). Radiogenic origin of the helium isotopes in rocks. *Annals of the New York Academy of Sciences* 62, 71–92.

Nishiizumi, K., Klein, J., Middleton, R., and Craig, H. (1990). Cosmogenic 10-Be, 26-Al, and 3-He in olivine from Maui lavas. *Earth and Planetary Science Letters* 98, 263–266.

Nishiizumi, K., Winterer, E. L., Kohl, C. P., Klein, J., Middleton, R., Lal, D., and Arnold, J. R. (1989). Cosmic ray production rates of ^{10}Be and ^{26}Al in quartz from glacially polished rocks. *Journal of Geophysical Research* 94(B12), 17907–17915.

Pomerantz, M. A., and Agarwal, S. P. (1962). Spatial distribution of cosmic ray intensity and geomagnetic theory. *Philosophical Magazine* 7, 1503–1511.

Rose, D. C., Fenton, K. B., Katzman, J., and Simpson, J. A. (1956). Latitude effect of the cosmic ray nucleon and meson components at sea level from the arctic to the antarctic. *Canadian Journal of Physics* 34, 968–984.

Staudacher, T., and Allegre, C. J. (1991). Cosmogenic neon in ultramafic nodules from Asia and in quartzite from Antarctica. *Earth and Planetary Science Letters* 106, 87–102.

Tarling, D. H. (1983). "Paleomagnetism: Principles and applications in geology, geophysics, and archaeology." Chapman and Hall, New York.

Trull, T. W., Kurz, M. D., and Jenkins, W. J. (1991). Diffusion of cosmogenic 3-He in olivine and quartz: Implications for surface exposure dating. *Earth and Planetary Science Letters* 103, 241–256.

Wetherill, G. W. (1954). Variations in the isotopic abundances of neon and argon extracted from radioactive minerals. *Physical Review* 96(1), 679–683.

Yokoyama, Y., Reyss, J., and Guichard, F. (1977). Production of radionuclides by cosmic rays at mountain altitudes. *Earth and Planetary Science Letters* 36, 44–56.

Chapter 4

Chronology of Taylor Glacier Advances in Arena Valley, Antarctica using *in situ* cosmogenic ^{3}He and ^{10}Be

* published in *Quaternary Research* v. 39, p. 11-23. Reprinted with permission from University of Washington Press.

Chronology of Taylor Glacier Advances in Arena Valley, Antarctica, Using *in Situ* Cosmogenic ^{3}He and ^{10}Be

EDWARD J. BROOK, MARK D. KURZ, AND ROBERT P. ACKERT, JR.
Department of Marine Chemistry and Geochemistry, Woods Hole Oceanographic Institution, Woods Hole, Massachusetts 02543

GEORGE H. DENTON
Department of Geological Sciences and Institute for Quaternary Studies, University of Maine, Orono, Maine 04469

AND

ERIK T. BROWN, GRANT M. RAISBECK, AND FRANCOISE YIOU
Centre de Spectrométrie Nucléare et de Spectrométrie de Masse, In$_2$P$_3$-CNRS, Bâtiment 108, 91405 Campus Orsay, France

Received December 4, 1990

In situ produced cosmogenic nuclides provide a new technique for constraining exposure ages of glacial deposits. *In situ* ^{3}He and ^{10}Be in quartz sandstone boulders from Arena Valley, southern Victoria Land, Antarctica, provide chronological constraints for a sequence of moraines ("Taylor II–IVb" moraines) related to expansions of Taylor Glacier and the East Antarctic Ice Sheet. Mean ^{3}He ages are 113,000 ± 45,000 yr, 208,000 ± 67,000 yr, 335,000 ± 187,000 yr, and 1.2 ± 0.2 myr, for Taylor II,III,IVa, and IVb moraines, respectively (mean ± 1σ). Corresponding mean ^{10}Be ages for Taylor II and IVb moraines are 117,000 ± 51,000 yr and 2.1 ± 0.1 myr. For the older deposits the ^{3}He ages are probably lower limits due to diffusive loss. Although the exposure ages appear consistent with the few previous age estimates, particularly with an isotope stage 5 age for Taylor II, each moraine exhibits a broad age distribution. The distribution probably results from a variety of factors, which may include prior exposure to cosmic rays, ^{3}He loss, erosion, postdepositional boulder movement, and radiogenic production of ^{3}He. Nonetheless, the exposure ages provide direct chronological constraints for the moraine sequence, and suggest a maximum thickening of Taylor Glacier relative to the present ice surface of ~500 m since the late Pliocene–early Pleistocene.

INTRODUCTION

The excellent preservation of surficial glacial deposits in Antarctica, in some cases for up to several million years, provides a unique long-term glacial record, but one that has until now lacked absolute chronological control. Due to recent advances in analytical techniques, cosmogenic nuclides produced *in situ* in rocks can now provide useful information about exposure ages and histories of geological surfaces, particularly in glaciated regions (e.g., Cerling, 1990; Phillips *et al.*, 1990; Nishiizumi *et al.*, 1991). Application of *in situ* cosmogenic nuclides to Antarctic glacial geology is ideal because soil development and weathering rates are extremely low in Antarctica. This paper describes the use of *in situ* cosmogenic ^{3}He and ^{10}Be to constrain the ages of Quaternary moraines and older deposits formed by Taylor Glacier in Arena Valley, in the Dry Valleys region of Antarctica (Figs. 1 and 2). This well-exposed moraine sequence has been linked with interglacial expansions of the East Antarctic Ice Sheet (Denton *et al.*, 1989) and the chronology of these deposits may have important ties to the global climate record. Brown *et al.* (1991) previously reported *in situ* ^{10}Be data for a subset of the Arena and Taylor Valley samples; new ^{10}Be data are reported here for a number of additional samples. A companion paper (Brook and Kurz, 1993) discusses the systematics of cosmogenic ^{3}He in these samples, and some aspects of the methodology, in more detail.

QUATERNARY MORAINES IN ARENA VALLEY

Arena Valley, a hanging valley on the southern side of upper Taylor Glacier (Figs. 1 and 2), contains an extensive, well-preserved sequence of moraines composed of boulders of Jurassic Ferrar Dolerite, Beacon Supergroup sandstones, and a small percentage of granitic rocks (Bockheim, 1982; McElroy and Rose, 1987). The moraines were formed as lateral moraines of Taylor Glacier when Taylor Glacier ice expanded into the valley (Figs. 1 and 2). Because Taylor Glacier drains the McMurdo Dome, a peripheral ice dome of the East Antarctic Ice Sheet, the moraine sequence records changes in the size of Taylor Glacier and this part of the polar plateau (Denton *et al.*, 1989; Marchant, 1990). Rock weathering, soil development, and stratigraphic relationships indicate that the relative ages of these deposits increase from Taylor II to Taylor IVb (Bockheim, 1982; Denton *et al.*, 1989; Marchant, 1990). There is little absolute chronological

0033-5894/93 $5.00

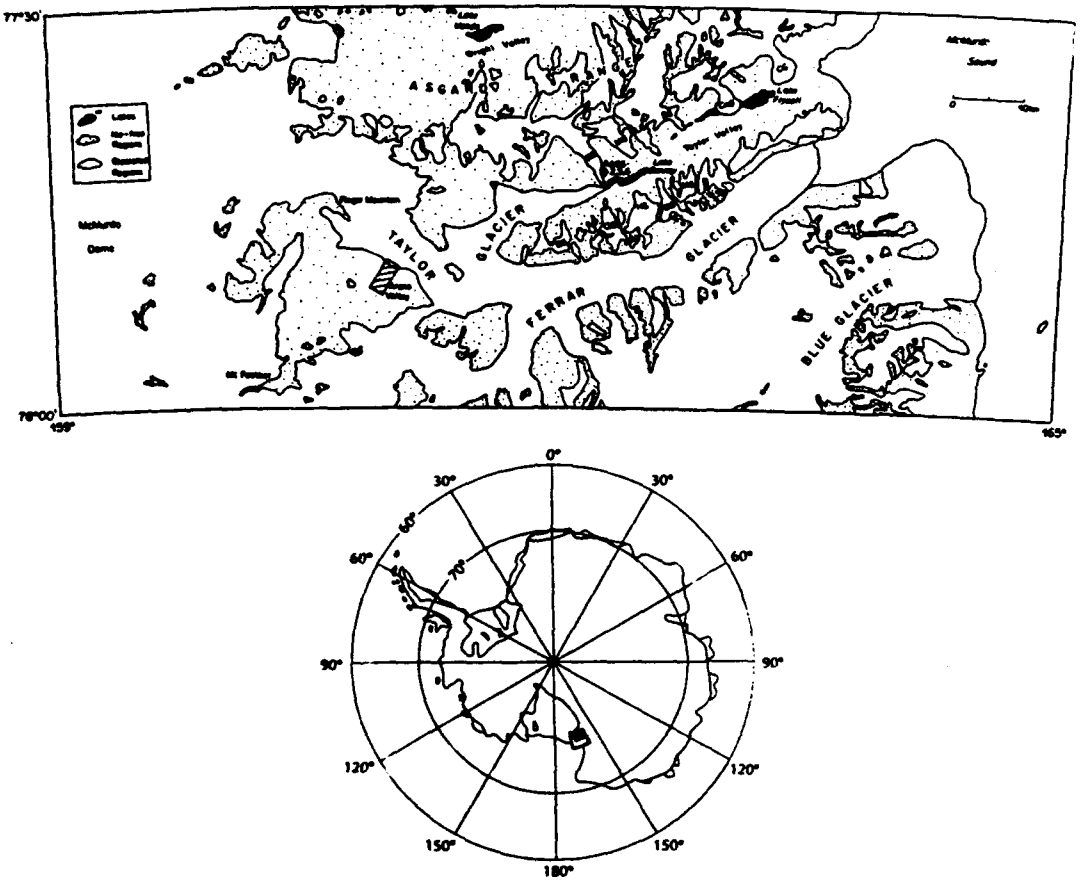

FIG. 1. Taylor Valley and Dry Valley region. Hatched region shows location of Arena Valley (Fig. 2). The McMurdo Dome of the East Antarctic Ice Sheet is at the edge of the polar plateau, and both Taylor and Ferrar glaciers flow directly from McMurdo Dome.

control for these deposits in Arena Valley, but U–Th dating of lake carbonates in lower Taylor Valley (Hendy *et al.*, 1979), suggests that Taylor Glacier and the East Antarctic Ice Sheet advance during global interglacial periods, when moisture supply to interior east Antarctica increases. Denton *et al.* (1989) and Marchant (1990) correlated the Taylor II and Taylor III moraines in Arena Valley with isotope stage 5 and 7 moraines in lower Taylor Valley on the basis of soil development and weathering characteristics. Apart from these correlations and the ^{10}Be and ^{26}Al data of Brown *et al.* (1991) (discussed below), there are no prior age constraints for these deposits.

SAMPLE COLLECTION

Samples were collected in the austral summers of 1984, 1986, 1987, and 1989 (Figs. 1 and 2). In addition to the Arena Valley moraines, samples were collected from a Taylor Glacier moraine on the north wall of Taylor Valley near Rhone Glacier (Fig. 1), and from the surface of Quartermain Drift, a glacial drift older than the oldest Taylor moraines (Marchant, 1990). Samples from boulders on the surface of Taylor Glacier were also collected for examining the production of cosmogenic nuclides during glacial transport.

Samples were collected from the tops of relatively horizontal (slopes normally less than 10°–15°) boulder surfaces, and wherever possible samples were taken from the moraine crest. Altitudes were determined from altimeter measurements calibrated with surveyed benchmarks. Measurement of surrounding topography using a hand-held clinometer indicated no significant shielding effects (e.g., Nishiizumi *et al.*, 1989; Zreda *et al.*, 1991) and no corrections to the data for boulder geometry

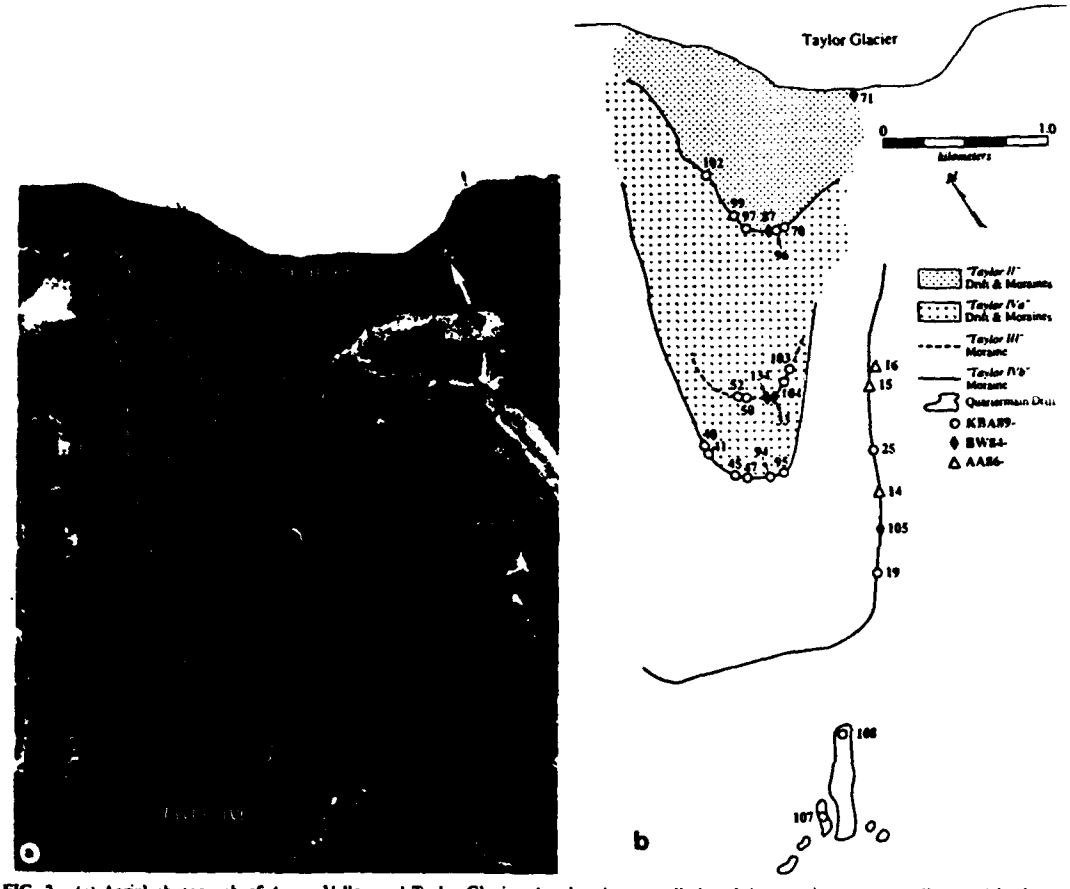

FIG. 2. (a) Aerial photograph of Arena Valley and Taylor Glacier showing the outer limits of the moraine sequence discussed in the text. Moraine ridges are composed of sandstone, granite, and dolerite boulders ranging in size from ~0.5 to 30 m^3. Note that the Taylor III deposit consists of two single ridges superimposed on the older Taylor IVa drift. Photo is an enlargement of a portion of an aerial photograph (TMA 2485, Frame 149) available from the U.S. Geological Survey. Location of Arena Valley is shown in Figure 1b. Scale is approximately 1:13,500. (b) Locations of samples discussed in the text; sample locations were located using air photographs. Only the outermost moraine loop in each sequence is shown. All sample locations as shown, except for SCW87-1-1.1-2, -3, -4, and -5, and KBA89-91-2. The SCW87 samples were collected from the moraines shown (except for SCW87-1 and -2 which are from the surface of the large patch of Quartermain Drift) but exact locations are not known. KBA89-91-2 was collected from the surface of Taylor Glacier near the mouth of Arena Valley.

were made. Most of the samples are sandstones, although a few are granites containing large (>1 mm) quartz grains. Sample descriptions are compiled in the Appendix. Sample processing and analytical techniques for ^{3}He and ^{10}Be are described in Brook and Kurz (1993) and Brown *et al.* (1991).

EXPOSURE AGES AND AGE DISTRIBUTION

To calculate exposure ages, ^{3}He concentrations were corrected for radiogenic production of ^{3}He (Brook and Kurz, 1993), and ^{3}He and ^{10}Be concentrations were adjusted for the depth of the sampling interval (normally 1 to 5 cm, see Appendix), and scaled to sea level, as described by Brook and Kurz (1993). Using a sea-level ^{3}He production rate of 191 ± 59 at g^{-1} yr^{-1} (Brook and Kurz, 1993) and a sea-level ^{10}Be production rate of 7 ± 1.4 at g^{-1} yr^{-1} (based on the Nishiizumi *et al.* (1989) production rate scaled to high latitude, and assuming a 20% uncertainty) these values were converted to ages using Eq. 1 (for ^{3}He, a stable isotope) and Eq. 2 (for ^{10}Be, half-life = 1.5 myr).

$$t = \frac{n}{P} \quad (1)$$

$$t = \frac{\ln\left(1 - \frac{n\lambda}{P}\right)}{-\lambda}, \quad (2)$$

where t is age, P is production rate, n is concentration, and λ is the decay constant.

Exposure ages based on these equations are model ages, subject to several assumptions. Production rates must be known as a function of altitude, latitude, and time. Samples must be closed systems (no loss or gain, except by *in situ* production). Because the cosmic-ray flux decreases with depth in the rock, erosion and cover by overlying material must be minimal or constrainable. In the case of boulders in glacial deposits, prior exposure to cosmic rays before deposition must also be considered.

The exposure ages for both isotopes (Figs. 3 and 4) show broad distributions within each deposit, which must result from some combination of the above factors. Erosion, soil or ice cover, and diffusion reduce the apparent exposure age. In contrast, anomalous trapped or radiogenic components (i.e., not included in corrections) or previous exposure to cosmic rays would increase the apparent age. Many of these factors can be at least partially constrained with available information and are discussed below.

Erosion, for example, should not have a major effect on ^{3}He exposure ages. Brown *et al.* (1991) calculated a model erosion rate of ~1–2 × 10^{-5} g cm^{-2} yr^{-1} (~0.4–0.8 × 10^{-5} cm yr^{-1}) for a subset of these samples, based on ^{10}Be and ^{26}Al data. The effect of erosion on the apparent ^{3}He age is described by:

$$t' = \frac{L}{E}(1 - e^{-Et/L}), \quad (3)$$

where t' is apparent age, E is erosion rate (g cm^{-2} yr^{-1}), L is attenuation length in rock (~160 g cm^{-2}: Brown *et al.*, 1992; Kurz, 1986), and t is true age. Erosion rates of 1–2 × 10^{-5} cm^{-2} yr^{-1} have minimal effect on ^{3}He exposure ages younger than 2 myr. For example, with an erosion rate of 1 × 10^{-5} g cm^{-2} yr^{-1}, and a true age of 2 myr, the apparent age is 1.9 myr, a 5% underestimate. Individual boulders might erode at more rapid rates, however, and in some cases spall large portions of their surfaces or split into two or more pieces. These processes might explain some of the scatter in Figure 3, particularly for the older moraines where the apparent results of such processes are often observed in the field; however, every effort is made to avoid collecting such samples. Erosion will affect ^{10}Be ages more significantly (the effect can be calculated by replacing λ in Eq. 2 with [λ + E/L]); for the scenario above, the apparent age for ^{10}Be would be ~1.8 myr, and the effect is more significant for older deposits (Brown *et al.*, 1991). Because erosional losses based on the ^{10}Be-based erosion rates are relatively minor and, because of the inherent uncertainty associated with constraining the erosional loss, no erosion corrections are made to the ages.

Significant soil cover in the past also seems unlikely because all of the samples were collected at or near crests of distinct moraines and most of the material carried by Taylor Glacier today, at least on the glacier surface, appears to be in the form of large boulders (personal observation). In addition, there appears to be no general correlation between boulder size and exposure age (see Appendix for sizes) as might be expected if the boulders were gradually uncovered by erosion of surrounding, finer grained material.

Radiogenic production of ^{3}He also does not appear significant. Brook and Kurz (1993) describe corrections to the ^{3}He data for a component produced by nuclear reactions within the rocks. These corrections are applied to the data in Table 1 and in most cases are much less than 5% of total ^{3}He and only greater than 5% for KBA89-94, KBA89-97, and KBA91-2 (14.3, 6.5, and 8.1%, respectively). Therefore, it is not likely that an error in the correction could explain the broad distribution of ages in Figure 3.

Prior exposure to cosmic rays is a more difficult issue to resolve. Most of the debris carried by Taylor Glacier probably originally fell on the surface of the glacier from surrounding cliffs; the glacier, at least now, is cold-based west of Arena Valley (Robinson, 1984) and presumably does not incorporate much bedrock debris into basal layers. A sandstone sample collected from the surface of the glacier near the mouth of Arena Valley had an exposure age of 9000 ± 3000 yr (Table 1, sample KBA89-91). If this low exposure age is typical of debris carried by the glacier, then ^{3}He production during glacial transport is minimal relative to the ages of the moraines in Arena Valley. This seems reasonable because current Taylor Glacier velocities are on the order of 1–15 m yr^{-1} (Robinson, 1984) and cliffs surrounding Finger Mountain (at maximum ~10 km away) probably supply most of the debris deposited in Arena Valley (Fig. 1), which suggests a maximum 10,000-yr travel time. However, possibly some boulders were exposed in cliff outcrops prior to incorporation into the glacial system, and this could be an important cause of outlying points in the age distributions.

Outlying ages would also result if younger glacial advances incorporate boulders from older moraines within Arena Valley. In addition, particularly in the Taylor III moraine, it is possible that older boulders exposed in "windows" through the younger moraines might be sampled inadvertently. This could explain the outlying ages in the Taylor III age distribution, particularly given that the Taylor III boulders are deposited directly on the older Taylor IVa drift and moraines (Fig. 2).

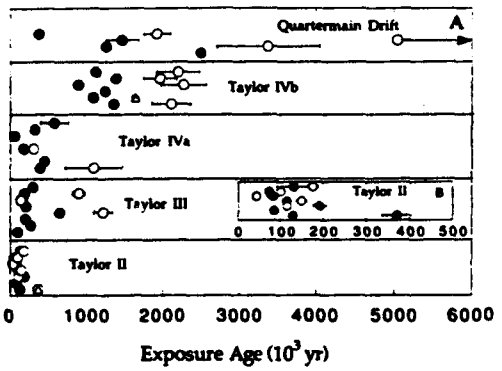

FIG. 3. (A) Distribution of ^{3}He and ^{10}Be exposure ages for Taylor II to Taylor IVb moraines and Quartermain Drift from Table 1. Closed circles show ^{3}He ages, open circles show ^{10}Be ages. The open triangles show two ^{3}He ages based on the ^{3}He data for 1.6- to 2-mm grains for samples SCW87-4-1 (Taylor II) and KBA89-25 (Taylor IVb) from Brook and Kurz (1993). Note the close agreement between ^{3}He age and ^{10}Be age for SCW87-4-1, suggesting no significant loss of ^{3}He in this size fraction. In the Taylor IVb distribution only the data for 1000- to 2000-μm quartz for sample KBA89-19 is plotted (Table 1). One-sigma error bars include analytical uncertainties only, allowing comparison of exposure ages within each moraine. For most of the ^{3}He ages the error bars are smaller than the plot symbols. (B) Inset shows ^{10}Be and ^{3}He ages for Taylor II in expanded scale; the data suggest that ^{3}He loss may not be significant for samples <~100,000 yr.

The most important violation of the assumptions necessary for calculating a ^{3}He exposure age is that ^{3}He does not appear to be completely retained in some of these samples (Brook and Kurz, 1993). For grains of uniform size, in samples with the same deposition age, diffusion might be expected to lower the exposure age of all samples uniformly. Some of the scatter in the ^{3}He ages in Figure 3, however, may be a result of different loss rates for different samples, due to differences in grain-size distribution within the size fraction or other physical properties (e.g., microcracks, silica cementation) that may influence diffusion rates.

In summary, several types of processes may affect the exposure ages of individual moraine boulders in Arena Valley, and probably exposure ages of all glacial deposits. The relative importance of all of these problems will depend on the geological situation and the isotopic system used. It is important to recognize that data from individual boulders must be interpreted with caution and that multiple samples from individual deposits are necessary to obtain adequate chronological information.

CHRONOLOGICAL INTERPRETATION

Exposure Age Distribution

Exposure ages are potentially useful as both absolute and relative ages. Although quoted uncertainties in the ^{3}He and ^{10}Be ages are large (Table 1), this is primarily due to the large uncertainties (~30% for ^{3}He and 20% for ^{10}Be) adopted for the production rates. Both are fairly conservative, although they probably represent reasonable present uncertainties in determining production rates and scaling them for latitude and altitude. If exposure ages are used as relative ages, the production rate uncertainties are not as relevant, however, and analytical uncertainties (long-term reproducibility for samples of this type is generally on the order of 5–7% for ^{3}He and ^{10}Be) are more appropriate for comparing ages of different samples (Figs. 3 and 4).

Use of the exposure ages in either a relative or absolute context, however, requires interpretation of the age distribution within single deposits. If the processes leading to distribution are random, then the mean age would be an appropriate estimate of the true age. However, the processes leading to older-than-expected ages (e.g., previous exposure or a radiogenic signal) may be distinctly different than processes that lead to younger-than-

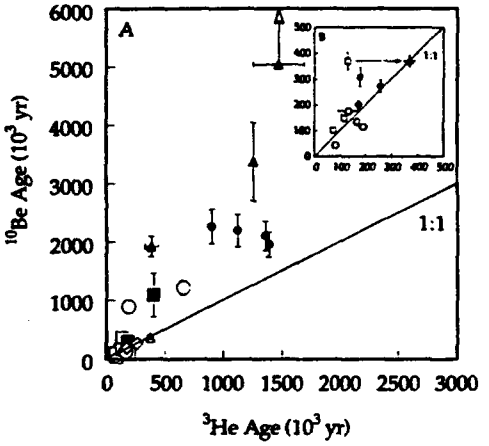

FIG. 4. (A) Scatter plot shows relationship between ^{3}He and ^{10}Be ages for all samples analyzed for both isotopes. Open squares, Taylor II: open circles, Taylor III; closed squares, Taylor IVa; closed circles, Taylor IVb; closed triangles, Quartermain Drift; open diamonds, Rhone Platform and moraine at base of Taylor Glacier; open triangle, age for sample SCW87-4-1 calculated with ^{3}He data from 1.6- to 2-mm grains (Brook and Kurz, 1993). For the oldest sample (KBA89-108), the ^{10}Be age is plotted as a lower limit because ^{10}Be concentrations are near steady state. The general relationship suggests about 40–50% loss of ^{3}He from quartz over ~2 myr; the significant scatter is probably a result of different loss rates for different samples due to differences in grain size or other physical properties. Error bars are propagated analytical error only (1σ) to allow comparison of relative sample ages. (B) Inset shows all samples with ^{10}Be and ^{3}He ages <500,000 yr; arrow shows the relationship between ^{3}He ages for SCW87-4-1 calculated with data from 0.5- to 1-mm grains (open square) and 1.6- to 2-mm grains (open triangle). In general, these data suggest minimal ^{3}He loss in these samples, although there are some unresolved complexities in the data for the youngest samples (see text and Brown *et al.*, 1991).

expected ages (e.g., erosion, past soil cover, diffusion). If the latter dominate, the oldest age in the distribution is closest to the true age; if the former dominate, the youngest age would be closest to the true age. In reality, of course, it is not necessary that either process dominate the distribution, making it more difficult to choose the best age estimate.

Table 2 summarizes the maximum, mean, and median ^{3}He and ^{10}Be exposure ages for the four Taylor moraines, and independent age estimates based on previous work. Because it is likely that processes like diffusion and erosion lower some apparent exposure ages the lowest ages in each distribution are not considered as valid age estimates. Also, two samples that appeared anomalous based on both ^{3}He and ^{10}Be data were omitted from the calculations of Table 2. The oldest sample in the Taylor III moraine (SCW87-5) has a ^{3}He age of 654,000 ± 202,000 yr (and a ^{10}Be age of 1.2−0.3/+0.4 myr) and can be rejected at >90% confidence using a simple Q-test (Shoemaker *et al.*, 1989); as suggested above, it is likely that this boulder is actually an older Taylor IVa or IVb boulder exposed in the Taylor III moraine. Sample SCW87-4-1 was omitted from calculations for Taylor II since both the ^{10}Be data and the ^{3}He data for individual size fractions (Brook and Kurz, 1993) indicate an age of ~370,000 yr, well outside the values for other Taylor II samples (Table 1).

Which of the values compiled in Table 2 is the best approximation of the true age? As mentioned above, one approach is to take the highest value for each moraine as the best estimate of true age, reasoning that erosion is the dominant process affecting the exposure ages (e.g., Phillips *et al.*, 1990). This assumes that prior exposure is not an important process and that outlying points in the age distributions can be successfully recognized. The validity of the mean, median, or maximum age, however, may depend on exposure time. In the older deposits, processes that lower the ^{3}He or ^{10}Be exposure age relative to the true age (i.e., ^{3}He loss, erosion, past soil cover) are probably much more significant than in younger deposits. In addition, the effects of prior exposure should be less evident in the older deposits (Brown *et al.*, 1991). Thus, the maximum age may better estimate the true age for older deposits. In contrast, for younger deposits the mean or median may be a more appropriate measure of the age, and this logic was used by Phillips *et al.* (1990) in interpreting ^{36}Cl ages for younger deposits in the Bloody Canyon moraine sequence in northern California. Given, however, that the assumptions discussed above are difficult to test, the median age is an appropriate approximation of the true age because it is least affected by the form of the age distribution. For the Arena Valley moraine sequence, the mean and median ages are very similar (Table 2), suggesting a normal distribution of ages. In addition, mean and median ages for Taylor II agree well with ages based on correlations with U–Th-dated deposits in lower Taylor Valley (Hendy *et al.*, 1979; Denton *et al.*, 1989; Marchant, 1990) (Table 2).

Constraints from Paired ^{3}He and ^{10}Be Data

As suggested by the above discussion, some of the problems leading to the distribution of ages for a single deposit can be addressed by measuring more than one cosmogenic nuclide in the same sample. For example, if samples have been exposed previously to cosmic rays, and then buried (either in glacier ice or soil), radioactive nuclides like ^{36}Cl, ^{26}Al, and ^{10}Be (half-lives 300,000 yr, 720,000 yr, and 1.5 myr, respectively) will not have significant "memory" of the prior exposure as stable cosmogenic nuclides (^{3}He, ^{21}Ne). In addition, the radionuclides listed above should not have diffusion problems.

Together, the ^{3}He and ^{10}Be data described here provide some constraints on the origin of the age distributions and the validity of ages. ^{10}Be ages are significantly greater than ^{3}He ages, except for the Taylor II samples (Figs. 3 and 4). There are two possible explanations for this. The production rates chosen for the age calculations may be incorrect; the ^{3}He production rate would have to be lower, or the ^{10}Be production rate higher, to bring the ages closer to concordance. Given, however, that the ^{10}Be production rate used agrees well with independent estimates (Brown *et al.*, 1991) and that other estimates of the ^{3}He production rate are only 15–20% lower than the rate used here (Brook and Kurz, 1993), loss of ^{3}He due to diffusion is probably the dominant factor controlling the discordance between ^{3}He and ^{10}Be ages for samples older than Taylor II. In theory, it is also possible that the correction for radiogenic ^{3}He is too large, although in general this would cause the difference between ^{3}He and ^{10}Be ages to be greatest for the youngest samples, which is not the case (Figs. 3 and 4). The fact that the discrepancy between ^{3}He and ^{10}Be ages is not a smooth function (Fig. 4) suggests that some of the scatter in the age distributions is a result of different rates of ^{3}He loss for samples from the same moraine. The general trend (Fig. 4) of ~40–50% loss over 2 myr is consistent, however, with estimates of loss due to diffusion based on grain-size experiments (Brook and Kurz, 1993) and on ^{3}He/^{21}Ne ratios in one Taylor IVb sample (Staudacher and Allegre, 1991).

For Taylor II, the mean and median ^{3}He and ^{10}Be ages agree fairly well (Table 2 and inset in Fig. 4). These data suggest that ^{3}He loss is not significant over ~100,000 yr of exposure to cosmic rays. In detail, however, there are some unresolved complexities in the Taylor II data. Two of the Taylor II samples (BW84-87 and KBA89-70-1) and one Taylor III sample (BW84-134) have ^{3}He ages older than ^{10}Be ages (Table 2 and Fig. 3). Brown *et al.* (1991) also reported excesses of ^{26}Al in the two BW84 samples,

and although the origin of these anomalies remains unclear, they might be indicative of unusual radiogenic production mechanisms (Brown *et al.*, 1991). Measurements of U and Th (Brown *et al.*, 1991) and Li (E. Brook, unpublished data) do not reveal any chemical anomalies that would support this hypothesis, however. Further details of this problem are discussed by Brown *et al.* (1991).

In the Taylor III and IVa data the few ^{10}Be ages are not consistent and generally are significantly higher than ^{3}He ages (Figs. 3 and 4). Because of the small amount of data this is difficult to interpret, but, as mentioned above, the sample with the highest ^{10}Be age from the Taylor III moraine (SCW87-5: 1.2−0.3/+0.4 myr) also has an unusually high ^{3}He age (654,000 ± 202,000 yr), suggesting prior exposure to cosmic rays. Taylor III sample BW84-33 also has a high ^{10}Be age (900,000 +252,000/−226,000 yr, ^{3}He age = 190,000 ± 59,000 yr). In both cases the discrepancy between ^{10}Be and ^{3}He ages is probably due to loss of ^{3}He; in the latter sample the small grain size probably explains the large discrepancy (see Appendix). These two ^{10}Be ages may indicate that the Taylor III moraine is significantly older than ^{3}He data and prior age constraints indicate, if there has been significant ^{3}He loss from all of the Taylor III samples. It is possible though, that in addition to some ^{3}He loss, the outlying points may reflect the difficulties in sampling this deposit, which is a less distinct belt of boulders than the others, and rests directly on the older Taylor IVa moraines and drift.

As suggested above, in the Taylor IVa and Taylor IVb moraines the discordance between ^{10}Be ages and ^{3}He ages (Table 1 and Figs. 3 and 4) probably reflects ^{3}He loss. Brown *et al.* (1991) also pointed out that the very close agreement for all the ^{10}Be ages on the Taylor IVb moraine (Table 1 and Fig. 3) argues against any influence of prior exposure to cosmic rays for these samples due to their long exposure time in their present positions.

Four samples from Quartermain Drift, the oldest glacial deposit in the valley that is believed to have been deposited by Taylor Glacier (Marchant, 1990), were also analyzed for ^{3}He and three of these were analyzed for ^{10}Be (Figs. 3 and 4). ^{3}He ages range from 382,000 ± 131,000 yr to 2.5 ± 0.8 myr; ^{10}Be ages are significantly older (Table 1). Because ^{10}Be is radioactive ($t_{1/2}$ = 1.5 × 10^{6} yr), for the older samples its concentration approaches steady state with respect to production and decay, and error limits for ^{10}Be exposure ages become large and asymmetric. For the oldest Quartermain Drift sample (KBA89-108), the data only provide a lower age limit of ~3 myr, (~5 myr assuming no error in the production rate; Table 1), but possibly the exposure period is significantly longer. As with the IVa and IVb samples, all of these samples show evidence of ^{3}He loss (Table 1, Figs. 3 and 4).

In summary, although the details of the processes leading to the distributions of ages for each deposit cannot be completely unraveled, the ^{10}Be and ^{3}He age distributions for the Arena Valley deposits illustrate that a number of different factors must be considered, including prior exposure to cosmic rays, loss of ^{3}He, and episodic surface erosion processes (spalling of boulder surfaces, for example). Because there is no way to constrain all these processes individually, the mean or median exposure ages are used here as age constraints for the Taylor moraines.

IMPLICATIONS FOR ANTARCTIC GLACIAL HISTORY

Both the mean and median ^{3}He and ^{10}Be ages are consistent with previous suggestions that the Taylor II moraine and drift were deposited during isotope stage 5 (~100,000 yr), and ^{3}He ages suggest that Taylor III was deposited during isotope stage 7 (~200,000 yr) (Table 2). Two of the three ^{10}Be ages for Taylor III samples suggest an even older age (~1 myr; Table 1 and Figs. 3 and 4). Given the discrepancy, and the evidence for ^{3}He loss, more ^{10}Be data will be necessary to make firm conclusions about the age of this deposit.

The mean and median ^{3}He ages for Taylor IVa samples are 335,000 ± 187,000 and 365,000 ± 181,000 yr, which would indicate deposition during isotope stage 11 at the earliest, assuming the deposit is interglacial. The limited ^{10}Be data, however (Fig. 3), suggest that the moraine may be significantly older than this (up to ~1 myr). Taylor IVb has mean and median ^{3}He ages of 1.2 ± 0.2 and 1.2 ± 0.3 myr and mean and median ^{10}Be ages of 2.1 ± 0.1 and 2.2 ± 0.7 myr; given the strong evidence for ^{3}He loss in this age range (Brook and Kurz, 1993), the latter ages are more reliable.

The ^{3}He and ^{10}Be ages for Quartermain Drift confirm that it is the oldest of the deposits studied, in agreement with the relative chronology of Marchant (1990). Based on stratigraphic position, outcrop pattern, and composition, Quartermain Drift was deposited prior to the Taylor IVb moraines by an expanded Taylor Glacier (Marchant, 1990). Quartermain Drift is the oldest deposit in Arena Valley that has been related to Taylor Glacier; the ^{10}Be ages provide evidence that a somewhat expanded Taylor Glacier existed in pre-Pleistocene time, perhaps as early as the middle Pliocene. Because ^{10}Be concentrations are near steady state in the Quartermain Drift samples, quite possibly this deposit is significantly older. It should also be noted that erosion corrections of these old ages would be significant. For example, an apparent ^{10}Be age of 3 myr would become 3.9 myr when corrected for a constant erosion rate of 1×10^{-5} g cm^{-2} yr^{-1} (e.g., Brown *et al.*, 1991).

^{3}He and ^{10}Be measurements for related glacial deposits in Arena and Taylor valleys suggest some tentative correlations with the Arena Valley moraines. Two samples from the moraine on the north wall of Taylor Valley near

TABLE 1
He and Be Data for Arena and Taylor Valley Samples

Sample	Altitude (m)	AD	An[a]	^{4}He	1σ	R/R$_a$[b]	1σ	^{3}He$_{cn}$	^{3}He Age[c] (10^3 yr)	1σ	^{10}Be	1σ	^{10}Be$_n$	^{10}Be Age[c] (10^3 yr)	−1σ	+1σ
Taylor II																
SCW87-4-1[d]	1100	905	1	32.88	0.40	1.11	0.06	24.35	130	41	*4.90*	*0.40*	2.38	370	85	89
			2	29.39	0.33	1.39	0.06	27.21								
			2	18.55	0.13	1.86	0.03	23.01								
			2	8.06	0.04	4.60	0.05	24.86								
KBA89-102	1140	901	2	34.19	0.24	0.75	0.02	16.18	85	26						
KBA89-70-1	1120	903	2	82.86	0.96	0.70	0.05	36.73	192	61	1.68	0.11	0.78	115	25	25
KBA89-96	1150	900	2	37.01	0.41	0.95	0.05	22.03	115	36	2.19	0.16	1.01	149	33	33
BW84-87[d]	1100	905	1	110.85	5.79	0.25	0.04	17.83	82	29	*0.61*	*0.07*	0.30	43	10	10
			2	71.20	3.85	0.29	0.01	13.39								
KBA89-99	1090	907	2	95.03	1.05	0.24	0.02	14.08	74	23	1.47	0.14	0.69	101	23	23
KBA89-97	1090	907	2	241.43	3.62	0.17	0.05	25.23	132	57	2.48	0.16	1.19	176	38	39
Base of Taylor Glacier																
BW84-71	1050	911	1	51.02	0.16	0.95	0.01	33.09	173	54	*2.70*	*0.20*	1.35	201	45	45
Taylor III																
KBA89-50	1130	902	1	35.04	0.26	0.93	0.02	20.48	102	31						
			2	98.61	1.08	0.30	0.03	18.30								
KBA89-105	1110	904	2	9.87	0.01	8.17	0.06	52.59	275	85						
KBA89-103	1160	899	2	38.11	0.43	1.65	0.06	39.46	207	64						
SCW87-5[d]	1150	900	2	102.99	1.15	1.88	0.02	124.89	654	202	*13.9*	*1.0*	6.53	1220	323	380
KBA89-52	1130	902	2	268.58	4.06	0.24	0.05	40.21	211	67						
BW84-134[d]	1150	900	1	45.91	0.92	1.10	0.03	31.77	166	51	*2.00*	*0.20*	0.92	135	31	31
BW84-33[d,e]	1150	900	1	63.82	1.33	0.91	0.03	37.66	190	59	*13.00*	*1.80*	6.15	900	226	252
			1	34.84	1.22	1.79	0.09	40.64								
			2	247.23	13.16	0.20	0.02	30.57								
KBA89-104	1150	900	2	35.37	0.42	2.59	0.06	58.00	304	94						
Rhone Platform																
AA86-6	940	923	1	94.77	0.39	0.38	0.01	25.76	147	45						
			1	99.13	1.63	0.43	0.02	30.31								
AA86-5	940	923	1	26.49	0.08	2.57	0.02	49.39	259	80	*3.40*	*0.30*	1.79	272	63	64
Taylor IVa																
KBA89-45-1	1160	899	1	97.25	1.05	1.29	0.03	79.79	400	124	*13.00*	*3.10*	6.02	1096	404	497
			1	46.22	0.54	2.47	0.06	72.31								
KBA89-47-1	1160	899	2	33.75	0.37	4.21	0.14	90.26	452[f]	140						
KBA89-47-2	1160	899	2	20.63	0.15	6.33	0.06	82.41								
KBA89-41-2	1170	898	2	70.94	0.79	0.75	0.03	32.48	179	56	*4.50*	*0.50*	2.01	308	75	77
				77.13	0.84	0.76	0.03	35.966								
KBA89-40-1	1170	898	2	90.65	1.07	0.28	0.02	15.02	79	25						
KBA89-95	1150	900	2	35.49	0.39	2.80	0.09	62.98	330	103						
KBA89-94	1140	901	2	2638.79	263.90	0.077	0.02	111.11	582	257						
Taylor IVb																
SCW87-3-1[e]	1600	852	1	44.47	0.27	12.08	0.13	259.48	1359	420	*27.00*	*1.80*	9.43	2110	646	926
KBA89-25	1320	882	2	106.93	1.21	3.49	0.05	208.58	1092	338						
KBA89-19[e]	1260	888	2	54.77	0.70	5.28	0.05	173.21	933	289						
			2	26.51	0.15	11.54	0.07	183.37								
			4	59.71	0.67	6.66	0.08	238.36	1248	386						
AA86-14[e]	1550	857	1	24.08	0.09	14.46	0.10	171.86	900	278	*27.60*	*1.90*	9.85	2273	717	1081
AA86-15	1600	852	1	32.59	0.15	17.21	0.12	265.24	1389	429	*26.40*	*1.70*	9.03	1962	584	803
BW84-105	1300	884	1	40.41	0.05	10.49	0.09	244.15	1122	347	*23.20*	*1.60*	9.66	2197	685	1008
			3	38.76	0.49	9.88	0.08	220.32								
			2	17.10	0.15	19.51	0.16	192.21								
			2	67.57	0.93	5.15	0.07	200.21								
Tor above Taylor IVb																
AA86-16	1650	847	1	45.06	0.95	11.28	0.33	233.66	1223	379	*29.40*	*1.80*	9.78	2244	698	1037
Quartermain Drift																
KBA89-108	1250	889	2	51.90	7.56	9.09	0.11	280.68	1470	502	33.60	1.81	14.46	>3000[h]		
KBA89-107	1321	882	2	47.97	6.99	2.69	0.03	73.04	382	131	21.70	1.17	8.92	1923	562	761
SCW87-1-2	1400	873	2	36.14	0.29	24.49	0.17	477.68	2501	773						
SCW87-1-1	1350	878	2	13.07	0.03	33.03	0.24	240.71	1260	389	*29.70*	*2.10*	11.97	3133	1136	2537
Surface of Taylor Glacier																
KBA89-91-2	1040	912	2	20.61	0.16	0.14	0.01	1.80	9	3						

Note. Units: ^{4}He in 10^{12} atg^{-1}; ^{3}He and ^{10}Be in 10^6 atg^{-1}. R/R$_a$ = ^{3}He/^{4}He ratio relative to atmospheric ratio (1.38×10^{-6}). Uncertainties in isotope concentrations are 1σ analytical uncertainties only. AD is atmospheric depth in g cm^{-2}. ^{3}He$_{cn}$ and ^{10}Be$_n$ are cosmogenic nuclide concentrations normalized to sea level and rock surface as described in text. Italics indicate ^{10}Be data originally published in Brown *et al.* (1991).

TABLE 2
Mean, Median, and Maximum Exposure Ages for Taylor Moraines in Arena Valley (10^3 yr)

Sample	^{3}He ages				^{10}Be ages[a]				Previous age constraint[b]
	Mean	Median	Max.	n	Mean	Median	Max.	n	
Taylor II[c]	113 ± 45	100 ± 22	192 ± 61	6	117 ± 51	115 ± 25	176 ± 39	5	72–98
Taylor III[c]	208 ± 67	207 ± 64	304 ± 94	7					
Taylor IVa	335 ± 187	365 ± 81	582 ± 257	6					none
Taylor IVb[d]	1185 ± 184	1185 ± 260	1389 ± 429	6	2135 ± 134	2154 − 471/+684	2273 − 717/+1081	4	none

[a] Sufficient data for calculating means are not available for Taylor III and IVa.
[b] Taylor II and III ages based on U–Th ages of Hendy *et al.* (1979) as summarized by Denton *et al.* (1989).
[c] SCW87-4-1 and SCW87-5 ommitted from calculations for Taylor II and III, respectively.
[d] For Taylor IVb sample KBA89-19, only the ^{3}He age calculated for 1- 2-mm grains was used in these calculations.

Rhone Glacier (Fig. 1b, Table 1), and parallel to Taylor Glacier, have ^{3}He exposure ages of 161,000 ± 50,000 and 284,000 ± 88,000 yr (samples AA86-5 and -6); AA86-5 has a ^{10}Be age of 272 ± 64,000 yr. This moraine may correlate with Taylor III or IVa drift. A bedrock tor sample (sample AA86-16) collected beyond the Taylor IVb limit yielded a ^{3}He age of 1.2 ± 0.4 myr and a ^{10}Be age of 2.2 −0.7/+1.0 myr, suggesting that this bedrock surface may be approximately the same age as the Taylor IVb moraine. One sample collected from a small moraine ridge near Taylor Glacier (BW84-71) has ^{3}He and ^{10}Be ages of 168,000 ± 52,000 yr and 201,000 ± 45,000 yr, suggesting that this moraine ridge may be the same age as the outer Taylor II or Taylor III moraine. These latter conclusions, based on small numbers of samples, must be considered tentative given the distribution of ^{3}He ages observed on the Arena Valley moraines.

^{10}Be data can also be used to place some constraints on suggested rapid uplift of the Transantarctic Mountains (Brown *et al.*, 1991). For example, McKelvey *et al.* (1991) have suggested uplift of 1300 m in the last 3 myr in the Beardmore Glacier region (an average of 4.2×10^{-4} m yr^{-1}), based primarily on paleobotanical and biostratigraphic evidence from the late Neogene Sirius Formation. Because production rates of cosmogenic nuclides increase exponentially with altitude, the old exposure ages for Taylor IVb moraines and Quartermain Drift indicate that such high uplift rates are unlikely in the McMurdo Sound–Dry Valleys region. For example, if the Quartermain Drift sample KBA89-108 was uplifted from sea level to its present position at a constant uplift rate of 4.2×10^{-4} m yr^{-1}, the ^{10}Be concentration could only reach ~1.8×10^7 at g^{-1} (using the uplift model of Brown *et al.* (1991) and assuming constant exposure to cosmic rays and the ^{10}Be production rate of 7 at g^{-1} yr^{-1} at sea level) which is ~50% lower than the measured concentration, suggesting that such high uplift rates are unlikely in the Dry Valleys region. A similar conclusion was reached by Wilch *et al.* (1990) based on K–Ar ages of Taylor Valley subaerial volcanic deposits. These results suggest either that the suggested uplift rates are too high or that the recent uplift history of the Beardmore Glacier region is significantly different than that of the McMurdo Sound–Dry Valleys region.

The moraine and drift sequence deposited by Taylor Glacier in Arena Valley is the most complete for any valley in the Transantarctic Mountains adjacent to the East Antarctic Plateau. Assuming that it is correct, the exposure-age chronology for this sequence permits maximum limiting values to be placed on Quaternary thick-

TABLE 1 Footnote—*Continued*

[a] An. Analysis code; 1, combination of crushing *in vacuo* and melting resulting powder; 2, melting whole grains *in vacuo*; 3, results of step heating experiment. All samples are 0.5- to 1-mm grains unless noted.
[b] For samples analyzed by crushing and melting the total ^{3}He/^{4}He ratios were calculated from the crushing and melting data of Brook and Kurz (1993).
[c] Ages calculated using ^{3}He production rate of 191 ± 59 and ^{10}Be production rate of 7 ± 1.4. Nuclide concentrations were normalized to rock surface assuming an exponential path length of 160 g cm^{-2} and the measured sampling interval, and normalized to sea level as described by Brook and Kurz (1993). The normalization to sea level is based on an exponential attenuation length in the atmosphere of 165 g/cm^2 (Lingenfelter, 1963). Uncertainties in exposure ages include uncertainties in ^{3}He and ^{10}Be production rates (see text). ^{3}He data were corrected for radiogenic ^{3}He assuming a ^{3}He/^{4}He of 0.011 ± 0.04 for radiogenic helium.
[d] Altitudes originally reported for these samples by Brown *et al.* (1991) have been corrected based on further field measurements. Sample BW84-33 is composed of 0.5- to 1-mm aggregates of < 0.5-mm grains.
[e] Noted analysis for KBA89-19 is for 1- to 2-mm grains; BW84-33 is 0.1- to 0.5-mm grains; SCW87-3-1 is 0.2- to 0.5-mm grains.
[f] Mean of 47-1 and 47-2.
[g] Sample altitude is uncertain by up to 150 m.
[h] The age is a lower limit defined by 1σ analytical and production rate uncertainties; in Figures 3 and 4 the lower limit plotted (5.0 myr) is based on only analytical uncertainties.

ening of upper Taylor Glacier and the adjacent East Antarctic Plateau surface. The Taylor IVa moraines and drift, the oldest deposits of definite Quaternary age, record a thickening of ~250 m for adjacent Taylor ice, which lies in the ablation zone of the glacier system. Assuming that the Taylor IVb and Quartermain Drift ages are correct, the data suggest a relative change in the height of Taylor Glacier of about 500 m since the early Pleistocene (and perhaps as early as the middle Pliocene).

SUMMARY AND CONCLUSIONS

The present ^{3}He and ^{10}Be data provide important chronological information about glacial deposits in Arena Valley, Antarctica. The data suggest that the Taylor II moraine and drift was deposited during oxygen isotope stage 5, ~100,000 yr B.P. The median ^{3}He age for Taylor III is consistent with a stage 7 age, but older ^{10}Be ages suggest that this is strictly a minimum estimate. Taylor IVa appears to be at least 400,000 yr old based on ^{3}He and ^{10}Be data. Taylor IVb is ~2 myr old based on ^{10}Be data. Quartermain Drift, a glacial drift deposited by Taylor Glacier prior to deposition of the Taylor moraines, has minimum ^{10}Be ages of ~3 myr and may be significantly older.

Several complexities that are important for using cosmogenic nuclides to determine the age of geological features are also revealed. Significant variability is found in both ^{3}He and ^{10}Be ages for individual deposits, as also found by Phillips *et al.* (1990) for ^{36}Cl ages of alpine moraine boulders in the western United States. The reasons for the age distribution within single deposits probably include prior exposure to cosmic rays, prior soil cover, the possibility of sampling older boulders exposed in windows in younger material, shifting of moraine boulders after deposition, and perhaps different erosion rates of individual boulders. In the case of ^{3}He, diffusive loss is also important, particularly for exposure ages >100,000 yr. Both the ^{3}He and the ^{10}Be data indicate that individual exposure ages must be interpreted with caution. Interpreting these age distributions fully, and taking full advantage of the potential of *in situ* cosmogenic nuclides, requires measurements of several cosmogenic nuclides in the same samples, as well as extensive field sampling.

Nonetheless, the data provide important chronological information, including minimum exposure ages for deposits that previously had no direct chronological constraints. In addition, the exposure ages for the moraine sequence in Arena Valley, which is the best developed sequence of Quaternary ice–marginal features in the Dry Valleys region, suggest that Taylor Glacier at Arena Valley has not changed thickness by more than ~500 m in the last 2 myr. Furthermore, the ^{10}Be data for Quartermain Drift suggest that a fully developed Taylor Glacier existed in pre-Pleistocene time, perhaps as early as the middle Pliocene.

APPENDIX

Headings list sample number, location, geological feature, altitude, sampling interval, and grain size. See Figure 1 for map locations. Unless noted all samples are whole quartz grains separated from the rocks. Further description of the geology of the Arena Valley region and petrology of the Beacon Supergroup can be found in McElroy and Rose (1987) and Matz *et al.* (1972).

SCW87-4-1, Arena Valley, Taylor II, 1100 m, 1–6 cm, 0.5–1 mm

Taylor II moraine quartz sandstone collected by S. Wilson in 1987.

KBA89-102, Arena Valley, Taylor II, 1140 m, 0–4 cm, 0.5–1 mm

Top surface of small ~0.25 m^3 quartz sandstone boulder perched on outer wall of Taylor II moraine. Collected on 12-21-89 from western side of outermost Taylor II moraine loop. Greenish gray color with brown weathered surface dipping 10°–20° to west.

KBA89-70-1, Arena Valley, Taylor II, 1120 m, 0–3 cm, 0.5–1 mm

Top surface of large, ~4-m-high, quartz sandstone boulder in Taylor II moraine, resting on small dolerite boulder. Collected on 12-18-89 from eastern side of outermost Taylor II moraine loop. Brown weathered crust on top surface.

KBA89-96, Arena Valley, Taylor II, 1150 m, 0–4 cm, 0.5–1 mm

Horizontal surface of 1 × 1 × 0.8-m-high sandstone boulder perched on several dolerite boulders on crest of moraine. Collected on 12-21-89 from eastern, central side of outermost Taylor II moraine loop. Brown staining on top and sides.

KBA89-99, Arena Valley, Taylor II, 1090 m, 0–2 cm, 0.5–1 mm

Top surface of 1 × 0.6 × 0.6-m-high sandstone boulder perched on several dolerite and granite boulders. Top surface dips ~10° to south. Collected on 12-21-89 from eastern, central side of outermost Taylor II moraine loop. Tan-brown-stained top surface.

KBA89-97, Arena Valley, Taylor II, 1090 m, 0–3 cm, 0.5–1 mm

Top surface of 0.6 × 1.2 × 0.6-m-high sandstone boulder perched on top of Taylor II moraine crest. Collected on 12-21-89 from central part of outermost moraine loop.

Top surface of sample dips ~30° to northeast. Brown-stained surface.

BW84-87, Arena Valley, Taylor II, 1100 m, 0–7 cm, 0.5–1 mm

Surface sample from Taylor II quartz sandstone boulder collected by R. Weed in 1984 from eastern side of outermost Taylor II moraine loop.

BW84-71, Arena Valley, Base of Taylor Glacier, 1050 m, 0–6 cm, 0.5–1 mm

Surface sample collected from quartz sandstone boulder in small moraine ridge nearest Taylor Glacier by R. Weed in 1984.

KBA89-50, Arena Valley, Taylor III, 1130 m, 0–2 cm, 0.5–1 mm

Top surface of small, 0.25 cm^3, quartz sandstone in Taylor III Moraine. Collected on 12-17-89 from near center of outermost Taylor III moraine loop. Bottom partially buried in loose gravel.

KBA89-52, Arena Valley, Taylor III, 1130 m, 0–6 cm, 0.5–1 mm

Horizontal top surface of 0.5 × 0.25 × 0.25 m-high quartz sandstone boulder perched on Taylor III moraine. Light yellowish brown weathered surface. Collected on 12-17-89 from near center of outermost Taylor III moraine loop, approximately 20 m west of KBA89-50.

KBA89-104, Arena Valley, Taylor III, 1150 m, 0–4 cm, 1–2 mm

Horizontal top surface of 0.5 × 0.8 × 0.4-m-high quartz sandstone boulder in Taylor III moraine. Reddish brown-stained surface. Collected on 12-21-89 from outermost Taylor III moraine loop on east side of Taylor Valley.

KBA89-103, Arena Valley, Taylor III, 1160 m, 0–4 cm, 0.5–1 mm

Horizontal top surface of 0.5 × 0.25 × 0.25 m-high sandstone boulder on crest of Taylor III moraine. Collected on 12-21-89 from outermost Taylor III moraine on east side of Arena Valley.

SCW87-5, Arena Valley, Taylor III, 1150 m, 1–6 cm, 0.5–1 mm

Taylor III moraine sample collected by S. Wilson in 1987.

BW84-134, Arena Valley, Taylor III, 1150 m, 0–3.5 cm, 0.5–1 mm

Top surface of Taylor III quartz sandstone boulder collected by R. Weed in 1984 from near center of outermost Taylor III moraine in Arena Valley.

BW84-33, Arena Valley, Taylor III, 1150 m, 0–8 cm, 0.5–1 mm

Top surface of Taylor III quartz sandstone boulder collected by R. Weed in 1984, approximately 50 m west of BW84-134. Grains (0.5–1 mm) separated from the rock are actually multigrain aggregates of 0.1- to 0.5-mm grains.

AA86-6c, Rhone Platform, 940 m, 0–5 cm, 0.5–1 mm

Top, horizontal surface of 2 × 2 × 0.5 m-high long granite boulder in moraine parallel to Taylor Glacier, east of Rhone Glacier, on lower slope of distinctive volcanic cone. Collected on 11-4-86 by R. Ackert.

AA86-5, Rhone Platform, 940 m, 0–3.5 cm, 0.5–1 mm

Top, horizontal surface of 1 × 0.5 × 0.25 m-high long quartz sandstone boulder in moraine parallel to Taylor Glacier, east of Rhone Glacier, on lower slope of distinctive volcanic cone. Collected by R. Ackert on 11-4-86. Top surface weathered brown.

KBA89-45-1, Arena Valley, Taylor IVa, 1160 m, 0–6 cm, 0.5–1 mm

Top, horizontal, surface of large, 2.5 m × 3 m × 3.5 m-high quartz sandstone boulder in Taylor IVA moraine with well-developed brown weathering rind on surface. Collected on 12-17-89 at very edge of Taylor IVA limit in center of Arena Valley.

KBA89-47-1, Arena Valley, Taylor IVa, 1160 m, 0–5 cm, 0.5–1 mm

Top, horizontal surface of large, 4 × 5 × 3-m-high quartz sandstone boulder in Taylor IVA moraine at the edge of Taylor IVA limit in center of Arena Valley. Sample from center of eastern side of boulder. Top surface is weathered brown and extensively iron stained. Collected on 12-17-91.

KBA89-47-2, Arena Valley, Taylor IVa, 0–4 cm

Same as KBA89-47-1, but from northwest corner of top of boulder.

KBA89-41-2, Arena Valley, Taylor IVa, 1170 m, 0–2 cm, 0.5–1 mm

Top, horizontal surface of large 2 × 2 × 0.5-m-high quartz sandstone boulder in outer Taylor IVA moraine

loop on western side of Arena valley. Collected on 12-16-89.

KBA89-40-1, Arena Valley, Taylor IVa, 1170 m, 0–4 cm, 0.5–1 mm

Top surface of large 2.5 × 2.5 × 1.5-m-high quartz sandstone boulder perched on several dolerite boulders at edge of Taylor IVA moraine limit on western side of Arena Valley. Collected on 12-16-89.

KBA89-95, Arena Valley, Taylor IVa, 1150 m, 0–4 cm, 0.5–1 mm

Horizontal top surface of 1 × 1 × 0.6-m-high sandstone boulder at center of outermost Taylor IVa limit. Brown stained surface. Collected on 12-21-89.

KBA89-94, Arena Valley, Taylor IVa, 1140 m, 0–3.5 cm, 1–2 mm

Top surface of 2 × 2 × 1-m-high granite boulder in center of Taylor IVa limit in east side of Arena Valley. Brown-stained surface, dips approximately 20° to north. Collected on 12-21-89.

SCW87-3-1, Arena Valley, Taylor IVa, 1300 m, 1–5.5 cm, 0.5–1 mm

Surface sample of Taylor IVB boulder collected by S. Wilson in 1987. Analyzed fraction composed of 0.5- to 1-mm aggregates of 200- to 500-μm-diameter grains.

KBA89-25, Arena Valley, Taylor IVb, 1320 m, 0–2 cm, 1–2 mm

Top surface of ~1.5 m^3 quartz sandstone boulder 50 m downslope from outer limit of Taylor IVB moraine on eastern wall of Arena Valley. Coarse-grained with some large pebbles. Collected on 12-15-89.

KBA89-19, Arena Valley, Taylor IVb, 1260 m, 0–6 cm, 0.5–1, 1–2 mm

Top surface of large, 2 × 2 × 2-m-high quartz sandstone boulder, resting on top of desert pavement. Weathering rinds on top and sides indicated that this boulder may have rolled over but sample was taken from corner of present top surface which would have been top in any case. Collected on 12-15-89.

AA86-14, Arena Valley, Taylor IVb, 1550 m, 0–5 cm, 0.5–1 mm

Top, horizontal surface of 0.5 m^3 quartz sandstone boulder in Taylor IVB moraine on eastern wall of Arena Valley. Upper surface weathered brownish orange. Collected by R. Ackert on 11-24-86.

AA86-15 Arena Valley, Taylor IVb, 1600 m, 0–3.5 cm, 0.5–1 mm

Top surface of large, approximately 2 m^3 quartz sandstone boulder in Taylor IVB moraine at Taylor IVB limit on east wall of Arena Valley. Upper surface weathered brown and sloping approximately 10° to the east. Collected by R. Ackert in 1986.

BW84-105, Arena Valley, Taylor IVb, 1300 m, 0–4 cm, 0.5–1 mm

Top surface of Taylor IVB sandstone boulder collected from limit of Taylor IVB moraine by R. Weed in 1984 on eastern wall of Arena Valley.

AA86-16, Arena Valley, Bedrock Tor, 1650 m, 0–4 cm, 0.5–1 mm

Top, horizontal surface of quartz sandstone bedrock tor beyond limit of Taylor IVB moraine on east wall of Arena Valley. Tor stands approximately 1 m above surrounding bedrock surface. Upper surface weathered dark brown. Collected by R. Ackert on 11-24-86.

SCW87-1-1, Arena Valley, Quartermain Drift, 1400 m, 0–4 cm, 0.5–1 mm

Top surface of quartz sandstone boulder in Quartermain Drift. Collected by S. Wilson in 1987.

SCW87-1-2, Arena Valley, Quartermain Drift, 1400 m, 0–4 cm, 0.5–1 mm

Top surface of quartz sandstone boulder in Quartermain Drift. Collected by S. Wilson in 1987.

KBA89-108, Arena Valley, Quartermain Drift, 1250 m, 0–4 cm, 0.5–1 mm

Top horizontal surface of 0.5 × 0.2 × 0.15 m sandstone boulder, top and lee side with brown, well-developed, varnished surface. From near top of low hill mapped as Quartermain Drift by Marchant (1990). Collected on 12-22-89.

KBA89-107, Arena Valley, Quartermain Drift, 1320 m, 0–4 cm, 0.5–1 mm

Small sandstone boulder, 0.5 × 0.5 × 0.2-m-high with horizontal, brown-stained leeward surface and heavy quartz rind development. Collected from small patch of drift mapped as Quartermain Drift by Marchant (1990) west of main exposure of Quartermain Drift. Collected on 12-22-89.

KBA89-91-2, Arena Valley, Taylor Glacier, 1040 m, 0–7 cm, 0.5–1 mm

Top surface of small sandstone boulder on surface of Taylor Glacier at mouth of Arena Valley. Collected on 12-21-89.

ACKNOWLEDGMENTS

Tom Trull and Debra Colodner made some of the early ^{3}He measurements reported here. We thank Tom Trull, Dave Marchant, and Marcia Davis for useful comments. Rebecca Weed and Scott Wilson kindly collected some of the initial samples analyzed, and D. Kammer, J. Lestringuez, D. Deboffle, and A. Guiesserian provided able laboratory assistance. M.D.K. also thanks Michael Bender for an early suggestion about exposure dating of Antarctic rocks. E.J.B. acknowledges support of a Department of Defense NDSEG Fellowship and the WHOI Education Office. This work was supported by the Division of Polar Programs of the National Science Foundation (NSF DPP 88-17406 and DPP 91-17458 to M. Kurz). E.T.B. acknowledges support from NSF through NSF-NATO Postdoctoral Fellowship and grant INT-9006641. The pilots and crew of U.S. Navy Antarctic Development Squadron VXE-6 and ITT/ANS support personnel are thanked for excellent logistical support in Antarctica. Tandetron operation is supported by the CNRS, CEA, and IN_2P_3. Woods Hole Oceanographic Institution Contribution 7898.

REFERENCES

Bockheim, J. G. (1982). Properties of a chronosequence of ultraxerous soils in the Trans-Antarctic Mountains. *Geoderma* **28**, 239–255.

Brook, E. J., and Kurz, M. D. (1993). Using *in situ* ^{3}He in Antarctic quartz sandstone boulders for surface-exposure chronology. *Quaternary Research* **39**, 1–10.

Brown, E. T., Brook, E. J., Raisbeck, G. M., Yiou, F., and Kurz, M. D. (1992). Effective attenuation lengths of cosmic rays producing ^{10}Be and ^{26}Al in quartz: Implications for exposure dating. *Geophysical Research Letters* **19**(4), 367–372.

Brown, E., Edmond, J. M., Raisbeck, G. M., Yiou, F., Kurz, M., and Brook, E. J. (1991). Examination of surface exposure ages of Antarctic moraines using *in situ* produced 10-Be and 26-Al. *Geochimica et Cosmochimica Acta* **55**(8), 2269–2284.

Cerling, T. E. (1990). Dating geomorphological surfaces using cosmogenic 3-He. *Quaternary Research* **33**, 148–156.

Denton, G. H., Bockheim, J. G., Wilson, S. C., and Stuiver, M. (1989). Late Wisconsin and early Holocene glacial history, inner Ross Embayment, Antarctica. *Quaternary Research* **31**, 151–182.

Hendy, C. H., Healy, T. H., Rayner, E. M., Shaw, J., and Wilson, A. T. (1979). Late Pleistocene glacial chronology of the Taylor Valley, Antarctica, and the global climate. *Quaternary Research* **11**, 172–184.

Kurz, M. D. (1986). *In situ* production of terrestrial cosmogenic helium and some applications to geochronology. *Geochimica et Cosmochimica Acta* **50**, 2855–2862.

Kurz, M. D., Colodner, D., Trull, T. W., Moore, R. B., and O'Brien, K. (1990). Cosmic ray exposure dating with *in situ* produced cosmogenic ^{3}He: Results from young lava flows. *Earth and Planetary Science Letters* **97**, 177–189.

Lal, D. (1991). Cosmic ray labeling of erosion surfaces: *In situ* nuclide production rates and erosion models. *Earth and Planetary Science Letters* **104**, 424–439.

Marchant, D. (1990) "Surficial Geology and Stratigraphy in Arena Valley, Antarctica: Implications for Antarctic Tertiary Glacial History." Unpublished MS thesis, University of Maine at Orono.

Matz, D. M., Pinet, P. R., and Hayes, M. O. (1972). Stratigraphy and Petrology of the Beacon Supergroup, Southern Victoria Land. *In* "Antarctic Geology and Geophysics" (R. J. Adie, Ed.), pp. 353–358. Universitetsforlaget, Oslo.

McElroy, C. T., and Rose, G. (1987). "Geology of the Beacon Heights Area: Southern Victoria Land, Antarctica." New Zealand Geological Survey Miscellaneous Series Map 15. DSIR, Wellington, New Zealand.

McKelvey, B. C., Webb, P. N., Harwood, D., and Mabin, M. C. G. (1990). The Dominion Range Sirius Group: A record of the late Pliocene–early Pleistocene Beardmore Glacier. *In* "Geological Evolution of Antarctica" (M. R. A. Thomson, J. A. Crame, and J. W. Thomson, Eds.), pp. 675–682. Cambridge Univ. Press, New York.

Nishiizumi, K., Winterer, E. L., Kohl, C. P., Klein, J., Middleton, R., Lal, D., and Arnold, J. R. (1989). Cosmic ray production rates of 10-Be and 26-Al in quartz from glacially polished rocks. *Journal of Geophysical Research* **94**(B12), 17907–17915.

Nishiizumi, K., Kohl, C. P., Arnold, J. R., Klein, J., Fink, D., and Middleton, R. (1991). Cosmic ray produced ^{10}Be and ^{26}Al in Antarctic rocks: Exposure and erosion rates. *Earth and Planetary Science Letters* **104**, 440–454.

Phillips, F. M., Zreda, M. G., Smith, S. S., Elmore, D., Kubik, P. W., and Sharma, P. (1990). Cosmogenic chlorine-36 chronology for glacial deposits at bloody canyon, eastern Sierra Nevada. *Science* **248**, 1529–1532.

Robinson, P. H. (1984). Ice dynamics and thermal regime of Taylor Glacier, south Victoria Land, Antarctica. *Journal of Glaciology* **30**(105), 153–160.

Shoemaker, D. P., Garland, C. W., and Nibler, J. W. (1989). "Experiments in Physical Chemistry." McGraw-Hill, New York.

Staudacher, T., and Allègre, C. J. (1991). Cosmogenic neon in ultramafic nodules from Asia and in quartzite from Antarctica. *Earth and Planetary Science Letters* **106**, 87–102.

Wilch, T. I., Lux, D. R., McIntosh, W. C., and Denton, G. H. (1990). Plio-Pleistocene uplift of the McMurdo Dry Valley Sector of the Transantarctic Mountains. *Antarctic Journal of the United States* **24**(5), 30–33.

Zreda, M. K., Phillips, F. M., Elmore, D., Kubik, P. W., Sharma, P., and Dorn, R. I. (1991). Cosmogenic chlorine-36 production rates in terrestrial rocks. *Earth and Planetary Science Letters* **105**, 94–109.

Chapter 5

Chronology of Antarctic Dry Valley Glacial Deposits Using Cosmogenic ^{10}Be, ^{3}He, and ^{26}Al: Implications for Antarctic Glacial History and Climate

Introduction

In the last decade cosmogenic nuclides produced *in situ* in terrestrial surface rocks have proved to be useful chronometers for studying surface processes (see Lal, 1991, Kurz and Brook, 1993, and Chapter 1 for reviews). In a recent set of papers Brown et al. (1991), Brook and Kurz (1991) [Chapter 3], and Brook et al. (1993) [Chapter 4]), investigated this use of *in situ* cosmogenic ^{3}He, ^{10}Be, and ^{26}Al for dating glacial deposits related to Quaternary and late Neogene expansions of the East Antarctic Ice Sheet in the Dry Valleys region of Antarctica (Fig. 1). These studies concentrated on an extremely well-exposed moraine sequence in Arena Valley (Fig. 1). This chapter includes additional ^{3}He, ^{10}Be, and ^{26}Al data for these deposits, uses the entire data set to improve the original chronology, and further demonstrates the utility of cosmogenic nuclides for dating Antarctic glacial deposits.

The previous work resulted in four major conclusions. First, ^{3}He, ^{10}Be, and ^{26}Al ages for Arena Valley moraines ranged from ~100 kyr to ~2 myr. This suggested that the East Antarctic Ice Sheet was near its present position throughout most of that time. ^{10}Be ages for a stratigraphically older glacial drift indicated that this conclusion could be extended back to at least 3 myr, suggesting little change in this part of the East Antarctic Ice Sheet throughout Quaternary and late Pliocene time (Brook et al., 1993 [Chapter 4]; Marchant et al., in press). Second, ^{10}Be and ^{3}He ages for the Taylor II moraine, the youngest well documented deposit in Arena Valley (Fig.1), gave concordant mean ages of ~120 kyr. These ages are consistent with previous suggestions that Taylor II correlates with "Bonney Drift," a Taylor Glacier drift deposited in middle Taylor Valley, which contains U-Th dated lake sediments with ages that range from 70-120 kyr

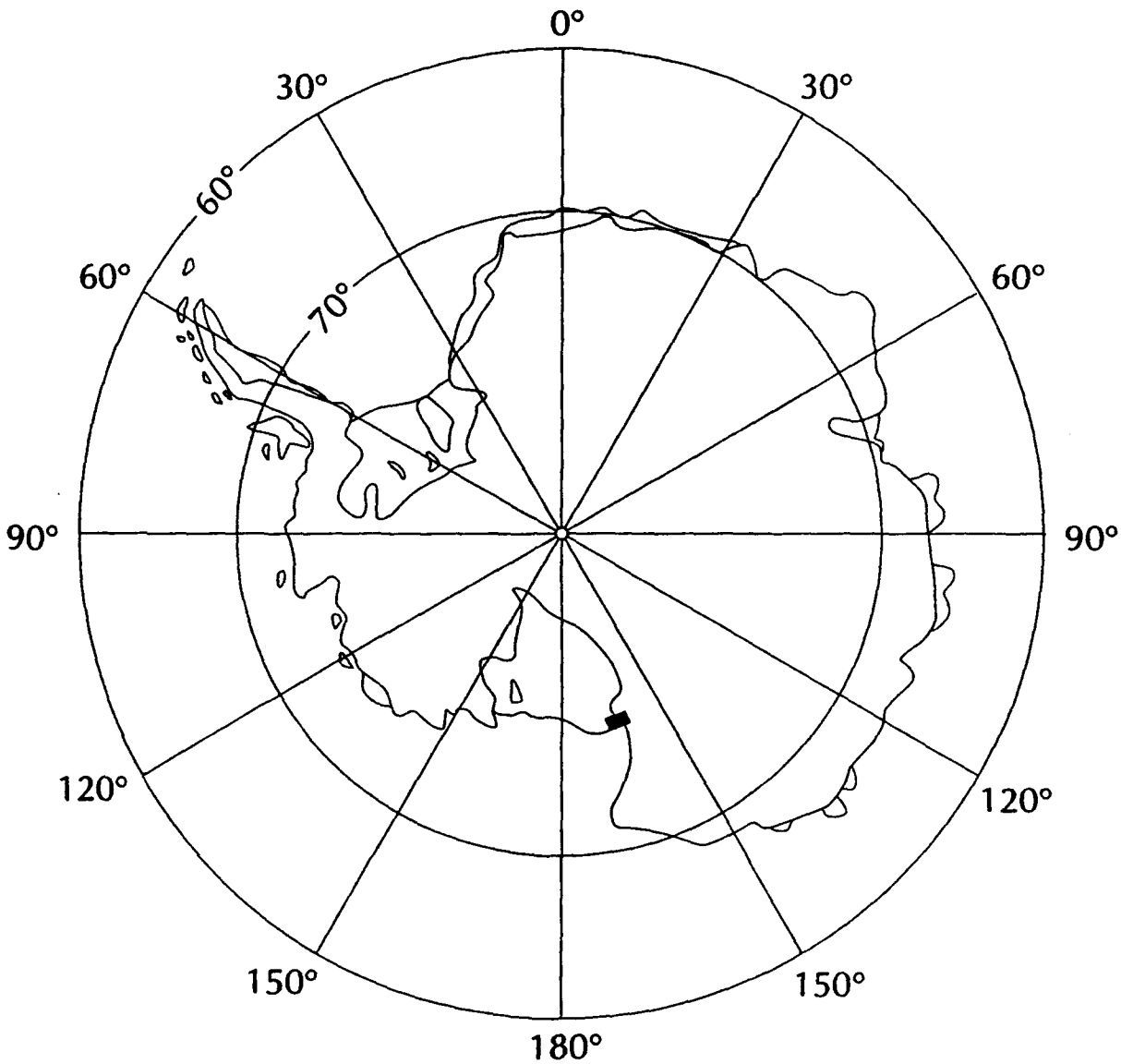

Figure 1a. Index map of Antarctica showing location of Dry Valleys region and Fig. 1b.

Figure 1b. Map of Dry Valleys region showing Taylor Glacier and Arena Valley.

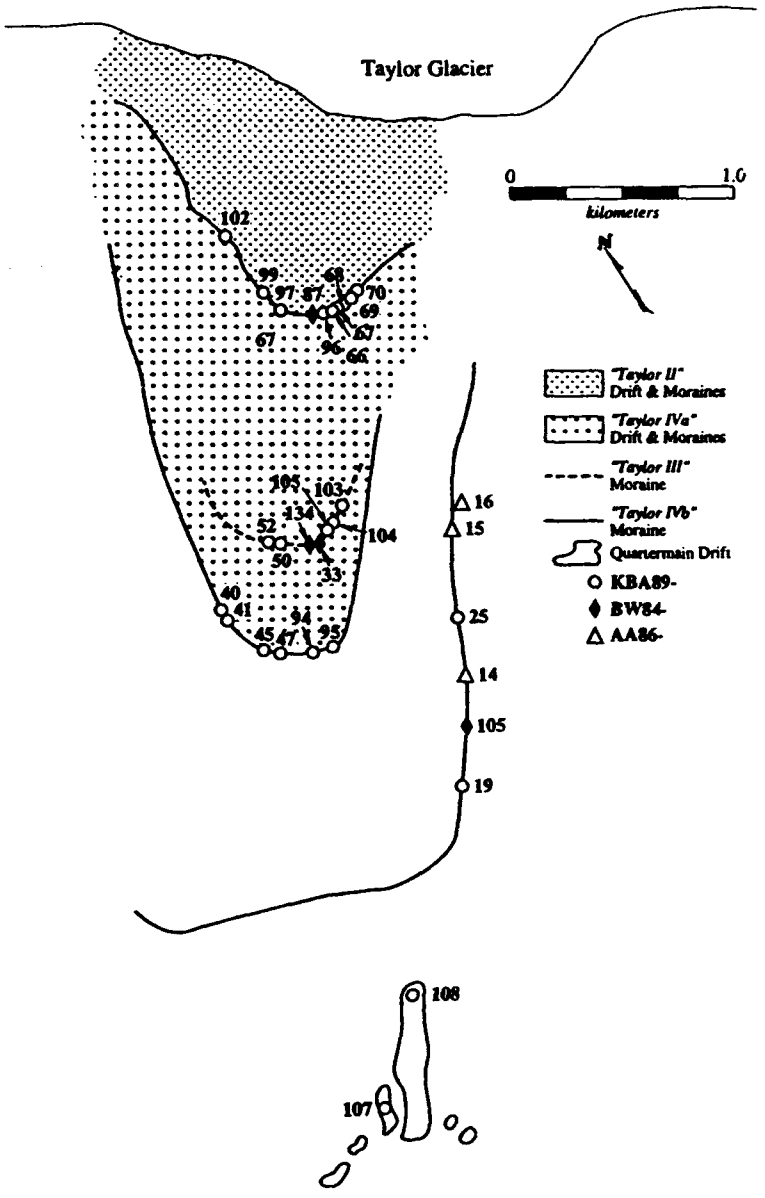

Figure 1c. Sketch map of Arena Valley moraines and sample locations. See Fig 2 in Chapter 4 for photograph of Arena Valley.

(Hendy et al., 1979; Higgins, 1993). Third, although ^{3}He and ^{10}Be ages were concordant in the younger deposits, this comparison in older samples indicated significant loss of ^{3}He from quartz (Brown et al., 1991; Brook et al., 1993 [Chapter 4]). Fourth, a preliminary analysis of ^{10}Be data from Quartermain Drift, the oldest deposit sampled in Arena Valley, allowed constraints on the uplift history of the Transantarctic Mountains (TAM). McKelvey et al., 1990, based on biostratigraphic evidence from Sirius Group tills in the Beardmore Glacier region, have suggested uplift of at least 400 m/myr over the last 3 myr. This suggestion is controversial (Wilch et al., 1993). Preliminary modeling of the effects of uplift on ^{10}Be production showed that the ^{10}Be data for Quartermain Drift were inconsistent with such high uplift rates (Brown et al., 1991; Brook et al., 1993 [Chapter 4]).

Several important issues remained unresolved and are addressed here. Because only a few samples of intermediate age moraines (Taylor III and IVa; Fig. 1) were previously available it was not possible to reliably constrain their ages. These deposits are crucial, however, for understanding the response of the East Antarctic Ice Sheet to Quaternary climate change before isotope stage 5. Also, due to the importance of the Taylor II moraine in chronological interpretations of late Quaternary Antarctic glaciation (e.g., Denton et al., 1989a), and scatter in the available data, additional measurements were obtained to constrain its age. Given the ease and reduced sample size requirements of ^{3}He analysis relative to ^{10}Be analysis (e.g., Brook and Kurz, 1993 [Chapter 3]; Chapter 2), and uncertainty about the age at which ^{3}He loss becomes significant to exposure dating, further comparison of ^{3}He and ^{10}Be exposure ages in quartz was also undertaken. Finally, the recent controversy over the age of the Sirius Group and its implications for the uplift history of the TAM and the glacial history of Antarctica (Clapperton and Sugden, 1990;

Webb and Harwood, 1991; McKelvey et al., 1991; ten Brink et al., 1993; Marchant, 1993; Barret et al., 1993; Wilch et al., 1993), were addressed with additional measurements of samples from pre-Pleistocene glacial deposits in the Dry Valleys, including the Sirius Group.

The general objective of this work is to constrain the Quaternary and earlier history of the East and West Antarctic Ice Sheets. A chronological model of Antarctic glaciation has been developed in the last few decades, based on ice-core studies and U-Th and ^{14}C dating of lake sediments in the Dry Valleys, that suggests that ice accumulation rates over East Antarctica increase by roughly a factor of two during interglacial periods (e.g., Yiou et al., 1985; Raisbeck et al., 1987; Jouzel et al., 1987; 1989; 1990), causing aerial expansion of the East Antarctic ice sheet and advance of East Antarctic outlet glaciers (Hollin, 1962; Stuiver et al., 1981; Denton et al., 1989a; Brook et al., 1993 [Chapter 4]). In contrast, sea level controls advances of the West Antarctic Ice Sheet, because grounding line advance or retreat controls the build up of west Antarctic Ice on the coast (Stuiver et al., 1981; Fastook et al., 1984; Denton et al., 1989a; Chapter 6). Glacial deposits in the McMurdo Sound region suggest that during the last glacial period ice advanced on to the coast of McMurdo Sound due to grounding and resulting ice thickening in the Ross Sea. Outlet glaciers and local mountain glaciers, in contast, apparently advanced during interglacial isotope stage 5, and are advancing today (Hendy et al., 1979; Stuiver et al., 1981; Denton et al., 1989a; Higgins, 1993; Chapter 6). Preliminary work in other parts of the Transantarctic Mountains suggests that this behavior is a regional phenomenon (Bockheim et al., 1989; Denton et al., 1989a; Denton et al., 1989b). This conceptual model suggests that ice growth in East Antarctica is "out of phase" with northern hemisphere glaciation and the

deep sea oxygen isotope record (Denton et al., 1989a). It predicts that during generally warmer global climates (e.g., interglacial periods) glaciers related to the East Antarctic Ice Sheet grow due to increased precipitation in the interior. It also suggests that growth of marine-based ice sheets like the Ross Ice Sheet is "in phase" with the marine record in that these ice sheets thicken during periods of relatively lower sea level (e.g., glacial periods).

Exposure ages using cosmogenic nuclides can improve the glacial chronology in three ways. First, they can extend its range. The age range for ^{3}He dating is theoretically infinite, but in practice limited by diffusion, the importance of which depends on sample mineralogy and environmental conditions (Trull et al., 1991; Brook and Kurz, 1993). ^{10}Be (half-life = 1.5×10^{6} yr) and ^{26}Al (half-life = 7.2×10^{5} yr) ages are limited by the half-lives of the nuclides. For example, with 5 % analytical error as the only uncertainty, ^{10}Be and ^{26}Al ages of 3 and 1.4 myr, respectively can be determined with only 10 % precision, due to radioactive decay. Nonetheless, due to the long half-lives, there is potential to extend the chronology significantly beyond the limit of U-Th dating (~400 kyr). Second, exposure ages can potentially provide age constraints for features directly related to ice margins (e.g., moraines), rather than associated material (e.g., lake sediments), thus determining both the timing and extent of glacier advances. Third, because cosmogenic nuclide production rates are exponential functions of altitude, measurements of cosmogenic nuclides in old, high altitude glacial deposits can be used to place limiting constraints on the uplift history of the Transantarctic Mountains.

Glacial Geology and Geochronology in Arena and Taylor Valleys

Absolute chronology of Quaternary glacial deposits in the McMurdo Sound-Dry Valleys region is almost exclusively based on U-Th and ^{14}C dating of marine and algal lake carbonate sediments (e.g., Hendy et al., 1979; Clayton-Greene et al., 1988; Higgins, 1993; Dagel et al., in press). *In situ* carbonate sediments that appear to have been deposited in a proglacial lake at the terminus of the Taylor Glacier, 4-6 km east of the present terminus, have U-Th ages of 70-120 kyr, suggesting deposition in isotope stage 5 (Hendy et al., 1979; Higgins, 1993). ^{14}C and U-Th dates for *in situ* carbonate sediments deposited in lakes formed in advance of Ross Sea Ice in Taylor, Miers, and Marshall Valleys (see Chapter 6) suggest deposition in stages 2 and 6 (Stuiver et al., 1981; Clayton-Greene et al., 1988; Denton et al., 1989a; Dagel et al., in press). This chronology provides support for the conceptual model outlined above through isotope stage 6, but relies heavily on stratigraphic interpretation of lake deposits in the Dry Valleys, and on the hypothesis (Clayton-Greene et al., 1988; Denton et al., 1989a) that large lakes existed in the region during isotope stages 2 and 6. In contrast, other evidence suggests cold temperatures and reduced precipitation during these time periods (e.g., Raisbeck et al., 1987; Jouzel et al., 1987; Denton et al., 1989a). Prior to stage 6, interglacial expansions of Taylor Glacier have been inferred from U-Th dates of detrital carbonate clasts found in stratigraphic sections in middle Taylor Valley and as lag deposits on the valley floor (Hendy et al., 1979; Higgins, 1993). These erratic clasts can not be directly associated with past ice margins, however.

The glacial geology of the Arena and Taylor Valley regions was recently described in detail by Denton et al. (1989a), Marchant (1990), Higgins (1993),

Marchant et al. (in press), and is also discussed in Brook et al. (1993) [Chapter 4]. Arena Valley is a small hanging valley lateral to Taylor Glacier, which drains the McMurdo Dome of the East Antarctic Ice Sheet (Drewery, 1983), which is in turn fed by the much larger Dome C (Fig. 1) (Drewry et al., 1982; Steed and Drewry, 1982). In lower Arena Valley a well preserved sequence of 39 boulder-rich moraines records four separate advances of the Taylor Glacier into the valley (Denton et al., 1989a; Brook et al., 1993 [Chapter 4]; Marchant et al., in press). The moraines are composed almost entirely of boulders and lack striated surfaces or other signs of wet-based glacial deposition (Marchant et al., in press). This is important because it suggests cold-based conditions for this lobe of the Taylor Glacier throughout the time represented by these deposits.

The Arena Valley moraines are composed primarily of dolerite, sandstone, and a small percentage of granitic rocks. All three rock types are found in the local bedrock of the region, which is primarily made up of flat-lying Devonian Beacon Supergroup sandstones and large sills and dikes of Jurassic Ferrar Dolerite. Granitic bedrock is not exposed in Arena Valley, however (McElroy and Rose, 1987; Marchant, 1990). Arena Valley surficial geology was mapped recenty by Marchant (1990) (also see Marchant et al., in press). The moraines and associated drift are divided into four groups: Taylor II, Taylor III, Taylor IVa, and Taylor IVb, from youngest to oldest (Fig. 1), following the nomenclature of Denton et al. (1989a). Relative ages of the four groups are based on rock and soil weathering, moraine morphology and stratigraphic position (Bockheim, 1982; Denton et al., 1989a; Marchant, 1990; Marchant et al., in press). Before the exposure age studies there were few absolute age constraints other than tentative correlations with the U-Th dated drift in middle Taylor Valley. In addition, an upper limit of ~ 2 myr can be

placed on Taylor IVb based on a number of ^{39}Ar-^{40}Ar dates of individual anorthoclase crystals in volcanic ash in "Granite Drift," an underlying glacial deposit (Marchant, 1990; Marchant et al., in press).

Outside the limit of the Taylor IVb moraine, Marchant (1990) mapped a number of older glacial deposits. The oldest of these that can be related to a past expansion of Taylor glacier is Quartermain Drift, which contains volcanic ash dated at ~ 11 myr (Marchant, 1990). ^{10}Be ages of Quartermain Drift suggested a minimum age of ~ 3myr, and their chronological interpretation is described in more detail in Brook and Kurz (1993) [Chapter 4]. The Quartermain Drift data, combined with data for two samples of the Sirius Group from Mt. Fleming (see Fig. 1), are used here to constrain uplift rates and the age of the Sirius Group. Two samples from Altar Drift, which, based on weathering characteristics and desert varnish development is one of the oldest deposits in Arena Valley (Marchant, 1990) , were also analyzed for this purpose.

Methods

Sample collection and rock processing are described in more detail in Chapter 2, Brook and Kurz (1993) [Chapter 3], and Brook et al. (1993) [Chapter 4]. Samples from the Arena Valley moraines and Quartermain and Altar Drift were collected from top, horizontal or sub-horizontal boulder surfaces with hammer and chisel. Taylor Valley moraine samples were collected from boulders in the terminal loop of each mapped deposit. No corrections for boulder geometry or the affects of surrounding topography on the cosmic ray flux were necessary (see Chapter 1). Sub-samples several centimeters thick were cut with a rock saw, crushed in a jaw crusher, and sieved. A small (< 2%) correction to the final cosmogenic nuclide concentrations was made for

the sampling interval by assuming an exponential dependence of production rate with depth with a scale length of 150 g cm^{-2} and a density of 2.2 g cm^{-2} (Brown et al., 1992; Chapter 7). Individual quartz grains, generally 0.5-1mm or 1-2 mm grains, were picked under a binocular microscope for helium isotope analysis. For ^{10}Be and ^{26}Al analysis bulk sub-samples of 0.5-1.0 or 0.5-2.0 mm fractions were used. Samples from Sirius Group deposits on Mt. Fleming (Fig. 1) were all quartzite cobbles or boulders imbedded in the surface of the deposit and were collected in their entirety, and cut with a rock saw in the laboratory. Analytical methods are described in detail in Chapter 2. Exposure ages were calculated using a sea level ^{3}He production rate at > 60° geomagnetic latitude of 118 at g^{-1} yr^{-1} (Chapters 1 and 6) and ^{10}Be and ^{26}Al production rates from Nishiizumi et al. (1989). ^{3}He production rates were scaled for altitude and latitude (Chapter 1) using the nuclear disintegration rate polynomials of Lal (1991). ^{10}Be and ^{26}Al production rates were scaled using the appropriate polynomial functions from Lal (1991), which take into account production by muons. All age calculations propagate analytical uncertainties only. Systematic uncertainties in production rates are estimated to be on the order of 15 % (see Chapter 1). A small correction (generally < 1%) was made to the ^{3}He data to account for nucleogenic production of ^{3}He by the reaction $^{6}Li(n,\alpha)T-^{3}He$ (Chapters 1 and 7), using ^{4}He concentrations and a $^{3}He/^{4}He$ nucleogenic production ratio of $0.01\pm0.04R_a$ (Trull et al., 1991; R_a is the atmospheric $^{3}He/^{4}He$ ratio). See Chapters 1, 3 and 7 for further discussion of this issue. ^{3}He, ^{10}Be, and ^{26}Al measurements and $^{3}He/^{10}Be$ and $^{26}Al/^{10}Be$ ratios are tabulated in Table 1. Previously unreported $^{3}He/^{4}He$ ratios and ^{4}He concentrations are listed in the Appendix to this chapter.

Results

Exposure-age dating using cosmogenic nuclides requires several assumptions (see Chapter 1 for a more detailed discussion). Production rates must be known and closed system behavior is required. In addition, the erosion and soil-cover history of the dated surface must be known, and it must have remained stable and well-exposed throughout it's history. Measurements of more than one cosmogenic nuclide in the same samples can test the validity of some of these assumptions. Figure 2 illustrates this approach by comparing the relationship between the measured ^{10}Be concentrations and $^{3}He/^{10}Be$ or $^{26}Al/^{10}Be$ ratios to model predictions that assume continuous exposure to cosmic rays (e.g., Klein et al., 1987; Nishiizumi et al., 1991; Lal, 1991). The basic equation governing the model curves in Fig. 2 describes the accumulation of a cosmognic nuclide with time as a function of erosion rate (E, in g cm^{-2} yr^{-1}), production rate (P, in at g^{-1} yr^{-1}), decay constant (λ, in yr^{-1}), and the exponential attenuation length that describes the decrease of the production rate with depth in rocks (L, in g cm^{-2}) (eq. 1):

$$N = \frac{P}{\lambda + E/L}(1 - e^{-(\lambda + E/L)t}) \quad (1),$$

where N is concentration and t is time.

At steady state with respect to erosion and radiodecay equation 2 reduces to:

$$N = \frac{P}{\lambda + E/L} \quad (2).$$

Both equations can be used to create the curves in Fig. 2 which show the allowed limits of the relationship between two cosmogenic nuclides. The curves show the predicted relationship between the two variables for two end member cases: no erosion, and steady state erosion (see caption for Fig. 2 for details). In theory, data falling between the two curves are consistent with continuous exposure of the surface in question with closed system behavior, although in practice this analysis is limited somewhat by present analytical uncertainties (Fig. 2).

Fig. 2 reveals several important aspects of the ^{3}He, ^{26}Al, and ^{10}Be system in quartz. First, as noted previously (Brook and Kurz, 1993 [Chapter 3]; Brook et al., 1993 [Chapter 4]), many of the ^{3}He concentrations fall well below the predicted values. Trull et al. (1991) and Brook and Kurz (1993) [Chapter 3] demonstrated that this is a result of ^{3}He loss due to diffusion. In the youngest samples (Taylor II moraine) most of the data fall near the predicted production ratio, with two low outliers (SCW87-4-1 and KBA89-66-1) and two high outliers (BW84-87 and KBA89-70-1). Note that the data in Fig. 2 are by necessity normalized to sea level and that because different normalization is used for ^{3}He and ^{10}Be (Lal, 1991; see above) the plotted ratios are slightly lower than tabulated ratios. One of the low outliers (SCW87-4-1) may be a remobilized boulder from an older deposit (see below). The low $^{3}He/^{10}Be$ ratio in KBA89-66-1 may reflect ^{3}He loss due to diffusion. The origin of the two points above the line is not clear, but one of them (BW84-87) has anomalously low ^{10}Be and ^{26}Al concentrations relative to the others. The other (KBA89-70-1) has a ^{10}Be concentration consistent with the other Taylor II samples but a relatively high ^{3}He concentration. Excess ^{3}He could have a variety of causes, including nucleogenic ^{3}He produced by the thermal

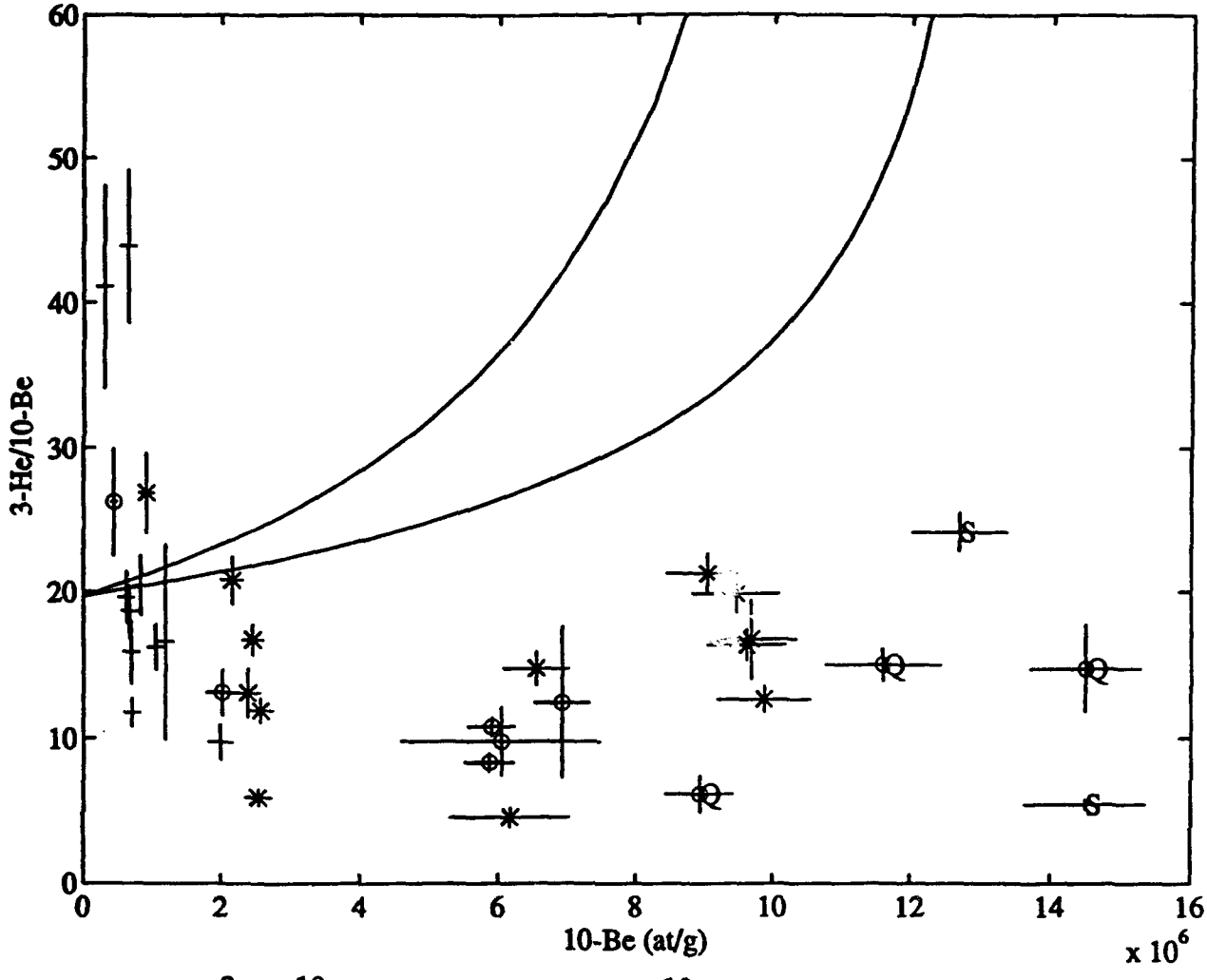

Figure 2a. $^{3}He/^{10}Be$ ratios plotted against ^{10}Be concentrations for Arena Valley and other Dry Valley samples described in text. +=Taylor II, *=Taylor III, o=Taylor IVa, x=Taylor IVb, S=Sirius Group, Q=Quarterman Drift, A=Altar Drift. The data are normalized to sea level as described in the text, different normalization for ^{10}Be and ^{3}He (Lal, 1991) accounts for the fact that plotted $^{3}He/^{10}Be$ ratios are slightly lower than tabulated ratios, which are calculated for the sample altitude. Curves on the figure are calculated using equations 1 and 2. The bottom curve shows the evolution of the relationship between the two variables assuming continuous exposure to cosmic rays with no erosion. The top curve is a locus of points corresponding to steady-state erosion (eq. 2). Data for samples exposed continuously, satisfying criteria for exposure dating, should fall between the two curves. That most data fall below the lower curve suggests loss of ^{3}He due to diffusion.

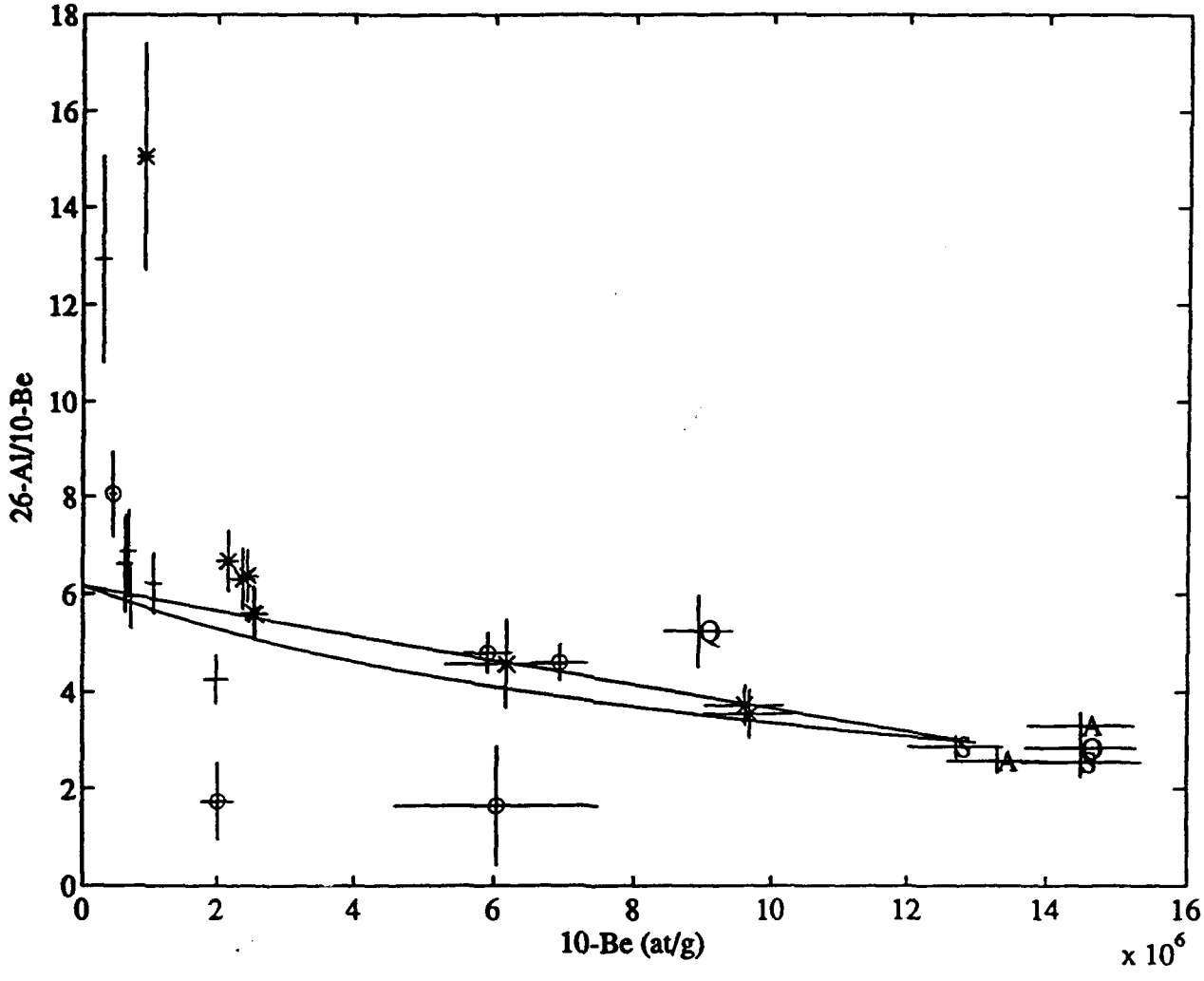

Figure 2b. Similar plot to 2a, but for ^{10}Be and ^{26}Al. Plot symbols and creation of the curves are the same, except that in this case the upper curve corresponds to continuous exposure with no erosion.

neutron reaction $^{6}Li(n,\alpha)T\text{-}^{3}He$ (Morrison and Pine, 1955), exposure to cosmic rays prior to deposition (Brook et al., 1993) or muon capture reactions (Brown et al., 1991; Chapter 7). The former seems unlikely since this sample does not contain excess U and Th, or Li relative to the other samples (Brown et al., 1991; Chapter 2) and no other evidence that this mechanism is important in these deposits has been found (Chapter 7). The latter two mechanisms may be important in some cases. Although the exact origin of these high ratios is not known, the isotope systematics (Fig. 2) suggest that the ^{3}He results from these points are anomalous.

The paired ^{26}Al and ^{10}Be data show much better agreement with predicted trends (Fig. 2b). However, the variability in the data is larger than the differences between the two end-member model calculations (Fig. 2b). This effect is probably partly due to analytical error, but also suggests that processes other than erosion affect the concentrations. For example, there are several notable outliers with high $^{26}Al/^{10}Be$ ratios in the youngest samples. As discussed in Chapter 6 such high ^{26}Al concentrations may represent nucleogenic production of ^{26}Al *via* the $^{23}Na(\alpha,n)^{26}Al$ reaction (e.g., Sharma and Middleton, 1989; Chapter 1). Excesses of ^{26}Al, assuming a $^{26}Al/^{10}Be$ production ratio of 6.1 (Nishiizumi et al., 1989) in these samples range from 6 to 10×10^{6} at g^{-1}. This value is significantly higher than Sharma and Middleton's calculation for average sandstone (6×10^{4} at g^{-1}). Brown et al. (1991), based on measurements of U and Th concentrations of less than 1 μg/g in some previously acid leached Arena Valley sandstones, concluded that there was not enough U and Th in the quartz grains to produce excess ^{26}Al. Because the acid leaching removed some uranium and thorium (Brown et al., 1991) it is possible that Brown et al. (1991) underestimated the significance

of this reaction. Based on Sharma and Middleton's (1989) calculations steady state concentrations of ^{26}Al produced by the $^{23}Na(\alpha,n)^{26}Al$ reaction are 97 and 86 at g^{-1} ^{26}Al per μg/g Na per μg/g U or Th, respectively. Brown et al. (1991) measured 3.3 μg/g Th and 1.4 μg/g U in a fraction of sandstone sample BW84-33 that had only been leached in HCl prior to analysis. Assuming these values are representative of U and Th concentrations in Arena Valley sandstones a Na concentration of 2.6 % would be necessary to produce the observed excess of 10^7 at g^{-1} ^{26}Al.. Such a high concentration seems unlikely in these samples, which are predominantly pure quartz. However, as the U, Th, and Na concentrations have not yet been adequately characterized in the samples where excess ^{26}Al is observed it is not possible to preclude the $^{23}Na(\alpha,n)^{26}Al$ reaction as the source of the excess.

Another possible explanation for the effect, considered by Brown et al. (1991), was that elevated ^{26}Al concentrations might be produced by excess production of ^{26}Al by muon capture reactions (see Chapter 1). Depth profiles of ^{26}Al concentrations (Brown et al., 1992; Chapter 7) show no signs of significantly elevated production by this mechanism, however. Therefore, it is hypothesized here that the exess ^{26}Al is nucleogenic. This issue warrants further study. If the effect is common it may limit the applicability of ^{26}Al for dating young quartz samples. Future investigation of this problem should attempt to characterize the U, Th, and Na concentrations in quartz samples with ^{26}Al anomalies.

Two samples (KBA89-41-2 and KBA89-45) have anomalously low $^{26}Al/^{10}Be$ ratios, but these ^{26}Al analyses have large errors due to low ion currents (Brown et al., 1991), so their significance is uncertain. However, the low ratios could be a result of a complex exposure history (see below).

Because of the potential problems with nucleogenic ^{26}Al in the young samples, and ^{3}He loss in the old samples, exposure ages are calculated using the ^{10}Be concentrations only, except for the Taylor II moraine where both ^{3}He and ^{10}Be isotopes are used for comparison. Agreement between ^{26}Al and ^{10}Be in all but the youngest samples, and agreement between ^{3}He and ^{10}Be in the youngest samples, supports this approach.

Discussion

Exposure Age Distribution

The distribution of ^{10}Be exposure ages on the four moraines is summarized in Fig. 3. The data show a tighter clustering than earlier work (Brook et al., 1993 [Chapter 4). Several outlying points are still apparent in the age distributions, however. In Taylor II and Taylor III there are outliers with both younger and older ages. These samples share several characteristics that suggest they could be rejected from mean age calculations. Apart from the age anomalies, all have significantly different $^{3}He/^{10}Be$ or $^{26}Al/^{10}Be$ ratios relative to other samples in each moraine (Table 1). These anomalous ratios could result from cosmic-ray exposure periods shorter or longer than the age of the moraine, perhaps due to post-depositional processes like boulders shifting on the moraine, surface spalling, or remobilization of older boulders by younger glacial advances. As discussed above, nucleogenic ^{26}Al, muogenic ^{3}He, and ^{3}He diffusion could also produce age anomalies. However, the older outlying ages in the Taylor II and III moraines are consistent with the ages for bulk of the samples in the next oldest deposit (Fig. 3), although note that the $^{26}Al/^{10}Be$ ratio for Taylor II sample

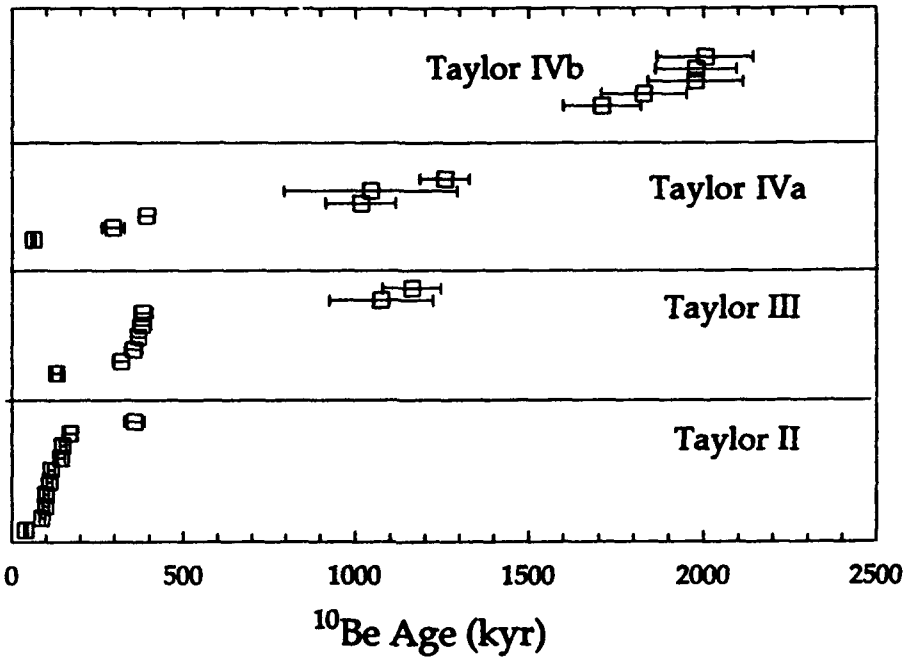

Figure 3. ^{10}Be age distribution for Arena Valley moraines. High outlying ^{10}Be ages in Taylor II and III are interpreted as remobilized or exposed boulders of the next oldest glacier advance (see text). Low ages have no definitive explanation but may be due to post-depositional fragmentation. In Taylor II and III the outlying ages all are for samples not specifically collected for this study, emphasizing the importance of sampling techniques in this application of cosmogenic nuclides. The low ages in Taylor IVa are believed to be a result of rock-falls from surrounding cliffs or complex exposure histories (see text). See Table 2 for age summary.

SCW87-4-1 (4.2±5.0) is lower than ratios for the Taylor III samples that have similar ^{10}Be exposure ages (6.7±0.7 to 8.0±0.7). Finally, note that all of the outlying points in Taylor II and Taylor III are from samples obtained during the beginning of this work, by field researchers without significant experience in sampling for exposure dating.

In Taylor IVa, where the moraine limit is more difficult to discern, there is a broader distribution of ages, with three anomalously low ages and three clustered old ages that have a mean of 1.1 ± 0.1 myr. Because the young ages are from samples collected just below steep sandstone and dolerite cliffs (KBA89-40, KBA89-47, and KBA89-95), these three samples may be rock-fall deposits, that came to rest at or near the Taylor IVa limit. This hypothesis does not immediately explain the low $^{26}Al/^{10}Be$ ratios observed for samples KBA89-45-1 and KBA89-41-2, although note that both analyses have fairly large uncertainties and the $^{26}Al/^{10}Be$ ratio for 45-1 is within 2-sigma of the concordance line in Fig. 2. As suggested above, the low ratios could be caused by complex exposure histories, e.g., exposure and burial, then re-exposure. In this context, KBA89-41-2 might be an older errratic boulder (from the Taylor IVb advance, for example) that was covered by Taylor IVa ice and drift. The two outlying ages in Taylor III support this idea, in that they may suggest the existence of 1 ~ 1.1 myr old moraine. The Taylor III moraine is a thin loop composed almost entirely of boulders deposited directly on the larger IVa sequence of moraines and drift (Marchant, 1990). The two outlying ages most likely represent IVa boulders that are exposed within the limit of the Taylor III advance, but were not recognized in the initial sampling (again, these earlier samples were not collected by our group).

The problems addressed above, particularly the outlying ages for samples collected at the beginning of this work, underscore the necessity of very careful field geology when sampling for exposure age dating. Specifically, during sample collection it was necessary to be aware of the morphology and positioning of boulders. Samples were collected from boulders perched solidly on other boulders in the moraine, primarily to avoid sampling older material exposed in "windows" in younger deposits. Care was also taken to avoid samples that showed any major signs of spalling or splitting of the surface and to collect from only flat upper surfaces. Through careful field geology the problems of outlying ages can be minimized, as suggested by the excellent ^{10}Be age agreement for the five Taylor II and five Taylor III samples (BAK90 and KBA89 samples) collected by our group for this work.

Arena Valley Glacial Chronology

Taylor II Moraine. The mean ages of the four deposits, both including and excluding the outliers discussed above, are tabulated in Table 2. The mean ^{10}Be age for Taylor II, the deposit with the most age information, is 122 ± 29 kyr (n=8) and the mean ^{3}He age is 134 ± 54 kyr. In previous work this deposit has been identified with marine oxygen isotope stage 5 (Denton et al., 1989a; Brook et al., 1993), although earlier it was assigned to stage 7 (Hendy et al., 1979). The stage 5 age is based on two related pieces of evidence. U-Th dates of *in situ* lake carbonate sediments interbedded in "Bonney Drift," a Taylor Glacier deposit down-valley of the present Taylor Glacier terminus in middle Taylor Valley (Hendy et al., 1979; Higgins, 1993), suggest growth of the Taylor Glacier at this time. The U-Th ages (70-120 kyr) span most of stage 5, although Higgins (1993) suggested, based on the distribution of U-Th ages in middle

Taylor Valley, that the maximum expansion happened during stage 5e (~ 120,000 kyr). The aerial distribution of Bonney Drift and apparently correlative deposits (based on weathering features and soil development) on the walls of Taylor Valley allow tentative physical correlation of Bonney Drift with the Taylor II moraines and Drift in Taylor Valley (Denton et al., 1989a). This correlation is complicated somewhat by the fact that Bonney Drift is difficult to separate from apparently older (possibly stage 7) deposits in middle Taylor Valley that may have been deposited at about the same level as Bonney Drift (Higgins, 1993; S. Higgins, personal communication, 1993). The exposure ages, however, suggest that the correlation of "Bonney Drift" in middle Taylor Valley with the Taylor II moraines is correct, and allows the Taylor II deposit to be used in reconstructions of the Taylor Glacier profile at this time (e.g., Denton et al., 1989a). In addition, the data show that the maximum expansion of Taylor Glacier in stage 5 happened during stage 5e, e.g., the last interglaciation (Fig. 4). Also plotted in Fig. 4 are ^{3}He exposure ages from Ross Sea Drift (Chapter 6), a glacial drift on the coast of McMurdo Sound that is believed to have been deposited by an expanded ice sheet in the Ross Sea at the last glacial maximum (Stuiver et al., 1981). Chapter 6 discusses these data in detail, but the fact that the ages of this deposit fall within the Wisconsin period strongly suggests that the conceptual model of Antarctic glaciation discussed above is valid.

In middle Taylor Valley, U-Th ages of 188-257 kyr for lacustrine carbonates suggest expansion of the Taylor Glacier during stage 7 (~200 kyr) (Hendy et al., 1979; Higgins, 1993). The aerial distribution of the dates suggests that the stage 7 advance was similar in magnitude (Higgins, 1993), or slightly smaller (Hendy et al., 1979) than the the stage 5 advance (Higgins,

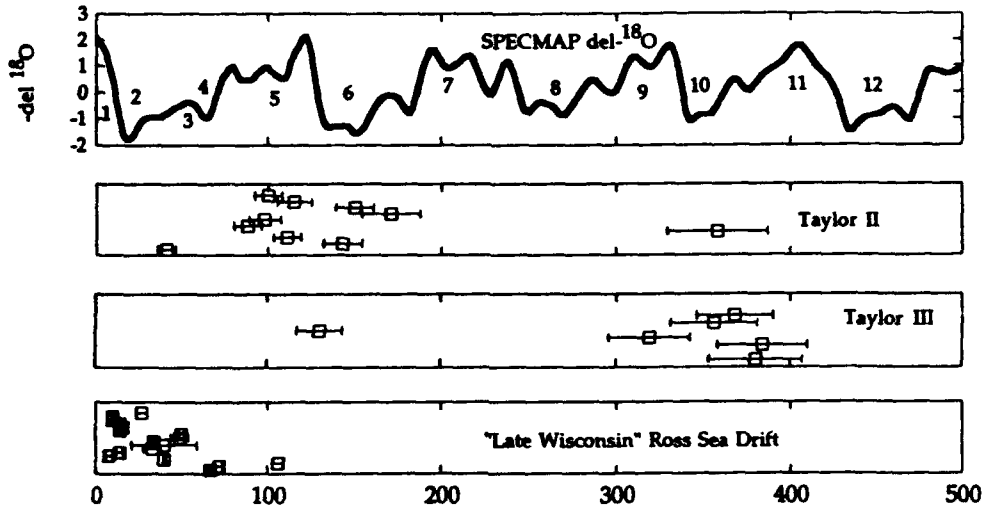

Figure 4. SPECMAP $\delta^{18}O$ curve (Imbrie et al., 1984) with labeled glacial and interglacial stages and ^{10}Be and ^{3}He exposure ages for Taylor II, Taylor III, and Ross Sea Drift (Chapter 6). The exposure age data are consistent with the suggestion that the Taylor II moraine in Arena Valley was deposited in interglacial stage 5. Assuming an interglacial origin for Taylor III, it may have been deposited in stage 11 (see text). Other evidence (Higgins et al., 1993) suggests that a stage 7 deposit, if it exists, is probably buried beneath the Taylor II ice. It is possible that stage 9 moraines are present in the valley but have not been recognized in existing mapping.

1993). The Arena Valley moraine samples came from the major morphological subdivisions of the Arena Valley moraines (Fig. 1). The exposure ages do not suggest that any of them correspond to a stage 7 advance (~ 200 kyr). This is consistent with the conclusion that the stage 7 advance was no larger than the stage 5 advance (Hendy et al., 1979; Higgins, 1993). The stage 7 deposits may be buried beneath the Taylor II drift in Arena Valley.

Taylor III. The Taylor III mean ^{10}Be age is 362 ± 26 kyr. Assuming that Taylor Glacier expands during interglacial periods this deposit could be assigned to isotope stage 9 (~300-350 kyr) or stage 11 (~270-440 kyr) (Fig. 4). Detrital carbonate clasts in middle Taylor Valley that may have been deposited during stage 9 range in age from 300-350 kyr (Higgins, 1979; Hendy et al., 1983). In addition, one *in situ* carbonate layer was dated at 300±50 kyr (Hendy et al., 1979). Older carbonate clasts found on the valley floor have ages of ~ 400 kyr, and may have been deposited during stage 11 (Higgins, 1993).

Based on the ^{10}Be ages, and the assumption that the Taylor Glacier expands during interglacial periods, Taylor III is assigned to isotope stage 11 here. Although the mean age actually falls within glacial stage 10 (~340 kyr), it is important to consider the effect of production rate uncertainties on these calculations. For example, only a 5% decrease in the ^{10}Be production rate would be required to shift the Taylor III mean age to ~ 380 kyr, where it would fall in stage 11. This change would not change the conclusions about the age of Taylor II or the younger Ross Sea Drift ages (Chapter 6) displayed in Fig. 4, and it is well within the estimates of 15% systematic uncertainty in production rates calculated in Chapter 1. Erosion corrections to the exposure ages (Brown et al., 1991) would also increase the ages slightly. Previous

estimates of erosion rates in the Dry Valleys, based on ^{10}Be and ^{26}Al, suggest that erosion rates in Arena Valley are at maximum 1-2 x 10^{-5} g cm^{-2} yr^{-1} (5-10 cm/myr). Assuming an erosion rate of 1 x 10^{-5} g cm^{-2} yr^{-1} (~ 5 cm/myr), a 360 kyr ^{10}Be exposure age would increased to ~ 370 kyr (eq. 1), but this correction would not change the Taylor II ages appreciably. These corrections are not made to the individual ages because uncertainties in calculated erosion rates are quite large, on the order of 100 % (Brook et al., 1993) [Chapter 4].

The assumption of an interglacial origin can be questioned given the uncertainties in the exposure ages. However, the combination of the ^{3}He exposure ages for Ros Sea Drift (Chapter 6 and Fig. 4) and the Taylor II data described above support the conceptual model suggesting that the East Antarctic Ice Sheet fluctuates "out of phase" with northern hemisphere glaciation and aerial expansions of the Ross Sea Ice Sheet. Further exposure dating in the Arena Valley sequence can be used to test the exposure ages for Taylor III. The mapped Taylor III moraines include two loops (Fig. 1) and only the outermost one was sampled, assuming, based on weathering and soil development, that the two are the same age (Marchant, 1990; Bockheim 1982). These methods are not sensitive enough to resolve stages 9 and 11 and it is possible that the inner loop represents a later glacial advance. Based on the results presented here, ^{10}Be and ^{26}Al exposure dating could provide relative age information that could evaluate this hypothesis, although present uncertainties in production rates may limit the accuracy of absolute ages and absolute correlation with the marine isotope record.

Taylor IVa and IVb. The Taylor IVa exposure dates suggest an age of 1.1± 0.1 myr. It is not possible to place this deposit in the context of the oxygen isotope record, which shows reduced power at the 100 kyr frequency before the

Bruhnes-Matuyama boundary (~ 800 kyr) (Ruddiman et al., 1989). The behavior of the Taylor Glacier system at this time may have been controlled by tectonic activity in the area rather than climatic events. The significance of the extensive Taylor IVa moraines and drift may be that they represent a relatively stable glacial system during the time of their deposition. Their altitude range (~1100-1200m) may reflect slight changes in the Taylor Glacier mass balance during that time period and/or gradual uplift of the region of ~ 100 m over the last 1-2 myr. The latter conclusion is consistent with the maximum uplift estimates of Wilch et al. (1993) based on the distribution Taylor Valley volcanic deposits (however, see discussion of uplift below). The mean age for the Taylor IVb moraine is 1.9 ± 0.1 myr and all samples (n=5) give essentially the same age. This age is a minimum age due to the effects of erosion (eq. 2). Again assuming an erosion rate of 1 x 10^{-5} g cm^{-2} (5 cm/myr), the erosion corrected age for Taylor IVb is 2.1 ± 0.1 myr. As suggested previously, these old ages indicate that the Taylor Glacier system was near its present configuration throughout much of the Quaternary and late Pliocene, arguing against a rapidly changing Antarctic ice sheet during this time period. Taylor IVb is also significant in that it is the oldest deposit in the valley that shows definitive signs of deposition by cold-based ice (Marchant et al., in press). The Taylor Glacier today is frozen to its bed near Arena Valley (Robinson. 1984), and the exposure ages of the four moraines provide evidence that climatic conditions similar to those of the present day may have persisted in Arena Valley throughout much of the last 2.1 myr.

Uplift History of the Transantarctic Mountains and Age of the Sirius Group

Discovery of Nothofagus sp. wood and late Pliocene diatoms in Sirius Group tills near the Beardmore Glacier (several hundred miles south of

McMurdo Sound) have led to the controversial suggestion that as much as 2.5 kilometers of uplift occured in parts of the Transantarctic Mountains (TAM) in the last 2-3 myr (Webb et al., 1984; McKelvey et al., 1991). This amount of tectonic activity is not supported by geophysical evidence (ten Brink et al., 1993). Furthermore, in the Dry Valleys-McMurdo Sound region the altitudinal distribution of subaerial volcanic cones suggests a maximum of 100 m of uplift in the last 2 myr (Wilch et al., 1993). The suggested high uplift rates based on the Sirius Group biostratigraphy are controversial (Clapperton and Sugden, 1990). If correct, however, the suggested high uplift rate has important climatic implications. This controversy is also part of a larger argument about the origin of the Sirius Group. It has been suggested that the diatoms and marine sediment found in Sirius Group tills originated in an inland sea in the Wilkes and Pensacola Basins in East Antarctica, implying significant deglaciation in the late Pliocene (Webb and Harwood, 1991). This controversy therefore has important implications for understanding mid-late Pliocene climate and Antarctic ice dynamics, particularly the question of possible Pliocene collapse of the Antarctic Ice Sheets (Clapperton and Sugden, 1990; Webb and Harwood, 1991; McKelvey et al., 1991; ten Brink et al., 1993; Marchant, 1993; Barret et al., 1993; Wilch et al., 1993).

The concentration of a cosmogenic nuclide in a surface rock depends on uplift through the altitude dependence of the production rate, which can be approximated by an exponential dependence on atmospheric pressure. Following Brown et al. (1991) this relationship is:

$$N = \frac{P_{sl}}{(U/L + \lambda)}(e^{tU/L} - e^{-\lambda t}) \qquad (3),$$

where U is uplift rate in g cm^{-2} yr^{-1}, L is the exponential attenuation length of the production rate in the atmosphere, P is the sea level production rate, and λ is the decay constant. This equation is an approximation in that the commonly used relationship between production rate and altitude is not a simple exponential function of atmospheric depth (Lal, 1991). The altitude-production rate relationship for ^{10}Be and ^{26}Al rate is well approximated (within 1-2 %) by an L of 145 g cm^{-2}, however. The relationship between nuclide concentration and uplift can be used to constrain uplift by comparing measured concentrations of the nuclide of interest to concentrations predicted by an uplift model (Fig. 5). To model the suggested high uplift rates based on the Sirius Group ages a linear uplift rate of 0.43 m/kyr was assumed, based on the conclusion of McKelvey et al. (1990) that the Beardmore Glacier region has been uplifted at least 1300 m in the last 3 myr. Model results were compared to the measured concentrations of ^{26}Al and ^{10}Be in the Sirius Group and Quartermain Drift samples (Table 3).

Assuming that the Sirius Group samples on Mt. Fleming were deposited 3 myr ago, as suggested by some interpretations of the paleobiological evidence (Mckelvey et al., 1991; Webb and Harwood, 1991), and uplifted 1300m, then their altitude at deposition was 765 m. If they were initially exposed at that time they should have final concentrations of ^{10}Be and ^{26}Al of 34 and 133 Mat/g (Table 3) if they experienced the model uplift rate. Assuming Quartermain Drift and Altar Diamicton, based on volcanic ash dates and glacial stratigraphy (Marchant, 1990) predate the Sirius Group, then they, according to the model, must have been uplifted from near or below sea level. Predicted concentrations based on this scenario are also lower than measured concentrations (Table 3). Both deposits may have been

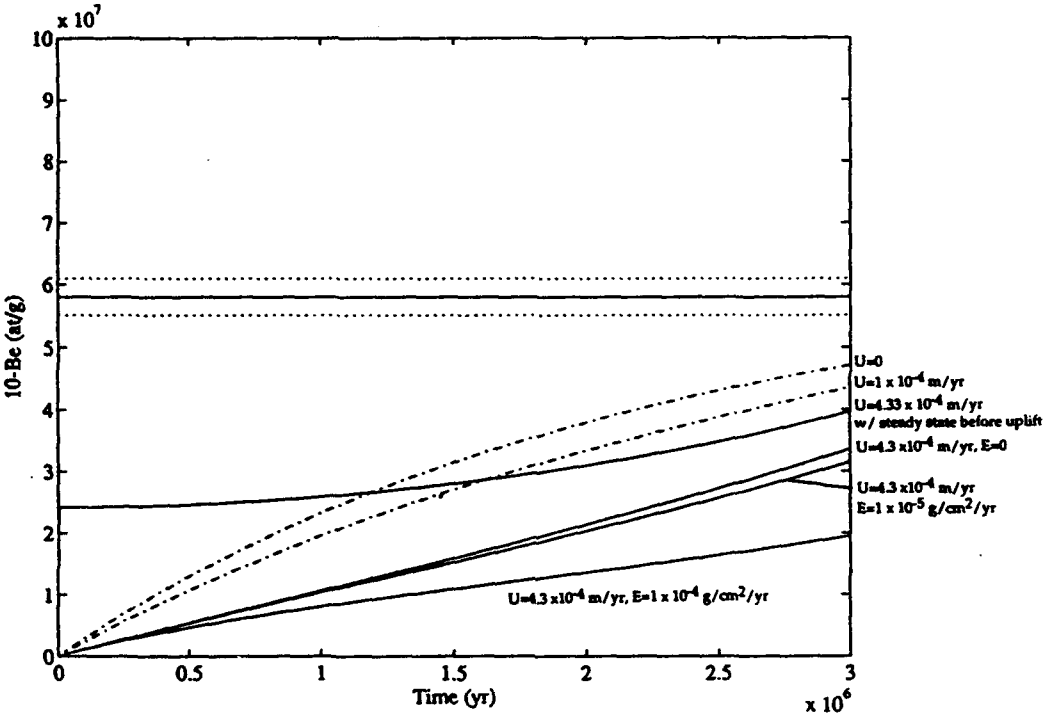

Figure 5. Example of uplift model for sample BAK90-32 (see Table 3) after Brown et al. (1991). The dotted curves show the relationship between ^{10}Be concentration and time for a sample undergoing uplift at a rate of 4.33 x 10^{-4} m/yr (1300m in 3 myr) from exposure at 765 m to the present altitude of 2065 m, at erosion rates of 0, 1x 10^{-5}, and 1x 10^{-4} g cm^{-2} yr^{-1} (from top to bottom). The solid horizontal line indicates the measured ^{10}Be concentration of the sample and ± 5 % analytical error. The solid curve uses the same uplift model but assumes that the sample was at steady state with respect to ^{10}Be production before uplift. The other two curves on the figure correspond to uplift at 100m/myr and no uplift. The analysis suggests that the suggested uplift rates based on the Sirius Group biostratigraphy are too high because it is not possible to reach the measured concentration in the given amount of time (see text for further discussion).

exposed to cosmic rays before uplift, but even if the samples were at steady state with respect to ^{10}Be and ^{26}Al production at that point the model concentrations after uplift are not significantly higher (Table 3; Fig. 5). In this analysis it is not possible to separate the effects of erosion and uplift because they both cause a decrease in concentration relative to continuous exposure at the present altitude with no erosion. However, the fact that in most cases the observed concentrations are significantly higher than predicted indicates that the model uplift rate is too high. The low measured concentration for KBA89-107 is probably a result of recent exhumation of this sample (Brook et al., 1993 [Chapter 4]).

A number of studies in the TAM have suggested much lower uplift rates, ~ 100 m/myr (Gleadow and Fitzgerald, 1987; Wilch et al., 1993). Modeling uplift of 100 m/myr in the same fashion as the higher rate (Fig. 5) shows that ^{10}Be data are not even consistent with this lower uplift rate. In fact, the model curve for no uplift shows that even in this situation the measured concentration is not reached in 3 myr. Accepting the production rates as accurate, this analysis suggests that the Sirius Group deposits are older than 3 myr. The ^{10}Be age for the Sirius Group sample BAK90-32-1, assuming no elevation change and no erosion, is 4.0 (-.6/+.8.) myr (Table 1) (1-sigma analytical uncertainty only). A correction for an erosion rate of 1 x 10^{-5} g cm^{-2} yr^{-1} would increase the age to ~ 4.7 myr. However, because the ^{10}Be concentration of this sample is near steady-state, production rate uncertainties cause large uncertainties in the age calculation. For example, including a 15 % uncertainty in the production rate (Chapter 1) gives an exposure age of 4.0 (-1.3/+3.5) myr and an erosion corrected age of 4.7 (-1.5/+4.1) myr. The discrepancy between the 3 myr age based on diatom

stratigraphy and older suggested ages for the Sirius Group has been discussed at length elsewhere (Clapperton and Sugden, 1991; Marchant et al., 1993). Perhaps the most promising potential resolution of the problem is the suggestion that the diatoms are allocthonous, perhaps due to transport and deposition by wind after deposition of the Sirius Group (Marchant et al., in press).

Conclusions

1) Exposure ages for the Taylor II moraines (mean ^{10}Be age of 122 ± 29 kyr) in Arena Valley suggest deposition in isotope stages 5e (~120 kyr). This conclusion is consistent with previous suggestions that East Antarctic outlet glaciers expand during interglacial periods due to increased precipitation in East Antarctica during relatively warmer climates. Stage 7 deposits, if present, are probably buried beneath the stage 5 deposits, suggesting that the stage 7 advance was limited in extent. The Taylor III moraine in Arena Valley has a mean ^{10}Be exposure age of 362 ± 26 kyr. If this moraine was deposited during an interglacial period it most likely represents deposition during stage 11. The fact that the relative exposure ages for these moraines cluster in distinct groups suggests that future work of this type can provide a correlation tool for mapping the response of the East Antarctic Ice Sheet throughout the Transantarctic Mountains to changing climate conditions.

2) Prior to the deposition of the Taylor III moraines, two deposits, Taylor IVa and Taylor IVb, were deposited at 1.1 and 2.1 myr, respectively. They can not be placed in the context of the marine oxygne isotope record with confidence based on the exposure ages. Given the low amplitude of the marine $\delta^{18}O$

record during this time, suggesting relatively small oscillations in global temperatures and northern hemisphere ice volume, they may simply reflect small fluctuations in the ice sheet, perhaps combined with gradual uplift of < 100 m/myr. The presence of these moraines, which appear to have been deposited by a cold-based lobe of the Taylor Glacier, however, indicates that the late-Pliocene-Pleistocene climate in Arena Valley was not significantly different than today.

Implications for the behavior of the East Antarctic Ice Sheet from the data presented here and from other studies of the Dry Valleys region depend on the physical link between the Taylor Glacier and the rest of the East Antarctic Ice Sheet. The Taylor Glacier is fed by ice from the McMurdo Dome, a small peripheral dome on the edge of the larger Dome C. The interpretation presented here relies on the inference of a link between the history of McMurdo Dome fluctuations and the dynamics of the rest of the ice sheet (e.g., Denton et al., 1989a). It has been suggested that local precipitation and temperature changes also influence the behavior of the McMurdo Dome and related outlet glaciers, however (Drewry, 1982). If this influence is important, the data presented here still have climatic significance, but their link to the behavior of the whole of the ice sheet may be complex. Exposure dating in other parts of Antarctica, and new ice core drilling on the McMurdo Dome, may help to resolve this question.

3) Combined ^{10}Be, ^{26}Al, and ^{3}He measurements on the same quartz samples from Arena Valley glacial deposits indicate significant loss of ^{3}He from quartz in samples older than ~ 200 kyr. General agreement between ^{3}He and ^{10}Be ages < 200 kyr suggests that ^{3}He is retained well in most cases in this age range in Antarctic quartz. Elevated $^{26}Al/^{10}Be$ ratios in some of these young

samples indicate a complication in using cosmogenic ^{26}Al for exposure chronology. These elevated ratios may be a result of nucleogenic production of ^{26}Al from the reaction $^{23}Na(a,n)^{26}Al$. Further work is necessary to allow a correction for this effect.

4) ^{10}Be and ^{26}Al concentrations in samples from Quartermain and Altar Drift in Arena Valley and from the Sirius Group on Mt. Feather are inconsistent with suggested uplift of the Transantarctic Mountains of over 1300m in the last 3 myr (McKelvey et al., 1991). The data suggest that even with no uplift, Sirius Group deposits in the McMurdo Sound region may be older than ages of 3 myr suggested by biostratigraphic evidence. ^{10}Be ages calculated assuming no uplift give a minimum age for the Sirius Goup samples of 4.0 (-1.3/+3.5) myr and an erosion corrected age of 4.7 (-1.5/+4.1) myr. Because the ^{10}Be concentrations are probably near steady state, measurements of a well-retained stable nuclide like ^{21}Ne are necessary to further constrain the age of these deposits.

Table 1. ^{3}He, ^{10}Be, and ^{26}Al data. All concentrations in Mat/g. ^{10}Be exposure ages calculated as described in text. Size fraction code (Sz) for ^{3}He: 1=0.5-1mm grains. 2=1-2 mm grains. Note that analytical errors only are propagated in age calculations. ^{10}Be and ^{26}Al data in bold were originally reported in Brown et al. (1991). All other data are from Brook et al. (1993) [Chapter 4] or are previously unreported (in italics). Details of helium isotopic measurements for the latter are reported in the appendix to this chapter.

Sample	Sz	Alt. (m)	^{3}He	1s	^{10}Be	1s	^{26}Al	1s	$^{3}He/^{10}Be$	1s	$^{26}Al/^{10}Be$	1s	^{10}Be Age (kyr)	1s-	1s+
Taylor II															
SCW87-4-1	1	1100	54.02	3.81	5.17	0.42	21.84	1.79	10.45	1.13	4.22	0.49	359	32	32
KBA89-102	1	1140	36.05	0.98	1.80	0.16	12.27	1.04	19.98	1.86	6.80	0.84	115	10	11
KBA89-70-1	1	1120	80.73	6.19	1.72	0.12			46.96	4.81			111	8	8
KBA89-96	1	1150	49.43	2.55	2.26	0.17			21.89	1.99			144	11	11
BW84-87	1	1100	33.92	3.30	0.64	0.07	9.91	1.16	52.73	7.93	15.41	2.53	42	5	5
KBA89-99	1	1090	30.32	2.23	1.49	0.14			20.31	2.42			99	9	9
KBA89-97	1	1090	54.36	16.49	2.56	0.25			21.25	6.78			172	18	18
KBA89-66-1	1	1110	23.39	0.41	1.54	0.12	10.95	0.81	15.14	1.22	7.09	0.77	100	18	18
KBA89-67	1	1110	47.61	2.30	2.28	0.16	16.98	1.20	20.87	1.81	7.44	0.75	150	11	11
KBA89-68	1	1110	34.12	0.52	1.36	0.12	10.74	1.30	25.08	2.24	7.89	1.18	88	8	8
KBA89-69	1	1110	29.83	1.07											
Taylor III															
KBA89-50	1	1130	42.89	2.08	5.58	0.40	37.47	2.46	7.68	0.66	6.71	0.65	381	29	30
KBA89-105	2	1110	114.89	0.90	5.34	0.32	40.52	2.41	21.51	1.28	7.59	0.64	369	24	24
KBA89-103	1	1160	89.12	0.93	5.77	0.39	38.56	2.51	15.44	1.05	6.68	0.63	385	28	29
SCW87-5	1	1150	280.58	4.83	14.66	1.05			19.14	1.42			1167	109	114
KBA89-52	1	1130	89.10	7.06	5.26	0.37	39.67	2.75	16.92	1.80	7.53	0.75	357	27	28
BW84-134	1	1150	71.25	1.45	2.05	0.21	37.08	4.42	34.69	3.54	18.05	2.81	130	13	13
BW84-33	1	1150	81.56	2.50	13.81	1.91	75.66	10.52	5.90	0.84	5.48	1.07	1080	186	203
KBA89-104	2	1150	130.12	3.49	4.84	0.34	38.66	2.34	26.91	2.03	8.00	0.74	320	24	24
Taylor IVa															
KBA89-45-1	1	1160	172.49	2.93	13.61	3.24	26.90	19.05	12.68	3.03	1.98	1.48	1048	300	348
KBA89-47-1	1	1160	203.92	6.98											
KBA89-47-2	1	1160	186.11	2.25	13.30	0.74	76.40	4.75	13.99	0.80	5.74	0.48	1018	71	74
KBA89-41-2	1	1170	77.73	2.33	4.57	0.51	9.54	4.26	17.01	1.96	2.09	0.96	296	35	36
KBA89-40-1	1	1170	34.15	3.05	1.00	0.08	9.72	0.68	34.01	4.16	9.68	1.05	62	5	5
KBA89-95	2	1150	141.30	4.91	5.86	0.35			24.13	1.67			394	26	26
KBA89-94	2	1140	247.56	78.46	15.41	0.88	84.84	4.72	16.07	5.17	5.51	0.44	1261	96	100
Taylor IVb															
SCW87-3-1	1	1600	780.36	7.18	28.37	1.89			27.50	1.85			1839	185	202
KBA89-25	2	1320	522.77	9.01	24.07	1.41	109.66	10.13	21.72	1.33	4.56	0.50	1981	182	199
KBA89-19	1	1260	430.46	3.73											
KBA89-19	2	1260	575.50	9.57											
AA86-14	1	1550	500.31	2.69	28.67	1.97			17.45	1.20			1985	213	236
AA86-15	1	1600	796.53	4.38	27.11	1.75			29.38	1.90			1714	162	175
BW84-105	1	1300	530.45	57.43	23.92	1.65	103.51	12.47	22.18	2.85	4.33	0.60	2011	218	242
Quartermain Drift															
SCW87-1-2	1	1400	1262.28	13.60											
SCW87-1-1	1	1400	615.78	4.67	30.62	2.17			20.11	1.43			2738	358	429
KBA89-108	1	1250	672.61	98.45	34.64	1.87	119.59	6.78	19.42	3.03	3.45	0.27	5237	951	1737
KBA89-107	1	1320	183.24	26.91	22.37	1.21	143.31	18.45	8.19	1.28	6.41	0.89	1764	142	152
Sirius Formation															
BAK90-32	2	2065	1790.29	18.92	50.75	2.69	192.36	11.97	35.28	1.91	3.79	0.31	2864	295	342
BAK90-32-1	2	2065	462.41	4.79	58.01	3.41	195.43	19.44	7.97	0.48	3.37	0.39	3950	577	790
Altar Drift															
BAK90-77	2	2065			47.12	2.50	154.34	9.91			3.28	.27	4424	660	954
BAK90-73-1	2	1720			42.97	2.32	141.20	11.25			3.29	0.32	3419	410	506

Table 2. Mean ^{10}Be and ^{3}He ages for Arena Valley moraines in kyr. Ages were calculated using production rates described in text. Adjusted mean is calculated after rejecting outlying points.

Moraine	^{10}Be	1s	n	^{3}He	1s
Taylor II					
mean	138	86	10	134	50
adjusted mean	122	29	8	134	54
Taylor III					
mean	524	380	8		
adjusted mean	362	26	5		
Taylor IVa					
mean	680	490	6		
adjusted mean	1109	132	3		
Taylor IVb					
mean	1906	127	5		

Table 3. Comparison of measured concentrations of ^{10}Be and ^{26}Al in Sirius Group and other old glacial deposits in the Dry Valleys with uplift model calculations. The fact that measured concentrations are higher than predicted concentrations in almost all cases suggests that suggested uplift rates based on Sirius Group biostratigraphy are too high (see text). Measured concentrations are from Table 1 and the uplift model is described further in the text.

Sample	Alt. (m)	Meas. Conc. (Mat/g)		Predicted Concentrations (Mat/g) No Prev. Exp.		Steady State Before Uplift	
		^{10}Be	^{26}Al	^{10}Be	^{26}Al	^{10}Be	^{26}Al
Sirius Group							
Assumptions: Uplift rate=4.33 x 10^{-4} m/yr. Age of deposit=3 x 10^{6} yr. Original altitude=(present altitude-1300m). Erosion Rate=0.							
BAK90-32	2065	51±3	192±12	34	133	400	144
BAK90-32-1	2065	58±3	195±19	34	133		
Quartermain and Altar Drift							
Assumptions: Uplift rate=4.33 x 10^{-4} m/yr. Age of deposit given by (altitude/uplift rate), e.g., predicted time that surface was at sea level. Original altitude=0 m. Erosion Rate = 0.							
SCW87-1-1	1400	31±2			21		24
KBA89-108	1250	35±2	120±7	18	73	12	79
KBA89-107	1320	22±1	143±18	19	77	23	83
BAK90-73-1	1720	43±2	141±11	27	105	50	112

References

Barrett, P. J., Adams, C. J., McIntosh, W. C., Swisher, III, C. C., and Wilson, G. S (1993). Geochronological evidence supporting Antarctic deglaciation three million years ago. *Nature* **359**, 816-818.

Bockheim, J. G. (1982). Properties of a chronosequence of ultraxerous soils in the Trans-Antarctic Mountains. *Geoderma* **28**, 239-255.

Bockheim, J. G., Wilson, S. C., Denton, G. H., Anderson, B. G., and Stuiver, M. (1989). Late Quaternary fluctuations of Hatherton Glacier, Transantarctic Mountains. *Quaternary Research* **31**, 229-254.

Brook, E. J., and Kurz, M. D. (1993). Surface exposure chronology using *in situ* cosmogenic ^{3}He in Antarctic quartz sandstone boulders. *Quaternary Research* **39**, 1-10.

Brook, E. J., Kurz, M. D., Ackert, R. P., Denton, G. H., Brown, E. T., Raisbeck, G. M., and Yiou, F. (1993). Chronology of Taylor Glacier Advances in Arena Valley, Antarctica, using *in situ* cosmogenic ^{3}He and ^{10}Be. *Quaternary Research* **39**, 11-23.

Brown, E., Edmond, J. M., Raisbeck, G. M., Yiou, F., Kurz, M., and Brook, E. J. (1991). Examination of surface exposure ages of Antarctic moraines using in-situ produced ^{10}Be and ^{26}Al. *Geochimica et Cosmochimica Acta* **55**, 2269-2283.

Brown, E. T., Brook, E. J., Raisbeck, G. M., Yiou, F., and Kurz, M. D. (1992). Effective attenuation lengths of cosmic rays producing ^{10}Be and ^{26}Al in quartz: Implications for exposure dating. *Geophysical Research Letters* **19**(4), 367-372.

Clapperton, C. M., and Sugden, D. E. (1991). Late Cenozoic glacial history of the Ross Embayment, Antarctica. *Quaternary Science Reviews* **9**(2/3), 253-272.

Clayton-Greene, J. M., Hendy, C. H., and Hogg, A. G. (1988). Chronology of a Wisconsin age proglacial lake in the Miers Valley, Antarctica. *New Zealand Journal of Geology and Geophysics* **31**, 353-361.

Dagel, M. A., Hendy, C. H., Denton, G. H., Stuiver, M. and Judd, F. M. (1993). Stratigraphy and chronology of isotope stage 6 and 2 drift, Marshall Valley, Antarctica. *Boreas*, in press.

Denton, G. H., Bockheim, J. G., Wilson, S. C., and Stuiver, M. (1989a). Late Wisconsin and early Holocene glacial history, inner Ross Embayment, Antarctica. *Quaternary Research* **31**, 151-182.

Denton, G. H., Bockheim, J. G., Wilson, S. C., and Leide, J. E. (1989b). Late Quaternary ice-surface fluctuations of Beardmore Glacier, Transantarctic Mountains. *Quaternary Research* **31**, 183-209.

Drewery, D. J. (1982). Ice flow, bedrock, and geothermal studies from radio-echo sounding inland of McMurdo Sound, Antarctica. In *Antarctic Geoscience* (Craddock, C., Ed.). University of Wisconsin Press, Madison, Wisconsin.

Fastook, J. L. (1984). West Antarctica, the sea-level controlled marine instability: past and future. In *Climate Processes and Climate Sensitivity, AGU Geophysical Monograph 29* (Hansen, J. E., and Takahashi, T., Eds.), pp. 275-287, American Geophysical Union, Washington, D.C.

Gleadow, A. J. W., and Fitzgerald, P. G. (1987). Uplift history and structure of the Transantarctic Mountains: new evidence from fission track dating of basement apatites in the Dry Valleys area, southern Victoria Land. *Earth and Planetary Science Letters* **82**, 1-14.

Hendy, C. H., Healy, T. H., Rayner, E. M., Shaw, J., and Wilson, A. T. (1979). Late Pleistocene glacial chronology of the Taylor Valley, Antarctica, and the global climate. *Quaternary Research* **11**, 172-184

Higgins, S. (1993). The glacial geology, geomorphology, and chronology of Bonney Drift, southern Victoria Land, Antarctica: Evidence for late Quaternary expansions of the east Antarctic Ice Sheet during interglacial stages 7, 7, and 9. M.S. Thesis, University of Maine, Orono, Maine.

Hollin, J. T. (1962). On the glacial history of Antarctica. *Journal of Glaciology* **4**, 173-195.

Imbrie, J., Hays, J. D., Martinson, D. G., McIntyre, A., Mix, A. C., Morley, J. J., Pisias, N. G., Prell, W. L., and Shackleton, N. J. (1982). The orbital theory of Pleistocene climate: support from a revised chronology of the marine $\delta^{18}O$ record. In *Milankovitch and Climate* (Berger, A., Imbrie, J., Hays, J., Kukla, G., and Saltzman, B., Eds.) D. Reidel, Boston.

Jouzel, J., Lorius, C., Petit, J. R., Barkov, N. I., Kotlyakov, V. M., and Petrov, V. M. (1987). Vostok Ice Core: a continuous record of isotope temperature record over the last climate cycle (160,000 years). *Nature* **329**, 403-408.

Jouzel, J., Petit, J. R., and Raynaud, D. (1990). Palaeoclimatic information from ice cores. *Transactions of the Royal Society of Eninburgh* **81**, 349-355.

Jouzel, J., Raisbeck, G., Benoist, J. P., Yiou, F., Lorius, C., Raynaud, D., Petit, J. R., Korotkevitch, Y. S., and Kotlyakov, V. M. (1989). A comparison of deep Antarctic ice cores and their implications for climate between 65,000 and 15,000 years ago. *Quaternary Research* **31**, 135-150.

Klein, J., Giegengack, R., Middleton, R., Sharma, P., Underwood, J., and Weeks, R. (1986). Revealing histories of exposure using ^{26}Al and ^{10}Be in Libyan desert glass. *Radiocarbon* **28**(2A), 547-555.

Kurz, M. D., and Brook, E. J. (1993). Surface exposure dating with cosmogenic nuclides (1993). In *Dating in a Surface Context* (Beck, C., Ed.), University of New Mexico Press, in press.

Lal, D. (1991). Cosmic ray labeling of erosion surfaces: In situ nuclide production rates and erosion models. *Earth and Planetary Science Letters* **104**, 424-439.

Marchant, D. (1990). Surficial geology and stratigraphy in Arena Valley, Antarctica: Implications for Antarctic Tertiary glacial history. M.S. Thesis, University of Maine, Orono, ME.

Marchant, D. R., Denton, G. H., Bockheim, J. G., and Wilson, S. C. (1993). Late Neogene Taylor Glacier fluctuations: implications for Antarctic paleoclimate and ice-sheet dynamics. *Boreas*, in press.

McElroy, C. T., and Rose, G. (1987). *Geology of the Beacon Heights Area: Southern Victoria Land, Antarctica.* New Zealand Geological Survey Miscellaneous Map Series Map 15, DSIR, Wellington, New Zealand.

McKelvey, B. C., Webb, P. N., Harwood, D. M., and Mabin, M. C. G. (1990). The Dominion Range Sirius Group: a record of the late Pliocene-early Pleistocene Beardmore Glacier. In *Geological Evolution of Antarctica* (Thomson, M. R. A., Crame, J. A., and Thomson, J. W., Eds.), pp. 675-682, Cambridge University Press, New York.

Morrison, P., and Pine, J. (1955). Radiogenic origin of the helium isotopes in rock. *Annals of the New York Academy of Sciences* **62**, 71-92.

Nishiizumi, K., Winterer, E. L., Kohl, C. P., Klein, J., Middleton, R., Lal, D., and Arnold, J. R. (1989). Cosmic ray production rates of ^{10}Be and ^{26}Al in quartz from glacially polished rocks. *Journal of Geophysical Research* **94**(B12), 17,907-17,915.

Nishiizumi, K., Kohl, C. P., Arnold, J. R., Klein, J., Fink, D., and Middleton, R. (1991). Cosmic ray produced ^{10}Be and ^{26}Al in Antarctic rocks: exposure and erosion rates. *Earth and Planetary Science Letters* **104**, 440-454.

Raisbeck, G. M., Yiou, F., Bourles, D., Lorius, C., Jouzel, J., and Barkov, N. I. (1987). Evidence for two intervals of enhanced ^{10}Be deposition in Antarctic ice during the last glacial period. *Nature* **326**, 825-826.

Robinson, P. H. (1984). Ice dynamics and thermal regime of Taylor Glacier, south Victoria Land, Antarctica. *Journal of Glaciology* **30**(105), 153-160.

Ruddiman, W. F., Raymo, M. E., Martinson, D. G., Clement, B. M., and Backman, J. (1989). Pleistocene evolution: northern hemisphere ice sheets and North Atlantic Ocean. *Paleoceanography* **4**(4), 353-412.

Sharma, P., and Middleton, R. (1989). Radiogenic production of ^{10}Be and ^{26}Al in uranium and thorium ores: implications for studying terrestrial samples containing low levels of ^{10}Be and ^{26}Al. *Geochimica et Cosmochimica Acta* **53**, 709-716.

Steed, R. H. N., and Drewry, D. J. (1982). Radio-echo sounding investigations of Wilkes Land, Antarctica. In *Antarctic Geoscience* (Craddock, C., Ed.), pp. 969-975, University of Wisconsin Press, Madison, WI.

Stuiver, M., Denton, G. H., Hughes, T. J., and Fastook, J. L. (1981). History of the marine ice sheet in West Antarctica during the last glaciation, a working hypothesis. In *The Last Great Ice Sheets* (Denton, G. H., and Hughes, T. J., Eds.), pp. 319-436, Wiley-Interscience, New York.

ten Brink, U. S., Bannister, S., Beaudoin, B. C., and Stern, T. A. (1993). Geophysical investigations of the tectonic boundary between east and west Antarctica. *Science* **261**, 45-50.

Trull, T. W., Kurz, M. D., and Jenkins, W. J. (1991). Diffusion of cosmogenic ^{3}He in olivine and quartz: implications for surface exposure dating. *Earth and Planetary Science Letters* **103**, 241-256.

Webb, P.-N., and Harwood, D. M. (1991). Late Cenozoic glacial history of the Ross Embayment, Antarctica. *Quaternary Science Reviews* **10**, pp. 215-223.

Webb, P. N., Harwood, D. M., McKelvey, B. C., Mercer, J. H., and Stott, L. D. (1984). Cenozoic marine sedimentation and ice volume variation on the Antarctic Craton. *Geology* **12**, 287-291.

Wilch, T. I., Lux, D. R., Denton, G. H., McIntosh, W. C. (1993). Plio-Pleistocene uplift of the McMurdo Dry Valley Sector of the Transantarctic Mountains: a key parameter in ice-sheet reconstructions. *Geology* **21**, 841-844.

Yiou, F., Raisbeck, G. M., Bourles, D., Lorius, C ., and Barkov, N. L. (1985). ^{10}Be in ice at Vostok, Antarctica, during the last climatic cycle. *Nature* **316**, 616-617.

Appendix

Previously unpublished ^4He concentrations and $^3He/^4He$ ratios for samples described in Chapter 5. All four Taylor II samples are whole grains in 0.5-1mm size fraction and 0-3 cm depth in rock. BAK90 samples are 1-2 mm chips from quartzite cobbles. All other helium isotopic data for samples discussed in Chapter 5 can be found in Chapters 3 and 4.

	^4He ($\mu cc\ g^{-1}$)	1s	$^3He/^4He$ (R/R_a)	1s	^3He ($Matg^{-1}$)	1s
Taylor II						
KBA89-66-1	93.4	0.02	0.67	0.01	23.2	0.4
KBA89-67	3.02	0.03	0.43	0.02	47.8	2.2
KBA89-68	67.5	0.01	1.34	0.02	33.6	0.5
KBA89-69	31.9	0.02	2.47	0.09	29.3	0.1
Sirius Group						
BAK90-32	0.15	0.01	319.13	3.23	1750	18.5
BAK90-32-1	0.20	0.01	62.17	.63	452	4.68

Sample Descriptions for samples not described in Brook et al. (1993) [Chapter 4].

KBA89-66-1

Taylor II sandstone boulder near central axis of valley. Fine-medium grained sandstone, 2m x 2m x 1m thick. Perched on other boulders on moraine. Sample from top corner of top surface of boulder.

KBA89-67

Fine-medium grained tabular shaped Taylor II sandstone boulder on crest of moraine 5 m east of KBA89-66. 1m high x 0.6 m long and wide.

KBA89-68

Taylor II sandstone, finely bedded with interbedded coarse and fine layers. Irregular shaped boulder, ~ 0.5 m high x 1 m long and wide. Surface is inclided 45 degrees to horizontal, sample comes from top upper corner.

KBA89-69

Small, 0.5 m wide x 1 m high x 0.5 m long, fine-medium grained sandstone boulder in Taylor II moraine. Brown, weathered surface dipping at 25°. Collected sample from top, upper corner.

BAK90-32

Coarse grained sandstone boulder on Sirius Group till surface at Mt. Fleming. 40 cm long x 20 cm wide x 10 cm high. Collected sample from top surface.

BAK90-32-1

Quartzite cobble, ~ 10 cm in diameter, collected from till surface near BAK90-32.

Chapter 6

Cosmogenic Nuclide Exposure Ages and Glacial History of Late Quaternary Ross Sea Drift in McMurdo Sound, Antarctica

Introduction

Glacial deposits in the McMurdo Sound-Dry Valleys region of Antarctica provide a well-preserved record of late Quaternary Antarctic glaciation (Denton et al., 1971; Hendy et al., 1979; Stuiver et al., 1981; Clayton-Greene et al., 1988; Denton et al., 1989a; Brook et al., 1993; Dagel et al., in press). Chronological control of this record is limited, however, primarily due to a lack of datable material in most deposits. Drift sheets rich in volcanic rocks on the coast of McMurdo Sound are the most prominent glacial deposits in the region. The distribution of the youngest of these has been used to reconstruct an expanded, grounded ice sheet in McMurdo Sound and the Ross Sea, during the last glacial maximum (~ 18 kyr B.P.) (Stuiver et al., 1981; Denton et al., 1989a). Although this reconstruction has provided important constraints for ice-sheet modeling (e.g., Thomas and Bentley, 1978; Stuiver et al., 1981; Fastook, 1984), studies of post-glacial sea level change (e.g., Clark and Lingle, 1979; Nakada and Lambek, 1988), and post-glacial uplift (e.g., Greischar and Bentley, 1980), direct dating of the drift sheets is necessary to establish the linkage between the timing of sea level changes and Antarctic glaciation.

Current theories of Antarctic glaciation suggest that when sea level falls, ice on the Ross Ice Shelf, fed by west Antarctic Ice Streams and, to a lesser extent, east Antarctic outlet glaciers, grounds in the Ross Sea, and the grounded ice sheet thickens and advances on to the coast (Hollin, 1961; Stuiver et al., 1981; Denton et al., 1989a).

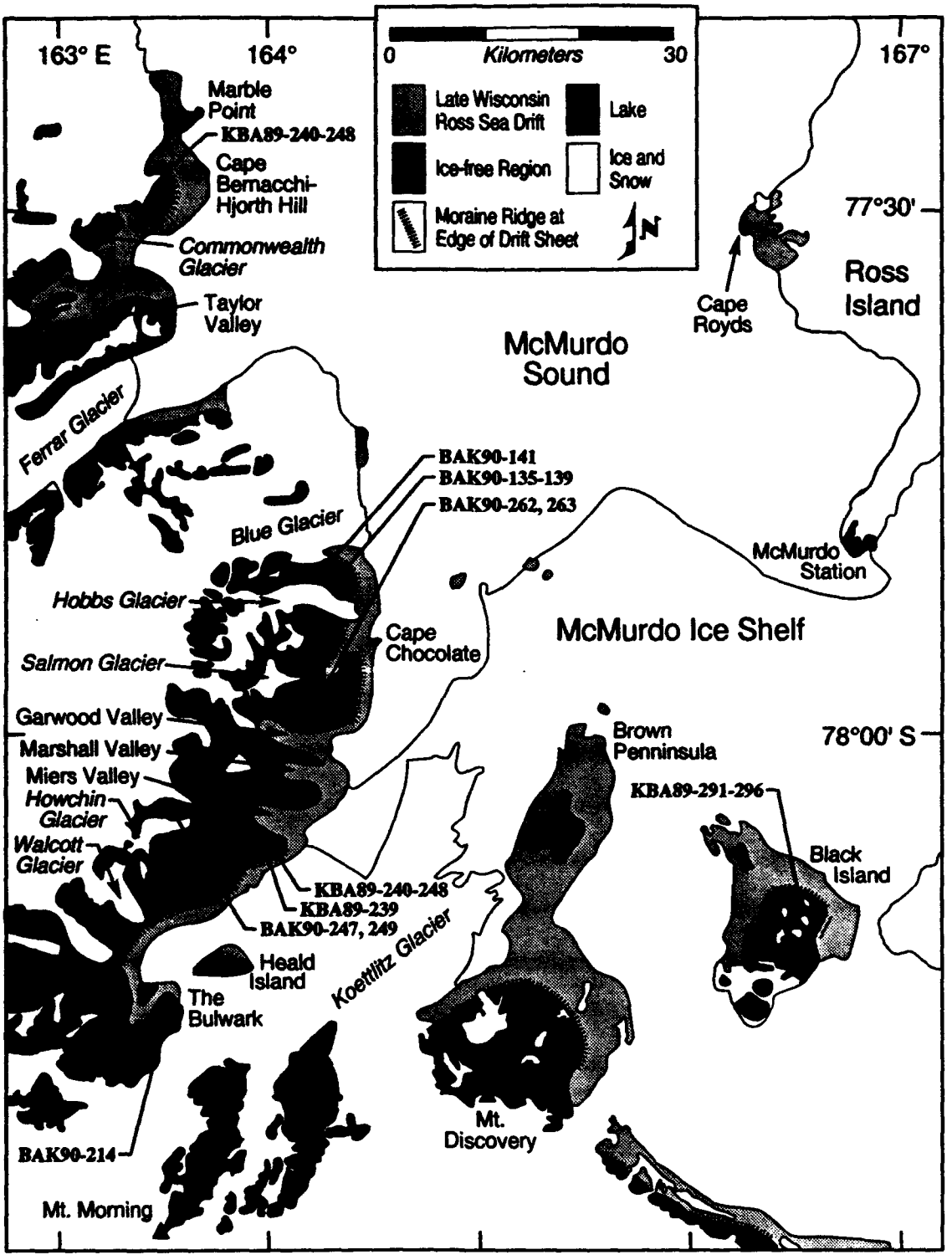

Figure 1. Distribution of Ross Sea Drift in the McMurdo Sound Region. Sample locations as shown.

Age constraints for the youngest drift sheet are based primarily on models and field observations suggesting that large lakes formed in the Dry Valleys when the grounded ice sheet dammed coastal valleys. Radiocarbon dates of lake sediments from 10 to 24 kyr BP provide, in the context of this model, absolute chronology for ice sheet expansion in isotope stage 2 (Stuiver et al., 1981; Clayton-Greene et al., 1988; Denton et al., 1989a; Dagel et al., in press). Older, analogous drift sheets occur above the assumed late Wisconsin limit, and are believed to represent grounded ice in McMurdo Sound during older glacial periods (Stuiver et al., 1981; Denton et al., 1989b). U-Th dates for lake carbonates in Marshall Valley (Fig. 1) provide evidence for one of these earlier episodes, apparently lasting throughout isotope stage 6 (Dagel et al., in press). The radiocarbon and U-Th dates, and correlation of McMurdo Sound deposits with glacial deposits in other coastal areas of Antarctica (Denton et al., 1989a,b; Bockheim et al., 1989) support the suggestion that advances of the ice sheet in McMurdo Sound, and by extension advances of the Ross Sea Ice Sheet, are primarily controlled by eustatic sea level change (Stuiver et al., 1981; Clayton-Greene et al., 1988; Denton et al., 1989a; Dagel et al., in press).

While the chronological evidence is compelling, the conceptual model relating lake sediment chronology and glacial history requires the existence of large lakes in the Dry Valleys during periods of generally cooler global climate (e.g., Clayton-Greene, 1988; Denton, 1989a), lower precipitation rates, and cooler temperatures in Antarctica (Jouzel et al., 1987; Denton et al., 1989a; Jouzel et al., 1989; Jouzel et al., 1990). The goal of this chapter is to provide new age constraints for both the youngest drift and analagous older deposits by measuring cosmogenic ^{3}He, ^{26}Al (half-live 7.2×10^{5} yr) and ^{10}Be (half-life 1.5×10^{6} yr) produced *in situ* in surficial material collected from the drift sheets. An additional goal is to examine the isotope systematics of

cosmogenic ^{3}He, ^{10}Be, and ^{26}Al in fairly young glacial moraines in Antarctica, where similar work has concentrated on older features (Brown et al., 1991; Nishiizumi et al., 1991; Brook and Kurz, 1993 [Chapter 3]; Brook et al., 1993 [Chapter 4]; Chapter 5). The ultimate objective is to establish the relative timing of glacial events related to the marine-based West Antarctic Ice Sheet and the terrestrial East Antarctic Ice Sheet, and to relate that timing to global climate history.

Description of Ross Sea Drift

The characteristics and distribution of the drift sheets were described in detail by Stuiver et al. (1981) and Denton et al. (1989a). The youngest drift is distinctively exposed on headlands around McMurdo Sound (Fig. 1), and in many places is bordered by a well-preserved moraine, analogous to moraines forming at the edge of the present ice shelf. Stuiver et al. (1981) refer to this deposit as Late Wisconsin Ross Sea Drift. Because the dating discussed below suggests that at least parts of the drift sheet may be early or even pre-Wisconsin in age, this drift sheet is refered to here simply as youngest Ross Sea Drift.

Ross Sea Drift is composed of till and stratified sediments made up of clasts of volcanic rocks, granite, a small percentage of a variety of metamorphic rocks, and rare sandstone. Clast sizes range from sand-gravel to boulders up to 2 m^3. Lithological characteristics, soil weathering, and clast sizes are described in detail by Stuiver et al. (1981). The basalts in the moraine are probably derived from the McMurdo Volcanic Group, which crops out to the south, on Ross Island, and in the foothills of the Royal Society Range, east of the Salmon-Walcott Glacier region (Fig. 1). The igneous and metamorphic rocks are probably derived from local granitic and metamorphic basement

rocks. Distinctive clasts of anorthoclase phonolite with large (up to 5 cm) anorthoclase crystals, a rock type known only on Ross Island, occur in some parts of the moraine (north of Blue Glacier and in the mouth of Taylor Valley, see Fig. 1) and these were used by Stuiver et al. (1981) to determine source areas and flow directions for the late Wisconsin ice advance.

The late Wisconsin drift is commonly fresh appearing and ice cored in some locations, cavernous weathering of boulders is rare, and striations are preserved on some protected clast surfaces. In contrast, the older drifts exhibit significant cavernous weathering and ventifacting of some boulder surfaces, and preservation of striations is rare. In most locations the older drift is not subdividable, although Stuiver et al. (1981) discussed earlier work that subdivided older Ross Sea Drift in a number of locations, including the Bulwark, lower Taylor Valley, and lower Wright Valley (Fig. 1). These subdivisions require revision (G.H. Denton, personal communication, 1993), and the work on the older deposits is intended to provide age constraints that can distinguish them from the younger drift.

Methods

Sample Collection and Processing

Samples were collected from Ross Sea Drift in the austral summers of 1989-1990 and 1990-1991. All samples of the youngest drift come from the terminal moraine of the drift sheet as mapped by Stuiver et al. (1981) (Fig. 1). Samples of the older drift were collected at several places within and at the edge of the drift sheets (Fig. 1). Two types of samples were collected: olivine and clinopyroxene bearing basaltic rocks intended primarily for analysis of cosmogenic ^{3}He in phenocrysts, and quartz bearing granites, metamorphic rocks, and sandstones, intended for ^{3}He, ^{10}Be, and ^{26}Al measurements. The

samples were collected from the largest clasts of appropriate lithology in each location (see appendix for more detail). Because of concern about post-depositional mobilization, samples were collected on the moraine crest, as far as possible from any frost cracks. Smaller samples were collected in their entirety, horizontal top surfaces were removed from larger samples. Shielding angles of surrounding topography were recorded for all sample regions, maximum shielding at any azimuth was 10 degrees. Assuming the approximate $\sin^2$ dependence on zenith angle for cosmic rays (Conversi and Rothwell, 1954; see Chapter 1) the associated shielding corrections are insignificant and were not applied.

Samples were cut with a rock saw at depths of ~ 2-6 cm depending on rock geometry, crushed in a jaw crusher, and sieved. For ^{3}He analysis individual mineral grains (quartz or olivine) were picked from the sieved fractions (0.5-1mm or 1-2mm), and rinsed in acetone, methanol, and ethanol. For ^{10}Be and ^{26}Al analysis 100-200 g of rock were needed because exposure ages are young and sample altitudes are low. Pure quartz samples (quartzites and sandstones) were sequentially leached in HF to remove meteoric ^{10}Be (Brown et al., 1991; Nishiizumi et al., 1989) until approximately 40-50 % of the mass was dissolved, then spiked with stable Be. Stable aluminum concentrations were determined by graphite furnace atomic absorption spectrophotometry (GFAAS) in Orsay or inductively coupled argon plasma spectromety (ICPES) in Woods Hole, and samples were spiked with stable Al to make a total of ~ 1 mg per sample. An intercalibration experiment between the two instruments gave excellent agreement (within 2-3 %) for samples originally prepared for GFAAS analysis (greater dilution than used for ICPES). Be and Al were separated from the spiked samples by solvent extraction of Be-acetylacetonate from Na-EDTA solution into carbon tetrachloride and

purification of Al from the aqueous phase by first extracting 2-methyl-8-quinolinol derivitaves of other elements into chloroform, then extracting Al-acetylacetonate into carbon tetrachloride. Purified BeO_2 and Al_2O_3 targets were prepared by precipitating the Be or Al as the hydroxide and heating at high temperature in a quartz crucible to convert to the oxide. The AMS targets were prepared by previously described techniques (Raisbeck et al., 1987). Further details of chemical procedures can be found in Raisbeck et al. (1987), Brown (1990), and in Chapter 2.

^3He analyses were performed in Woods Hole using a mass spectrometer dedicated to analysis of helium isotopes in terrestrial rocks (Table 1). The machine and gas processing are described in more detail by Kurz et al. (1987), Trull (1989), and in Chapter 2. Olivine samples were analyzed by first crushing the samples *in vacuo* and then melting the resulting powder in an ultra-high vacuum resistively heated furnace with a tantalum crucible. In volcanic rocks the two analyses are necessary to separate magmatic ^3He from cosmogenic ^3He. Magmatic ^3He concentrations are calculated using the $^3He/^4He$ ratio of helium released by crushing, which is dominantly magmatic (Kurz, 1986a; Kurz, 1986b) and the total ^4He in the sample:

$$^3He_m=(^3He/^4He)_{cr}(^4He)_t \qquad (1)$$

Cosmogenic ^3He is then given by:

$$^3He_c=^3He_t-^3He_m. \qquad (2),$$

where cr, t, m, and c stand for crushing, total, magmatic, and cosmogenic, respectively. $^3He/^4He$ ratios of helium released by crushing the Ross Sea Drift olivine samples are fairly uniform, between 6.1 and 7.1 R_a (R_a is atmospheric $^3He/^4He$ ratio: 1.384×10^{-6}), with the exception of the sample with the oldest exposure age. This sample, BAK90-214-2, has $^3He/^4He_{cr}$ of 11.2 ± 1.3 (Table 1) and exposure age of 570 kyr; the high ratio probably represents contamination of the magmatic component by a small amount of cosmogenic ^3He (note that the effect on the age calculation is insignificant). The other $^3He/^4He_{cr}$ ratios are consistent with measurements for McMurdo Group volcanic rocks collected from outcrops in the region (M. Kurz, unpublished data).

Quartz samples were analyzed by melting only or by crushing and melting. It was assumed that all ^3He in quartz was either cosmogenic or nucleogenic (Brook and Kurz, 1993 [Chapter 3], Brook et al., 1993 [Chapter 4], Chapter 2). A correction was applied to the total ^3He concentrations for nucleogenic production of ^3He in quartz by thermal neutrons *via* $^6Li(n,\alpha)t$-^3He (e.g., Morrison and Pine, 1955) using the total ^4He concentration and a nucleogenic production ratio for Dry Valley quartz sandstone from Trull et al. (1991) of 0.011 ± 0.004 R_a (where R_a is the atmospheric $^3He/^4He$ ratio of 1.384×10^{-6}). This correction may be inaccurate if Li, U, and Th concentrations are significantly different in the Ross Sea Drift samples than in the Trull et al. (1991) samples. However, because the corrections range from less than 1 % to 8 % of the total ^3He in the four quartz samples, this uncertainty is not of great importance. In a fifth quartz sample, an extremely large concentration of ^4He (sample KBA89-244, ^4He: 4×10^{-5} cc STP g^{-1}) prevented the inlet of enough gas to the mass spectrometer to make an accurate ^3He measurement without compromising the low blank level of the system.

^{3}He and ^{4}He blanks ranged from ~ 3-6 x 10^{-11} cm^3 STP for ^{4}He and ~3-8 x 10^{-17} cm^3 STP for ^{3}He. Reported precision of ^{3}He concentrations reflects uncertainties in analysis (typically ~2-5 %, 1 sigma), based on repeated analysis of air standards and uncertainties related to blank corrections for smaller samples. Uncertainties in ^{10}Be and ^{26}Al concentrations reflect counting statistics and a 5 % uncertainty accounting for variations in machine stability (Brown et al., 1991). Blank corrections are < 2%. All data are compiled in Tables 1 and 2. See Chapter 2 for further analytical details.

Exposure ages were calculated using ^{10}Be and ^{26}Al production rates from Nishiizumi et al. (1989) and Lal (1991). Calibrations of the ^{3}He production rate give variable results (Cerling, 1990; Kurz et al., 1990). The production rate of Cerling (1990), recalculated to account for the (Bard et al., 1990) ^{14}C-calendar year calibration, is 398 ± 8 at g^{-1} yr^{-1} at 1445 m altitude. The Kurz et al (1990) production rate is based on ^{14}C-dated Hawaiian lava flows at different altitudes. Scaling it to sea level using Lal (1991) gives a mean of 178 ± 41 at g^{-1} yr^{-1}. To arrive at an Antarctic production rate the altitude and latitude scaling factors of Lal (1991) were used to scale the two production rates to sea level and high latitude (> 60° N or S); the uncertainty-weighted mean production rate is then 118 ± 9 at g^{-1} yr^{-1}. Previous papers (Brook and Kurz, 1993; Brook et al., 1993) used scaling for altitude and latitude based on Lingenfelter (1963). The scaling factors of Lal (1991), however, allow simple comparison with data from other studies, are generally used by other workers, and are easily available in polynomial form, and are a complete and self-consistent treatment of the scaling problem. This issue is discussed further in Chapter 1. Uncertainties in production rates have been discussed previously (Lal, 1987; Nishiizumi et al., 1989; Cerling, 1990; Kurz et al., 1990; Brook and Kurz, 1993). A 15 % uncertainty in all the production rates is suggested as an

appropriate estimate of the true uncertainly applicable to calculating an absolute age (see Chapter 1 for further discussion of production rates).

No corrections for erosion (e.g. Brown et al., 1991) are made to the data because these features are fairly young and estimated Antarctic erosion rates of ~ 10^{-5} g $cm^{-2}yr^{-1}$ (Brown et al., 1991; Nishiizumi et al., 1991) have no significant affect on exposure ages < 500 kyr. ^{3}He exposure ages are simply calculated by dividing the concentration by the appropriately scaled production rate. ^{10}Be and ^{26}Al ages are given by:

$$t = \frac{\ln(1 - \frac{N\lambda}{P})}{-\lambda} \qquad (3),$$

where t is time, P is production rate, λ is decay constant and N is concentration.

Results and Discussion

^{3}He Exposure Ages

^{3}He exposure ages for the youngest Ross Sea Drift (Fig. 2) show significant scatter, as has been observed in exposure age distributions on other moraine deposits (Phillips et al., 1990; Brook et al., 1993; Chapters 4 and 5) but most are significantly lower than 100 kyr. Figure 1 includes three ^{3}He exposure ages from quartz samples. The utility of quartz for dating with cosmogenic ^{3}He has been questioned because of diffusion problems (e.g. Cerling, 1990; Brook and Kurz, 1993); the figure includes quartz ^{3}He exposure ages only where the $^{3}He/^{10}Be$ ratio is consistent with calculated production ratios (excludes only one sample-see below), indicating minimal ^{3}He loss. Ages for the older deposits also show significant scatter, suggesting that they represent more than one drift sheet, but are distinctly older than the ages for youngest Ross Sea Drift.

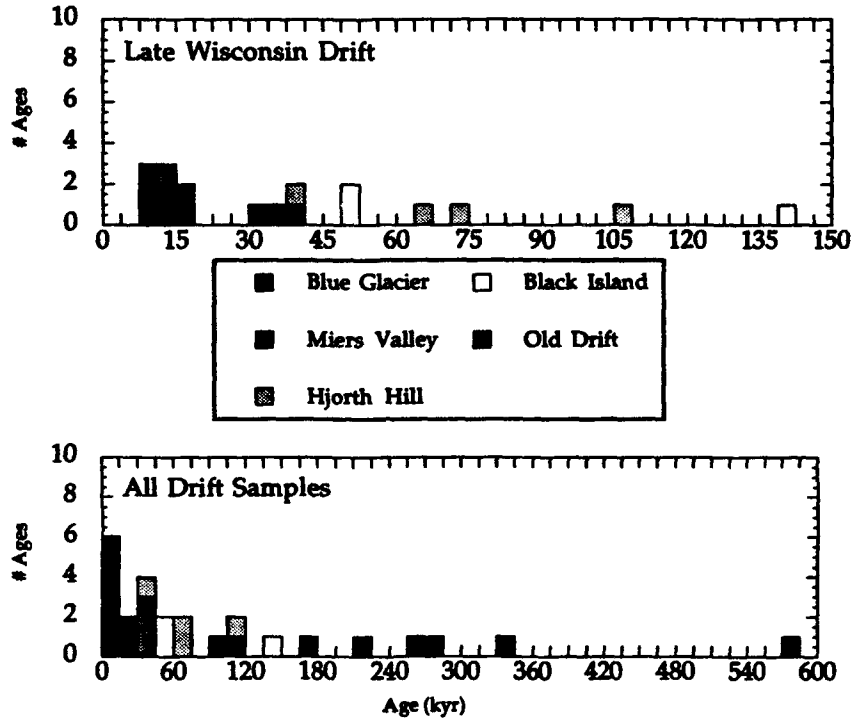

Figure 2. Histogram of ^{3}He ages for youngest Ross Sea Drift and older drifts. ^{3}He ages for both olivine and quartz are plotted, with the exception of quartz sample KBA89-248, where $^{3}He/^{10}Be$ and $^{3}He/^{26}Al$ ratios indicate significant ^{3}He loss (see text and Fig. 3).

^{10}Be and ^{26}Al Ages

The five ^{10}Be and ^{26}Al measurements and ^{10}Be and ^{26}Al exposure ages are compiled in Table 2. Due to the young ages, large sample sizes (final sample after cleaning was ~30-50 g) were required and some analytical errors are on the order of 10% (one-sigma). $^{26}Al/^{10}Be$ ratios for these samples range from 6.2 ± 0.6 to 14.1 ± 2.5 (Figure 3). The predicted production ratio at sea level from Lal (1991) is 6.1 ± 0.4, and samples with exposure ages < 100 kyr should have $^{26}Al/^{10}Be$ ratios indistinguishable from this value. $^{26}Al/^{10}Be$ ratios higher than the production ratios in quartz with low exposure ages have been observed before (Chapter 5; Brown et al., 1991; E. Brown, unpublished data, E. Brook, unpublished data) but their origin is uncertain. The most likely cause, however, is an excess of ^{26}Al produced by nuclear reactions resulting from U and Th decay. The most significant reaction producing ^{26}Al is $^{23}Na(\alpha,n)^{26}Al$. Sharma and Middleton (1989) estimated steady state concentrations of ~10^5 - 10^7 at g^{-1} ^{26}Al produced by this mechanism in a variety of common rock types. The excesses of ^{26}Al in these samples, assuming a $^{26}Al/^{10}Be$ production ratio of 6, range from 7×10^4 at g^{-1} in KBA89-148, a metasandstone, to 3×10^6 at g^{-1} in KBA89-143, a granite. These values are very similar to those calculated by Sharma and Middleton (6×10^4 at g^{-1} for sandstone and 5×10^6 at g^{-1} for granite). The exact value for an individual rock depends on U,Th, and Na concentrations and on their proximity in the mineral matrix (see Chapter 5 for further discussion). These measurements have not been made but this problem is under investigation, since accurate knowledge of production ratios is necessary for many of the suggested geochronological uses of cosmogenic nuclides (e.g., Lal, 1991; Brown et al., 1992). Nucleogenic ^{26}Al may be an important factor to consider in using ^{26}Al to date recently exposed surfaces.

^{10}Be ages (Table 2) are consistent with the ^{3}He results and geographic trends along the moraine described below. The ^{26}Al ages are less precise due to analytical uncertainties, and are also influenced by the probable presence of nucleogenic ^{26}Al. Despite these uncertainties the fact that the ratios are equal to or higher than production ratio demonstrates that chemical processing effectively removes any atmospheric ^{10}Be contamination.

^{3}He Loss , Inherited, and Nucleogenic ^{3}He

Because ^{3}He is a stable noble gas there are a number of factors to consider in using it as a geochronometer. These include the possibility of loss of ^{3}He due to diffusion, and the possibility of retention of ^{3}He from previous periods of exposure (note that the radioactive cosmogenic nuclides are not immune to this problem, which depends on the time scale of previous exposure), and the necessity of correcting total concentrations of ^{3}He in olivine for the magmatic component.

^{3}He loss from quartz has been demonstrated to be a significant problem in older Antarctic glacial deposits (Brook and Kurz, 1993; Brook et al., 1993). These two studies suggested, based on comparisons of ^{10}Be and ^{3}He ages, that loss would not be significant on time scales of less than 100 kyr. The Ross Sea Drift quartz samples provide an opportunity to examine this hypothesis. With no diffusion, the ^{3}He/^{10}Be and ^{3}He/^{26}Al ratios in these samples should be equal to the production ratios. The production ratios of ^{3}He/^{10}Be and ^{3}He/^{26}Al have not been measured directly in quartz, but based on the production rates assumed above the ratios are 20 ± 6 and 3 ± 0.9. The production ratios can also be calculated using measurements of ^{3}He, ^{10}Be, and ^{26}Al in olivine (Nishiizumi et al., 1990). Scaling those results to the chemical composition of quartz using the elemental production rate

dependence given by Nishiizumi et al. (1990) suggests production ratios of 24 ± 7 and 4 ± 0.7, respectively. For three of the four Ross Sea Drift quartz samples, $^{3}He/^{10}Be$ ratios are fairly consistent with each other and with the calculated production ratios (Table 2; Fig. 3). (Because of the potential problem of nucleogenic ^{26}Al, $^{3}He/^{26}Al$ ratios can not be used in this fashion.) These three samples are a quartz sandstone (BAK90-135), an extremely well-lithified quartzite cobble (KBA89-148), and a granite (KBA89-143). The quartz in all three samples is composed of discrete, isotropic mineral grains with well-defined boundaries and grain sizes between 0.5 and 2 mm (see appendix for details). The fourth sample (KBA89-248) is a metamorphic rock composed of what is probably metamorphosed vein quartz in a feldspathic matrix. In thin section this quartz is microcrystalline, with individual domains of ~ 10 um. Although the exact protolith of this sample is not known, this texture is in fact common in hydrothermal vein quartz (e.g., Boiron et al., 1992). Previous work suggested that the petrographic characteristics of quartz samples play an extremely important role in controlling ^{3}He diffusion rates (Brook and Kurz, 1993). Specifically, the size of individual diffusion domains, not the macroscopic grain size, is obviously crucial. This results for KBA89-248, combined with unpublished observations of significant discrepancies between ^{3}He, ^{10}Be and ^{26}Al concentrations in vein quartz samples in western Norway (E. Brook, unpublished data), suggest that vein quartz is particularly poor in retaining ^{3}He.

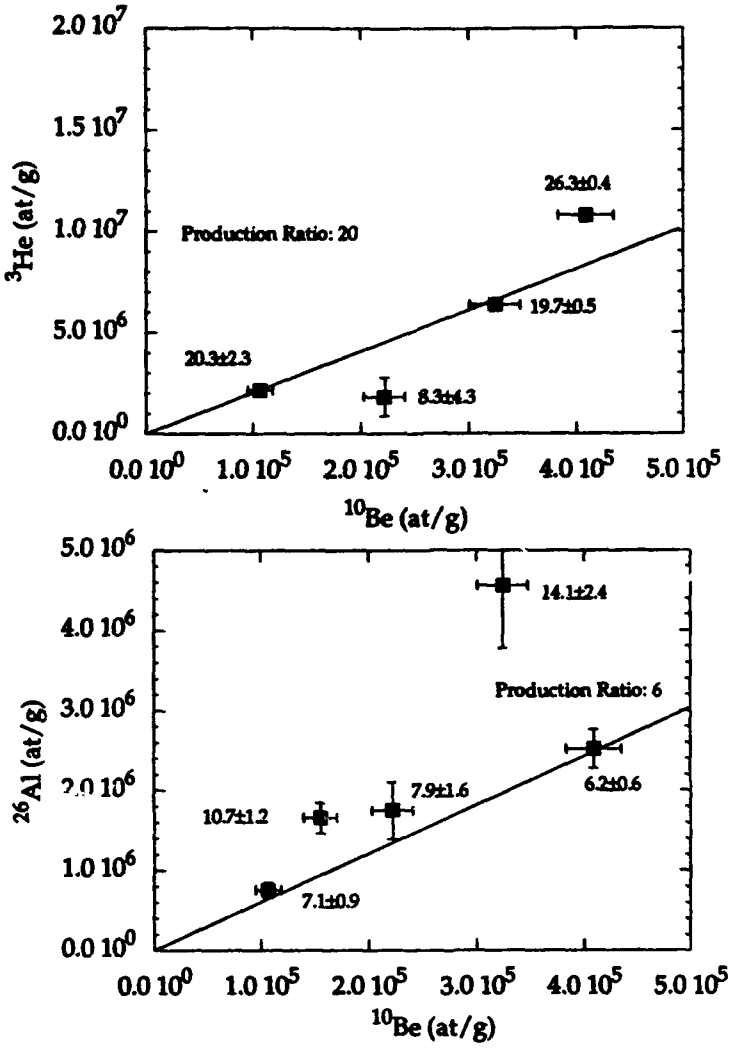

Figure 3. Scatter plots of ^{10}Be, ^{3}He, and ^{26}Al data. Solid lines show predicted production ratios (see text). As discussed in the text, $^{3}He/^{10}Be$ ratios agree fairly well with predicted values in three of four samples suggesting that ^{3}He is well retained in quartz on time scales of < 100 kyr. The fourth sample, with a low $^{3}He/^{10}Be$ ratio, contains what appears to be r ıorphosed vein quartz with very small optical domains and this cha. ıstic is probably the cause of ^{3}He poor retentivity. Ratios for individual samples are printed on the figure. Elevated $^{26}Al/^{10}Be$ ratios are probably a result of nucleogenic production of ^{26}Al (see text).

Some unusual helium isotopic effects in two basalt samples from Black Island have also been observed. As described above, measuring cosmogenic ^3He in olivine or clinopyroxene consists of crushing the mineral separate *in vacuo*, releasing magmatic helium, and then melting the resulting powder in a vacuum furnace, releasing a mixture of cosmogenic helium and magmatic helium (Kurz, 1986a; Kurz, 1986b; Kurz et al., 1990). Although cosmic rays produce ^3He and ^4He in a ratio of ~ 0.2 (Mazor et al., 1970), cosmogenic ^4He is insignificant relative to magmatic ^4He in most terrestrial rocks. $^3He/^4He$ ratios obtained by crushing are therefore normally lower than $^3He/^4He$ ratios obtained by melting, allowing the simple separation between the two ^3He components (e.g., eqs. 1 and 2).

In two of the Black Island samples (KBA89-291 and KBA89-294, Table 2), however, the $^3He/^4He$ ratios in the gas released by melting olivine powders are **lower** than the $^3He/^4He$ ratio released by crushing. The origin of this effect is not entirely clear but may reflect the implantation of alpha particles from the surrounding groundmass or a uranium rich phase in the olivines themselves. This effect is believed to be confined to these samples, however it is possible that a similar ^4He component is present in other samples. This "extra" ^4He component would cause overcorrection of the of total ^3He for magmatic ^3He (eq. 2), and therefore cause underestimation of ^3He exposure ages. The general agreement between ^{10}Be, ^{26}Al, and ^3He data suggests that this effect, if present, is small, but it could explain some of the young outlying ages in the Miers Valley section of the drift sheet (Fig. 2).

As a preliminary test of the hypothesis that implantation of ^4He caused the depressed ratios, olivine grains from KBA89-291 and KBA89-294 were abraided with silica beads in an air-abrasion chamber (Table 3). The whole, abraided grains were analyzed by melting in the vacuum furnace and the

results compared to the $^3He/^4He$ ratios predicted for the whole grains from the crushing and melting data (Table 3). In one case (KBA89-291) the abraided grains had a lower ^4He concentration than the unabraided grains, suggesting that the low ratios in the melted powder are not related to implantation of ^4He. For KBA89-294, abraiding the grains resulted in a slightly higher ^4He concentration, suggesting removal of a low $^3He/^4He$ ratio phase. Apart from the fact that opposite effects were observed for the two samples this experiment is not conclusive because total ^4He concentrations in other replicate analyses of olivine from Ross Sea Drift samples (Table 1) often vary by a factor of two or more. More detailed abrasion experiments can probably provide more information about the cause of these anomalies.

Glacial Chronology of Ross Sea Drift

The primary chronological conclusion from these data is that most of the exposure ages along the sampled area of the presumed late Wisconsin Ross Sea Drift fall within the interval of 10-70 kyr, and therefore span most of the last glacial period. The fact that samples from the older Ross Sea drift are significantly older (Fig. 2) demonstrates that the two deposits can be separated the basis of exposure ages. It is quite possible that several different drift sheets are represented by the older ages, and it is therefore difficult to interpret the age distribution. Further work on these deposits, combined with detailed geological mapping, could significantly improve understanding of pre-late Wisconsin glaciation of the region.

As discussed by Brook et al. (1993), Brown et al. (1991) and Phillips et al. (1990), scatter in data like these can result from a variety of factors, including prior exposure to cosmic rays in outcrop or during transport, incorporation of older material by a younger glacial advance, spalling or erosion of boulder

surfaces, past soil cover, or post-deposition shifting of boulders. In addition, in the case of the Ross Sea Drift sheets the possibility that the individual regions sampled are not the same age must be allowed. Because the youngest drift sheet and associated moraine are fairly young features in an extremely arid and cold environment, the effects of erosion and other physical weathering, and past soil or snow cover, are minimal. Scatter is more likely produced by previous exposure or incorporation of older deposits into younger glacial advances. The oldest ages from the youngest Ross Sea Drift deposit fall within the range of ages for the older drift (Fig. 2), which is consistent with the latter hypothesis.

Assuming the oldest two samples (KBA89-292 and KBA89-243) were originally deposited by an older glaciation and remobilized by a younger advance, the ^{3}He ages for the youngest drift sheet range from 8-106 kyr. One simple interpretation of the ages is that they represent an ice-sheet margin active throughout the last glacial period. ^{14}C dating of lake sediments in Taylor, Marshall, and Miers Valleys suggests that ice dammed the valley mouths sometime prior to ~23-24 kyr B.P (Hendy et al., 1979; Clayton-Greene et al., 1988; Denton et al., 1989a; Dagel et al., in press), but there is no evidence constraining the timing of earlier expansions. U-Th dating of glacial deposits apparently related to expansion of Ross Sea ice in isotope stage 6, however, suggest that during that time ice dammed the mouth of Marshall Valleys from ~ 129,000 to 182,000 years BP, i.e., spanning much of the previous glacial period. This exposure age data do not require that a grounded ice sheet exist in McMurdo Sound throughout isotope stages 2 and 3; there may have been repeated grounding episodes that occupied approximately the same marginal position, resulting in a mixture of exposure ages along the present moraine marking the limit of the youngest drift sheet. This suggestion is consistent

with rapid oscillations in northern hemisphere climate, and by inference ice volume and sea level, observed in recent ice core and climate records (e.g., Dansgaard et al., 1993). This possibility was also considered by Denton et al. (1989a) in discussing reconstructions of the Late Wisconsin Ross Sea Ice Sheet based on the drift limits shown in Fig. 1.

The age scatter within the youngest drift is fairly large, and based on previous work on alpine glacier moraines, and on similar studies of other moraine systems (Phillips et al., 1990; Brook et al., 1993 [Chapter 4]; Chapter 5), it is larger than expected for an individual moraine. Figure 2 shows, however, that there is an apparent geographic pattern in the exposure ages. Mean ages for the three main regions sampled decrease in the order Hjorth Hill (71 ± 27 kyr, n=4), > Miers Valley (26 ± 14 kyr, n=5) > Blue Glacier (15 ± 6 kyr, n=6). If this geographic pattern is real it suggests additional complexities in the depositional history of the drift sheet.

The mapping of Stuiver et al. (1981) suggests a clear separation between the young drift, which is, at most, early Wisconsin in age based on the exposure ages, and the older drift, which appears to be much older. In a number of locations, however, field observations and aerial photographs show what appear to be multiple drift limits at the approximate location of the boundary mapped by Stuiver et al. (1981). This is particularly evident in the region between the Howchin and Blue Glaciers, and at Hjorth Hill on Cape Bernachii. Samples described here were collected from the mapped drift limit in all cases, but it is possible that the mapping may be in error. As suggested above, there have been multiple ice sheet advances throughout the Wisconsin period, and the samples described here may actually, but inadvertently, may have come from different glacial deposits.

An alternative explanation of the data suggests that the drift was all emplaced at the last glacial maximum and age differences along the moraine represent prior exposure to cosmic rays before or during supraglacial transport of the material on the Ross Ice Sheet. Reconstructed ice flow directions for the late Wisconsin Ice suggest from Stuiver et al. (1981) are shown in Fig. 4. The reconstruction suggests that ice flowed west and southwest between Ross Island and Brown Peninsula, and southwest between Cape Royds and Cape Bernacchi. Because the Blue-Glacier region might have been supplied by material from the Blue Glacier itself, it is possible that material deposited there experienced shorter travel times than material in other segments of the moraine (Fig. 4). If this is correct, then the youngest ages, at Blue Glacier, most closely date the last presence of ice on the coast. The mean age for the Blue Glacier samples (15 ± 6 kyr) is very close, considering production rate uncertainties, to a radiocarbon date of 12,330 ± 50 yr (QL-1146) obtained for an algae layer deposited on an ice-contact delta just landward of the moraine segment samples near the Blue Glacier by Stuiver et al. (1981). They discussed this region in detail and suggested, based on curvature of the drift margin where it meets the Blue Glacier, that Ross Sea ice and Blue Glacier ice coalesced at the maximum expansion of Ross Sea Ice Sheet in McMurdo Sound (Fig. 1). Stuiver et al. also suggested, based on the radiocarbon date and the morphology of the delta, that the delta was abruptly truncated at it seaward side by ice recession at ~ 12 kyr (Stuiver et al., 1981). The fact that the ^{3}He and ^{10}Be exposure ages agree quite well with the radiocarbon date may indicate that they both are dating the maximum time of ice recession at this region. If the older ages in Fig. 2 are a result of previous exposure during glacial

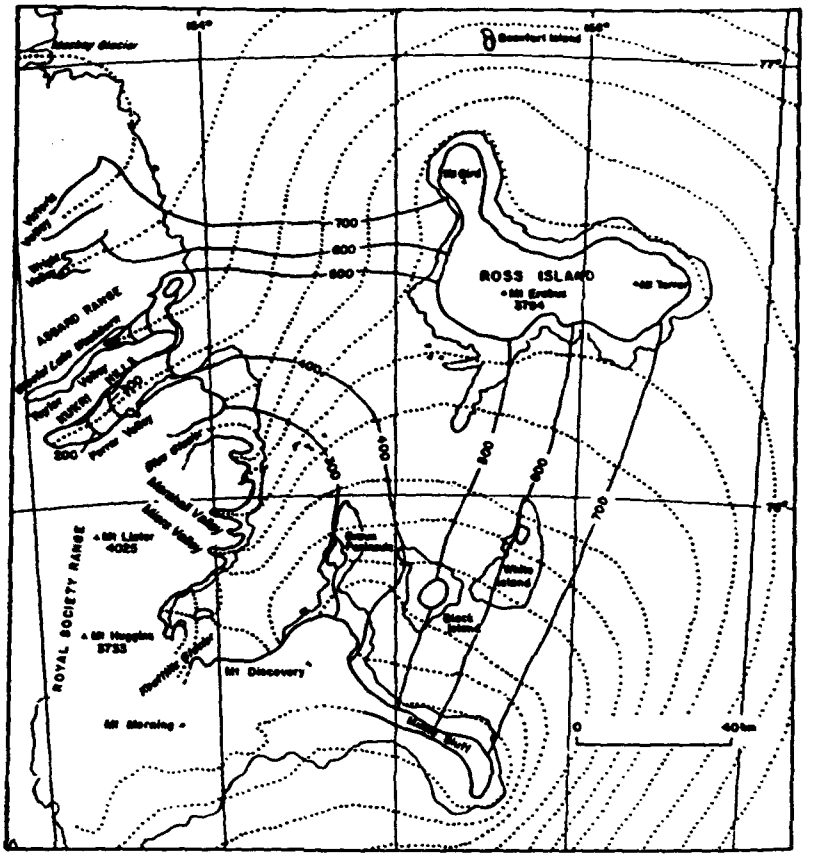

Figure 4. Reconstructed ice flow directions for late Wisconsin Ice in McMurdo Sound, Antarctica, from Stuiver et al. (1981). Flow directions are based on striation directions and the distribution of anorthoclase phonolite erratic boulders, which are derived from Mt. Erebus on Ross Isand.

transport they still suggest an active glacial system in McMurdo Sound and the Ross Sea during the last glacial period, but their implications for the history of grounded ice throughout that time are not as clear.

It is also possible that some of the spread in the data results from exposure to cosmic rays prior to incorporation in the glacial deposit. This hypothesis is difficult to test, but is important in using cosmogenic nuclides to date any glacial deposit. For the Ross Sea Drift samples this is probably not an important process because the Ross Sea ice sheet must have actively eroded its bed, based on the presence of striated stones in the drift, the large quantities of material deposited, and bedrock striations found in the region (Stuiver et al., 1981).

The explanations for the exposure age scatter discussed above are not mutually exclusive. However, the former interpretation, calling on a periodically "reactivated" glacial limit is favored here, primarily because significant exposure during supraglacial transport seems unlikely in a dynamic, wet-based, ice sheet. Due to the small number of samples it is difficult to prove that geographical differences in exposure ages are real, whatever their origin, and more data will be necessary to investigate this problem further.

Conclusions

^{3}He, ^{10}Be, and ^{26}Al exposure ages from the limit of "Late Wisconsin" Ross Sea Drift suggest that it was deposited during the last glacial period (isotope stage 2), consistent with models that suggest eustatic sea level control of grounded ice in the Ross Sea. The age distribution (8-106 kyr) suggests that, rather than a single late Wisconsin glacial event, the drift limit represents several periods of ice sheet grounding. ^{3}He exposure ages from the older, but

analogous, drift sheets exposed above the "late Wisconsin" limit are distinctly older than ages from the young drift and range from 104 - 567 kyr. These samples probably represent a number of older ice advances, but the clear difference demonstrates that the younger drift can be distinguished from the older deposit on the basis of exposure ages.

In contrast to the eustatic sea level control of Ross Sea ice expansion, it has been suggested that the continental east Antarctic ice sheet fluctuates out of phase with global Quaternary glaciations, expanding during interglacial time when moisture supply to interior east Antarctica increases. Exposure dating of Dry Valley glacial deposits related to expansion of the East Antarctic ice sheet in isotope stage 5, described in Chapters 4 (Brook et al., 1993) and 5, in combination with the results reported here, support this view (Fig. 5). Further tests of this chronological model will require both further work on older Ross Sea Drift, and on analogous glacial deposits in other parts of Antarctica (e.g. Denton et al., 1989b; Bockheim et al., 1989).

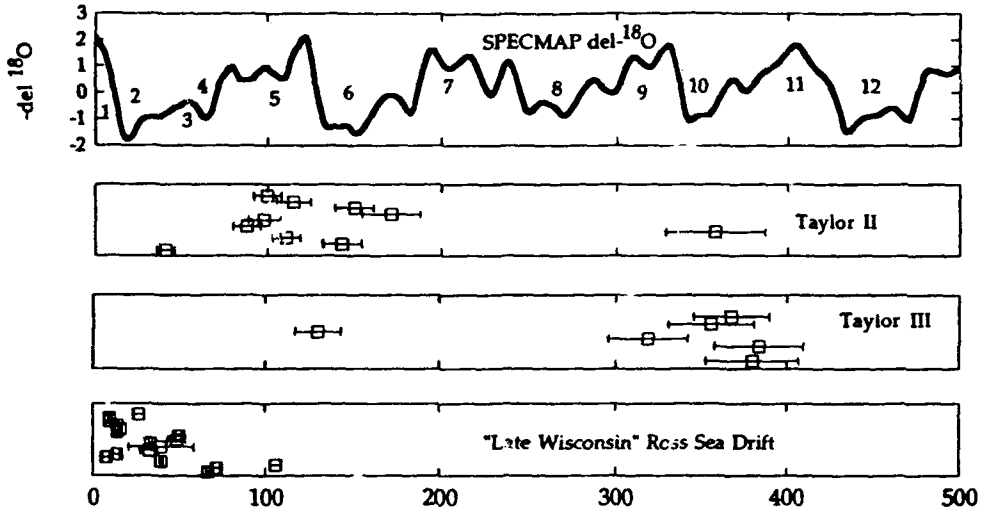

Figure 5. SPECMAP deep sea oxygen isotope stratigraphy over the last 500 kyr (Imbrie et al., 1982) and age distributions for Ross Sea Drift and East Antarctic outlet glacier moraines Taylor II and III (Brook et al. (1993) [Chapter 4]; Chapter 5). Ross Sea Drift ages are ^{3}He ages from this paper, Taylor moraine ages are ^{10}Be ages from Chapter 5. The Taylor Glacier drains the East Antarctic plateau (Fig. 1) and is theorized to be controlled primarily by moisture supply to the Antarctic interior. The Ross Sea ice sheet is believed to be controlled primarily by eustatic sea level, leading to the postulated "out of phase" behavior of the two ice margins in the Dry Valleys region (Denton et al., 1989b). The exposure ages support this suggestion in that the Ross Sea Drift ages fall mainly within isotope stage 2, while Taylor II ages suggest deposition in isotope stage 5 (see Brook et al., 1993 and Chapter 5 for more details). Taylor III is more difficult to place in the ^{18}O stratigraphy, but assuming it is an interglacial deposit, may represent isotope stage 9 or 11. Note that the use of somewhat uncertain production rates (see text) could impose systematic errors in age calculations. For example, if the ^{10}Be production rate were 5% lower than the rate used the conclusions about the Ross Sea Drift ages and the Taylor II ages would not change, but the Taylor III ages would increase enough to be superimposed on the stage 11 maximum in the isotope curve.

Table 1. Helium isotopic data for Ross Sea Drift samples. R/R_a is $^3He/^4He$ ratio relative to atmospheric ratio (1.384 x 10^{-6}). ol=olivine, q=quartz, cr-crushing, m=melting. Sz=grain size: 1= 0.5-1mm, 2=-2 mm, 3=>2mm. Exposure ages calculated as described in text. Age uncertainties are propagated analytical uncertainties only.

Sample	Alt.	An.	Sz	^4He cc STP/g x 10^9	1s	R/Ra	1s	^3He 10^6 at/g	1s	^3He_c 10^6 at/g	1s	^3He Age kyr	1s	
"Late Wisconsin" Drift Sheet														
Hjorth Hill														
KBA89-148 q	309	cr	2	67.6	0.2	2.20	0.04	5.54	0.10	10.75	0.14	67	1	
		m		34.0	0.1	4.16	0.08	5.25	0.10					
KBA89-140 ol	309	cr	2	9.2	0.1	6.94	0.29	2.38	0.10	11.58	0.37	72	2	
		m		18.1	0.1	24.18	0.29	16.24	0.20					
KBA89-142 ol	309	cr	2	13.4	0.1	7.08	0.19	3.52	0.10	17.01	0.54	106	3	
		m		45.3	0.1	17.17	0.19	28.93	0.33					
KBA89-143 q	309	cr	2	44.0	0.1	2.28	0.04	3.73	0.07	6.38	0.15	40	1	
		m		369.3	1.4	0.21	0.01	2.81	0.08					
Miers Valley														
KBA89-240 ol	253	cr	2	79.5	0.1	7.02	0.05	20.73	0.15	1.27	0.27	8	2	
		m		28.8	0.1	8.21	0.08	8.78	0.08					
KBA89-241 ol	253	cr	3	13.1	0.1	6.32	0.13	3.08	0.06	2.10	0.24	14	2	
		m		23.3	0.1	8.74	0.17	7.57	0.15					
KBA89-243 ol	253	cr	2	13.3	0.1	7.21	0.17	3.57	0.08	40.05	0.26	263	2	
		m		14.1	0.1	83.51	0.35	43.84	0.18					
KBA89-244 q	253	cr	1	568.6	2.5	0.09	0.04	1.92	0.74	8.95	9.72			
		m		39038.5	2081.7	0.02	0.01	23.23	16.02					
KBA89-246-2 ol	253	cr	1	27.0	0.2	6.74	0.07	6.77	0.09	4.74	0.45	33	5	*
		m		100.6	0.3	8.01	0.08	29.98	0.29					
		cr	2	25.9	0.1	6.62	0.13	6.37	0.13	5.78	0.30			
		m		19.4	0.1	14.61	0.22	10.56	0.16					
		cr	3	159.0	0.1	6.70	0.07	39.65	0.41	4.33	0.79			
		m		76.0	0.3	8.24	0.09	23.27	0.28					
KBA89-245 o	253	cr	2	54.5	0.3	6.86	0.06	13.88	0.13	6.03	2.83	40	19	
		m		19.9	0.4	15.00	3.71	11.11	2.81					
KBA89-247 ol	253	cr	2	32.3	0.1	7.00	0.07	8.39	0.09	5.16	0.19	34	1	
		m		16.2	0.1	15.55	0.18	9.37	0.11					
KBA89-248 q	253	m	2	1982.2	3.7	0.04	0.01	2.65	0.96	1.84	0.96	13	4	*
		m		1166.5	0.4	0.06	0.01	2.47	0.61	2.00	0.61			
Black Island														
KBA89-291 ol	393	cr	2	1.0	0.1	4.89	0.98	0.19	0.04					
		m		12.6	0.1	0.79	0.07	0.37	0.03					
KBA89-292 ol	393	cr	2	30.7	0.1	6.74	0.13	7.71	0.14	24.59	0.33	141	2	
		m		19.3	0.1	41.09	0.26	29.42	0.19					
KBA89-293 ol	393	cr	2	94.6	0.1	6.60	0.04	23.23	0.14	8.46	0.83	49	5	
		m		116.9	0.1	8.55	0.17	37.15	0.76					
KBA89-294 ol	393	cr	2	7.4	0.1	6.82	0.30	1.89	0.08					
		m		14.5	0.1	4.49	0.54	2.42	0.29					
KBA89-296 o	393	cr	1	7.0	0.1	6.79	0.36	1.78	0.10	8.71	0.39	50	2	
		m		16.1	0.1	21.31	0.37	12.78	0.22					

Table 1 continued.

Sample	Alt	An.	Sz	^4He	1s	R/Ra	1s	^3He	1s	^3He_c	1s	^3He Age	1s	
Blue Glacier														
BAK90-135 q	265	m	1	478.0	0.1	0.00	0.01	2.36	0.21	2.17	0.24	14	2	
BAK90-136 ol	265	cr	1	26.1	0.1	0.13	0.09	6.41	0.08	2.48	0.16	16	1	
		m		12.7	0.1	0.00	0.14	5.61	0.06					
BAK90-137 ol	265	cr	2	28.1	0.1	6.66	0.09	6.96	0.10	1.88	0.19	14	1	*
		m		6.6	0.1	14.36	0.44	3.50	0.11					
		cr		75.5	0.1	6.82	0.09	19.16	0.26	2.30	0.40			
		m		5.7	0.1	17.60	0.60	3.76	0.13					
BAK90-138 ol	265	cr	2	22.9	0.1	7.09	0.30	6.04	0.25	1.52	0.46	10	3	
		m		8.8	0.1	11.72	0.50	3.85	0.17					
KBA89-139-1 ol	265	cr	2	31.3	0.1	6.87	0.10	7.98	0.11	1.58	0.19	10	1	
		m		7.2	0.1	12.79	0.25	3.40	0.07					
BAK90-139-2 ol	265	cr		86.3	0.4	6.11	0.07	19.63	0.24	4.16	0.53	27	3	
		m		23.6	0.1	10.84	0.41	9.53	0.36					
Older Drift														
KBA89-239 ol	374	cr	2	1.1	0.1	7.64	0.81	0.31	0.03	28.66	0.38	167	2	
(Miers Valley)		m		5.2	0.1	155.66	1.51	30.14	0.32					
BAK90-141 ol	495	cr	2	36.6	0.1	6.86	0.16	9.33	0.22	38.54	0.66	212	5	*
(Blue Glacier)		m		4.5	0.1	238.09	3.31	39.68	0.56					
		cr		83.6	0.4	6.80	0.09	21.12	0.29	42.19	1.82			
		m		28.5	0.1	46.67	0.68	49.38	0.72					
BAK90-247 ol	545	cr	2	6.6	0.1	6.30	0.49	1.54	0.12	66.19	4.14	330	21	
(Howchin Glacier)		m		29.8	0.1	66.08	1.63	73.17	1.81					
BAK90-249 ol	545	cr	2	117.2	0.6	6.74	0.09	29.39	0.42	22.04	1.34	110	7	
(Howchin Glacier)		m		103.2	0.6	12.49	0.25	47.91	1.01					
BAK90-263 ol	510	cr	2	34.4	0.2	6.82	0.13	8.73	0.17	52.49	1.42	272	7	
(Garwood Valley)		m		8.4	0.1	175.74	4.48	54.61	1.40					
BAK90-262-1 ol	510	cr	2	3.2	0.1	5.85	0.72	0.81	0.09	20.07	0.53	104	3	
(Garwood Valley)		m		10.1	0.1	60.30	1.00	22.64	0.38					
BAK90-214-2 ol	480	cr	2	1.9	0.1	11.19	1.27	0.78	0.09	108.70	6.59	572	35	
(Bulwark)		m		129.7	0.8	33.73	0.40	162.69	2.16					

* mean of replicates

Table 2. ^{3}He, ^{10}Be, and ^{26}Al data for Ross Sea Drift Quartz Samples. Age uncertainties reflect analytical error only.

Sample	Gm. Sz. (mm)	^{3}He (Mat/g)	1s	^{10}Be (Mat/g)	1s	^{26}Al (Mat/g)	1s
BAK90-135	0.5-1	2.17	0.24	0.11	0.01	0.75	0.10
KBA89-143	1.0-2.0	6.38	0.15	0.32	0.02	4.56	0.78
KBA89-148	1.0-2.0	10.75	0.14	0.41	0.03	2.52	0.24
KBA89-248	1.0-2.0	1.84	0.96	0.22	0.02	1.75	0.36
KBA89-244	0.5-1			0.16	0.02	1.66	0.19
		$^{3}He/^{10}Be$	1s	$^{3}He/^{26}Al$	1s	$^{26}Al/^{10}Be$	1s
BAK90-135		20.26	3.16	2.88	0.49	7.05	0.90
KBA89-143		19.68	1.50	1.40	0.24	14.07	2.41
KBA89-148		26.29	1.71	4.27	0.41	6.16	0.60
KBA89-248		8.30	4.37	1.05	0.59	7.88	1.60
KBA89-244						10.71	1.24
	Alt. (m)	^{3}He Age (kyr)	1s	^{10}Be Age (kyr)	1s	^{26}Al Age (kyr)	1s
BAK90-135	265	14.2	1.6	13.7	1.5	16.1	2.0
KBA89-143	309	39.9	0.9	40.0	2.9	97.3	16.6
KBA89-148	309	66.6	0.9	51.2	3.3	52.6	5.1
KBA89-248	253	12.7	3.8	28.7	2.4	38.2	7.7
KBA89-244	253			20.1	2.0	36.2	4.2

Table 3. Results of air abrasion experiment for olivine mineral separates from Black Island basalt samples.

		^4He (cc STP/g)	1 s	R/R_a	1 s	^3He (cc STP/g)	1 s
KBA89-294	crush	7.45e-09	9.63e-12	6.82	0.30	7.03e-14	3.13e-15
1-2mm grains							
Before Abrasion	melt	1.45e-08	1.07e-11	4.49	0.54	9.00e-14	1.08e-14
	total	2.19e-08	1.44e-11	5.28	0.37	1.60e-13	1.13e-14
KBA89-294	total	1.52e-08	1.69e-11	5.84	0.09	1.23e-13	1.96e-15
0.5-1mm grains							
After Abrasion							
Abrasion weight loss = 29%							
KBA89-291	crush	1.02e-09	1.29e-12	4.89	0.98	6.89e-15	1.37e-15
1-2 mm grains							
Before Abrasion	melt	1.26e-08	8.07e-12	0.79	0.07	1.38e-14	1.13e-15
	total	1.36e-08	8.17e-12	1.10	0.09	2.07e-14	1.78e-15
KBA89-291	total	1.10e-07	8.44e-11	0.56	0.02	8.45e-14	3.19e-15
1-2 mm grains							
After Abrasion							
Abraision weight loss = 60 %							

References

Bard, E., Hamelin, B., Fairbanks, R. G., and Zindler, A. (1990). Calibration of the ^{14}C timescale over the past 30,000 years using mass-spectrometric U-Th ages from Barbados corals. *Nature* **345**, 405-410.

Bockheim, J. G., Wilson, S. C., Denton, G. H., Anderson, B. G., and Stuiver, M. (1989). Late Quaternary fluctuations of Hatherton Glacier, Transantarctic Mountains. *Quaternary Research* **31**, 229-254.

Boiron, M. C., Essarraj, S., Sellier, E., Cathelineau, M., Lespinasse, M.. and Poty, B. (1992). Identification of fluid inclusions in relation to their host microstructural domains in quartz by cathodoluminescence. *Geochimica et Cosmochimica Acta* **56**(1), 175-186.

Brook, E. J., and Kurz, M. D. (1993). Surface exposure chronology using in situ cosmogenic ^{3}He in Antarctic quartz sandstone boulders. *Quaternary Research* **39**, 1-10.

Brook, E. J., Kurz, M. D., Ackert, R. P., Denton, G. H., Brown, E. T., Raisbeck, G. M., and Yiou, F. (1993). Chronology of Taylor Glacier advances in Arena Valley, Antarctica, using in situ cosmogenic ^{3}He and ^{10}Be. *Quaternary Research* **39**, 11-23.

Brown, E. (1990). The geochemistry of the beryllium isotopes: applications in geochronometry. Ph.D. Thesis MIT/WHOI, WHOI-90-47.

Brown, E., Edmond, J. ., Raisbeck, G. ., Yiou, F., Kurz, M., and Brook, E. J. (1991). Examination of surface exposure ages of Antarctic moraines using in-situ produced ^{10}Be and ^{26}Al. *Geochimica et Cosmochimica Acta* **55**, 2269-2283.

Brown, E. T., Brook, E. J., Raisbeck, G. M., Yiou, F., and Kurz, M. D. (1992). Effective attenuation lengths of cosmic rays producing ^{10}Be and ^{26}Al in quartz: Implications for exposure dating. *Geophysical Research Letters* **19**(4), 367-372.

Cerling, T. E. (1990). Dating geomorphological surfaces using cosmogenic ^{3}He. *Quaternary Research* **33**, 148-156.

Clark, J. A., and Lingle, C. S. (1979). Predicted relative sea-level changes (18,000 years B.P. to present) caused by late-glacial retreat of the Antarctic Ice Sheet. *Quaternary Research* **11**, 279-298.

Clayton-Greene, J. M., Hendy, C. H., and Hogg, A. G. (1988). Chronology of a Wisconsin age proglacial lake in the Miers Valley, Antarctica. *New Zealand Journal of Geology and Geophysics* **31,** 353-361.

Conversi, M., and Rothwell, P. (1954). Angular distributions in cosmic ray stars at 3500 meters. *Il Nuovo Cimento* **XII**(2), 191-210.

Dagel, M. A., Hendy, C. H., Denton, G. H., Stuiver, M., and Judd, F. M. (1993). Stratigraphy and chronology of isotope stage 6 and 2 drift, Marshall Valley, Antarctica. *Boreas,* in press.

Denton, G. H., Armstrong, R. L., and Stuiver, M. (1971). The late Cenozoic glacial history of Antarctica. In *The Late Cenozoic Glacial Ages* (Turekian, K. K., Ed.), pp. 267-306, Yale University Press, New Haven, CT.

Denton, G. H., Bockheim, J. G., Wilson, S. C., and Stuiver, M. (1989a). Late Wisconsin and early Holocene glacial history, inner Ross Embayment, Antarctica. *Quaternary Research* **31,** 151-182.

Denton, G. H., Bockheim, J. G., Wilson, S. C., and Leide, J. E. (1989b). Late Quaternary Ice-Surface Fluctuations of Beardmore Glacier, Transantarctic Mountains. *Quaternary Research* **31,** 183-209.

Fastook, J. L. (1984). West Antarctica, the sea-level controlled marine instability: Past and future. In *Climate Processes and Climate Sensitivity, AGU Geophysical Monograph 29* (Hansen, J. E., and Takahashi, T., Eds.), pp. 275-287, American Geophysical Union, Washington, D.C.

Greischar, L. L., and Bentley, C. R. (1980). Isostatic equilibrium grounding line between the West Antarctic inland ice sheet and the Ross Ice Shelf. *Nature* **283,** 651-654.

Hendy, C. H., Healy, T. R., Rayner, E. M., Shaw, J., and Wilson, A. T. (1979). Late Pleistocene glacial chronology of the Taylor Valley, Antarctica, and the global climate. *Quaternary Research* **11,** 172-184.

Hollin, J. T. (1962). On the glacial history of Antarctica. *Journal of Glaciology* **4,** 173-195.

Imbrie, J., Hays, J. D., Martinson, D. G., McIntyre, A., Mix, A. C., Morley, J. J., Pisias, N. G., Prell, W. L., and Shackleton, N. J. (1982). The orbital theory of Pleistocene climate: support from a revised chronology of the marine $\delta^{18}O$ record. In *Milankovitch and Climate* (Berger, A., Imbrie, J., Hays, J., Kukla, G., and Saltzman, B., Eds.), D. Reidel, Boston.

Jouzel, J., Lorius, C., Petit, J. R., Barkov, N. I., Kotlyakov, V. M., and Petrov, V. M. (1987). Vostok Ice Core: a continuous record of isotope temperature record over the last climate cycle (160,000 years). *Nature* **329,** 403-408.

Jouzel, J., Petit, J. R., and Raynaud, D. (1990). Palaeoclimatic information from ice cores. *Transactions of the Royal Society of Eninburgh* **81,** 349-355.

Jouzel, J., Raisbeck, G., Benoist, J. P., Yiou, F., Lorius, C., Raynaud, D., Petit, J. R., Korotkevitch, Y. S., and Kotlyakov, V. M. (1989). A comparison of deep Antarctic ice cores and their implications for climate between 65,000 and 15,000 years ago. *Quaternary Research* **31,** 135-150.

Kurz, M. D. (1986a). Cosmogenic helium in a terrestrial igneous rock. *Nature* **320**(6061), 435-439.

Kurz, M. D. (1986b). In situ production of terrestrial cosmogenic helium and some applications to geochronology. *Geochimica et Cosmochimica Acta* **50,** 2855-2862.

Kurz, M. D., Colodner, D., Trull, T. W., Moore, R. B., and O'Brien, K. (1990). Cosmic ray exposure dating with in-situ produced cosmogenic ^{3}He: results from young lava flows. *Earth and Planetary Science Letters* **97,** 177-189.

Kurz, M. D., Gurney, J. J., Jenkins, W. J., and Lott, D. E. (1987). Helium isotope variability within single diamonds from the Orapa kimberlite pipe. *Earth and Planetary Science Letters* **57-68,** 57-68.

Lal, D. (1987). Production of ^{3}He in terrestrial rocks. *Chemical Geology (Isotope Geoscience Section)* **66,** 89-98.

Lal, D. (1991). Cosmic ray labeling of erosion surfaces: In situ nuclide production rates and erosion models. *Earth and Planetary Science Letters* **104,** 424-439.

Lingenfelter, R. E. (1963). Production of carbon-14 by cosmic ray neutrons. *Reviews of Geophysics* **1**(1), 35-55.

Mazor, E., Heymann, D., and Anders, E. (1970). Noble gases in carbonaceous chondrites. *Geochimica et Cosmochimica Acta* **34,** 781-824.

Morrison, P., and Pine, J. (1955). Radiogenic origin of the helium isotopes in rock. *Annals of the New York Academy of Sciences* **62,** 71-92.

Nakada, M., and Lambek, K. (1988). The melting history of the late Pleistocene Antarctic ice sheet. *Nature* **333,** 36-40.

Nishiizumi, K., Winterer, E. L., Kohl, C. P., Klein, Middleton, R., Lal, D., and Arnold, J. R. (1989). Cosmic ray production rates of ^{10}Be and ^{26}Al in quartz from glacially polished rocks. *Journal of Geophysical Research* **94**(B12), 17,907-17,915.

Nishiizumi, K., Klein, J., Middleton, R., and Craig, H. (1990). Cosmogenic ^{10}Be, ^{26}Al, and ^{3}He in olivine from Maui lavas. *Earth and Planetary Science Letters* **98**, 263-266.

Nishiizumi, K., Kohl, C. P., Arnold, J. R., Klein, J., Fink, D., and Middleton, R. (1991). Cosmic ray produced ^{10}Be and ^{26}Al in Antarctic rocks: exposure and erosion rates. *Earth and Planetary Science Letters* **104**, 440-454

Phillips, F. M., Zreda, M. G., Smith, S. S., Elmore, D., Kubik, P. W., and Sharma, P. (1990). Cosmogenic chlorine-36 chronology from glacial deposits at Bloody Canyon, eastern Sierra Nevada. *Science* **248**, 1529-1532.

Raisbeck, G. M., Yiou, F., Bourles, D., Lestringuez, J., and Deboffle, D. (1987). Measurements of ^{10}Be and ^{26}Al with a tandetron AMS facility. *Nuclear Instruments and Methods in Physics Research* **B29**, 22-26.

Sharma, P., and Middleton, R. (1989). Radiogenic production of ^{10}Be and ^{26}Al in uranium and thorium ores: Implications for studying terrestrial samples containing low levels of ^{10}Be and ^{26}Al. *Geochimica et Cosmochimica Acta* **53**, 709-716.

Stuiver, M., Denton, G. H., Hughes, T. J.. and Fastook, J. L. (1981). History of the marine ice sheet in West Antarctica during the last glaciation, a working hypothesis. In *The Last Great Ice Sheets* (Denton, G. H., and Hughes, T. J., Eds.), pp. 319-436, Wiley-Interscience, New York.

Thomas, R. H., and Bentley, C. R. (1978). A model for Holocene retreat of the West Antarctic Ice Sheet. *Quaternary Research* **10**, 150-170.

Trull, T. (1989). Diffusion of helium isotopes in silicate glasses and minerals: implications for petrogenesis and geochronology. Ph.D. Thesis MIT/WHOI, WHOI-89-15.

Trull, T. W., Kurz, M. D., and Jenkins, W. J. (1991). Diffusion of cosmogenic ^{3}He in olivine and quartz: implications for surface exposure dating. *Earth and Planetary Science Letters* **103**, 241-256.

Chapter 6 Appendix. Ross Sea Drift Sample Descriptions.

Cape Bernacchi/Hjorth Hill

KBA89-140

Olivine and clinopyroxene phyric basalt 20 cm wide x 15 cm wide x 7 cm high, half-buried in sand/gravel moraine matrix, with large, 1-3 mm olivine and 2-5 mm clinopyroxene grains. Bottom half of boulder has extensive soil carbonate coating.

KBA89-142

Massive, olivine and clinopyroxene phyric basalt cobble half-buried in moraine crest. Boulder is ~ 10 cm x 10 cm x 10 cm, sub-angular, with soil carbonate on lower surfaces, 2-3 % 1-3 mm olivine and 2-4 % 2-4 mm clinopyroxene.

KBA89-143

Coarse-grained granite boulder, approximately 60 cm long x 40 cm wide x 25 cm high. Collected 1 m from crest of Ross Sea Drift moraine. Sample collected from top, horizontal surface of boulder. 1-2 mm whole quartz grains free of surface alteration picked from sieved fraction.

KBA89-148

Extremely well lithified quartzite clast approximately 10 cm long x 5 cm wide and high. Bottom surface buried in drift, top exposed. Entire clast collected. Original 0.5-2mm quartz grains of sample are visible in rock but crushing sample produced fragments broken across grain boundaries. 1-2 mm quartz grains free of surface alteration picked from sieved fraction.

Miers Valley

KBA89-241

Basalt cobble, 12 cm long x 10 cm wide x 5 cm high. Collected about 1 m seaward of moraine crest in a slight swale. Contains several olivine-rich and clinopyroxene-rich xenoliths or megacrysts up to 4 cm diameter. Sampled olivine from one xenolith for analysis at 0-4 cm depth.

KBA89-243

Rounded, 25 cm long x 10 cm wide x 12 cm high, basalt boulder on crest of moraine, partially buried in volcanic rich moraine. Approximately 3-4 % 1-4 mm olivine and 2-3 % 1-10 mm clinopyroxene grains in fine grained black-gray matrix.

KBA89-244

Pegmatite or metapegmatite cobble ~ 17 cm long x 10 cm wide x 5-10 cm high, collected 1 m landward of moraine crest. Contains large, up to 3-4 cm quartz and feldspar grains within foliated biotite layers. 70 % feldspar, 20-25 % quartz, 5-10 % biotite.

KBA89-245

Vesicular, olivine phyric basalt cobble, 20 cm long x 12 cm wide x 6 cm high. Collected 0.5 m from moraine crest on seaward side. Rock is ~ 20 % vesicles and ~ 15 % 0.1-3mm olivine crystals in grey matrix.

KBA89-246-2

Massive basalt boulder, 15cm long x 10 cm wide x 6 cm high, resting in gravel at moraine crest, with thick accumulation of salts on lower surfaces. Rock is 5-10 % clinopyroxene, 2-5 % olivine.

KBA89-247

Angular olivine phyric basalt cobble 15 cm long x 10 cm high x 10cm wide. 5 % olivine phenocrysts up to 4 mm. Collected from top of moraine crest.

KBA89-248

Metamorphic rock composed of thick bands of feldspar and quartz - probably a metamorphosed pegmatite or quartz vein. 15 cm wide x 25 cm long x 15 cm high. Outer surface weathered brown.

Black Island

KBA89-291

Basalt cobble, 1-4 % 1-3 mm olivine phenocrysts, 5-10 % 1-6 mm clinopyroxene phenocrysts.

KBA89-292

Basalt cobble, 10 cm x 10 cm x 10 cm. 5 % olivine and 1-2 % clinopyroxene phenocrysts up to 2 mm. Moraine limit here composed of several anastomosing ridges, this sample was collected from the second-outermost ridge at this location.

KBA89-293

Basalt cobble, 20 cm long x 10 cm wide x 10 cm high. Bottom half of boulder encrusted with soil carbonate. 5 % olivine, 1-2 % clinopyroxene phenocrysts up to 5 mm. Collected from moraine ridge just below ridge containing KBA89-292.

KBA89-294

Rounded basalt cobble, 15 cm long x 10 cm wide x 6 cm high. 3-4 % 1-4 mm olivine, 5-10 % 1-10 mm clinopyroxenes. Collected from crest of moraine ridge.

KBA89-295

Basalt cobble with polished, flat upper surface, 30 cm long x 30 cm wide x 10 cm high. 1-2 % olivine and 3-4 % clinopyroxene in grey massive matrix.

KBA89-296

Basalt cobble, 30 cm wide x 30 cm long x 10 cm thick. 5 % 0.5-1mm olivine and clinopyroxene in dark black masive matrix.

Blue Glacier

BAK90-135

Sandstone boulder, 40 cm long x 25 cm wide x 20 cm high, composed of moderately sorted, rounded, 0.5-1mm quartz grains, ~100 % quartz. Boulder on moraine surface, not buried in gravel matrix.

BAK90-136

Basalt cobble, 20 cm long x 14 cm wide x 10 cm high, with thick carbonate encrustation on bottom half. 2 % olivine phenocrysts up to 1 mm. Collected 2 m from crest of moraine.

BAK90-137

Basalt boulder on moraine crest, 20 cm wide x 30 cm long x 11 cm high. Sparsley olivine and clinopyroxene phyric. Bottom half of boulder buried in moraine crest, soil carbonates coat bottom surface.

BAK90-138

Large olivine and clinopyroxene basalt boulder, 30 cm wide x 30 cm long x 8 cm high. 5 % olivine and clinopyroxene (up to 2 mm).

BAK90-139-1

Dense basalt cobble with 3-5 % 1-3 mm olivine phenocrysts. Carbonate encrustation on bottom half of cobble. Sample collected from crest of moraine 150 m south of BAK90-137.

BAK90-139-2

Vesicular basalt boulder, irregular shape, 24 cm long and wide, 12 cm high. 2- 4 % 2-3 mm olivine. Carbonate crust on bottom surfaces.

Older Ross Sea Drift

Miers Valley
KBA89-239

Basalt cobble (erratic) on granitic bedrock above limit of late Wisconsin Drift. Olivine phyric basalt with significant evidence of wind abrasion (pitted surfaces and ventifation). Sample is pyramidal, 15 cm at base and 120 cm high. 5-8 % 1-5 mm olivine in massive black matrix.

Blue Glacier
BAK90-141

Basalt cobble in drift above late Wisconsin limit at Blue Glacier region. Vesicular basalt cobble, 40 cm long x 30 cm wide x 10 cm long, with 5 % 1-3 mm olivine phenocrysts.

Howchin Glacier
BAK90-247

Older Ross Drift basalt boulder, 15 cm wide x 15 cm long x 10 cm high, partially buried in moraine. 15% 0.1-5 mm olivine grains in grey, fine grained ground mass. Sample collected from low morainal feature parallel to, but above and outside of, the Late Wisconsin Drift limit.

BAK90-249-2

Older Ross Drift basalt boulder from same location as BAK90-247. 13 cm long x 10 cm wide x 8 cm high. Contains ~ 3-4 % olivine with several olivine megacrysts or xenoliths up to 1.5 cm diamater, in grey-black aphanitic matrix.

Garwood Valley
BAK90-263

Older Ross Sea Drift basalt, collected at contact of surface of older drift with metamorphic bedrock. Pyramidal in shape, 11 cm at base and 9 cm high; ~ 5% olivine, 5% clinopyroxene, with two visible olivine and clinopyroxene megacrysts on surface.

BAK90-262-1

Same location as BAK90-263. Basalt boulder, 20 cm x 20 cm x 10 cm high with irregular but approximately flat upper surface. ~ 5 % up to 10 mm clinopyroxene and 2-3 % 0.5-1mm olivine in grey aphanitic matrix.

Chapter 7

Depth profiles of cosmogenic ^{3}He, ^{10}Be, and ^{26}Al in Antarctic Sandstone Bedrock

Introduction

The accumulation of cosmic-ray produced nuclides in terrestrial rocks provides a new geochronometer that has great potential for dating exposed geological and archeological surfaces. Although application of cosmogenic nuclides to geological problems is beginning (e.g., Kurz et al., 1990; Phillips et al., 1990; Brown et al., 1991; Nishiizumi et al., 1991; Phillips et al., 1991; Brook et al., 1993), further understanding of cosmogenic nuclide systematics, including production mechanisms, production rates, and noble gas diffusion, is necessary to fully utilize cosmogenic nuclides in surface exposure studies.

Depth profiles of cosmogenic nuclides in terrestrial bedrock can shed light on many of these processes (e.g., Kurz, 1986; Brook et al., 1992; Brown et al., 1992; Olinger et al., 1992). For example, cosmogenic nuclides like ^{3}He, ^{10}Be, and ^{26}Al can be produced by both neutrons and muons in terrestrial rocks (see Chapter 1). Although the muogenic component in most cases appears to be a minor percentage (< 10-15 %) of the total (Kurz, 1986; Nishiizumi et al., 1989; see Chapter 1) the production rates of cosmogenic nuclides *via* this mechanism are not well determined. Muons are weakly interacting particles relative to neutrons; the exponential path length for muon stopping is approximately an order of magnitude greater than for neutron interactions (Lal, 1987). Therefore, the importance of muogenic production of cosmogenic nuclides increases with depth in rocks (Kurz, 1986; Lal, 1987) and depth profiles can potentially separate the muon-produced and neutron-produced components of cosmogenic nulcide production. Constraining the production rates due to both mechanisms is important for further application of cosmogenic nuclides to geological problems.

Depth profiles can also potentially shed light on processes affecting the retention of cosmogenic noble gases in minerals. For example, Trull et al. (1991), Brook and Kurz (1993), and Trull et al. (1993), suggested that solar heating of rock surfaces might cause accelerated loss of ^{3}He due to diffusion. Because the importance of solar heating should decrease with depth in the rock (Trull et al., 1993), this effect, if significant, should be evident in drill core data.

This chapter describes results from two bedrock cores taken from sandstone bedrock surfaces in the Antarctic Dry Valleys region. The goal was to use depth profiles of ^{3}He, ^{10}Be ($t_{1/2}=1.6 \times 10^{6}$ yr), and ^{26}Al ($t_{1/2}=7.2 \times 10^{5}$ yr) in the same samples to further understand production mechanisms of these nuclides and loss mechanisms of cosmogenic ^{3}He in quartz. ^{3}He results for one of the two cores (KBA89-77) were presented by Brook et al. (1992) and the ^{10}Be, and ^{26}Al data for this core were published originally by Brown et al. (1992).

Methods

Samples

The cores were drilled in two sandstone bedrock surfaces in the Asgard range of the Transantarctic Mountains near McMurdo Station (Fig. 1). The first (KBA89-77), collected in the 1989-90 field season, came from a flat, exposed, bedrock terrace on a saddle above the east wall of Arena Valley at 1700 m altitude and was drilled in the Beacon Heights Orthoquartzite, an upper Devonian formation of the Beacon Supergroup (McElroy and Rose, 1987). This rock is a 95-100 % quartz, fine-medium grained, well-sorted, sandstone with well-rounded 0.1-0.7 mm grains and a small percentage of interstitial clay minerals and iron oxide cement. The second core (BAK90-79)

was collected from a flat bedrock surface at 2065 m altitude near the summit of Mt. Fleming in the 1990-91 field season, and was drilled in the Feather Conglomerate, a Permo-Triassic formation of the Beacon Supergroup. This surface is on a broad terrace, ~ 1 km in diameter, and is near outcrops of the late Pliocene Sirius Group, that have been interpreted to be as young as 3 myr based on biostratigraphic evidence (McKelvey et al., 1991). This rock is a coarse-grained, poorly sorted sandstone, with ~90-95 % angular quartz grains from 0.1-2mm diameter, with 5-10 % interstitial clay minerals and minor carbonate cement.

The cores were collected with a gasoline powered JKS-Bowles Model 10 rock drill with a diamond impregnated coring bit and extensions. A water-ethanol mixture was used as a cutting fluid and drill coolant. Sections of 5-20 cm were cored and removed sequentially.

Subsamples of 2-3 cm were cut from individual sections at approximately equally spaced intervals. Rock densities were determined by weighing core sections and measuring exterior dimensions to calculate volume. No significant variations of density with depth were apparent from these measurements. Mean densities were 2.1 g cm^{-3} for KBA89-77 and 2.2 g cm^{-3} for BAK90-79. Rock depths in units of g/cm^2 were calculated using measured densities and mean depths of the subsamples. These units are used throughout to normalize for density variations and allow comparison with other studies. Core recovery was generally complete in the sense that there were few gaps in the sections that represented void-spaces in the rocks. Both cores are quite friable and material was lost during recovery of the samples, making the density calculation necessary (as opposed to weighing the recovered pieces).

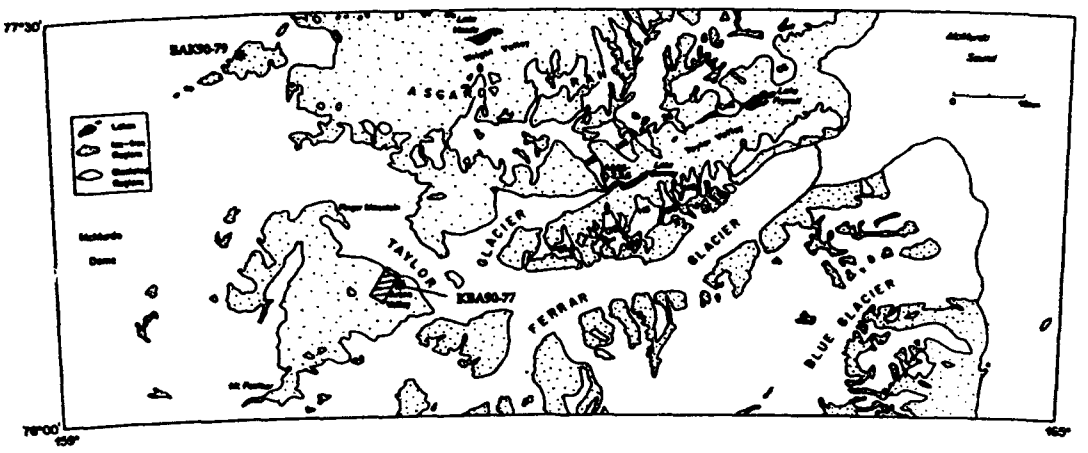

Figure 1. Location map showing locations of two bedrock cores described in text. KBA89-77 was collected in 1989 at an altitude of 1700 m. BAK90-79 was collected in 1990 at an altitude of 2065 m.

Analytical Methods

Helium isotopes were measured in handpicked, sieved, size fractions of the sub-sampled sections. For KBA89-77, the 0.5-0.7 mm diameter fraction was selected; these are the largest grains in the rock. All grains analyzed were whole, rounded quartz grains; multi-grain aggregates of smaller grains, common in sieved fractions, were excluded. The 0.2-0.3 mm fraction was also separated from some samples from this core to examine the effect of grain size on cosmogenic ^{3}He concentrations. In BAK90-79 both 0.5-0.7 mm and 1.0-1.3 mm grains were analyzed. Helium isotopes were measured at WHOI and all samples were melted in a resistively heated ultra-high vacuum furnace with a tantalum crucible. Gas processing and mass spectrometry are described in Chapter 2.

^{10}Be and ^{26}Al were measured at the AMS facility in Gif-sur-Yvette, France. Because several grams of material are needed, a larger range of grain sizes were used than in the ^{3}He analysis. The KBA89-77 measurements were made by Brown et al. (1992) and used either the 0.5-1.0 or 0.25-1.0 mm size fraction. Analytical techniques for the KBA89-77 samples are described by Brown et al. (1992). The BAK90-79 samples were processed in Woods Hole using essentially the same techniques except that the samples were not sieved because adhering clay minerals were not effectively removed by sieving. Instead, fine material was removed by rinsing with distilled water and decanting fine material in suspension. Removal of fine material is a precaution against meteoric ^{10}Be contamination that may be present on mineral surfaces (Brown et al., 1991). Li was measured in surface samples collected near the core sites by flame atomic absorption spectrophotometry using methods described in Chapter 2. Li concentrations were measured in a 1 N HCl leach (70°C) and in the residue remaining from the leach step. For

further information about analytical methods see Brown et al. (1992) and Chapter 2.

Results

^{3}He, ^{10}Be , and ^{26}Al data for the two cores are tabulated in Tables 1-4 and Li concentrations are tabulated in Table 5. A small correction was made to the total ^{3}He concentrations to account for nucleogenic ^{3}He produced by the thermal neutron reaction $^{6}Li(n,\alpha)T$-^{3}He, where the thermal neutrons are indirect products of U and Th decay *via* (α,n) reactions (Morrison and Pine, 1955; Trull et al., 1991; Brook and Kurz (1993) [Chapter 3]). The correction employs the measured ^{4}He concentration and an assumed $^{3}He/^{4}He$ ratio for nucleogenic production of 0.011 ± 0.004 R_a (where R_a is the atmospheric $^{3}He/^{4}He$ ratio: 1.384×10^{-6}). This ratio is based on a step-heating experiment of a Beacon Supergroup quartz sandstone sample from Arena Valley (Trull et al., 1991). The exact nucleogenic $^{3}He/^{4}He$ production ratio depends on the ratio of Li/(Th+U) and may vary from sample to sample. The correction is quite small, however (see Tables 1 and 3) and uncertainty in the exact correction does not contribute large uncertainties to the total cosmogenic ^{3}He concentrations (see Chapters 1 and 3).

To check the validity of the correction, the top sample from KBA89-77 was measured in replicate. Because replicate analyses of quartz samples, based on this and previous work (Brook and Kurz, 1993 [Chapter 3]), have widely varying ^{4}He concentrations but constant ^{3}He concentrations they allow an independent constraint on the nucleogenic $^{3}He/^{4}He$ ratio. Figure 2 illustrates this approach, plotting $1/^{4}He$ vs. the $^{3}He/^{4}He$ ratio (normalized to the atmospheric ratio) for four replicate analyses of the top section of core KBA89-77 and for two similar sandstone samples from moraine boulders in

Arena Valley used as internal mass spectrometer standards (data in Chapter 2). Spallation produces helium with a $^3He/^4He$ ratio of ~0.2 (Mazor et al., 1970), but in quartz radiogenic ^4He concentrations are several orders of magnitude greater than cosmogenic ^4He concentrations, and the latter can be ignored. As a result, the linear relationship in Figure 2 can be interpreted as a mixture of nucleogenic and cosmogenic helium and the y-intercept gives the $^3He/^4He$ ratio of the nucleogenic component. For KBA89-77 this analysis gives a nucleogenic $^3He/^4He$ ratio of -0.05±0.01, suggesting that although the correction for nucleogenic ^3He is not well constrained, it is insignificant in the core samples. The negative intercept may indicate the presence of a minor third component, however, its identity can not be constrained with these data. For the two quartz standards the y-intercept ratios are slightly higher (Fig. 2) but still quite close to the value used in the correction. For BAK90-79 enough replicate analyses for the curve fitting in Fig. 2 are not available, but examination of the duplicate measurements in Table 3 indicates that the nucleogenic correction cannot be significant. In one duplicate (KBA89-77-11, 1-1.3 mm grains) the cosmogenic ^3He concentration is **higher** in the duplicate with the **higher** ^4He concentration, suggesting that the nucleogenic correction for ^3He cannot be an underestimate. In KBA89-77-8 (0.5-0.7 mm grains), despite the 35 % difference in ^4He concentration in the replicate analyses, the cosmogenic ^3He concentrations are within 1-sigma of each other. The poor agreement for the KBA89-77-11 replicates is probably due to the poor quality of the grains available for the second replicate, which has a significantly lower concentration than the first. Only a small sample (~ 20 mg) was available and the grains were significantly fractured and contained some tightly cemented smaller grains. The low concentration may be a result of diffusive loss and this point is not used in the curve fitting below.

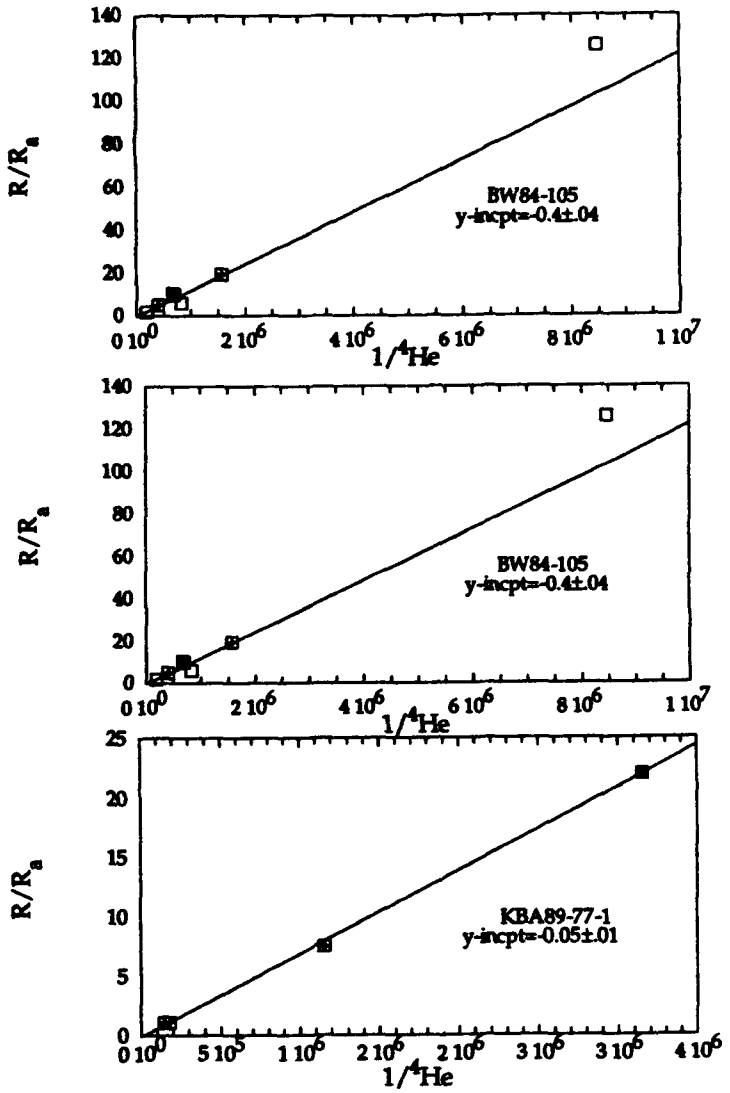

Figure 2. Plots of $1/^4He$ vs $^3He/^4He$ ratio for replicate analyses of two sandstone standards and replicates of top section of KBA89-77. Due to heterogeneity in ^4He concentrations and constant cosmogenic ^3He concentrations the data fall on a straight line. The y-intercept corresponds to an infinite ^4He concentration and is interpreted as the $^3He/^4He$ ratio for nucleogenic production of ^3He by the reaction $^6Li(n,\alpha)T\text{-}^3He$. See text for further discussion.

Exponential profiles were fit to the ^{10}Be and ^{26}Al data for both cores, the ^{3}He data for both 0.5-0.7 mm and 1-1.3 mm grains in BAK90-79 and the 0.5-0.7 mm grains in KBA89-77 (Figs. 3 and 4), assuming the relationship:

$$N = N_0 \exp(^{-d}/_{L}) \qquad (1),$$

where N_0 is the surface concentration, N is concentration at depth d (d in g cm^{-2}), and L is the exponential attenuation length (Kurz, 1986; Brook et al., 1992; Brown et al., 1992). A weighted least squares method was used for the curve fitting. ^{10}Be and ^{26}Al attenuation lengths for KBA89-77 are 145 ± 5 and 153 ± 13 g cm^{-2}, respectively, and for BAK90-79 the values are 145 ± 6 and 152 ± 5 g cm^{-2}. The ^{10}Be attenuation length in KBA89-77 is slightly lower than reported by Brown et al. (1992) for the same data (156 ± 13 g cm^{-2}), presumably due to slight differences in curve fitting.

The ^{3}He attenuation lengths for both size fractions in BAK90-79 are slightly lower, 152 ± 7 g cm^{-2} for 1-1.3 mm grains and 135± 6 g cm^{-2} for 0.5-0.7 mm grains. The two profiles are offset, presumably due to greater loss of ^{3}He from the smaller grains (see below). The ^{3}He results from 0.5-0.7 mm grains in KBA89-77 are unusual in that they give a much longer attenuation length, 227 ± 14 g cm^{-2} (Fig. 3). Samples of 200-300 micron grains from three different depth intervals in this core (Fig. 3; Table 1) verify the observation from the BAK90-77 core that although smaller grains have lower ^{3}He concentrations the offset between different grain sizes does not appear depth dependent. Small deviations from the exponential fits are apparent in Figs 3 and 4. In the ^{3}He, ^{10}Be, and ^{26}Al data for KBA89-77 these deviations are apprently correlated and may reflect density variations in the rock surface.

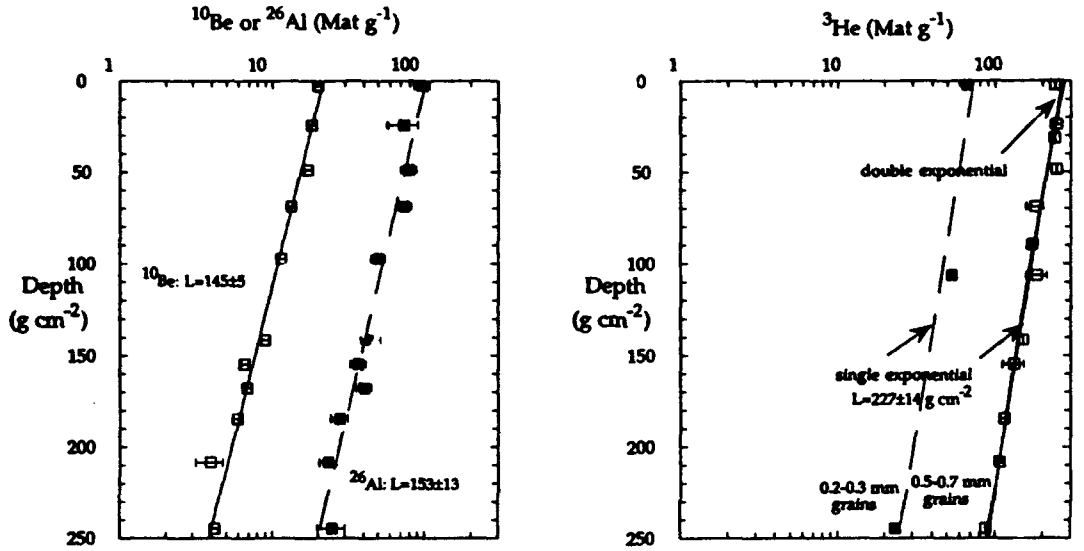

Figure 3. Depth profiles of ^{3}He (0.2-0.3 mm and 0.5-0.7 mm grains) ^{10}Be and ^{26}Al in core KBA89-77. Exponential scale lengths for ^{10}Be and ^{26}Al are 145 ±5 and 153 ± 13 g cm^{-2}, respectively. The ^{3}He exponential scale length is significantly greater, 227±14 g cm^{-2}. Dashed line in right hand figure is an exponential curve fit to the three data points for 0.2-0.3 mm grains and has a scale length identical to that for the larger grains. The curve labled "double exponential" is a curve fit assuming two production mechanisms, one with an exponential scale length of 1700 g cm^{-2} (muons) and one with a scale length of 150 g cm^{-2} (neutrons). The results of this fit suggest that 214 ± 15 x 10^{6} at g^{-1} of the ^{3}He in the surface was produced by neutrons and 61 ± 8 10^{6} at g^{-1} was produced by muons. See text for further details.

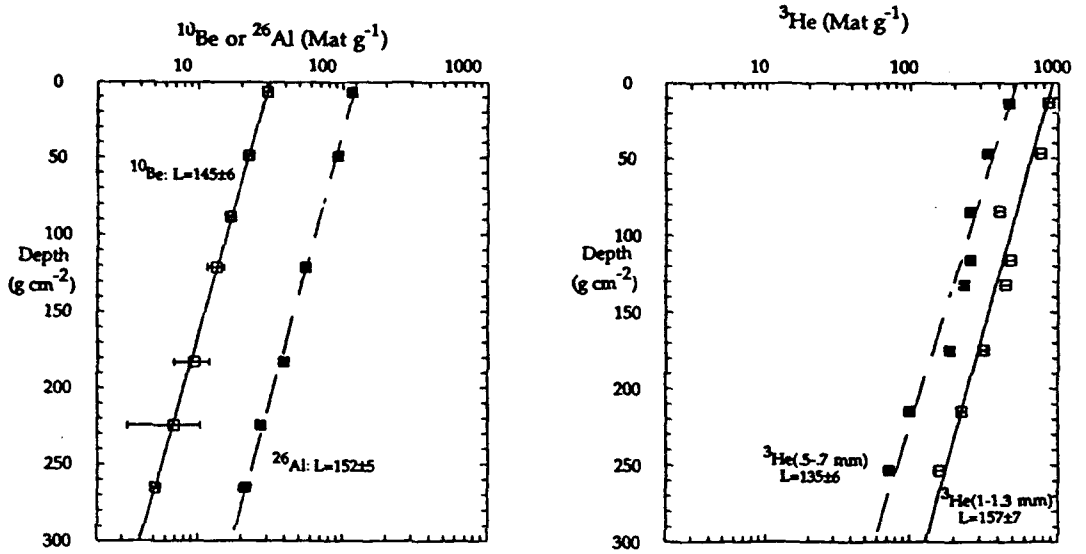

Figure 4. Depth profiles of ^{3}He (500-700 micron and 1000-1300 micron grains), ^{10}Be, and ^{26}Al in BAK90-79. Exponential scale lengths for ^{10}Be and ^{26}Al are 145 ± 6 and 152 ± 5, respectively. Scale length for ^{3}He in 500-700 micron grains is 135 ± 6 g cm^{-2} and 157 ± 7 g cm^{-2} for 1-1.3 mm grains.

In BAK90-79 the ^{3}He and ^{10}Be or ^{26}Al data do not appear correlated but the^{3}He data for 0.5-0.7 and 1.0-1.3 mm grains do vary about the fitted exponential curve in a similar fashion. The origin of the effect is not clear but one possibel explanation is that the variations reflect small errors in correcting for nucleogenic ^{3}He.

Discussion

^{10}Be and ^{26}Al Attenuation Lengths

Brown et al. (1992) concluded from KBA89-77 that the attenuation lengths for ^{10}Be and ^{26}Al are not significantly different from each other. This conclusion is confirmed by the results from the second core. These results are important for two reasons. First, the agreement between the two cores and the excellent fit of the exponential profiles for the ^{10}Be and ^{26}Al data indicate that the density measurements are valid and the assumption of constant density throughout the cores is valid. This permits simpler interpretation of the variability observed in ^{3}He attenuation lengths.

Second, as suggested by Brown et al. (1992), the agreement between attenuation lengths for ^{10}Be and ^{26}Al indicate that the $^{26}Al/^{10}Be$ ratio does not change significantly with depth. This allows the ratio, which should change as a function of time due to the different half-lives of the two nuclides, to be used as a chronometer independent of shielding by surrounding topography, erosion, or changes in production rate (Brown et al., 1992). Present analytical uncertainties limit this approach but future technical improvements should allow broad applicability.

The only other report of ^{10}Be or ^{26}Al depth profiles for comparison is a ^{10}Be profile of Olinger et al. (1992) from a 7m core in the Bandolier Tuff, in New Mexico. They reported a much higher value of 178 g cm^{-2} (no quoted uncertainty). The origin of the discrepancy between the results for this core and the Antarctic ^{10}Be data presented here is not clear but it may reflect differences in latitude of the samples (e.g. Olinger et al., 1992). Atmospheric neutron monitor data suggest that the attenuation length for cosmic ray neutrons increases with decreasing geomagnetic latitude (Lingenfelter, 1963), presumably due to the increase in cosmic ray cut-off rigidity with decreasing latitude. The core described by Olinger et al. (1992) is also significantly longer than the cores described here. The longer scale length for ^{10}Be in that core may reflect production of ^{10}Be by muons, which, as discussed above, is relatively more important at greater depths.

^{3}He Attenuation Lengths and Production Mechanisms

The ^{3}He data for KBA89-77 are difficult to explain because the high scale length, 227 ± 14 g cm^{-2}, is much greater than expected for interactions with neutrons, e.g., ~150 g cm^{-2} (Lal and Peters, 1967; Mabuchi et al., 1971). It is also higher than ^{3}He production attenuation lengths of 160-165 g cm^{-2} measured in Hawaii (Kurz, 1986) and higher than the ^{3}He attenuation lengths in BAK90-79. There are at least two possible explanations for this result, each with implications for using cosmogenic nuclides for exposure age-dating.

Diffusion of ^{3}He could cause this effect if diffusive loss were depth dependent. Such loss might be driven by solar heating of rock surfaces (Brook et al., 1992; Trull et al., 1993). Production of ^{3}He by interactions with muons

(Chapter 1) could also produce this effect since the scale length for muon interactions is considerably longer than for neutron interactions.

Diffusion. A number of studies have demonstrated the ^{3}He is not quantitatively retained in quartz on million year time scales (Graf et al., 1991; Trull et al., 1992; Brown et al., 1991; Staudacher and Allegre, 1991; Brook and Kurz, 1993 [Chapter 3]). Brook and Kurz (1993) [Chapter 3] and Trull et al. (1991) showed that ^{3}He loss occurs at a greater rate than predicted by experimental measurements of ^{3}He diffusion in quartz (Trull et al., 1991). ^{3}He loss in 0.5-1 mm quartz grains with ^{10}Be exposure ages of ~ 2 myr is approximately 30-50% (Chapter 5), while diffusion measurements predict less than 10 % loss over this time period.

As suggested above, diffusion might explain the anomalous depth profile if the loss process was depth dependent, e.g., producing greater loss at the surface than at depth. In principle, solar heating of the rock surface could cause such an effect, and elevated temperatures of Dry Valley rock surfaces due to solar heating have been documented by biologists studying endolithic microorganisms (e.g., McKay and Friedman, 1985). These studies demonstrate that short-term variations in insolation cause significant increases (up to 25 degrees C) in rock temperatures on sub-diurnal time scales. These measurements extend only a few centimeters at most into the surface, however, and show that these sub-diurnal temperature variations are damped significantly over that distance.

Although diffusion was originally considered as a mechanism for producing the anomalous profile (Brook et al., 1992), the present measurements suggest that this is incorrect. Loss due to diffusion should be a function of grain size (Trull et al., 1991) and should result in different

apparent attenuation lengths for different grain sizes. The ^{3}He measurements in different size fractions at the same depth intervals in both cores show that although smaller grains have lower concentrations, there is no such depth dependent pattern in the difference between concentrations in large and small grains (Figs 3 and 4, Tables 1 and 3). In fact, in BAK90-79, the exponential scale length is slightly lower in the smaller grains (Fig. 4), the opposite of the effect expected if loss is enhanced at the surface. The lower concentrations in the smaller grains at all depths indicate that diffusion is significant, but it does not appear to be dependent on depth in either core. Although there are less data for two size fractions in the KBA89-77 core, where the unusual profile exists, it seems unlikely that solar insolation could affect only one of two surfaces from the same region. In addition, recent modeling studies of thermally driven diffusion of ^{3}He in quartz (Trull et al., 1993) suggests that significant ^{3}He loss caused by sub-diurnal heating should be confined to the upper 10-20 cm of the core. The depth profile for ^{3}He in 0.2-0.3 mm grains in KBA89-77 (Fig. 3) is identical to that for 0.5-0.7 mm grains, indicating that loss at the surface is not greater than loss at depth.

^{3}He Production By Muons. The primary production mechanism of ^{3}He in terrestrial rocks is spallation by cosmic ray neutrons, but muons also produce small quantities of ^{3}He through a variety of mechanisms. Production of ^{3}He by muons could produce a depth profile of the type observed because muons have a much longer exponential path length in rocks than neutrons. In fact, Kurz (1986) explained an anomalous ^{3}He profile in a Hawaiian lava flow by invoking this mechanism. Experimental measurements show that the stopping rate of muons in sand has an exponential path length of ~ 1700 g cm^{-2} (Hall and Richmond, 1974). In addition, Hampel and Kirsten (1975)

calculated a similar profile for rocks although they suggest, as do Bilokon et al. (1989), that over the first ~500 g cm^{-2} the muon stopping rate in rocks increases slightly or at least remains constant. The scale length for production of ^3He by muons used by Lal (1987) in calculating ^3He production rates is ~ 1500 g cm^{-2}, and is based on observations of nuclear disintegrations in nuclear emulsions exposed underground (George and Evans, 1950). The results of Hall and Richard (1974) are used here because they were obtained in material similar to the Beacon Supergroup sandstones and because they are based on experimental measurements *in situ* in that material.

As described above, the combination of the neutron and muon component would produce an exponential profile with an apparent scale length between 150 and 1700 g cm^{-2}, depending on the relative contribution of both mechanisms. Because of the differences in the scale lengths, erosion is also a factor; the higher the surface erosion rate, the more important the muon component will be. The erosion rate of this surface, based on the ^{10}Be and ^{26}Al measurements, is ~ 1×10^{-4} g cm-2 yr-1 (Brown et al., 1992). This value is somewhat higher than values of 1-2 x 10^{-5} g cm^{-2} yr^{-1} suggested by Brown et al. (1991) and Nishiizumi et al. (1991) for other Dry Valley glacial deposits. However, due to the exposed position of the outcrop this rate is not unreasonable, and corresponds to the removal of ~ 50 cm of material in one million years (assuming a density of 2 g cm^{-3}).

Constraining the importance of ^3He production by muons also requires knowledge of production rates due to muon and neutron interactions. These rates are not well known (Chapter 1), although several measurements of the total rate of ^3He production (~ 120 at g^{-1} yr^{-1} at sea level, > 60° N geomagnetic latitude; see Chapter 1) are available (Cerling, 1990; Kurz et al., 1990). The most important cosmogenic ^3He production mechanisms are spallation by

cosmic ray neutrons, capture of cosmic ray thermal neutrons by ^{6}Li (producing ^{3}He *via* the reaction $^{6}Li(n,\alpha)T\text{-}^{3}He$), spallation reactions caused by neutrons produced by muon interactions, and thermal neutron capture in ^{6}Li of thermal neutrons produced by muon interactions (Lal, 1987; Kurz, 1986). The former two mechanisms should have a scale length of ~ 150 g cm^{-2}, the latter ~ 1700 g cm^{-2}.

Of the production mechanisms due to muons only production of ^{3}He from muogenic thermal neutrons can produce appreciable amounts of ^{3}He in most terrestrial rocks. Direct muon capture in lithium is not important, producing less than 10^{-3} at g^{-1} yr^{-1} of ^{3}He (Kurz, 1986; Lal, 1987). Neutrons produced in muon capture reactions (see Chapter 1) have energies of 5 to several tens of MeV (Charalumbus, 1971; Lal, 1987) and have not been considered energetic enough to produce ^{3}He by spallation in common rocks (Lal, 1987). ^{3}He-producing spallation reactions with lower energy thresholds (3-8 MeV) are discussed by Lal (1987), but their targets (^{7}Li, ^{14}N, ^{19}F, ^{40}K, ^{50}V, ^{40}Ca, ^{58}Ni, ^{64}Zn) are not significant in quartz. Muogenic thermal neutrons produce ^{3}He *via* the $^{6}Li(n,\alpha)t\text{-}^{3}He$ reaction, and the rate varies with rock composition, depending on the thermal neutron flux, lithium concentration, and the concentrations of all other thermal neutron absorbers and their thermal neutron capture cross sections. The production rate can be calculated with equations 2 and 3:

$$f = \frac{[Li]\sigma_{Li}}{\sum [X]_i \sigma_i} \qquad (2)$$

$$P_{^{3}He} = fF_{n-m} \qquad (3),$$

where f is the fraction of thermal neutrons that produce ^3He, σ is the thermal neutron capture cross section, [X] denotes concentration, $P_{^3He}$ is production rate of ^3He from muon-produced thermal neutrons, and $F_{n\text{-}m}$ is the muogenic thermal neutron production rate.

To calculate the ^3He production rate from muogenic thermal neutrons a muon stopping rate in sand of 195 muons g^{-1} yr^{-1} (Hall and Richmond, 1974), a neutron multiplicity in muon capture of 1.5 (Charalumbus, 1971) and an f value of 0.017 (calculated for 5 ppm Li in quartz assuming a composition of Si, Li, and O only - see Table 5) were used to arrive at a sea level production rate of 5 at g^{-1} yr^{-1}. This is a maximum estimate because the effects of other thermal neutron absorbers are not considered.

Time and Depth Dependence of Muon Production. The ^3He data for the KBA89-77 core can be modeled as the sum of exponential production terms for ^3He production by muons and neutrons:

$$P(^3He_t) = P(^3He_m)e^{(-\rho/1700)} + P(^3He_n)e^{(-\rho/150)} \qquad (4),$$

where P is production rate, t is total, m is muon, n is neutron, and 150 and 1700 g cm^{-2} are attenuation lengths for production by neutrons and muons, respectively. Fitting equation 4 to the ^3He profile for KBA89-77 gives 214 ± 15 x 10^6 at g^{-1} ^3He for the neutron component and 61 ± 8 x 10^6 at g^{-1} for the muon component, suggesting that 22 ± 3 % of the total ^3He at the surface was produced by muons (Fig. 3).

At face value, this analysis suggests that muons are more efficient at producing ^3He than previous calculations indicate. Scaling the sea level production rate of 5 at g^{-1} yr^{-1} ^3He produced by muons (calculated above) to

1700 m, assuming an exponential path length in the atmosphere of 250 g cm^{-2} (Conversi, 1950; Nishiizumi et al. 1989), gives a production rate at altitude of 11 at g^{-1} y^{-1} at 1700 m. Assuming the total ^3He production rate (from neutrons and muons) at sea level is 118 at g^{-1} yr^{-1} (Chapter 1) then the sea level neutron-produced component is 113 at g^{-1} yr^{-1} and scales to 505 at g^{-1} yr^{-1} at 1700 m (using scaling from Lal, 1991). This calculation therefore suggests that only 2 % of the total ^3He could be produced by muons at the altitude of the core.

Erosion changes the fraction of muon-produced ^3He in the core due to differences in muon and neutron attenuation lengths, however. For a stable isotope like ^3He, assuming no diffusion, the effect of erosion can be described by:

$$[^3He] = \frac{PL}{E}(1 - e^{-\rho(E/L)}) \qquad (5),$$

where L is the attenuation length for ^3He production by muons or neutrons and E is erosion rate in g cm^{-2} yr^{-1}. Because L for neutrons (150 g cm^{-2}) is << L for muons (1700 g cm^{-2}), erosion changes the fraction of the total ^3He in the rock that was produced by muons. Figure 5 shows the development of a depth profile with time over 300 g cm^{-2} for the combination of the two production mechanisms and shows that the profile becomes steeper with time, reaching a steady state after several tens of millions of years, with an apparent single exponential scale length of 230 g cm^{-2}. Figure 5 also compares the model profiles with the measured profiles for ^3He in the two cores. Figure 6 shows the apparent exponential scale length as a function of time for different erosion rates, showing that the steady state value is not a function of erosion rate, but that erosion changes the time needed to reach steady state.

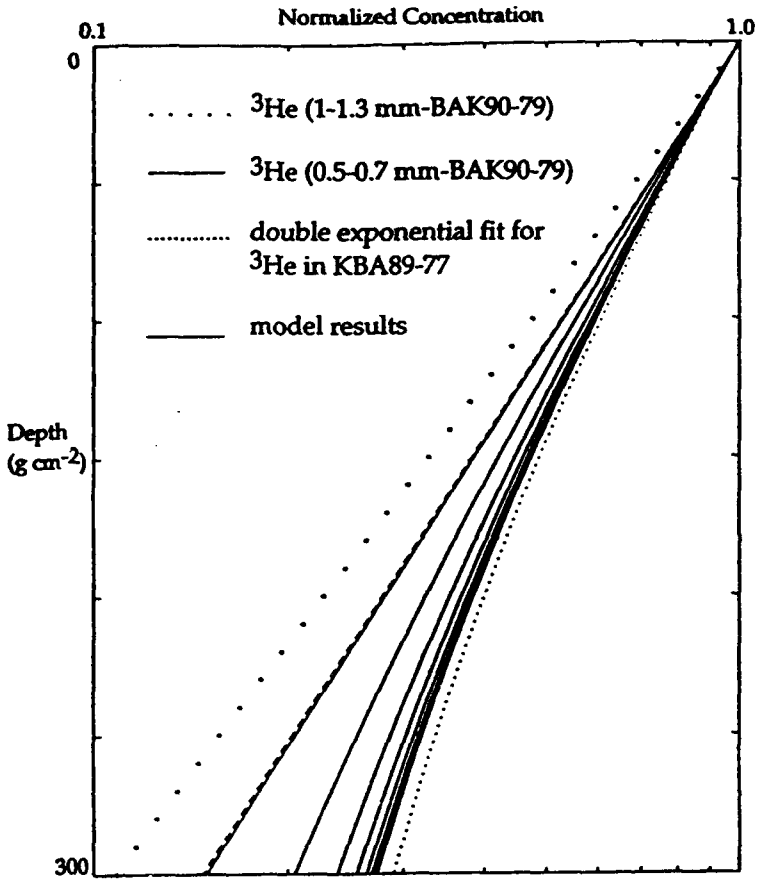

Figure 5. Calculated depth profiles as a function of time (solid lines) using ^{3}He production rates by muons and neutrons discussed in text and assuming an erosion rate of 1 x 10^{-4} g cm^{-2}. Time increases from left to right, starting at 0 and increasing to 100 myr with a time step of 10^7 yr. Scale lengths increase with time because muons have a significantly higher scale length for interactions than neutrons (1700 g cm^{-2} vs. 150 g cm-2). The profile reaches a steady state that corresponds to an apparent single exponential scale length of ~ 230 g cm^{-2}, calculated by fitting an exponential curve to the results. Other profiles on the plot show the ^{3}He depth dependence shown in Figs. 3 and 4.

These values were calculated by extrapolating the muon and neutron produced ^3He concentrations downward using the appropriate exponential attenuation lengths and fitting an exponential curve to the results. As shown in Fig. 3 this approach gives an excellent fit. Figs 5 and 6 indicate that this combined process of erosion, ^3He production by muons, and ^3He production by neutrons could, in theory, explain the anomalous ^3He profile. However, this model predicts steady state concentrations that range from 8.8×10^8 at g^{-1} to 8.8×10^{10} at g^{-1}, significantly higher than the measured surface concentration of $\sim 2.8 \times 10^8$ at g^{-1} (Fig. 3).

The reason that the model overestimates the measured concentration is that the above discussion ignores the effects of diffusion on the development of the depth profile. Diffusion could change the temporal development of the ^3He profile because the loss process essentially limits the "memory" of the profile for past production, in a manner analogous to radioactive decay. Diffusion of cosmogenic ^3He in quartz has been shown to be a complex process and laboratory measurements of diffusivity, which suggest low diffusion rates on million year time scales (Trull et al., 1991), do not accurately describe the observed loss (Trull et al., 1991; Brook and Kurz, 1993 [Chapter 3]). Previously observed grain size dependence of ^3He concentrations in quartz and a comparison of ^{10}Be ages and ^3He ages calculated with the data in Chapter 5 both suggest effective ^3He diffusion coefficients in quartz in the Dry valleys of 10^{-19} to 10^{-17} cm^2 s^{-1} (e.g., Brook and Kurz, 1993). These values are one to three orders of magnitude above the value of $\sim 10^{-20}$ g cm^{-2} s^{-1} predicted by extrapolating results of step-heating experiments to 0 degrees C (Trull et al., 1991).

The combined effects of production of ^3He by muons and neutrons, diffusion, and erosion can be described in differential form in an analogous way to the production and diffusion problem discussed by Trull et al. (1991):

$$\frac{dN}{dt} = D\nabla^2 N + P_m e^{-E/L_m'} + P_n e^{-E/L_n'} \qquad (6),$$

where N is concentration, t is time, P_m and P_n are ^3He production rates by muons and neutrons, respectively, and L_n and L_m are the respective attenuation lengths. The first term describes loss of ^3He due to diffusion and the second two terms describe the production rate as a function of time in the sample as it is "unburied" by erosion.

This equation was solved with a finite-difference method similar to the solution described in Trull (1990). The model was run from $T=1x10^8$ yr to the present and ^3He depth profiles over 300 g cm^{-2} depth were calculated from the results. Resulting apparent exponential scale lengths are plotted in Fig. 7 as function of time. Solutions for values of D between 10^{-19} to 10^{-17} cm^2 s^{-1} show that a profile with maximum scale length of 210 g cm^{-2} can be produced when diffusion is accounted for. As in the "no diffusion" case the time to reach near-steady state is relatively long, up to ~20 myr for $D=1x\ 10^{-19}$ g cm^{-2}. The predicted steady-state ^3He concentrations are also listed in Figure 7 and show that given the production rates used in the calculation, the model can not reproduce both the concentration (2.8×10^8 at g^{-1}) and apparent attenuation length (227 g cm^{-2}) observed in the core. Reasonable values of D and P_m can be chosen that do reproduce the observed profile, however. For example, increasing the fraction of total production due to muons to 10% roughly reproduces the observed profile at steady state for a value of $D=2 \times 10^{-18}$ cm^2 s^{-1}.

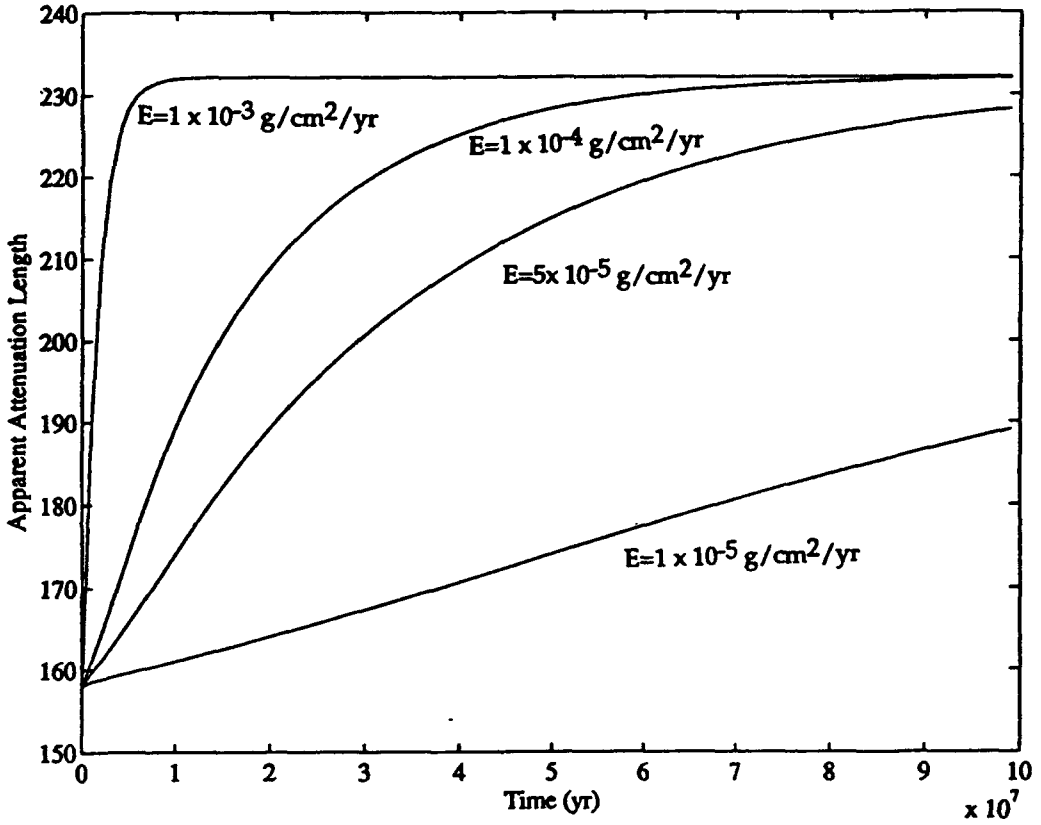

Figure 6. Total apparent exponential scale length as a function of time for ^3He production by neutrons and muons, for erosion rates of $1x10^{-5}$, 5×10^{-5}, $1x10^{-4}$, and $1x10^{-3}$ g cm^{-2} yr^{-1} (bottom to top). These curves were calculated using the production rates at 1700 m calculated in the text and assume no loss of ^3He due to diffusion. Corresponding steady state surface concentrations range from 8.8×10^8 to 8.8×10^{10} at g^{-1}, significantly greater than the measured concentration of 2.8×10^8 at g-1. This discrepancy is due to the fact that this simple model does not include the effects of loss of ^3He due to diffusion (see Fig. 7).

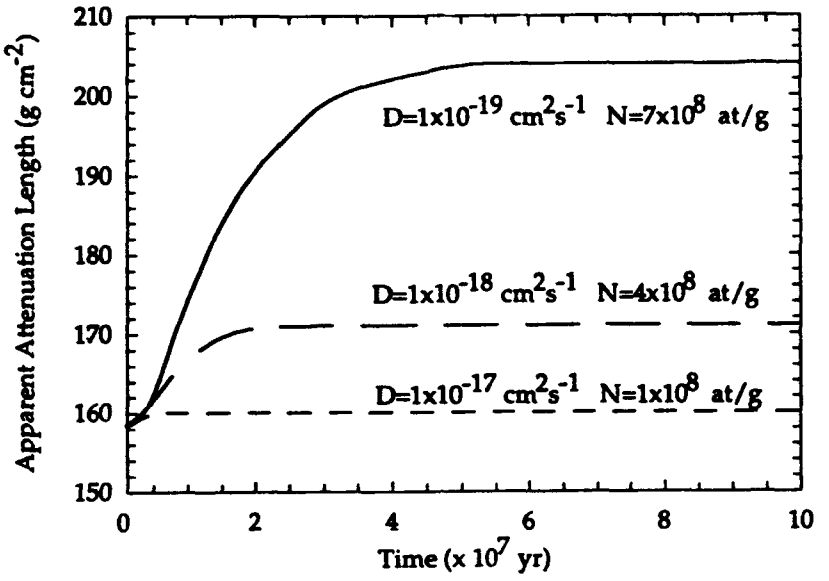

Figure 7. Apparent exponential scale lengths calculated from a finite difference solution for a model of erosion, production of ^{3}He by muons and neutrons, and diffusion, as a function of time. Steady state concentrations are included on the figure. As discussed in the text the model cannot reproduce the concentration (~2.8 x 10^{8} at g^{-1}) and attenuation length (227 g cm^{-2}) observed in core KBA89-77.

This analysis suggests that the production rate of ^{3}He by muons is higher than predicted based on the theoretical calculations described above. The origin of this discrepancy is not clear. It is possible, however, that production rates have been underestimated. In the discussion of production mechanisms given earlier it was assumed that ^{3}He production by low energy spallation due to neutrons produced in muon capture reactions was not significant. Cross sections and excitation functions for isotope production by neutron induced spallation are not well known, and are often based on cross sections for proton interactions (Lal, 1991). As a result, it is possible that the importance of this mechanism has been underestimated. Comparison of excitation functions for ^{3}He production by neutrons and protons in aluminum offer support for this suggestion. Threshold energies for ^{3}He production by neutrons in ^{27}Al are ~ 12 MeV (Qaim and Wolfe, 1982), while Walton et al. (1976) reported values of ~ 25 MeV for production of ^{3}He by protons. If this difference between proton and neutron induced threshold energies is a general effect in most common elements, as suggested by theoretical cross-section calculations (R. Reedy, personal communication) then ^{3}He production by muons may be more important than expected. Further investigation of this problem will require measurement of the ^{3}He production rate by muons in deeply buried rocks. Such a measurement may be difficult because it requires a well-dated sample with a well-constrained erosion rate, but having an age great enough to permit an accurate measurement.

The fact that the ^{3}He profile in BAK90-77 is not significantly different from the ^{10}Be and ^{26}Al profiles presents an apparent dilemma, in that this core does not suggest the effect of ^{3}He production by muons, although the lithium concentration is not appreciably different (Table 5). One possible

explanation is that the exposure histories of these surfaces are very different. KBA89-77 comes from a bedrock saddle almost devoid of signs of glacial deposition and erosion and may have been formed during the original cutting of the Dry Valleys topography, sometime in the mid-Miocene. Although the idea is controversial, Denton et al. (1984) suggested that a large ice sheet overrode most of the TransAntarctic mountains, cutting the present valley topography, both before and after 9 to 15 myr. Marchant (1990) later used K-Ar dates from volcanic ash to suggest that Arena Valley topography (Fig. 1) has been extant for at least 11.3 myr. Therefore, it is possible that this surface has been exposed for > 10 myr. In addition, overriding ice at high altitudes may not have removed much bedrock material, leaving open the possibility that the bedrock surface saw an even longer effective exposure to cosmic rays.

BAK90-79 was collected near outcrops of Sirius Group tills on Mt. Fleming. The age and glacial history of the Sirius Group are also controversial (see discussion in Brook et al. (1993) [Chapter 4] and Chapter 5), but it has been suggested that Sirius Group tills were deposited as late as 2.5 myr ago (McKelvey et al., 1991; Barret et al., 1993). The absence of a steep ^{3}He depth profile in the core collected there is consistent with the hypothesis that the bedrock surface on Mt. Fleming is related to a glacial event occuring within the last ~ 5 myr.

Conclusions

1) Depth profiles of ^{10}Be and ^{26}Al in two sandstone bedrock cores from the Dry Valleys region of Antarctica exhibit exponential scale lengths of 145 ± 5 and 145 ± 6 for ^{26}Al and 153 ± 13 and 152 ± 5 g cm^{-2} for ^{10}Be. The excellent agreement between the two cores strengthens earlier suggestions that the $^{26}Al/^{10}Be$ ratio in terrestrial rocks does not change with depth and therefore does not change with erosion rate, and may be a useful dating tool (Brown et al., 1992).

2) ^{3}He depth profiles in the two cores are significantly different, giving exponential scale lengths of 135 ± 6 (0.5-0.7 mm grains) and 152 ±7 (1-1.3 mm grains) for one of the cores and 227 ± 14 for the second. The latter is higher than expected for neutron interactions in rocks (~ 150 g cm^{-2}). Models of the combined effects of ^{3}He production by *neutrons and muons* coupled with bedrock erosion and diffusion suggest that the combination of these processes can, in principle, produce exponential profiles like the one observed. Estimates of ^{3}He production rates by previously suggested muon-induced mechanisms, however, fail to reproduce the observed core-profiles and ^{3}He concentrations, suggesting that an additional muon-induced production mechanism is important. (n,T) or (n,^{3}He) reactions with neutrons produced in muon capture are possible ^{3}He-producing mechanisms that have not previously been considered important in this context. Muon-produced ^{3}He may be important in surface exposure studies, particularly in deeply eroded terraines.

Table 1. Helium isotopic data for Core KBA89-77. Unless noted all data are for 0.5-0.7 mm quartz grains. $^3He/^4He$ ratios relative to atmospheric ratio (R_a) (1.384×10^{-6}). ^3He_t= total ^3He. ^3He_r= radiogenic ^3He, ^3He_c=cosmogenic ^3He. $^3He_r = {}^4He \times (^3He/^4He)_r$ where $(^3He/^4He)_r = 0.011 \pm 0.004$ (see text). Means are weighted for analytical uncertainty.

Sample	Depth Int. (cm)	Depth (g)	^4He ccSTP/gx10^8	1s	R/R_a	1s	^3He_t Mat/g	1s	^3He_r Mat/g	1s	^3He_c Mat/g	1s
77-1	0	2.4	2.7	31.7	0.2	21.94	0.19	258.69	2.76	0.13	0.08	258.57	2.76
	0	2.4	2.7	697.0	7.9	1.05	0.05	273.18	13.07	2.85	1.72	270.33	11.35
	0	2.4	2.7	556.1	2.8	1.14	0.01	235.12	2.75	2.27	1.37	232.84	1.37
	0	2.4	2.7	86.7	0.4	7.47	0.04	240.85	1.74	0.35	0.21	240.49	1.53
			2.7								mean	239.18	1.05
77-2a	8.3	13	24.3	654.5	10.3	1.02	0.08	248.49	20.34	2.68	1.61	245.81	20.40
77-2b	13	14.9	31.8	57.0	0.3	11.07	0.05	234.53	1.77	0.23	0.14	234.30	1.77
	13	14.9	31.8	51.2	0.3	13.79	0.19	262.61	3.93	0.21	0.13	262.40	3.93
			31.8								mean	239.04	0.62
77-2c	19.9	22.9	48.8	85.5	0.5	7.69	0.16	244.54	5.23	0.35	0.21	244.19	5.23
	19.9	22.9	48.8	5634.7	85.4	0.12	0.04	249.34	81.80	23.05	13.90	226.29	82.98
			48.8								mean	244.12	0.19
77-3	28.8	31.8	69.1	3529.9	39.6	0.15	0.02	244.26	19.81	14.44	8.71	179.83	21.64
77-4	37.2	41.3	89.5	385.9	5.2	1.21	0.04	175.33	5.81	1.58	0.95	171.75	5.89
77-5	45.1	48.3	106.5	168.6	24.6	2.95	0.05	184.86	27.09	0.69	0.43	184.17	27.10
77-6	60.5	63.5	141.4	70.8	0.2	5.70	0.04	150.20	1.02	0.29	0.17	149.91	1.03
77-7a	66.4	69.3	154.7	397.4	57.9	0.90	0.03	133.01	19.89	1.63	1.01	131.38	19.91
77-7b	72	75	167.6	1239.0	180.5	0.24	0.02	108.27	18.75	5.07	3.14	103.21	19.01
77-8	79.6	82.1	184.3	212.7	2.9	1.45	0.08	115.02	6.67	0.87	0.52	114.15	6.69
77-9	90.1	92.7	208.4	245.1	2.8	1.19	0.05	108.19	5.07	1.00	0.60	107.19	5.11
77-10	105.4	109.2	244.6	580.5	84.6	0.39	0.03	83.97	14.16	2.37	1.47	81.59	14.23
	105.4	109.2	244.6	593.3	3.1	0.41	0.01	90.45	1.20	2.43	1.46	88.02	1.89
			244.6								mean	87.91	0.53
77-1 (.2-.3 mm)	0	2.4	2.7	87.2	0.1	2.06	0.02	66.78	0.75	0.36	0.22	66.43	0.78
77-5 (.2-.3 mm)	45.1	48.3	106.5	736.0	4.3	0.16	0.01	44.33	3.02	3.01	1.82	41.32	3.52
	45.1	48.3	106.5	196.8	1.0	0.75	0.01	55.04	0.78	0.81	0.49	54.23	0.92
			106.5								mean	53.41	1.12
77-10 (.2-.3 mm)	105.4	109.2	244.6	98.5	0.1	0.66	0.02	24.02	0.59	0.40	0.24	23.62	0.63

Table 2. ^{10}Be and ^{26}Al data for KBA89-77 core from Brown et al. (1992).

Sample	Depth (g)	^{10}Be (Mat g-1)	1s	^{26}Al (Mat g-1)	1s
77-1	2.7	20.00	1.18	97.00	10.96
77-2a	24.3	18.30	1.10	74.00	16.58
77-2c	48.8	17.10	1.04	78.90	8.84
77-3	69.1	13.30	0.78	73.90	8.20
77-4+5	97.5	11.50	0.64	50.20	5.17
77-6	141.4	8.96	0.53	45.00	6.57
77-7a	154.7	6.56	0.39	36.90	4.28
77-7b	167.6	6.86	0.41	40.30	4.72
77-8	184.3	5.90	0.38	27.70	3.60
77-9	208.4	3.92	0.79	23.40	3.11
77-10	244.6	4.20	0.25	25.00	5.15

Table 3. Helium isotopic data for BAK90-79 core. $^3He/^4He$ ratios relative to atmospheric ratio (1.384×10^{-6}). ^3He_t= total ^3He. ^3He_r= radiogenic ^3He, ^3He_c=cosmogenic ^3He. $^3He_r = ^4He \times (^3He/^4He)r$ where $(^3He/^4He)r = 0.011 \pm 0.004$ (see text). Means are weighted for analytical uncertainty.

Sample	Depth Int. (cm)		Depth (g)	Size Fract. (mm)	^4He cc STP $\times 10^8$	1s	R/Ra	1s	^3He (Mat/g)	1s	^3Her (Mat/g)	1s	3Hec (Mat/g)	1s
79-1+2	4.1	8.9	13.6	1-1.3	121.29	1.04	19.05	0.19	859.13	11.29	0.50	0.18	858.64	11.29
79-1+2	4.1	8.9	13.6	.5-.7	98.39	14.34	12.71	0.14	464.96	67.96	0.40	0.16	464.56	67.96
79-3	19.1	25.4	46.7	1-1.3	32.63	0.09	63.06	0.46	765.22	5.97	0.13	0.05	765.09	5.97
79-3	19.1	25.4	46.7	.5-.7	79.15	2.12	11.49	0.10	338.04	9.52	0.32	0.12	337.71	9.52
79-6	38.1	42.2	84.3	1-1.3	96.63	0.08	11.23	0.12	403.32	4.32	0.40	0.14	402.93	4.33
79-6	38.1	42.2	84.3	.5-.7	374.11	5.96	1.85	0.04	257.08	7.02	1.53	0.56	255.55	7.04
79-7	53.3	57.2	116.0	1-1.3	145.91	2.41	8.85	0.07	480.00	8.71	0.60	0.22	479.41	8.71
79-7	53.3	57.2	116.0	.5-.7	39.16	0.11	17.64	0.14	256.90	2.13	0.16	0.06	256.74	2.13
79-8	61.0	64.8	132.0	1-1.3	564.63	82.26	2.15	0.04	450.78	66.21	2.31	0.90	448.47	66.21
79-8	61.0	64.8	132.0	.5-.7	135.18	1.42	4.61	0.08	231.63	4.61	0.55	0.20	231.07	4.62
79-8	61.0	64.8	132.0	.5-.7	99.06	0.52	6.43	0.08	236.74	3.24	0.41	0.15	236.34	3.24
			132.0									mean	234.60	0.38
79-11	81.3	85.1	174.7	1-1.3	162.65	4.35	5.22	0.06	315.95	9.15	0.67	0.24	315.29	9.15
79-11	81.3	85.1	174.7	1-1.3	51.92	0.13	10.61	0.12	204.94	2.39	0.21	0.08	204.72	2.39
			174.0									mean	211.80	0.43
79-11	81.3	85.1	174.7	.5-.7	42.32	0.12	11.87	0.10	186.78	1.60	0.17	0.06	186.60	1.60
79-12	100.3	104.1	214.7	1-1.3	166.23	2.73	3.65	0.05	225.69	4.79	0.68	0.25	225.01	4.79
79-12	100.3	104.1	214.7	.5-.7	90.49	0.32	2.96	0.03	99.44	1.16	0.37	0.13	99.07	1.17
79-14	116.8	124.5	253.4	1-1.3	182.75	1.94	2.33	0.05	158.40	3.55	0.75	0.27	157.65	3.56
79-14	116.8	124.5	253.4	.5-.7	143.96	1.53	1.36	0.02	72.59	1.50	0.59	0.21	72.00	1.51

Table 4. ^{10}Be and ^{26}Al data for core KBA89-77. Sample 79-1+2 is combination of 79-1 and 79-2. Means are weighted for analytical uncertainties.

Sample	Depth (g)	^{10}Be (Mat g-1)	1s	^{26}Al (Mat g-1)	1s
79-1+2	6.5	30	1.77	116	6.58
79-3	48.9	20.9	1.17	92.7	6.19
79-3	48.9	25.3	1.48		
	mean	22.59	1.09		
79-6	88.3	16.9	0.845		
79-7	121.5	13.5	0.796	55.3	3.67
79-7	121.5	13.3	0.781		
	mean	13.40	1.79		
79-11	183.0	9.01	0.533	38.9	2.76
79-11	183.0	9.7	0.573		
	mean	9.33	2.56		
79-12	224.9	6.5	0.381	27.4	1.96
79-12	224.9	7.2	0.414		
	mean	6.82	3.57		
79-14	265.4	5.05	0.291	21.25	2.125

Table 5. Lithium concentrations in core top sandstones.

Mt. Fleming	
BAK90-81 leach	4.6
BAK90-81 bulk	3.28
Arena Valley Terrace	
KBA89-77-12 bulk	below detection
KBA89-77-12bulk	5.0

References

Barret, P. J., Adams, C. J., McIntosh, W. C., Swisher, C. C., and Wilson, G. S. (1993). Geochronological evidence supporting Antarctic deglaciation three million years ago. *Nature* **359**, 816-818.

Bilonkon, H., Castagnoli, G. C., Castellina, A., D'Ettore, B., Mannocchi, G., Meroni, E., and Vernetto, S. (1989). Flux of the vertical negative muons stopping at depths of 0.35-1000 hg/cm^2. *Journal of Geophysical Research* **94**(B9), 12,145-12,152.

Brook, E. J., and Kurz, M. D. (1993). Surface exposure chronology using in situ cosmogenic ^{3}He in Antarctic quartz sandstone boulders. *Quaternary Research* **39**, 1-10.

Brook, E. J., Kurz, M. D., Ackert, R. P., Denton, G. H., Brown, E. T., Raisbeck, G. M., and Yiou, F. (1993). Chronology of Taylor Glacier Advances in Arena Valley, Antarctica, using in situ cosmogenic ^{3}He and ^{10}Be. *Quaternary Research* **39**, 11-23.

Brook, E. J., Kurz, M. D., and Brown, E. T. (1991). Depth dependence of *in situ* produced cosmogenic ^{3}He in Antarctic Sandstone Bedrock. *EOS* **72**(44), 575.

Brown, E., Edmond, J. M., Raisbeck, G. M., Yiou, F., Kurz, M., and Brook, E. J. (1991). Examination of surface exposure ages of Antarctic moraines using in-situ produced ^{10}Be and ^{26}Al. *Geochimica et Cosmochimica Acta* **55**, 2269-2283.

Brown, E. T., Raisbeck, G. M., Yiou, F., Kurz, M. D., and Brook, E. J. (1991). Effective attenuation lengths of cosmic rays producing ^{10}Be and ^{26}Al in quartz. *EOS* **72**(44), 575.

Cerling, T. E. (1990). Dating geomorphological surfaces using cosmogenic ^{3}He. *Quaternary Research* **33**, 148-156.

Charalumbus, S. (1971). Nuclear transmutation by negative stopped muons and the activity induced by the cosmic ray muons. *Nuclear Physics* **A166**, 145-161.

Conversi, M. (1950). Experiments on cosmic-ray mesons and protons at several altitudes and latitudes. *Physical Review* **79**(5), 749-767.

Denton, G. H., Prentice, M. L., Kellog, D. E., and Kellog, T. B. (1984). Late Tertiary history of the Antarctic ice sheet: evidence from the Dry Valleys. *Geology* **12**, 263-267.

George, E. P., and Evans, J. (1955). Further observations of cosmic ray events in nuclear emulsions exposed underground. *Proceedings of the Physical Society of London* **68**, 829-835.

Graf, T., Kohl, C. P., Marti, K., and Nishiizumi, K. (1991). Cosmic-ray produced neon in Antarctic rocks. *Geophysical Research Letters* **18**(2), 203-206.

Hall, H. E., and Richmond, M. E. (1974). Stopping rate and energy loss of cosmic ray muons in sand. *Journal of Geophysical Research* **35**, 5503-5506.

Hampel, W., and Kirsten, T. (1975). Measurement of cosmic ray muon-induced radioisotopes. *Proceedings of the 14th International Cosmic Ray Conference*, 1895-1899.

Kurz, M. D. (1986). In situ production of terrestrial cosmogenic helium and some applications to geochronology. *Geochimica et Cosmochimica Acta* **50**, 2855-2862.

Kurz, M. D., Colodner, D., Trull, T. W., Moore, R. B., and O'Brien, K. (1990). Cosmic ray exposure dating with in-situ produced cosmogenic ^{3}He: results from young lava flows. *Earth and Planetary Science Letters* **97**, 177-189.

Lal, D. (1987). Production of ^{3}He in terrestrial rocks. *Chemical Geology (Isotope Geoscience Section)* **66**, 89-98.

Lal, D. (1991). Cosmic ray labeling of erosion surfaces: In situ nuclide production rates and erosion models. *Earth and Planetary Science Letters* **104**, 424-439.

Lal, D., and Peters, B. (1967). Cosmic ray produced radioactivity on the earth. In *Handbuch der Physic* (Flugge, S., Ed.), pp. 551-612, Springer-Verlag, New York.

Lingenfelter, R. E. (1963). Production of carbon-14 by cosmic ray neutrons. *Reviews of Geophysics* **1**(1), 35-55.

Mabuchi, H., Gensho, Y., Wada, Y., and Hamaguchi, H. (1971). Phosphorous-32 induced by cosmic rays in laboratory chemicals. *Geochemical Journal* **4**, 105-110.

Marchant, D. (1990). Surficial geology and stratigraphy in Arena Valley, Antarctica: Implications for Antarctic Tertiary glacial history. MS Thesis, University of Maine at Orono.

Mazor, E., Heymann, D., and Anders, E. (1970). Noble gases in carbonaceous chondrites. *Geochimica et Cosmochimica Acta* **34**, 781-824.

McElroy, C. T., and Rose, G. (1987). *Geology of the Beacon Heights Area: Southern Victoria Land, Antarctica*. New Zealand Geological Survey Miscellaneous Series Map 15. DSIR, Wellington, New Zealand.

McKay, C. P., and Friedman, E. I. (1985). The cryptoendolithic microbial environment in the Antarctic cold desert: temperature variations in nature. *Polar Biology* **4**, 19-25.

McKelvey, B. C., Webb, P. N., Harwood, D. M., and Mabin, M. C. G. (1990). The Dominion Range Sirius Group: a record of the late Pliocene-early Pleistocene Beardmore Glacier. In *Geological Evolution of Antarctica* (Thomson, M. R. A., Crane, J. A., and Thomson, J. W., Eds.), pp. 675-682, Cambridge University Press, New York.

Morrison, P. and Pine, J. (1955). Radiogenic origin of the helium isotopes in rock. *Annals of the New York Academy of Sciences* **62**, 71-92.

Nishiizumi, K., Kohl, C. P., Arnold, J. R., Klein, J., Fink, D., and Middleton, R. (1991). Cosmic ray produced ^{10}Be and ^{26}Al in Antarctic rocks: exposure history and erosion rates. *Earth and Planetary Science Letters* **104**, 440-454

Nishiizumi, K., Winterer, E. L., Kohl, C. P., Klein, J., Middleton, R., Lal, D., and Arnold, J. R. (1989). Cosmic ray production rates of ^{10}Be and ^{26}Al in quartz from glacially polished rocks. *Journal of Geophysical Research* **94**(B12), 17,907-17,915.

Olinger, C. T., Poths, J., Nishiizumi, K., Kohl, C. P., Finkel, R. C., Caffee, M. W., Southon, J., and Proctor, I. (1992). Attenuation lengths of cosmogenic production of ^{26}Al, ^{10}Be, and ^{21}Ne in Bandolier Tuff. *EOS* **73**(14), 185.

Phillips, F. M., Zreda, M. G., Smith, S. S., Elmore, D., Kubik, P. W., Dorn, R. I., and Roddy, D. J. (1991). Age and geomorphic history of Meteor Crater, Arizona, from cosmogenic ^{36}Cl and ^{14}C in rock varnish. *Geochimica et Cosmochimica Acta* **55**, 2695-2698.

Phillips, F. M., Zreda, M. G., Smith, S. S., Elmore, D., Kubik, P. W., and Sharma, P. (1990). Cosmogenic chlorine-36 chronology from glacial deposits at Bloody Canyon, eastern Sierra Nevada. *Science* **248**, 1529-1532.

Qaim, S. M., Wolfe, R., and Liskien, H. (1982). Exitation functions of (n,t) reactions on ^{27}Al, ^{59}Co, and ^{93}Nb. *Physical Review* C **25**(1), 203-207.

Staudacher, T., and Allegre, C. J. (1991). Cosmogenic neon in ultramafic nodules from Asia and in quartzite from Antarctica. *Earth and Planetary Science Letters* **106**, 87-102.

Trull, T., Brown, E., Marty, B., Raisbeck, G. M., and Yiou, F. (1993). Cosmogenic ^{10}Be and ^{3}He exposure ages of Pleistocene beach terraces in Death Valley: Implications for cosmic ray exposure dating of young surfaces in hot climates. *Chemical Geology*, submitted.

Trull, T. W., Kurz, M. D., and Jenkins, W. J. (1991). Diffusion of cosmogenic ^{3}He in olivine and quartz: implications for surface exposure dating. *Earth and Planetary Science Letters* **103**, 241-256.

Walton, J. R., Heymann, D., Yaniv, A., Edgerley, D., and Rowe, M. W. (1976). Cross-sections for He and Ne isotopes in natural Mg, Al and Si, He isotopes in CAF_2, Ar isotopes in natural Ca, and radionuclides in natural Al, Si, Ti, Cr, and stainless steel induced by 12 to 45 MeV protons. *Journal of Geophysical Research* **81**(32), 5689-5699.

Yokoyama, Y., Reyss, J., and Guichard, F. (1977). Production of radionuclides by cosmic rays at mountain altitudes. *Earth and Planetary Science Letters* **36**, 44-56.

Chapter 7 Appendix. Matlab code "difpro.m." Finite difference solution to equation 6 in text. Representative results are shown in Fig. 7.

```
% Chapter 7 Appendix
%Matlab M-file "difpro.m" Aug 19 1993 E. Brook
% Adapted from Findif program of Trull (1990).
%
%The program is a finite difference model designed to
%calculate concentration versus time for spherical grains
%experiencing 3He production by muons
%and neutrons, including the effects of diffusion and erosion.

%The results of the finite difference calculations are presented in Figure 7.

%tmax=1e8;
%k=1;
%while tmax<=1e8                    %loop to calculate profile

%Parameters
e=1e-4;                                 %erosion in g cm-2 yr-1
D=2e-18;                            %Diffusion coefficient in cm2 s-1
Dyr=D*365*24*60^2;                  %Diffusion coefficient in cm2 yr-1
rho=2.8;                            %density in g cm-3
Pn=454;                                 %prod. from neutrons at g-1 yr-1
Pnv=Pn*rho;                         %Pn in at cc-1 yr-1
Pm=50.5;                                %prod. from muons at g-1 yr-1
Pmv=Pm*rho;                         %Pm in at cc-1 yr-1
a=.03;                              %grain radius in cm
vgrain=(4/3)*pi*a^3;                %grain volume in cc
Ln=150;                                 %neutron att length g cm-2
Lm=1700;                            %muon att length g cm-2
gridsp=50;                          %radial step dist
dr=a/(gridsp);                      %radial grid spacing
%dt=.2*dr^2/Dyr;                    %stability parameter
tmax=2e7;                           %total time in yr
tstep=100000;                       %time grid
dt=tmax/tstep;                          %grid time interval in yr
dc=Dyr*dt/dr^2;                         %flux increment

%vector parameters
tp=(0:tmax/tstep:tmax);                 %time variable
t=(tmax-tp);                        %time backward for time-variant production rates
Pnvt=Pnv.*exp(-1*e.*t/Ln);          %neutron-3He production rate each time step
Pmvt=Pmv.*exp(-1*e.*t/Lm);          %muon-3He production rate at each time step

%initialize cold                    %set initial conc. to 0
for i=1:gridsp+1;                   %+1 to set boundary conditions
        cold(i)=0;
        cnew(i)=0;
end

%nested loops to calculate radial profile at each time step
for j=1:tstep
```

```
        for i=2:gridsp

%algorithm below is standard finite difference solution for spherical geometry
%(Crank, J. (1975) The Mathematics of Diffusion. Oxford University Press. 414pp.)

                cnew(i)=cold(i)+(dc/i)*((i-1)*cold(i-1)-
2*i*cold(i)+(i+1)*(cold(i+1)))+Pnvt(j)*dt+Pmvt(j)*dt;
                cnew(1)=cold(1)+6*dc*(cold(2)-cold(1))+Pnvt(j)*dt+Pmvt(j)*dt;
                M(:,j)=cnew';
        end;
cold=cnew;
end;

%Calculate total 3He in grain with volume-weighted average
%For time steps correspon ing to last 300 g cm-2 of model


        for i=2:gridsp
                volout(i)=(4/3)*pi*(i*dr)^3;            %outer volume
                volin(i)=(4/3)*pi*((i-1)*dr)^3;                 %inner volume
                volshell(i)=volout(i)-volin(i);                 %net shell volume
                wtshell(i)=volshell(i)/vgrain;                  %wt for conc. calc.
                wtshell(1)=(4/3)*pi*dr^3/vgrain;        %wt for center conc.
        end


M1=M(1:gridsp,:);               %remove boundary conc.
lplm=300/((tmax/tstep)*e)       %time step corresponding to 300 g cm-2
for i=1:lplm                    %calculate total conc. for 0-300 g cm-2
        fconc(i)=(1/rho)*sum(wtshell'.*M1(:,i+(tstep-lplm)));
end
save
% last section of loop to calculate attenuation length as a function of time
%sol(k)=fconc(1)/fconc(lplm);  %apparent attenuation factor at time index k
%csol(k)=fconc(lplm);          %concentration at time index k
%isol(k)=lplm;                          %step corresponding to 300 g cm-2
%k=k+1;
%tmax=tmax+5e6;
%end
%save dfdat1
```

Biographical Note

Edward Jeremy Brook was born on April 26, 1963, in New York City. He grew up in the small town of Bloomsburg, Pennsylvania, where he attended the local public schools. He received a Bachelors of Science degree, *magna cum laude* , in Geology from Duke University in 1985, and a Masters of Science degree in Geology from the University of Montana in 1988. Ed entered the MIT/WHOI Joint Program in 1988 and was supported by a Department of Defense National Defense Science and Engineering Graduate Fellowship. He married Sally Hacker, a Ph.D. candidate in ecology and evolutionary biology at Brown University, in 1993. In 1993 he received a NOAA Climate and Global Change Post-Doctoral Fellowship in 1993 to study trapped gases in ice cores at the University of Rhode Island.

DOCUMENT LIBRARY

Distribution List for Technical Report Exchange – July 1, 1993

University of California, San Diego
SIO Library 0175C (TRC)
9500 Gilman Drive
La Jolla, CA 92093-0175

Hancock Library of Biology & Oceanography
Alan Hancock Laboratory
University of Southern California
University Park
Los Angeles, CA 90089-0371

Gifts & Exchanges
Library
Bedford Institute of Oceanography
P.O. Box 1006
Dartmouth, NS, B2Y 4A2, CANADA

Office of the International Ice Patrol
c/o Coast Guard R & D Center
Avery Point
Groton, CT 06340

NOAA/EDIS Miami Library Center
4301 Rickenbacker Causeway
Miami, FL 33149

Library
Skidaway Institute of Oceanography
P.O. Box 13687
Savannah, GA 31416

Institute of Geophysics
University of Hawaii
Library Room 252
2525 Correa Road
Honolulu, HI 96822

Marine Resources Information Center
Building E38-320
MIT
Cambridge, MA 02139

Library
Lamont-Doherty Geological Observatory
Columbia University
Palisades, NY 10964

Library
Serials Department
Oregon State University
Corvallis, OR 97331

Pell Marine Science Library
University of Rhode Island
Narragansett Bay Campus
Narragansett, RI 02882

Working Collection
Texas A&M University
Dept. of Oceanography
College Station, TX 77843

Fisheries-Oceanography Library
151 Oceanography Teaching Bldg.
University of Washington
Seattle, WA 98195

Library
R.S.M.A.S.
University of Miami
4600 Rickenbacker Causeway
Miami, FL 33149

Maury Oceanographic Library
Naval Oceanographic Office
Stennis Space Center
NSTL, MS 39522-5001

Library
Institute of Ocean Sciences
P.O. Box 6000
Sidney, B.C. V8L 4B2
CANADA

Library
Institute of Oceanographic Sciences
Deacon Laboratory
Wormley, Godalming
Surrey GU8 5UB
UNITED KINGDOM

The Librarian
CSIRO Marine Laboratories
G.P.O. Box 1538
Hobart, Tasmania
AUSTRALIA 7001

Library
Proudman Oceanographic Laboratory
Bidston Observatory
Birkenhead
Merseyside L43 7 RA
UNITED KINGDOM

IFREMER
Centre de Brest
Service Documentation - Publications
BP 70 29280 PLOUZANE
FRANCE

50272-101

REPORT DOCUMENTATION PAGE	1. REPORT NO. WHOI-93-50	2.	3. Recipient's Accession No.

4. Title and Subtitle
Surface Exposure Geochronology Using Cosmogenic Nuclides: Applications in Antarctic Glacial Geology

5. Report Date
February 1994

6.

7. Author(s)
Edward J. Brook

8. Performing Organization Rept. No.

9. Performing Organization Name and Address
Woods Hole Oceanographic Institution
Woods Hole, Massachusetts 02543

10. Project/Task/Work Unit No.
WHOI-93-50

11. Contract(C) or Grant(G) No.
(C) DPP88-17406
(G) DPP91-17458
EAR91-06820

12. Sponsoring Organization Name and Address
Funding was provided by the National Science Foundation under Grants DPP88-17406, DPP91-17458, EAR91-06810, the Ocean Ventures Fund of the Woods Hole Oceanographic Institution and by a National Defense Science and Engineering Graduate Fellowship from the Office of Naval Research.

13. Type of Report & Period Covered
Ph.D. Thesis

14.

15. Supplementary Notes
This thesis should be cited as: Edward J. Brook, 1994. Surface Exposure Geochronology Using Cosmogenic Nuclides: Applications in Antarctic Glacial Geology. Ph.D. Thesis. MIT/WHOI, WHOI-93-50.

16. Abstract (Limit: 200 words)

Cosmogenic ^{3}He, ^{26}Al, and ^{10}Be were measured in Antarctic glacial deposits in the McMurdo Sound-Dry Valleys region to constrain surface exposure ages. Moraines deposited by the Taylor glacier, an outlet glacier of the East Antarctic Ice Sheet, have exposure ages from ~120 kyr to 2myr. ^{10}Be and ^{3}He ages of 122 ±29 and 134±54 kyr, respectively, for the Taylor II moraine are consistent with deposition during isotope stage 5e (~120 kyr). Mean ^{10}Be exposure ages for older moraines in the valley of 362 ±26 kyr (Taylor III), 1.1±0.1 myr (Taylor IVa) and 1.9±0.1 myr (Taylor IVb) suggest that major ice sheet advances during the last 2 myr were similar in extent to changes during the last glacial-interglacial cycle. Exposure ages for the "late Wisconsin" Ross Sea Drift, deposited on the coast of McMurdo Sound by the Ross Sea Ice Sheet, range from 8-106 kyr, suggesting that this deposit does not, as previously thought, represent a single ice advance in response to lowered sea level at the last glacial maximum. The data suggest instead that the Ross Sea Ice Sheet may have grounded and advanced on the coast several times during the last glacial period.

17. Document Analysis **a. Descriptors**
Antarctica
geochronology
glacial geology

b. Identifiers/Open-Ended Terms

c. COSATI Field/Group

18. Availability Statement
Approved for publication; distribution unlimited.

19. Security Class (This Report)
UNCLASSIFIED

20. Security Class (This Page)

21. No. of Pages
234

22. Price